JAERI-Review
2004-030

ANNUAL REPORT OF KANSAI RESEARCH ESTABLISHMENT 2003
APRIL 1,2003-MARCH 31,2004

February 2005

Kansai Research Establishment

日本原子力研究所
Japan Atomic Energy Research Institute

本レポートは，日本原子力研究所が不定期に公刊している研究報告書です。
入手の問合わせは，日本原子力研究所研究情報部研究情報課（〒319－1195 茨城県那珂郡東海村）あて，お申し越しください。なお，このほかに財団法人原子力弘済会資料センター（〒319－1195 茨城県那珂郡東海村日本原子力研究所内）で複写による実費頒布をおこなっております。

This report is issued irregularly.
Inquiries about availability of the reports should be addressed to Research Information Division, Department of Intellectual Resources, Japan Atomic Energy Research Institute, Tokai-mura, Naka-gun, Ibaraki-ken 〒319－1195, Japan.

編集兼発行　日本原子力研究所

JAERI-Review 2004-030

Annual Report of Kansai Research Establishment 2003
April 1, 2003—March 31, 2004

Kansai Research Establishment

Japan Atomic Energy Research Institute
Kizu-cho, Souraku-gun, Kyoto-fu

(Received December 14, 2004)

This report is the fifth issue of the annual report of Kansai Research Establishment, Japan Atomic Energy Research Institute. It covers status reports of R&D and results of experiments conducted at the Advanced Photon Research Center and the Synchrotron Radiation Research Center during the period from April 1, 2003 to March 31, 2004.

Keywords: Annual Report, Kansai Research Establishment, JAERI, R&D, Advanced Photon Research Center, Synchrotron Radiation Research Center, SPring-8

関西研究所年報 2003
2003 年 4 月 1 日－2004 年 3 月 31 日

日本原子力研究所
関西研究所

(2004 年 12 月 14 日受理)

本報告書は、日本原子力研究所関西研究所の第 5 号の年報であり、2003 年 4 月 1 日から 2004 年 3 月 31 日までの期間（平成 15 年度）に行われた光量子科学研究センター及び放射光科学研究センターの研究活動をまとめたものである。

関西研究所：〒619-0215　京都府相楽郡木津町梅美台 8－1

Contents

This is a blank page.

Foreword

This Annual Report of Kansai Research Establishment (KRE) is delivered to you for the fifth time, covering the KRE activities in FY2003. Number 5 is memorable not only for this reason, but also it signifies that the KRE head quarters have come to the present campus of Kizu, Kyoto 5 years ago (July 1,1999). On June 30, 2004, With the presence of the past three Director Generals (Dr. Masashi Iizumi, the founding DG; Dr. Hideo Ohno, the second DG; Dr. Yoshiaki Kato, the third DG and current Executive Director of JAERI), a celebrative gathering without fanfare was held to commemorate the fifth anniversary of this campus. With the new HQ campus established, KRE has been working as a COE on photon research relevant to energy research, consisting of the Synchrotron Radiation Research Center (SRRC) in Harima (SPring-8) and the Advanced Photon Research Center (APRC) at Kizu.

At SRRC the new beam line (BL22XU) in the RI (radio isotopic) Laboratory has begun its work to investigate, among other things, the magnetic property of heavy metal materials such as uranium and actinides. Their 5f electrons exhibit puzzling properties characteristic of their strongly coupled condensed matter states. A number of breakthrough discoveries are memorable, among which, for example, the amazing and multi-faceted behavior of perovskites has emerged. As we described last year, the Pd-doped perovskite exhibits the self-healing property as a catalytic converter of automobile exhaust gases. The synchrotron X-ray observation revealed this mechanism. In addition SR research shows that the famous high temperature superconductivity of perovskite stems, at least partially, from the phonon (the "BCS") coupling. We also discovered in quantum dielectric matter the radiation-induced unusually large electric susceptibility, which might serve as an agent for the direct energy converter from waste radioactivity to electricity.

The APRC scientists have managed to apply their coherent X-ray laser to investigate the paraelectric property of yet another perovskite material. The first set of 100 TW laser acceleration experiment has commenced, exhibiting an unusually large (>MA) amount of peaked electric current driven by the laser acceleration. The direct observation of the stress in the stainless steel surface by the SPring-8 synchrotron radiation, followed by the removal of this residual stress by the femtosecond laser irradiation, has been demonstrated. This helps the troublesome stress-corrosion cracking (SCC) that has been observed and shown responsible for the shroud cracks found in many BWR's in Japan last summer.

International initiatives to promote the world-wide and Asia-wide photon research have been taken by the leadership of JAERI (Japan Atomic Energy Research Institute) and Kansai. For example, International Committee for Ultrahigh Intensity Lasers (ICUIL) has been initiated by the leadership of JAERI and other world scientists to lead the world-wide organization on emerging intense laser science and technology under the auspices of IUPAP (International Union of Pure and Applied Physics). The Tri-lateral collaboration (Japan-Korea-China) on the same subject has been agreed upon by the Director-Generals of the Science Ministries of the three countries. (JAERI Kansai chosen as the hub for Japan.) We believe that the frontier science of photon needs the concentrated effort of a COE as well as broad network of world-wide scientists. Also initiated this year is the Asian Intense Laser Network.

We invite your participation to KRE whether in the collaborative lab work, in theoretical long-distance web work, or in science outreach activities. Happy photon research and welcome to Kansai!

Toshiki Tajima
Director General

1. Summary

JAERI is a research institute complex of nuclear science and technology where broad-ranged top-of-the-line energy research facilities can be synthetically utilized that encompass from synchrotron radiation, X-ray laser, to high-intensity proton accelerator(under construction), accelerators of electron beam and ion beam, nuclear research reactors and advanced computer system. Kansai Research Establishment was established in 1995 to promote the research of laser and synchrotron radiation with the integrated theme of bright 'light'.

A new Long-Term Program for research, development and utilization of nuclear energy was drawn up in The Atomic Energy Commission of Japan in November 2000. This Program summarizes that nuclear science and technology has achieved remarkable developments in the 20th century and brought about substantial changes in lives and lifestyles. In the 21st century, the advance of nuclear science and technology is expected not only to form the basis for development of new energy technologies but also to serve to explore new frontiers. High brilliant synchrotron radiation and ultrahigh intensity lasers can contribute to the advance of life science and materials science related to nano-structure, environment and information technology. As JAERI is expected to join with JNC(Japan Nuclear Cycle Development Institute) in 2005 to become an integrated independent agency responsible for the over all atomic energy researcher in Japan our research will be pivotal in promoting the new direction in atomic energy research in Japan.

This Annual Report summarizes the research activities at both Synchrotron Radiation Research Center and Advanced Photon Research Center in the period from April 1, 2003 until March 31, 2004. Previous Annual Reports of Kansai Research Establishment of JAERI are shown in Table 1.

Table 1 Previous Annual Reports of Kansai Research Establishment of JAERI

JAERI-Review 2001-003	(March 2001)
JAERI-Review 2001-046	(February 2002)
JAERI-Review 2002-042	(February 2003)
JAERI-Review 2003-042	(February 2004)

2. Facilities of the Advanced Photon Research Center

The core competence of APRC is advanced lasers with high brilliance and high fluence. These lasers include a compact ultra short pulse peta watt laser, a fully spatially coherent X-ray laser, and high-power extremely efficient free-electron laser. These lasers are dedicated as tools for the exploration of new nuclear energy science and technology and the development of novel radiation sources of X-rays, γ -rays, electrons and ions. In order to support this development, simulation research using supercomputers (Super Simulation Center for Photon-SSCP) and development of fundamental technologies of optical elements and devices like laser crystals, mirrors, gratings, etc. are also implemented in the APRC.

The APRC has engaged in the research and development of advanced lasers such as compact high power lasers with a peak power of petawatts (10^{15} watts), X-ray lasers with full coherency, and free electron lasers with high average power and high efficiency. Utilizing these lasers, the APRC also challenges generation and application of high-energy ion and X-ray, development of new particle sources, X-ray microscopes, etc.

These advanced lasers and generated highly energetic ions and X-rays have distinctive characteristics such as high intensity, high coherency, or short pulse, which are different from conventional radiations. The APRC develops various techniques for utilizing these high quality radiations to various fields of science and technologies, along with JAERI's own knowledge of neutrons, synchrotron radiation, and ion beams research. The APRC also collaborates with industries and universities in research and development activities.

A bird's-eye view of the Advanced Photon Research Center is shown in Fig. 1. Research activities are mainly progressing in a laboratory building where four big laboratories for development and applications of high power lasers are provided, and the researchers' office building where a super computer is equipped. There are a conference hall where we can hold symposiums and meetings to introduce research results of Kansai Research Establishment, and the guesthouse for accommodation.

The buildings with a dome at the right foot in the photograph is the "Kids' Science Museum of Photons", which was opened in July 2001, contributing to science educations for the younger generation in Keihanna Science City. The number of visitor has counted up to 100,000 on 11 February 2004. The IT-based laboratory (ITBL) building shown at the left top was opened in March 2002.

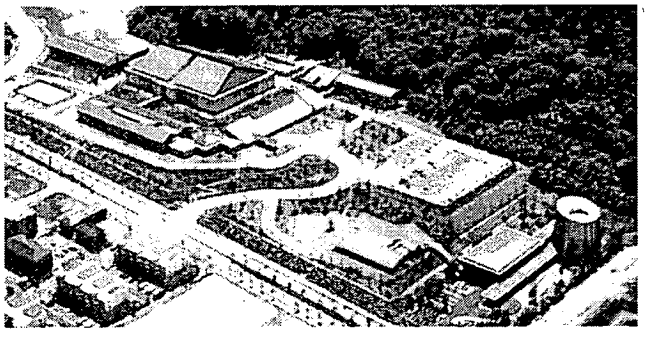

Fig. 1 The Advanced Photon Research Center

High average power laser lab.

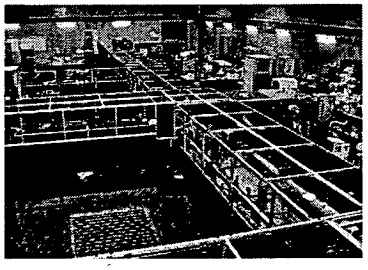

High peak power laser lab.

Laser acceleration and high field science lab.

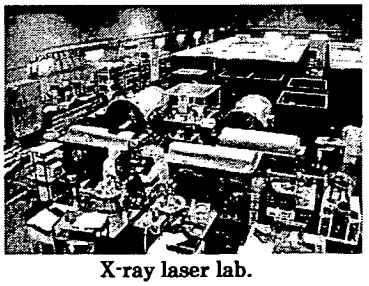

X-ray laser lab.

Fig. 2 Four main laboratories of the Advanced Photon Research Center

3. Facilities of the Synchrotron Radiation Research Center

SPring-8 is a synchrotron radiation photon source, the brightest third-generation photon source in the world. Such a bright photon source can be employed to advance the materials science research, environmental research and nanoscience and biological research. SRRC of JAERI has contributed crucially to take a leadership in applications of this facility, in particular to materials science.

SPring-8 was operated in the 2003 fiscal year as scheduled. Four JAERI beam lines were also operated favorably. In the beamline **BL11XU** (see Fig. 1), research of nuclear resonant scattering of materials, resonant inelastic scattering of colossal magnetoresistance manganites and surface structure during molecular beam epitaxy growth were done. In the beamline **BL14B1** (see Fig. 2), structure analysis under high pressure, correlation between structure and function of materials were investigated. The **BL22XU** (see Figs. 3 and 4) beamline has the experimental equipments for high pressure studies and X-ray diffraction and also for studying the magnetic structure of uranium materials in the radioisotope laboratory (RI lab.). In the beamline **BL23SU** (see Figs. 5 and 6), surface chemistry, radiation effect on DNA and electronic structure of electronic materials were studied, and Uranium compounds were investigated by using the x-ray absorption magnetic circular dichroism (MCD) and the photoelectron spectroscopy in the RI lab..

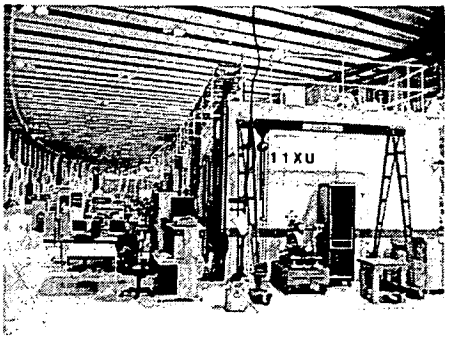

Fig. 1 BL11XU

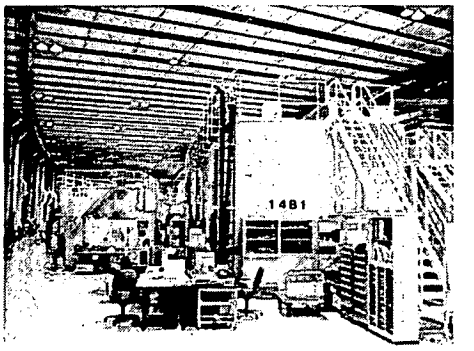

Fig. 2 BL14B1

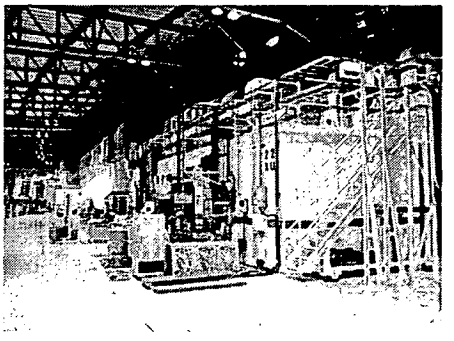

Fig. 3 BL22XU

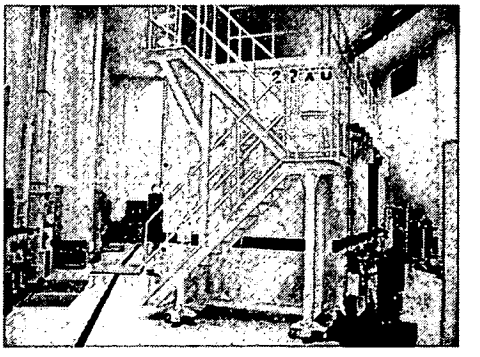

Fig. 4 BL22XU（in the RI lab.）

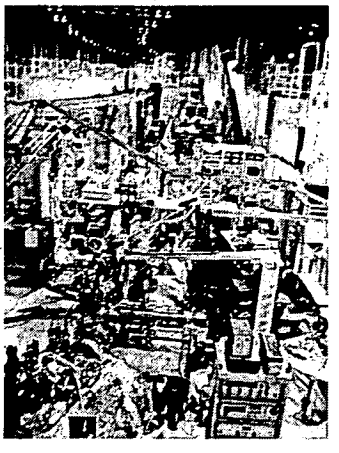

Fig. 5 BL23SU

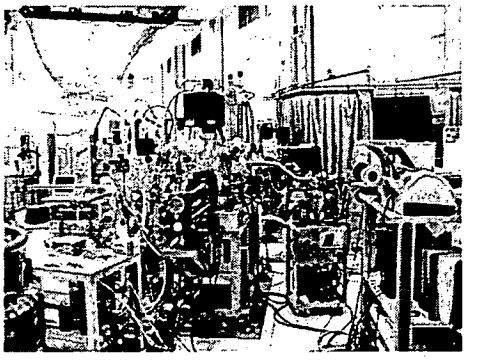

Fig. 6 BL23SU（in the RI lab.）

4. Advanced Photon Science

Toyoaki KIMURA

The APRC is pursuing the research and development of advanced photon sources such as a compact, ultra-short, high intensity laser, x-ray laser, and a superconducting linac-based free electron laser (FEL) and their applications. In the report on integration of the Japan Atomic Energy Research Institute (JAERI) and the Japan Nuclear Cycle Development Institute (JNC) the research on the advance photon science is defined as the research and development of radiation applications.

In FY2003, the following remarkable progress has been made in the development of advanced photon sources. In the development of a compact, ultra-short, high intensity laser, the average output power of 360 W and a repetition rate of 1 kHz have been achieved in the development of a LD-pumped Nd:YAG laser, which is a pumping light source applicable to a titanium-doped sapphire (Ti:sapphire) chirped pulse amplification (CPA) laser system. For the experiments on laser-driven radiation sources of high energy ions and electrons and X-rays a 100-TW laser system has been operated for about 2 months (122 hours). We have also developed a next generation of ultra-short, high intensity laser by using a laser material with high excitation density and efficiency. The output energy of 20 mJ/pulse was obtained in the regenerated amplifier at 20 Hz with a liquid nitrogen-cooled laser crystal of Yb:YLF. This result encouraged the development of an over peta-watt laser system.

In the R&D of the X-ray laser system, spatial distributions of electron density profiles in laser-produced plasmas were successfully obtained with an X-ray interferometer in a joint-experimental campaign with University Paris Sud. In the experiments for increasing the output intensity of X-rays with spatially full coherence, the amplification gain of about 1000 was obtained by optimizing the parameters relevant to the amplification such as spatial uniformity of target plasma density in the double silver target system.

In the research of the free-electron laser (FEL), we have started to increase the output power of the energy-recovery type linac (ERL) -based FEL system up to 20 kW. We also confirmed the FEL pulse shows self-chirping behavior. We successfully hosted the 25th International Conference on Free Electron Lasers (FEL 2003) at Tsukuba in September.

Remarkable progress was made in the application of these advanced lasers. In the research on high field science, the study on the generation of high energetic protons is aimed at developing a compact laser-driven ion source which is applicable as an injector of a proton accelerator for cancer therapy. We observed energetic electrons (>2 MeV) and protons (>1 MeV) produced by focused 50 fs Ti:sapphire laser pulses at the intensity of $>10^{18}$W/cm^2. We have also installated a target chamber system for the experiments with the 100 TW Ti:sapphire CPA laser. In the research on laser wakefield acceleration, we carried out the experiments by using 20 TW, 20 fs laser pulses. The experiments resulted in ultrahigh current relativistic electron beam acceleration of the order of mega ampere with an energy spectrum up to 40 MeV.

In the application research with femto-scond lasers, we investigated a new method for preventing stress-corrosion cracking in which serious phenomena were recently found in core shrouds of nuclear power reactors in Japan. We demonstrated that we could remove the surface layer including residual stress which is the origin of SCC without giving any additional thermal effects to the material.

In the developments of laser optical elements, we optimized the temperature of heat conduction in the Nd:YVO_4 and YVO_4 bonding process to prevent precipitates at the bonded interface. In the developments of soft x-ray optical elements, we fabricated the multilayer mirrors consisting of oxide and nitride layers for use around the K-absorption edge of carbon (λ = 4.4 nm). The measured values of soft X-ray reflectivity of the CO_3O_4/SiO_2 and the Mix/BN multilayer mirrors are about 2.0 % and 1.5 % at the wavelength of 4.5 nm, respectively. We also examined a natural muscovite mica crystal to develop the polarization elements in the soft X-ray region of 1-2 keV and confirmed that muscovite mica is a promising candidate as a reflection-type polarizer, with approximately 1.4% reflectance for s-polarization around 0.9 keV.

In the research on computer simulation and analysis, we found the possibility to generate ions with energy region above GeV by irradiating laser pulses with an intensity of 10^{23} W/cm^2 or more onto plasmas with a thickness of 1 μm and a solid density. The atomic data and atomic process codes, which have originally been developed for the study of X-ray lasers, are applied to the investigation of the complex spectrum of Xe and Sn plasmas in the extreme-ultra-violet (EUV) wavelengths. It was found that the effect of satellite lines and opacity are essential for estimating the conversion efficiency of the laser pumped Xe and Sn sources.

4.1 High Peak Power Laser Development

Laser System Development Group

Koichi YAMAKAWA

The research activities of the Laser System Development Group in 2003 are focused on the following topics:

- Understanding the dynamical behavior of atoms and clusters exposed to extreme fields.
- Development of compact , high repetition rate, diode pumped solid-state lasers.
- Quantum control of chemical reactions.

Production of highly charged ions via laser-matter interactions has been a subject of great interest ever since high power laser sources became available. Over the last two decades the number of groups have studied the interaction of strong laser fields with atoms in the regime from multiphoton to tunneling ionization[1]. In the tunneling regime, ionization of atoms exposed to the strong laser fields has been investigated extensively for many atomic gases in the intensities ranging from 10^{13} to 10^{16} W/cm^2 [2-5]. Understanding the dynamical behavior of atoms exposed to external fields is fundamental to provide knowledge of properties of matter under such extreme conditions, as well as solutions to control new physical effects for many applications.

Modern high-power lasers can now access to extraordinary high intensities of 10^{20} W/cm^2 in extremely short durations of 10-fs at unprecedented high repetition rates of 36,000 shots per hour. Such super-strong fields correspond to 60 times the field binding the ground state electron in the hydrogen atom and inner shell electrons for heavy (high Z) atoms do not remain within the atomic center. At such intensities the electron velocity in the laser field also becomes relativistic. Thus, the free electrons move at close to the speed of light and their mass changes dramatically compared to their rest mass. Consequentially, it is now possible to test many-electron dynamics of complex atoms in radically new ways.

We have studied tunneling ionization of complex rare gas atoms (Xe, Kr and Ar) by using a 100-TW, 20-fs, 10-Hz Ti:sapphire laser system. Highly charged ions as high as Xe^{26+}, Kr^{19+} and Ar^{16+} have been observed at the laser intensity up to 2.6 x 10^{19} W/cm^2 [6]. We have found that the ionization of many electron atoms at a given intensity is dependent both on the ionization potential and on the atomic species in the fully relativistic field for the first time to our knowledge. It is also concluded that the conventional treatments of multiple ionization do not correspond to our experimental findings for the Xe atom. The essential findings were (1) unexpected ionization probabilities for lower charge states, also (2) no interplay between the inner- and outer-shells by screening, and (3) suppression of nonsequential ionization towards relativistic intensity and also few optical cycle regimes. These new findings have given us a hint of how many-electron systems behave in such fields [7].

References

1) See for example, *Multiphoton Processes*, edited by L. F. DiMauro, R. R. Freeman and K. C. Kulander, AIP Conf. Proc. No. **525** (AIP, New York, 2000).
2) F. Yergeau, S. L. Chin, and P. Lavigne, J. Phys. B **20**, 723 (1987).
3) S. Augst, *et al.*, Phys. Rev. Lett. **63**, 2212 (1989).
4) E. Mevel, *et al.*, Phys. Rev. Lett. **70**, 406 (1993).
5) S. Larochelle, A. Talebpour, S. L. Chin, *J. Phys. B* **73**, 1201 (1998).
6) K. Yamakawa, *et al.*, Phys. Rev. A **68**, 065403 (2003).
7) K. Yamakawa, *et al.*, Phys. Rev. Lett. **92**, 123001 (2004).

4.1.1 Optical field ionization of rare gas atoms by ultrashort laser pulses with peak intensities greater than 10^{19} W/cm^2

Yutaka AKAHANE, Yuji FUKUDA, Makoto AOYAMA, Norihiro INOUE,

Takayuki UTSUMI, Koichi YAMAKAWA

1. Introduction

The presence of strong laser fields radically alters the nature of atomic systems. Nowadays, the evolution of reliable, ultrafast, chirped-pulse-amplification (CPA) technologies has allowed systems to produce 10-fs-range, multiple-terawatt peak power pulses[1]. Such lasers can access to focused peak intensities of 10^{20} W/cm^2 at 36,000 shots per hour. These intensities correspond to 60 times the field binding the ground state electron in the hydrogen atom and inner shell electrons for heavy (high z) atoms can not be stayed within the atomic center. At such intensities the electron velocity in the laser field also becomes relativistic. Thus the free electrons move at close to the speed of light and their mass changes dramatically compared to their rest mass. Consequentially, it is now possible to study of ionization dynamics of the atoms in entirely new regimes. We report on optical field ionizations of complex rare gas atoms exposed to super-intense 800-nm, 10-Hz laser pulses of 25-fs duration. We have studied multiple ionizations of three rare gases (Xe, Kr and Ar) and observed charge-states as high as Xe^{26+}, Kr^{19+} and Ar^{16+} at the laser intensity of up to ~ 3 x 10^{19} W/cm^2 in vacuum[2]. We have compared integral ionic charge state yields of these atoms with those results from the ADK model[3]. We found that the ionization of many-electron atoms is dependent both on the ionization potential and on the atomic species in the fully relativistic field. It is suggested that the non-relativistic ADK tunneling ionization theory is still valid to describe the bulk of the ion yields of various complex atoms even in the relativistic regime.

2. Experiment

To perform an ultrahigh-field atomic phtoionization experiment, we used a state-of-the-art 100-TW, 20-fs, 10-Hz Ti:sapphire CPA laser system which is capable of producing focused laser intensity up to 10^{20} W/cm^2 [4]. The diameter of the focal point of the attenuated laser beam was analyzed by an objective lens associated with a CCD camera. Using an off-axis parabolic mirror of focal length of 161 mm, we obtain the spot diameter of 11 μm at 1/e^2 with 53% of full energy, which corresponds to the estimated peak intensity of 2.6 x 10^{19} W/cm^2. Rare gases such as Xe, Kr, and Ar were introduced into the chamber with a precision leak valve. Gas pressures in the chamber were controlled typically below 1 x 10^{-7} Torr in order to reduce space charge and collective effects. The ion species are separated with a 1-m time-of-flight (TOF) mass spectrometer and detected with a dual micro channel plates (MCP).

3. Results

Figure 1 shows the typical TOF mass spectrum of Xe ions produced at the laser intensity of up to 2.6 x 10^{19} W/cm^2. As shown in Fig. 1, the charge states up to Xe^{26+}, which corresponds to Ni-like Xe have been observed. The appearance of Ar^{8+} is due to the result of mixed gases in order to determine the relative laser intensities among the gases. As for Kr and Ar, the charge states have also been detected as high as19 and 16, which corresponds to Cl-like Kr and He-like Ar, respectively. These are the highest charge states produced by the collisionless ionization of these atoms to our knowledge. In order to clarify the ionization dynamics of the different atomic species in the fully relativistic laser field, we first compare the integral ionic charge state yields of Xe, Kr and Ar with those results from the ADK model. We calculate the minimum sum of squares differences between the experimental values obtained at the intensity of 2.6 x 10^{19} W/cm^2 and the calculated yields at the various intensities between 1.0 x 10^{18} W/cm^2 and 3.0 x 10^{19} W/cm^2 for Xe, Kr and Ar, respectively. The best agreement between the experimental and theoretical yields occurs at the theoretical laser intensities of 3.5 x 10^{18} W/cm^2, 4.1 x 10^{18} W/cm^2 and 1.3 x 10^{19} W/cm^2 for Xe, Kr and Ar, respectively. The

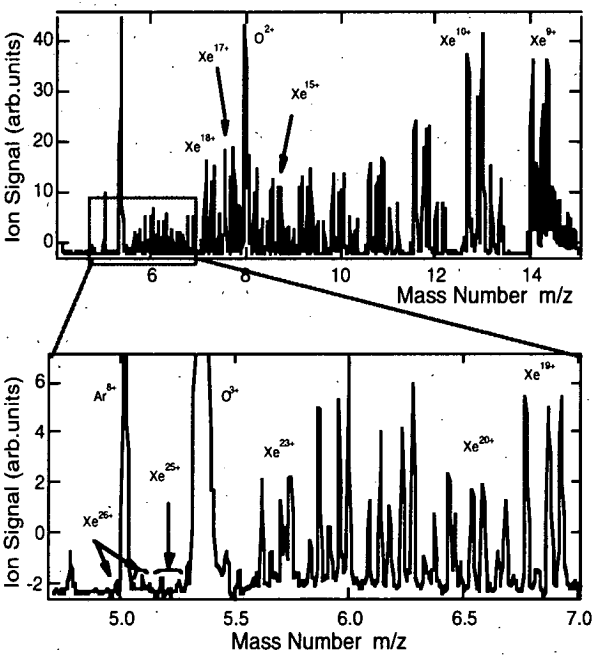

Fig. 1 Time-of-flight ion mass spectrum of xenon at the laser intensity of 2.6 x 10^{19} W/cm^2.

calculated intensity disagrees with the experimental one for Ar by a factor of 2, while a comparison between the theoretical intensities from the ADK model and the experimental ones for Kr and Xe shows rather poor agreement. As a result, the model derived the peak intensities vary by a factor of 3.7. We emphasize that we repeated the measurements for several times and saw no discernible changes in the relative intensities between all these atoms, which means that the disagreements are due to some physical differences in the ionization processes.

In 1989, Augst et al. have found that the appearance intensity is dependent both on the ionization potential and on the atomic species[5]. The appearance intensity is defined as the intensity at which a small number of ions are produced on a particular charge state. It was observed that there was systematic lowering of the appearance intensity with increasing atomic number. Considering the situation of our results, we first predicted the saturation intensities on each charge state of the three rare gases by the ADK model. The saturation intensity is where the growth in the ion-yield curve levels off to a 3/2 power law in intensity. We use the saturation intensity instead of the appearance intensity, since the saturation threshold is independent of the gas pressures and therefore eliminates an experimental uncertainty somewhat. Fig. 2 shows a plot of the calculated saturation intensities for the each charge state of ions of the three rare gases versus the ionization potential. The saturation intensities of Xe, Kr and Ar shown in Fig. 2 separate into a group of curves. The curves of smaller atomic numbers lie above those of larger atomic numbers. This ordering means that the laser fields remove electrons from higher valence shells more easily than from lower valence shells for a fixed ionization potential. Because the ion yields of Xe^{25+}, Kr^{19+} and Ar^{15+} are close to or above saturations at the highest laser intensities, the saturation intensities of these charge states were calculated to be 3.2 x 10^{18} W/cm^2, 5.0 x 10^{18} W/cm^2 and 1.0 x 10^{19} W/cm^2, respectively. Across all the three rare gases the calculated peak intensities is differ by a factor of 3.1, indicating a validation of relative agreement between the experimental data and the calculated yields.

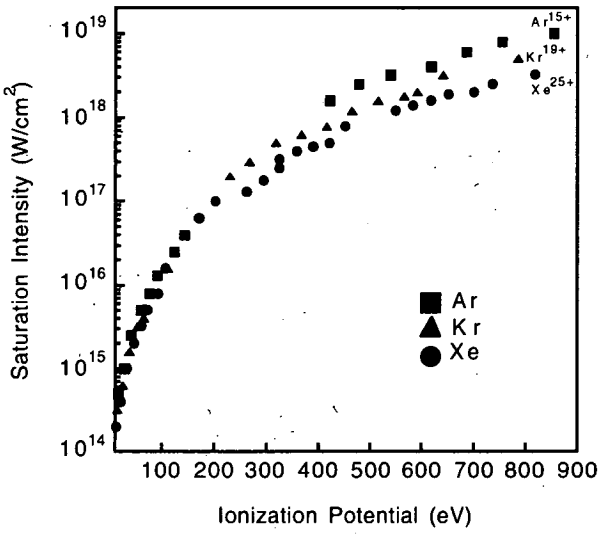

Fig. 2 Calculated saturation intensity versus ionization potential for three rare gas atoms.

It is therefore suggested that the non-relativistic ADK tunneling ionization theory is still valid to describe the bulk of the ion yields of various complex atoms even in the relativistic regime. Though our result shows initial ionization process is non-relativistic even in the relativistic field, an ejected electron should obtain the relativistic energy in the final continuum state that is on the order of its rest energy mc^2. For example, the ponderomotive energy of the free electron is on the order of 1 MeV at laser intensity of over 1 x 10^{19} W/cm^2 and therefore the electron velocity becomes fully relativistic. Further experiments are currently underway to measure a forward electron momentum due to the relativistic quiver motion and kinetic energy of electrons[6] and relativistic high-order harmonics[7] in the super-strong laser field.

References

1) K. Yamakawa and C. P. J. Barty, IEEE J. Select. Topics Quantum Electron. **6**, 658 (2000).
2) K. Yamakawa, *et al.*, Phys. Rev. A **68**, 065403 (2003).
3) M. V. Ammosov, N. B. Delone, and V. P. Krainov: Sov. Phys. JETP **64**, 1191 (1986).
4) K. Yamakawa, *et al.*, Opt. Lett. **23**, 1468 (1998).
5) S. Augst, *et al.*, Phys. Rev. Lett. **63**, 2212 (1989).
6) C. I. Moore, J. P. Knauer, and D. D. Meyerhofer, Phys. Rev. Lett. **74**, 2439 (1995).
7) S. X. Hu and C. H. Keitel, Phys. Rev. A **63**, 053402 (2001).

4.1.2 Ionization dynamics of a Xe atom in super-strong laser fields

Yutaka AKAHANE, Yuji FUKUDA, Makoto AOYAMA, Norihiro INOUE,
Takayuki UTSUMI, Koichi YAMAKAWA

1. Introduction

Understanding the dynamical behavior of atoms exposed to external fields is fundamental to provide knowledge of properties of matter under such extreme conditions, as well as solutions to control new physical effects for many applications. In this report, we present on optical field ionization of a Xe atom by 800-nm, 10-Hz laser pulses of 20-fs duration with peak intensities ranging from 10^{13} to 10^{18} W/cm^2.

2. Experiment

The present work uses a table-top, next generation Ti:sapphire chirped-pulse amplification (CPA) system that generates 100-TW, 20-fs, 10-Hz pulses[1]. In order to clarify the ionization dynamics of the Xe atom, measurements of the ion yields as a function of the laser intensity were carried out with the signal-averaging technique at the intensity range from 10^{13} to 10^{18} W/cm^2. In our experiment, the linearly polarized laser light was focused using an off-axis parabolic mirror of focal length 161 mm in the center of the ionization chamber having a background pressure below 8 x 10^{-9} Torr. The Xe pressure in the chamber was controlled typically below 10^{-7} Torr in order to reduce space charge and collective effects. Three sets of intensity scans were performed with a combination of different amplifier stages and partial reflection mirrors in the intensity range from (1) 6 x 10^{13} to 9 x 10^{15} W/cm^2, (2) 6 x 10^{14} to 1.5 x 10^{17} W/cm^2, and (3) 1 x 10^{17} to 1.5 x 10^{18} W/cm^2, respectively. The ion species are separated with a 1-m time-of-flight mass spectrometer and detected with dual micro channel plates. Each data run consists of 1,000 laser shots with the laser energy-fluctuations of less than 5%.

3. Results

The results of the ion-yield data for Xe as a function of laser intensity are shown in Fig. 1. The theoretical curves calculated by the ADK model are also shown as the references in this figure. The results presented in Fig. 1 clearly show disagreement between the experimental ion curves and those from the ADK model along the laser intensity scale. In order to compare between the experimental ion curves and those obtained theoretically, we evaluate a shift factor on each ion curve along the intensity scale by the least-squares method. The experimental curve of Xe^{2+} already begins to disagree with the theoretical one by 15%, while a comparison between the experimental curves of Xe^{3+} to Xe^{6+} and those from the ADK model shows rather poor agreement. For example, the experimental curve of Xe^{4+} disagrees with the theoretical one by nearly 50%.

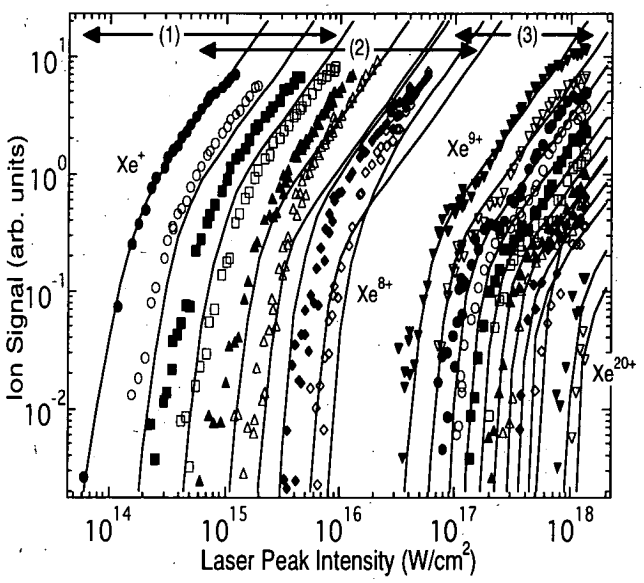

Fig. 1 Comparison of experiment and theory for tunneling ionizations in Xe as a function of laser intensity. Experiment: λ = 800-nm, τ = 20-fs, Theory: the quasi-classical tunneling theory (solid curves) with no shift in laser intensity.

In general, the atomic ionization energy is a unique and fundamental property for all elements. Therefore, the influence of the many-electron dynamics in the strong laser field should not be neglected. More surprisingly, the experimental curve for Xe^{9+} returns to fit the theoretical one subsequently ejecting all the electrons from the n = 5 shell of Xe. This result indicates the absence of a relationship between the

4d inner shell and the n = 5 outer shell. Therefore, we may emphasize that the ionization processes strongly depend on the atomic structure and outermost shell density. So far, a small amount of theoretical work has been carried out to test the dynamics and interplay of outer and inner shells in complex atoms. L'Huillier et al. have shown that the 4d inner shell will be shielded from the external field by the outer 5p shell[2]. In the case, multiple ionization in the n =5 shell, therefore, varies by screening effects. For a given external laser intensity, the effective (local) intensity should increase for each step of the stripping process by screening, increasing the probability for creation of higher charge states. This is what we observe in the experimental ion curves towards lower intensities. Considering the result in the case of Xe^{9+}, it is also favorable to the case suggested by L'Huillier et al. It is simply explained as follows. Stripping of the outer shell occurs by the leading edge of the pulse, which reduces the screening. The effective intensity in the 4d inner shell then approaches the given external intensity and leads to sequential tunneling ionization.

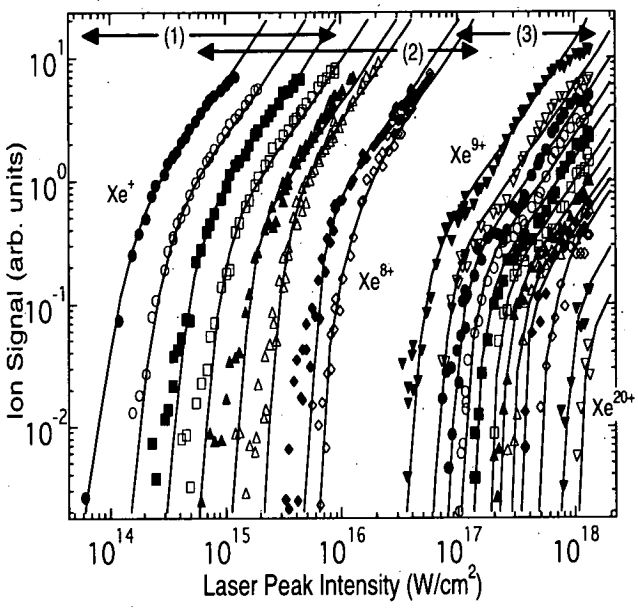

Fig. 2 Comparison of experiment and theory for tunneling ionizations in Xe as a function of laser intensity that is identical to Fig. 1, but with shift the theoretical curves along the laser intensity scale to match the experimental data.

As part of the comparison between the experimental curves and those obtained theoretically, we shift the theoretical ones along the laser intensity scale to match the data in order to look at the presence of the knee structures described previously. This is presented in Fig. 2 and made based on the shift factor. From Fig. 2, it is clear that the experimental ion yields of Xe^{2+} to Xe^{7+} are more effective by orders of magnitude than predicted by the ADK model at the laser intensities below saturation of ionizations while the ion yields of Xe^{8+} to Xe^{20+} can be thought to follow the calculations. The discrepancies in Xe^{2+}- Xe^{7+} yields between the experiment and the ADK model at these intensities are a signature of NS ionization. From a classical point of view, the tendency of the ionic charge state yields of over Xe^{9+} can be qualitatively explained by suppression of NS ionization with increasing laser intensities towards the relativistic regime. In this regime the magnetic field component is no longer negligible, causing a forward drift momentum of photoelectrons in the laser propagation direction. For example, a result of a classical trajectory of the ionized electron by our one-dimensional calculation shows that the displacement of the electron along to the laser propagation direction is of the order of 10-nm over the half laser cycle at the laser intensity of 10^{17} W/cm^2. Then, the electron loses the parent ion and no rescattering will occur. Our experimental result, therefore, confirms the indirect evidence for the suppression of NS ionization of Xe at the *fixed* relativistic laser intensity[3]. It is concluded that the conventional treatments of multiple ionization do not correspond to our experimental findings for the many-electron atom[4]. The essential findings were (i) unexpected ionization probabilities for lower charge states, also (ii) no interplay between the inner- and outer-shells by screening, and (iii) suppression of nonsequential ionization towards relativistic intensity and also few optical cycle regimes. These new findings have given us a hint of how many-electron systems behave in such fields.

References

1) K. Yamakawa, *et al.* Opt. Lett. **23**, 1468 (1998).
2) A. L'Huillier, L. Jönsson, G. Wendin, Phys. Rev. A. **33**, 3938 (1986).
3) M. Dammasch, *et al.* Phys. Rev. A **64**, 061402(R) (2001).
4) K. Yamakawa, *et al.*, Phys. Rev. Lett. **92**, 123001 (2004).

4.1.3 100-mJ, 1-kHz, single-stage amplifier of femto-second pulses

Junji KAWANAKA, Hajime NISHIOKA[a)], Koichi YAMAKAWA, and Ken-ichi UEDA[a)]
a) Institute for Laser Science, University of Electro-Communications

1. Introduction

Femto-second pulse lasers with sub-joule output power in kilo-hertz repetition rate are in high demands for advanced application fields such like high order harmonic generation and micro-processing. A 60-mJ diode-pumped chirped-pulse regenerative amplifier has been developed.[1] A cryogenically cooled Yb: $LiYF_4$ (YLF) crystal are used to improve the laser characteristics in diode-pump. The repetition rate was, however, still 20 Hz. Our next goal is 100 mJ, 1 kHz operation. Thermal effects are significantly serious especially in high energy density operation of Yb-doped materials. Fortunately, thermal conductivity of the laser crystal is significantly improved at low temperature. In addition, the thermo-optic coefficient (dn/dT) and the coefficient of the thermal expansion become lower. In this letter, temporally integrated crystal temperature has been calculated for sapphire-sandwiched Yb:YLF crystal in 100 mJ, 1kHz operation.

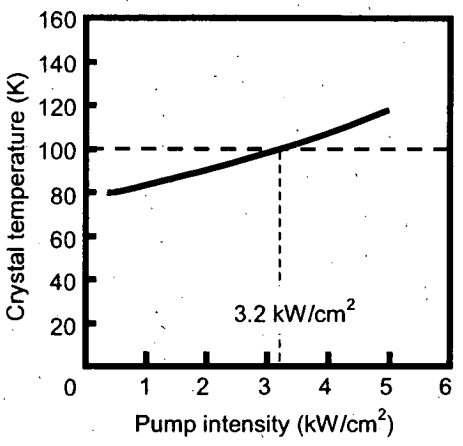

Fig. 1 Crystal temperature as a function of pump intensity.

2. Regenerative amplifier design

A 0.6-mm thick Yb:YLF disk crystal is sandwiched with 2-mm thick sapphire plates for efficient heat removal. The crystal is conductively cooled by a liquid nitrogen cryostat. The crystal temperature was calculated as a function of a pump intensity shown in fig. 1. The pump intensity should be below 3.2 kW/cm^2 to keep the crystal temperature below 100 K, where the 4-level laser system is realized. The small increase of the crystal temperature with 23 K is not serious problem for thermal lensing and thermal birefringence. Figure 2 shows our designed regenerative amplifier. A three-pass amplification system is adopted in a regenerative cavity to realize efficient energy extraction. Because a single-pass laser gain is not so high in such low pump intensity. A calculated total pump power for 100 mJ, 1 kHz operation was 235 W in cw pump.

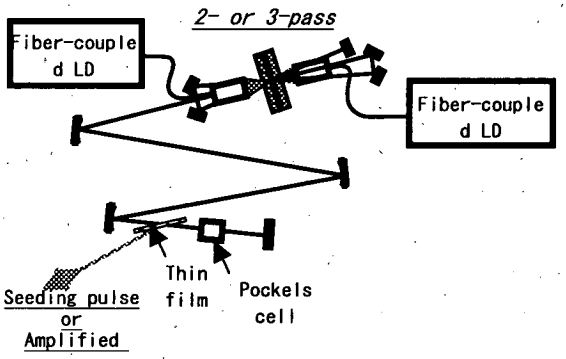

Fig. 2 Regenerative amplifier at 1-kHz rep. rate.

3. Results

A 100 mJ, 1 kHz regenerative amplifier has been designed. The temporally integrated heat effects due to pump power are not serious yet in such low pump intensity. Crystal damage in transient heating due to reabsorption of an amplified pulse must be studied around 100 K.

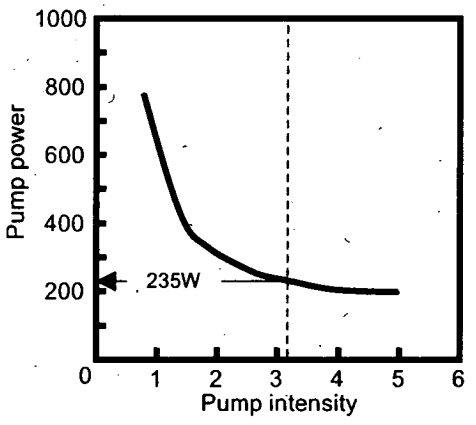

Fig. 3 Pump power for 100-mJ, 1-kHz operation.

References

1) J. Kawanaka, K. Yamakawa, H. Nishioka, and K. Ueda, 2004 Advanced Solid-State Photonics (2004 ASSP OSA) MC5, 2004.

4.1.4 Generation of broadband mid-infrared pulses

Keiichi YOKOYAMA, Akihiro SUGITA, Hidetaka YAMADA, Makoto AOYAMA,
Yutaka AKAHANE, Norihiro INOUE, Hideki UEDA, Koichi YAMAKAWA

1. Introduction

The vibrational frequency of most chemical bonds falls into the mid-infrared (MIR) region of light. In this respect, pulse shaping of MIR pulses will play a key role for the development of molecular manipulation by light[1]. In the MIR region, however, such a light source is not available at this point.

We examine the difference-frequency mixing (DFM) of ultrashort laser pulses in the near infrared (NIR) region as a light source of MIR pulses. Since the pulse shaping in the NIR region has been most intensively studied in all spectral region studied so far, generated MIR pulses should be modulated to some extent through the pulse shaping of incident NIR pulses. In fact, two groups have already demonstrated the pulse shaping in the MIR region using this approach[2,3]. They showed the production of MIR pulses in the spectral range of 3 to 10 μm and around 3 μm using two-stage OPA scheme with $AgGaS_2$ as nonlinear crystals. We are using the same $AgGaS_2$ crystal but one-stage DFM of two-color Ti:sapphire laser to generate the MIR pulses in the region of slightly different wavelength of 7 - 12 μm, i.e., the finger print region of molecular vibrational spectra. Strickland and coworkers and Yamakawa and Barty have also reported generation of MIR pulses with similar methods.[4,5]

In our preliminary study, MIR pulses were observed in a collinear phase-matching of both 760- and 830-nm pulses having a bandwidth of ~15 nm for each. The tunable spectral range was measured to be 7 to 11 μm by adjusting the crystal angle. However, the bandwidth (43 cm^{-1}) was not satisfactorily large for the coherent quantum control. The bandwidth was thought to be limited by the phase-matching angle, so that the spectral component of the input pulse was not fully used. Therefore, we make an attempt to another DFM experiment with a noncollinear configuration of two incident pulses to extend the bandwidth of the MIR pulses. A preliminary result is reported here.

2. Calculation

Noncollinear phase-matching in DFM has advantages over collinear one in terms of the generation of ultrafast pulses, mainly because the group velocity mismatch in the nonlinear crystal can be relaxed in many cases. For example, an optical parametric amplification with noncollinear phase-matching was shown to generate ultra-broadband pulses in the visible region from 550 to 690 nm. Figure 1 shows calculated phase-matching curves for type I and type II in $AgGaS_2$ pumped at 760 nm with different noncollinear angles α. The internal angular bandwidth is calculated to be 0.9° for the DFM in 1mm-thick $AgGaS_2$ crystal, as shown by the dashed lines in Fig. 1 (a) for Type I. The widest spectral range of the signal pulse

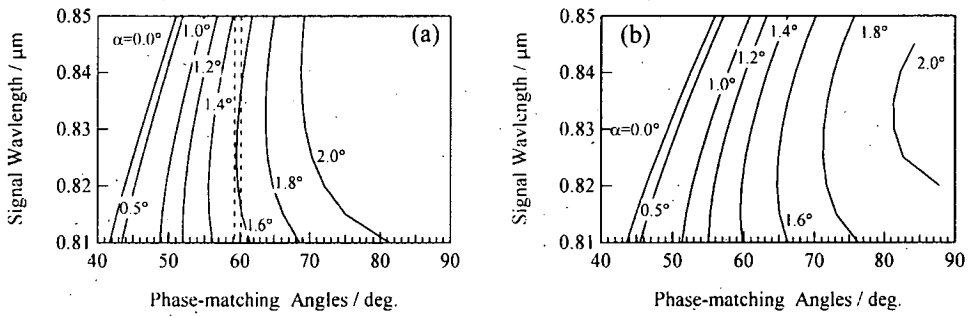

Fig. 1. Theoretical phase-matching curve of θ in the DFM pumped at 760 nm with various noncollinear angles α in $AgGaS_2$ (a) type I and (b) type II
The internal angular bandwidth is shown by the two dashed lines around θ = 59.7° in (a), indicating that a wide spectral range of the signal pulse (815-835 nm) would be phase-matched when α = 1.6°.

would be simultaneously phase-matched with a combination of θ = 59.7° and α = 1.6° in type I $AgGaS_2$, indicating the generation of the broadest MIR pulses with these parameters. On the other hand, the phase-matching curves calculated for Type II (Fig. 1b) show that the phase-matching is possible in relatively narrow spectral region of the signal pulse compared to that of Type I.

3. Experiment and Results

The layout of optics configuration used in the noncollinear DFM experiments is illustrated in Fig. 2. The pump and signal pulses centered at 760 and 830 nm were generated by the spectral shaping in a broadband

Ti:sapphire amplification system. The bandwidth of each pulse was ~15 nm. For typical experiments, the pulse duration was around 200 fs and the pulse energy was 1 mJ at the exit of the pulse compressor. The apparatus consisted of a beam splitter for the separation of the incident two-color pulse into the signal and pump pulses, a delay line in the signal pulse line, a grating in the pump pulse line, an $AgGaS_2$ crystal (type I or type II) at the crossing point of the two pulses, and MIR detection system after the crystal. Considering the refraction in the $AgGaS_2$ crystal, the external noncollinear angle α_{ext} is calculated to be 4.2° to let the internal noncollinear angle α = 1.6°. For efficient temporal overlap of both pulses in a limited thickness of the crystal, the waterfront of the pump pulse was tilted prior to the incidence with a grating of 75 l/mm.

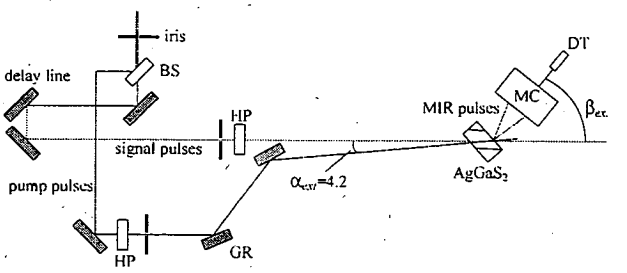

Fig. 2. A schematic diagram for broadband MIR pulse generation by noncollinear DFM

MIR pulses were generated by mixing the pump and signal pulses in a 1-mm thick $AgGaS_2$ (type I or II, θ = 45°). The spectrum of the dispersed MIR pulses was measured with an HgCdZnTe detector-preamplifier system through a monochromator at several output angles of MIR pulses. Typical spectra are shown in Fig. 3(a) for type I crystal and Fig. 3(b) for type II. It is apparent that the spectrum is quite broad for the type I crystal and ranging from 9 to 12 μm. The spectral bandwidth is determined as 230 cm^{-1} in FWHM which is five times larger than the value obtained by the previous collinear DFM experiment (~43 cm^{-1}). The relative value of the bandwidth to the central wavenumber is 23 % and thought to be widest so far in the MIR region, to our knowledge. Also, we found that the spectral range can be tuned from 7.5 μm to 12 μm by adjusting the phase-matching angle. This wide bandwidth and tunable range of wavelength should be useful for the coherent quantum control. On the other hand, the spectrum for the type II crystal shows very small increase in the bandwidth (55 cm^{-1}) from the collinear one. Both results on the bandwidth are in fully consistent with the theoretical prediction. At this point, the pulse energy and duration have not been measured yet. To use these MIR pulses for the coherent quantum control, we plan to

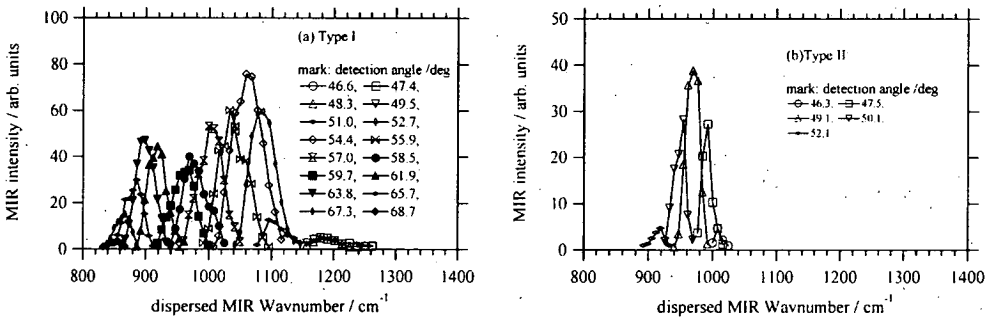

Fig. 3. Dispersed spectra of the MIR pulse is obtained at a fixed angle of a crystal $AgGaS_2$ for (a) Type I and (b) Type II with various angles of a monochromator and detector system. The resolution of monochromator was 12 cm^{-1} in all measurements. The bandwidth of single spectrum obtained at each detection angle is determined by the bandwidth of both pump and signal pulses.

compensate the spatial and temporal dispersion with cylindrical mirrors and gratings.

In conclusion, the use of a type I crystal of $AgGaS_2$ and the noncollinear phase-matching in the difference frequency mixing of NIR pulses was shown to be a useful method to generate broadband MIR pulses, which is desired for the coherent quantum control.

References

[1] H. Rabitz, R.d.Vivie-Riedle, M. Motzkus, and K. Kompa, Science **288**, 824, 2000

[2] T. Witte, K.L. Kompa, and M. Motzkus, Appl. Phys. B **76**, 467, 2003

[3] H.-S. Tan and W.S. Warren, Opt. Express **11**, 1021, 2003

[4] J. Song, J.F. Xia, Z. Zhang, and D. Strickland, Opt. Lett. **27**, 200, 2002

[5] K. Yamakawa and C.P.J. Barty, Opt. Lett. **28**, 2402, 2003

4.1.5 Femtosecond laser ablation for SCC mitigation on nuclear grade SUS

Akihiko NISHIMURA, Yukihiro SHIMADA, Hiroshi MURAKAMI, Eisuke MINEHARA, Alexander PIROZHKOV, Takahisa SHOUBU, Junichi. NAKANO [a)], Takashi TSUKADA [a)], Atsuo KAWASUSO [b)]

a) Department of Nuclear Energy System, b) Advanced Science Research Center

Stress corrosion cracking (SCC) has been studied in nuclear safety research. The SCC has recently become a very serious problem for electric power companies in Japan. Since the first SCC at the Fukushima boiling water reactors (BWRs), a lot of SCC incidents were reported in welded core shrouds and recirculation pipes of coolant water. By May 2003, Tokyo Electric Power Company (TEPCO) had shut down all of its 17 reactors for inspections. Fortunately, TEPCO succeeded in making its 14 reactors back on line by the summer of 2004. However, no SCC mitigation has been applied to its reactors. JAERI and its collaborators immediately clarified that work hardening layers on nuclear grade SUS had caused these SCC incidents. The investigations for the BWR core shrouds clarified that transgranular SCCs were developed from the initiation of intergranular SCCs and were caused by work hardening layers from the surface to the depth of a few hundreds μm[1]. Development of the new SCC mitigation was started in 2003. This study is one of the new branches of applications of femtosecond lasers in APRC, which belongs to "material control research" where precise machining, isotope separation, ultrafast spectroscopy and X-ray microscopy are now categorized. The purpose of this study is to demonstrate the SCC mitigation on the nuclear grade SUS by chirped pulse amplification (CPA) and to realize laser processing by the JAERI-FEL.

To simulate the processing of the shroud surface of BWRs, a milling machine was used to reproduce the work hardening layers on the 250 × 50 mm face of a SUS316L plate. The typical processing condition of 3000 mm/min cutting speed, 0.5 mm depth and 0.25 mm pitch with a SKH-4 bite successfully induced the work hardening layers with slip lines around 100μm depth on the plate. The plate was cut into pieces with the size of 10 mm cubic for laser ablation experiments. Ti:Sapphire CPA lasers produced femtosecond laser pulses and a plane-concave lens focused them on the surface of the cubic fixed on a translation stage. A frequency resolved optical gating (FROG) system was prepared to analyze the femtosecond laser pulses. To reduce the heating effects by oxidization, argon gas was supplied to the stage. Figure 1 shows an example of the edge view of the femtosecond laser ablated sample of target. Measurement of Vickers hardness distribution of the cubic target made it clear that the femtosecond laser pulses successfully ablated a 2 × 2 mm area with 300μm depth without thermally induced hardening[2]. Furthermore x-ray diffraction measurement clarified that the residual tensile stress of the ablated surface was changed to the compressive stress with increasing laser shot number.

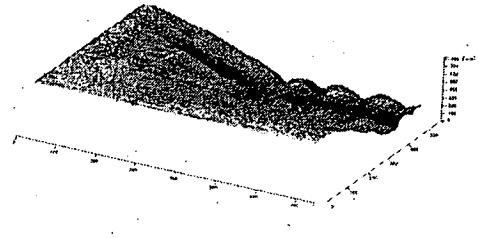

Fig. 1 An edge view of fs laser ablation

To promote the new SCC mitigation, the above mentioned femtosecond laser ablation should be coupled with the following advanced measurements for material properties. The BL22XU in SPring-8 has been prepared to measure the distribution of the residual stress ranging from the surface down to 1mm depth by the high energy X-ray diffraction. High energy positrons can penetrate the SUS to 100μm depth and are trapped at micro vacancies made by milling machining. The measurement of the lifetime of positrons can give us the information about the existence of dislocations in SUS materials with the induced tensile stress.

References

[1] T. Tsukada, et al., JAERI-Tech 2004-044, (2004).

[2] A. Nishimura, et al., LPM2004 in NARA, May 11-14, 2004, Proceedings of SPIE, (2004), in press.

4.2 X-ray Laser Development

Keisuke NAGASHIMA, Maki KISHIMOTO, Tetsuya KAWACHI, Noboru HASEGAWA, Momoko TANAKA, Yoshihiro OCHI, Youji SUZUKI, Kouta SUKEGAWA, Masaharu NISHIKINO, Renzhong TAI

Outline of x-ray laser research

The x-ray laser research at Advanced Photon Research Center has started on April 1998. The main purpose is to develop compact and repetitive x-ray lasers with full spatial coherence and saturated intensity. The results in the first period, from 1998 to 2001, are 1) development of the compact CPA laser system for transient collisional excitation (TCE) x-ray laser experiments, 2) demonstration of lasing in the wavelength range of 8.8-46.9 nm by using various solid and gas targets, and 3) saturated amplification at 12.0 nm and 13.9 nm. The objectives in the second period, from 2002 to 2006, are 1) full spatial coherence with coherent length larger than beam size and 2) higher repetition rate up to ~ 0.1 Hz for practical applications.

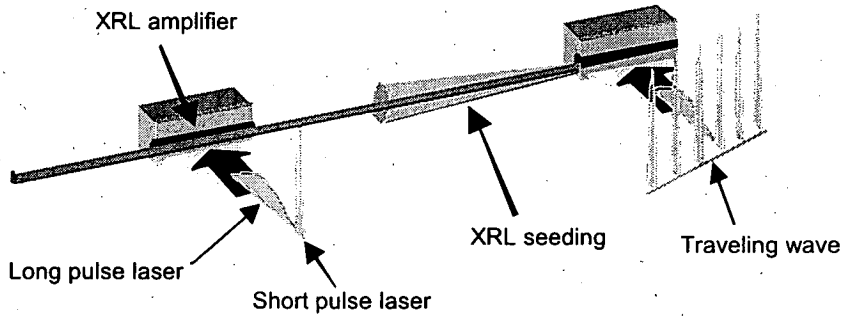

Fig.1 Experimental configuration of the double target experiment

In 2002, we succeeded in developing a laser-pumped x-ray laser with full spatial coherence at 13.9 nm. A very narrow x-ray laser beam with the divergence of 0.2 mrad was generated from the double target experiment (Fig.1), where a seeding light from the first laser medium was amplified in the second medium. The observed divergence was close to the diffraction limited value within a factor of two. The seeding light was amplified in the second medium without refraction influence and the gain coefficient was 7.9 cm^{-1}. The gain region of the second medium was far away from the target surface compared with that of the first medium and located in the considerably low density region. From the measurement of visibility, it was found that the spatial coherent length was longer than the beam diameter.

In 2003, we have improved the output energy of the full coherent x-ray laser in the double target experiment (**4.2.1**). The most important point of the double target experiment is spatial and temporal behaviors of the second medium (amplifier). So, we measured near-field images of the x-ray lasers, from which it was found the gain region moved with the delay time (**4.2.2**). Temporal durations of the x-ray lasers were examined also (**4.2.3**). We tried to generate an x-ray laser with full temporal coherence using high-order harmonic light as a seeding light (**4.2.4**). In order to improve the experimental system, we are developing new devices, which are an OPCPA front-end laser system (**4.2.5**) and a full-auto target alignment system (**4.2.6**).

4.2.1 Improvement of output energy of a fully coherent x-ray laser

Masaharu NISHIKINO, Momoko TANAKA, Noboru HASEGAWA, Yoshihiro OCHI,
Maki KISHIMOTO, and Keisuke NAGASHIMA

1. Introduction

Recently, a fully coherent x-ray laser (XRL) at 13.9 nm was generated by the double-target configuration.[1,2] The observed XRL beam had the fully spatial coherence and the nearly diffraction limited divergence of 0.2 mrad. In that experiment, the output energy of 25 nJ was lower than the saturation intensity by two-orders[3]. An increase in the output energy is expected by increasing the injection energy and the length of the gain medium. In order to improve the output energy, the amplification properties of the XRL beam have been investigated with longer plasma length of the second amplifier target.

2. Experiment and Results

The double-target configuration in this experiment is similar to the former experiment.[1, 2] Two slab silver targets were irradiated with two pumping laser beams from a pumping laser system operating at 1.053 μm.[4] The first target was irradiated by the laser pulse, which consists of a 110-ps prepulse and a 4-ps main pulse with the quasitraveling-wave pumping.[3] The irradiation intensity of the prepulse and the main pulse on the first target were 9×10^{12} and 1×10^{15} W/cm^2, respectively. The second target was irradiated by the laser pulse, which consists of a 110-ps prepulse and a 15-ps main pulse without the quasitraveling-wave pumping. The irradiation intensity of the prepulse and the main pulse on the second target were 1×10^{13} and 3×10^{14} W/cm^2, respectively. The focusing line width was about 20-μm and the length was about 6.5-mm on the first target, and 11-mm on the second target. Figure 1(a) shows the far-field pattern (FFP) of the XRL beam after amplification with the second medium length of 11 mm. In Figure 1(a), the beam divergences (FWHM) along the vertical and horizontal directions are 0.5 and 0.3 mrad, respectively. The FFP of the amplified XRL is affected by the refraction in the longer amplifier medium. However, we found the spatial coherence length is longer than the XRL beam diameter from Young's double slit interferometry. Therefore, the XRL beam affected by the refraction satisfies the condition for fully spatial coherence[5]. The output energy of the XRL beam after amplification is plotted with the second medium length in Fig. 1(b). The output energy increases exponentially with the gain medium length until about 9 mm. The output energy shows the saturation behavior for gain medium length longer than 9 mm, because the gain duration is shorter than the duration of the x-ray propagation in the amplifier medium over 9-mm region. In Fig. 1(b), the gain coefficient is estimated to be 7.6 cm^{-1} in the exponentially increasing region. This gain coefficient results in a gain length product gL = 6.8 and total gain of $G = \exp(gL) \sim 900$. Although the saturated amplification was not achieved yet, the maximum output energy of the XRL beam was about 170 nJ at the gain medium length of 11 mm.

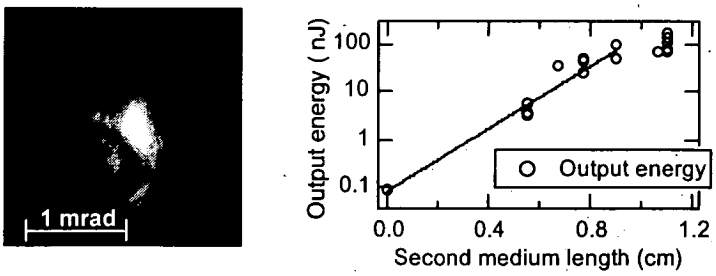

Fig. 1.(a) FFP of the XRL beam after amplification. (b) Output energy of the XRL beam after amplification plotted with the second medium length. The solid line shows a fit with an exponential fitting.

References

1) M. Tanaka *et al.*, Opt. Lett. **28**, 1680-1682, 2003.
2) M. Nishikino *et al.*, Phys. Rev. A **68**, 061802(R), 2003.
3) T. Kawachi *et al.*, Phys.Rev. A **66**, 033815, 2002.
4) T. Kawachi *et al.*, Appl. Opt **42**, 2198, 2003.
5) L. Mandel and E. Wolf, Optical coherence and quantum optics (Cambridge University Press, NY, 1995)

4.2.2 Near field imaging of x-ray lasers generated by the double target amplification

Momoko TANAKA, Masaharu NISHIKINO, Noboru HASEGAWA, Masahiko ISHINO, Maki KISHIMOTO, Kouta SUKEGAWA, Tetsuya KAWACHI, Masataka KADO, and Keisuke NAGASHIMA

1. Introduction

Recently, we demonstrated generation of the spatially full coherent x-ray laser by the double target amplification [1,2]. On this experiment, a part of the x-ray laser generated in the first medium was used as a seed light, and it was injected into the second medium, which was used as an amplifier. Delaying the injection time of the seed light for 15 ps, the influence of the refraction due to the density gradient of the second medium plasma is decreased. This suggests the gain region is moved to the low density area, where the density gradient of the plasma is calm. In order to measure the position of the gain region, we have observed the near field pattern of the x-ray laser.

2. Experiments and results

Two gain medium plasmas are generated by a picosecond glass laser system with two beam-lines. Each beam consists of two pulses; a pre-pulse with a pulse duration of 100 ps and a picosecond heating pulse with a temporal delay of 800 ps from the pre-pulse. The pulse duration of the heating pulse for the first target is 4 ps with the quasi-traveling wave arrangement and that for the second target is 14 ps without the traveling wave. The energy ratio of the pre-pulse and the heating pulse is 1:4. The laser pulses are focused with 20 μm width line shape on flat silver targets with an irradiance of the heating pulse of ~10^{15} W/cm^2. The length of the line focus for the first target is 6.5 mm and that for the second target is 4.3 mm. The distance between the two targets is 20 cm. The injection time of the x-ray from the first medium to the second medium is varied by an optical delay of the pump laser.

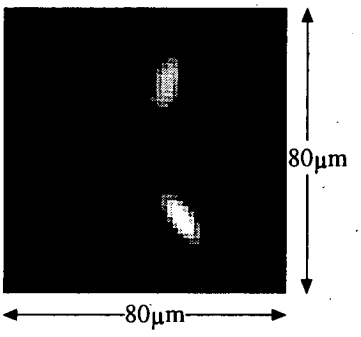

Fig. 1 Near field image of the double target x-ray laser at the end of the second target. The surface of the second target is right end of the image.

The near field imaging system with magnification of 8.5 is constructed with a concave mirror, and a soft x-ray CCD. The x-ray laser light is focused at the CCD using a concave mirror with curvature of 2 m (radius) and the diameter of 25 mm. The mirrors are coated with molybdenum/silicon multilayer for 13.9 nm x-ray. The x-ray laser beam is filtered with a zirconium foil of 1 μm to eliminate the visible emission of the gain medium plasma.

Figure 1 shows the near field image at the end of the second plasma. The surface of the second target is right hand side of the figure. The size of the gain region is 50μm, and it includes the several intense spots with the size of 10~30 μm. Figure 2 shows the distance of the intense spots from the second target surface. The gain region is 30~50 μm distant from the target, and it moves away from the target surface with delaying the injection time of the seed light. On the previous study, the refraction effect was disappeared at the delay time of 15 ps [1]. These results suggest that the density gradient of the plasma is drastically changed in the distance of 10~20 μm.

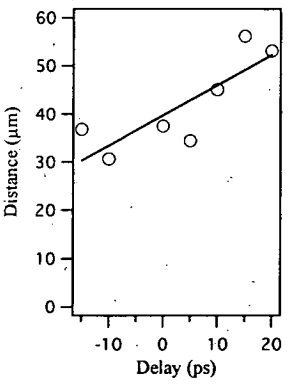

Fig. 2 Distance of the intense spots in the near field pattern from the target surface.

References

1) M. Tanaka *et.al.*, Opt. Lett. **28**, 1680 (2003)
2) M. Nishikino *et.al.*, Phys. Rev. A **68**, 61802R (2003)

4.2.3 Temporal characteristics of the TCE X-ray lasers

Yoshihiro OCHI, Tetsuya KAWACHI, Akira SASAKI, Keisuke NAGASHIMA

1. Introduction

At the Advanced Photon Research Center (APRC) we have demonstrated the transient collisional excitation (TCE) [1] X-ray laser (XRL) amplification for Ni-like Ag (13.9 nm), Sn (12.0 nm), and La (8.8 nm). Recently spatially fully coherent XRL beam has been demonstrated by means of the double target scheme [2]. Here we report temporal characterization of the TCE-XRLs. The XRL pulse duration were measured with three target materials, silver (Ag: Z = 49), palladium (Pd: Z = 48), and molybdenum (Mo: Z = 42). Atomic number dependence of XRL pulse duration was observed. We considered atomic processes determining the XRL duration.

2. Experiments and results

The experiments were made at the APRC with a compact CPA Nd:glass laser system [3]. The central wavelength was 1053 nm and the spectral bandwidth after the amplifier chain was 3.5 nm. In the present experiment, 400-ps prepulse and 4.8-ps main pulse with separation of 500 ps were focused in 4-mm length and 20-μm width. A quasi-traveling wave pumping with velocity of 1.03c, c represents the light speed, was employed using 6-step mirror [4]. Pulse duration of Ni-like Ag-, Pd- and Mo- XRLs were measured using an x-ray streak camera coupled with a flat field spectrometer. The instrumental width was determined by the time resolution of the streak camera and the temporal smearing in the flat field spectrometer, which resulting 3.1 ps for Ag-XRL, 3.2 ps for Pd-XRL, and 3.9 ps for Mo-XRL. XRL pulse duration obtained by deconvoluting the instrumental width from measured value was 7.0 ps for Ag-XRL, 5.6 ps for Pd-XRL, and <3.3 ps for Mo-XRL. These results show that the XRL pulse duration increases with increasing atomic number. The output temporal XRL profile $I(t)$ was determined by the temporal gain profile $g(t)$ by a relationship as $I(t) = \exp(g(t) \cdot l)$, where l was the gain length. By assuming the Gaussian shape for the temporal gain profile, the gain duration was calculated to be 23.1 ps, 18.5 ps, and <10.9 ps for Ag-, Pd-, and Mo-XRLs respectively.

In the TCE scheme, at first, target materials are ionized to the Ni-like stage by means of the prepulse. Then this Ni-like ion dominated plasma is heated by means of the main pulse to generate the gain. A fact that the obtained gain duration is longer than plasma heating time, i.e. the main pulse duration 4.8 ps, shows that the gain duration is not determined by the pumping pulse duration. We consider two atomic processes to decrease the population inversion; one is the collisional l-mixing in excited levels and the other is collisional ionization from the Ni-like ground state. At the typical plasma parameters of the gain region, Te = 400 eV and Ne = 5×10^{20} cm^{-3}, the collisional l-mixing time is < ps because the energy gap between the excited levels are small. Therefore the excited levels are quasi-steady state in the gain plasma. On the other hand, the collisional ionization time is > ps. Figure 1 shows the collisional ionization time from the Ni-like ground state for Ne = 5×10^{20} cm^{-3}. The collisional ionization rate is calculated using Landshoff –Perez's formula [5]. At 400 eV, calculated collisional ionization times show good agreements with obtained gain durations. It suggests that the collisional ionization plays an important role to determine the XRL pulse duration.

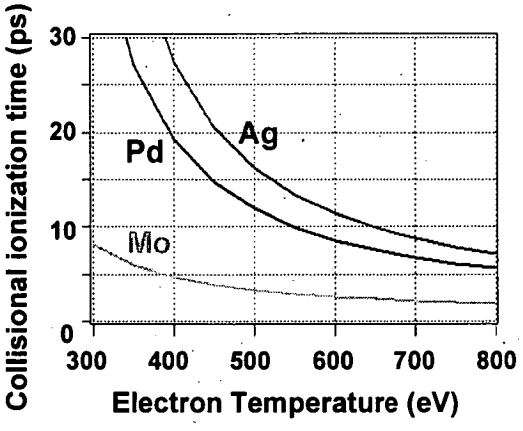

Fig. 1 Collisional ionization time from the Ni-like ground state for Ne = 5×10^{20} cm^{-3}.

References

1) P. V. Nickles, et al, Phys. Rev. Lett. **78**, 2748, 1997
2) M. Nishikino, et al, Phys. Rev. A **68**, 0261802, 2003
3) T. Kawachi, et al, Appl. Opt. **42**, 2198, 2003
4) T. Kawachi, et al, Phys. Rev. A **66**, 033815, 2002
5) R. K. Landshoff and J. D. Perez, Phys. Rev. A **13**, 1619, 1976.

4.2.4 Transform limited x-ray laser generation with the high order harmonic light

Noboru HASEGAWA, Tetsuya KAWACHI, Maki KISHIMOTO, Kouta SUKEGAWA, Momoko TANAKA, Masataka KADO, RENZHONG Tai, Yoshihiro OCHI, Masaharu NISHIKINO, and Keisuke NAGASHIMA

1. Introduction

Recently, we have improved the spatial coherence of the x-ray laser at a wavelength of 13.9 nm by using the double target experiment[1),2)]. The next step is to improve the temporal coherence, which is only 6% at the present[3),4)], in other words, to generate the Fourier transform limited x-ray laser. To improve the temporal coherence, we proposed a method in which high order harmonic light was used as a seed x-ray and was injected into a laser-produced x-ray amplifier.

2. Improvement of the temporal coherence

The x-ray amplifier amplifies a part of the harmonic light in frequency. The x-ray amplifier has quite narrow spectral width compared with the harmonic light, so the x-ray amplifier works as an active mode selector, it selects and amplifies only temporally coherent mode of the harmonic light. The electromagnetic waveform function of the amplified x-ray was described as a product of the waveform function of the harmonic light and the x-ray amplifier, where we assumed a Gaussian spectral profile (eq.1). γ and b represented by the frequency bandwidth of the harmonic light and the x-ray amplifier ($\gamma = 0.035/\Delta\nu_{HHG}^2$, $b = 0.035/\Delta\nu_{amp}^2$), respectively, and β was the chirp of the harmonic light. The term of $\exp(-b\omega^2)$ in eq.1 showed that the frequency bandwidths of the harmonic light was selected by the x-ray amplifier. By taking Fourier transformation of eq.1, we obtained the uncertainty relation btween the frequency bandwidth ($\Delta\nu_{XRL}$) and the duration ($\Delta\tau_{XRL}$) of the amplified x-ray as shown in eq.2, where a factor of 0.441 was originated from the gaussian profile.

$$E_{XRL}(\omega) = E_0 \exp(-\gamma\omega^2 + i\beta\omega^2)\exp(-b\omega^2) \qquad \text{(eq.1)}$$

$$\Delta\nu_{XRL}\,\Delta\tau_{XRL} = 0.441[1+\{\beta/(\gamma+b)\}^2]^{1/2} \qquad \text{(eq.2)}$$

In eq.2 with increasing b compared with β (i.e. $\Delta\nu_{amp} << \Delta\nu_{HHG}$), the temporal coherence of the amplified x-ray is increased.

3. Experiment of the x-ray laser with the seed x-ray

In this experiment, Ti:Sapphire laser generated high-order harmonics, and the 29th harmonic light was injected into the neon-like manganese x-ray laser medium (λ=26.9nm). The beam divergence of the x-ray laser with the seed x-ray was measured to be 2.0 mrad, which was nearly equal to that of the seed x-ray (1.8 mrad) and apparently narrower than that without the seed x-ray (3.8mrad). This result implies the seed x-ray amplification was obtained. The energy and gain length product (gl) of the x-ray laser with the seed x-ray were measured to be 3 nJ and 6.5, respectively.

We estimated the temporal coherence of the x-ray laser. The line width of the 29th harmonic light ($\Delta\lambda_{HHG}$) was measured to be 0.12 nm (i.e. $\gamma = 1.35\times10^{-29}$), the duration ($\Delta\tau_{HHG}$) and β were estimated to be 30 fs[5)] and 4.5×10^{-29}, respectively, and b was estimated from the intrinsic line width of the x-ray amplifier ($\Delta\lambda_{amp}$ = 0.0056 nm, b = 6.2×10^{-27}). Thus, the temporal coherence , $[1+\{\beta/(\gamma+b)\}^2]^{1/2}$, was 1.00003. This leads to the amplified x-ray was nearly equal to the transform limited pulse.

It is noticed that in the present case, an effect of the additional chirp in the x-ray amplifier was negligibly small. Thus, the x-ray laser was expected to be highly temporal coherent.

References

1) M. Tanaka *et al.*, Opt. Lett. **28**, 1680 (2003).
2) M. Nishikino *et al.*, Phys. Rev. A **68**, 61802 (2003).
3) Y. OCHI *et al.*, Appl. Phys. B **78**, 961 (2004).
4) J. A. Koch *et al.*, Rev. A **50**, 1877 (1994).
5) T. Sekikawa, *et al.*, Phys. Rev. Lett. **83**, 2564 (1999).

4.2.5 Properties of optical parametric chirped pulse amplification (OPCPA) for X-ray laser driver

Maki KISHIMOTO and Kouta SUKEGAWA

1. Introduction

We have been developing a compact x-ray laser system and its application facility for studying nano-structure material and biological researches since 1998, and it has been demonstrated that high gain coefficients in soft x-ray amplification can be achieved using the compact CPA (chirped pulse amplification) tabletop sized Nd:glass laser system with about 10J energy and several picoseconds pump laser pulse duration as a x-ray laser driver in TCE scheme. To widen the field of applications of the x-ray laser, higher repetition rate of the x-ray laser is needed. For that, the effective generation of x-ray laser by optimizing pumping conditions is very important. Optical parametric chirped pulse amplification (OPCPA) is an ideal laser source and we can control the pumping conditions such as contrast ratio of pre-pulse and main pulse. Then we have started the development of an OPCPA system for x-ray laser driver.

2. Experimental setup for OPCPA

Fig.1 shows the schematic diagram of an OPCPA system pumped by the second harmonic of a Nd:YAG laser. The nonlinear crystal for OPCPA is a 5 × 5 × 15 mm^3 BBO crystal (Type I, ooe). A 1053 nm chirped pulse from the regenerative amplifier at the front-end system of the CPA glass laser system is used as a seed light. A 532 nm pump laser beam with a pulse duration of 7 ns is introduced coaxially with a seed light pulse into the BBO crystal. The regenerative amplifier and the Nd:YAG laser are synchronized with a precision master clock generator[1] and the timing jitter between the seed pulse and the pump laser pulse at the BBO crystal is about ±200 ps.

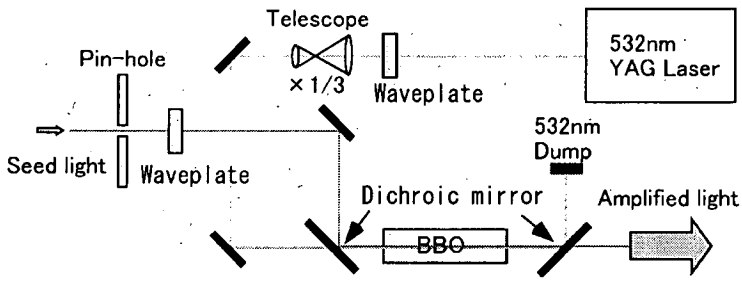

Fig.1 Schematic diagram of OPCPA Experiment

3. Amplification property of OPCPA

Fig.2 shows the amplification property of OPCPA. The seed light energy before optical parametric amplification at the BBO crystal is 0.15 μJ. As shown in the figure, a seed light is amplified exponentially and achieves saturated amplification at a pumping intensity of about 200 MW/cm^2. A gain of 2500 is obtained at a pumping intensity of 200 MW/cm^2, and the maximum gain is 8000, which is obtained at a 540 MW/cm^2 pumping intensity.

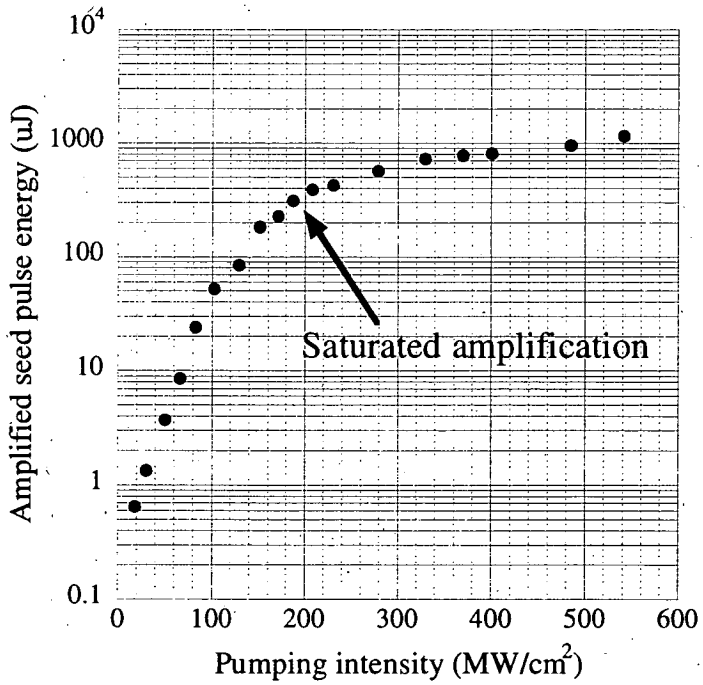

Fig.2 Amplification property of OPCPA

References

1) M. Kishimoto and K. Sukegawa, JAERI-Review 2003-042, 22, 2004

4.2.6 Development of the target alignment system for double target x-ray laser

Kouta SUKEGAWA and Maki KISHIMOTO

1. Introduction

In X-ray laser research group at JAERI, the high brightness and highly coherence X-ray laser using double targets have been developed for the applications of the X-ray laser such as X-ray interference measurement and material science. We have succeeded in the generation of a full coherent X-ray laser beam in 2002[1-2]. In the double target x-ray laser experiment, a seed pulse from the first target must be introduced into the second target plasma with sufficient accuracy. Therefore the double target X-ray laser requires higher accuracy for target alignment. We have started the development of a new type of high precision auto target alignment system using laser diode (LD) and position sensitive detector (PSD) and a high stability target chamber from 2003. In the present article, we report the development of the new target vacuum chamber and the performance evaluation of target position stability.

2. High stability target chamber and monitoring of the target position

Fig. 1 shows the schematic diagram of the target chamber. The target chamber consists of a cylindrical vacuum chamber and a breadboard in it, which are mechanically independent of each other. Moreover, the breadboard is supported by a vibration isolation optical table independent of the vacuum chamber. A target is placed on the breadboard and is irradiated with a LD set on the optical table from the outside of the vacuum chamber. By measuring the beam pointing of the LD light reflected by the target with the PSD, we monitor the exact target position.

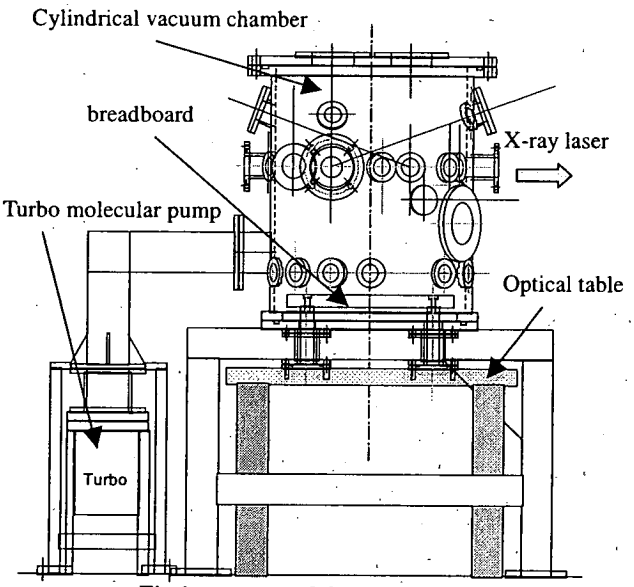

Fig.1 structure of the target chamber

In order to evaluate the position stability of the optical table, namely the target in the vacuum chamber before and after evacuation, we measured the LD beam pointing with the PSDs placed on the optical table independent of the target chamber. The changes in position of the optical table measured are shown in Fig. 2. The horizontal axis in Fig. 2 is the elapsed time since the start of evacuation and the vertical axis is the changes in position in μm. As shown in the figure, the change in position of the optical table measured by the LDs and the PSDs before and after evacuation was less than ±10μm. We confirmed that the target chamber manufactured was stable enough for the double target x-ray laser experiment.

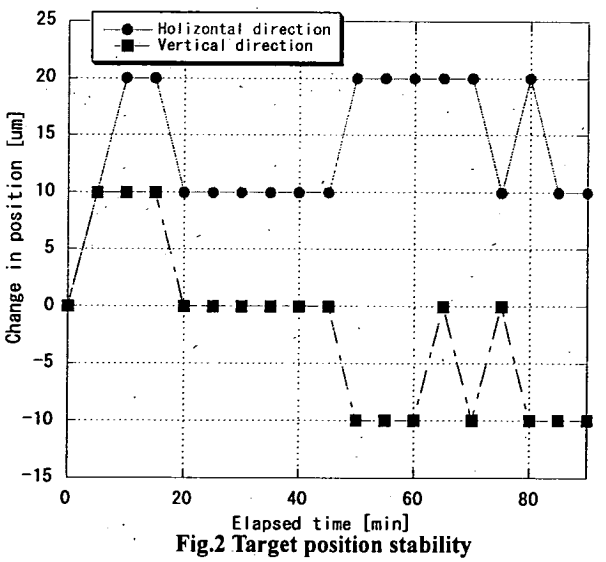

Fig.2 Target position stability

3. Conclusion

The new target chamber for the double target x-ray laser experiment was designed and manufactured, and then we evaluated the performance of it. As a result, the change in position of the target by vacuum pumping was evaluated to be less than ±10μm.

References

1) M.Tanaka, et al., Opt. Lett. 28, 1680, 2003
2) M.Nishikino, et al., Phys. Rev. A 68, 0681802R, 2003

4.3 Free-Electron Laser Development

Eisuke J. MINEHARA

The 25th International Free-Electron Laser (FEL) Conference and 10th Free-Electron Laser Users Workshop was held on September 8-12th at Epochal TSUKUBA, Tsukuba, Ibaraki, JAPAN. The Conference and the Workshop, which is abbreviated as FEL2003, was organized by FEL laboratory at Tokai, Advanced Photon Research Center, Kansai Research Establishment, Japan Atomic Energy Research Institute JAERI. A total of 221 participants (22 inside JAERI, 66 inside Japan, 133 from overseas) from 18 different countries attended the conference, presented 51 talks and 204 posters, and submitted 131 papers, which will be published in the conference proceedings as the Nuclear Instruments and Method special issue[1] by Elsevier Science Publishing Company, The Netherlands. The JAERI FEL group has successfully and firstly confirmed the frequency self chirping phenomenon in the free-electron laser systems. The JAERI FEL group was very proud to issue the press release of the FEL self chirping confirmation and the FEL 2003 to the mass media.

The JAERI FEL group has started to develop the femtosecond and 20kW high power superconducting rf linac-based FEL for nuclear industry, heavy industries and so on. In the first fiscal year of the high power FEL developmental program, the low level rf signal phase and amplitude control circuits, high current 250kV high voltage power supply, computer control system, Inductive Output Tube rf amplifiers were built to increase the electron beam power, and FEL laser power over longer pulse duration than 1s or 10s.

The JAERI FEL group has firstly reported that the femtosecond lasers like low average power Ti:Sapphire lasers, the JAERI high average power free-electron laser and others could peel off and remove two stress corrosion cracking (SCC) origins of the cold-worked and the cracking susceptible material, and residual tensile stress in hardened and stretched surface of low-carbon stainless steel cubic samples for nuclear reactor internals as a proof of principle experiment except for the third origin of corrosive environment. Because a JIS (Japan Industrial Standards) - specified 143 °C and 43% $MgCl_2$ hot solution SCC test was performed for the samples to simulate the cold-worked SCC phenomena of the internals to show no crack at the laser-peered off strip on the cold-worked side and hundred-thousands of cracks at the non-peeled off on the same side, it has been successfully demonstrated that the femtosecond lasers could clearly remove the two SCC origins and could resultantly prevent the cold-worked SCC.

We could succeed to run the JAERI originally-developed stand-alone and zero-boil-off cryostat system continuously with a few short stops and troubles for these 3 years from 2001 up to 2003 Japanese fiscal year and without warming up, and any liquid He evaporation because the original tools and technique were successfully adopted to exchange quickly 4K and 10K/50K He refrigerators for 15 minutes each without any damage and any bad effects to the heat exchange and absorber agents in a He gas atmosphere. After we have repeated to exchange the refrigerators a few tens of times, a continuous low-temperature operational interval was estimated to be very long, longer than 10 or 20 years or more. No warm-up operation of the superconducting rf linacs over 20 years looks very promising to realize maintenance-free and easy-operation in the linacs.

Our reports and discussions on the FELs in the subsections will also cover some conceptual design works of the energy-recovery linac based light source and applications of the FEL and nuclear isomer studies.

References

1) E.J. Minehara, R. Hajima and M. Sawamura, Nucl. Instr. and Meth. Phys. Res. A 528 Issues1-2,(1 August 2004) page1-660. Proceedings of the 25th International Free Electron Laser Conference, and the 10th FEL Users Workshop, Tsukuba, Ibaraki, Japan, 8 - 12 September 2003

4.3.1 Study of HOM Instability of the JAERI ERL-FEL

Masaru SAWAMURA, Ryoichi HAJIMA, Ryoji NAGAI, Nobuhiro KIKUZAWA,
Nobuyuki NISHIMORI, Eisuke MINEHARA

1. Introduction

Energy recovery is the process by which the energy invested in accelerating a beam is returned to the rf cavities by decelerating the beam. Energy recovery of an FEL beam driven by a superconducting linac is a possible way of greatly increasing the efficiency of the laser since most of the beam energy remains after lasing occurs. This energy-recovery technology with a superconducting linac is the most promising for the next stage of 10kW FEL lasing owing to increasing the beam current without additional rf power sources.

In a recirculating linac, a feedback system is formed between the beam and the rf cavities, so that instabilities can arise at high currents. These instabilities become important and can potentially limit the average beam current especially for the high-Q superconducting cavities.

2. HOM Power Spectrums

Each module has five rf couplers such as a main power coupler, a pick-up coupler and three HOM couplers. Two HOM couplers are designed to damp transverse modes and the other to damp longitudinal modes. All HOM couplers are terminated to the dummy loads out of the cryostats. This makes it possible to measure the excited HOM powers inside the cavity through the HOM couplers.

Figure 1 shows the waveforms of the rf power extracted from the HOM couplsers with and without energy recovery. Though the amplitudes increasing due to the beam with energy recovery seems to be greater than those without energy recovery, the main part of the amplitudes was due to the wake field caused by the electron beam passing near the HOM couplers.

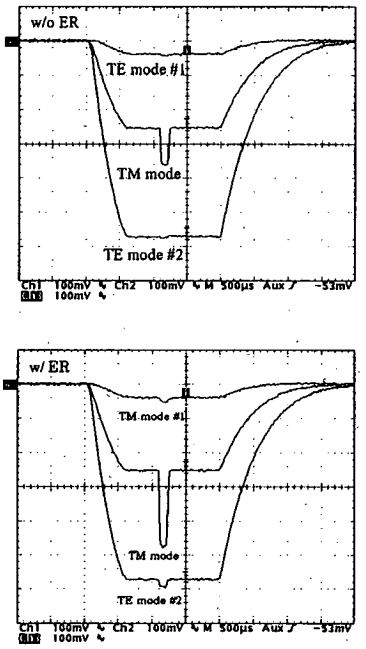

Fig. 1 Output from the HOM couplers without ER (upper) and with ER (lower)

The dummy load was exchanged for a real-time spectrum analyzer to measure frequencies and powers of the HOMs. Figure 2 shows the amplitude of the HOMs. There seems to be four groups of the HOMs or more. The group near 630MHz is considered to be TE111 mode and that near 700MHz to be TM110 mode. The groups over 850MHz have not been identified yet.

The mode of the highest power of TE111 is considered to be $3\pi/5$ mode of 634MHz and that of TM110 to be $4\pi/5$ mode of 715MHz. The calculated threshold current is 34.36A for TE111-$3\pi/5$ mode and 16.79A for TM110-$4\pi/5$ mode. While these modes of small threshold current show high HOM powers, the modes of the smaller threshold current for such as TM110-$3\pi/5$ and TM110-$2\pi/5$ modes show fairly low HOM powers. Measured HOM coupling factors do not vary so much with the difference of the modes. The small spectrums for the low threshold current might be caused by the short macropulse or the low beam current. The further analysis is required to understand the HOM instabilities.

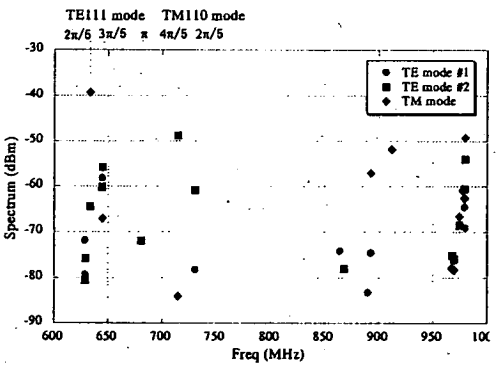

Fig. 2 HOM power spectrums

3. Conclusion

The HOM spectrums were measured from three HOM couplers. The mode of the smallest threshold current by calculation is not detected from the HOM couplers. The more precise measurement is required to well-understand the HOM instabilities.

4.3.2 Replacement of the JAERI ERL-FEL control system

Nobuhiro KIKUZAWA

1. Introduction

A home-made personal computer (PC) based distributed control system for the JAERI FEL has been developed and operated since 1992. Maintenance of the control system was difficult because these PC's specification was obsolete during a use more than 10 years and applications, which didn't work on an old operating system increased. Therefore the upgrade of the control system was carried out in 2003[1].

2. Configuration of the new control system

In order to minimize costs and works of the replacement, it decided that a new control system was designed so that the device interface layer under CAMAC might not be changed. Therefore, a new local controller that performs an interface with CAMAC needed to be developed[2]. The local controller employed an embedded μITRON operating system machine (Nichizo Densi-seigyo Co. ND-MCU) with 100Base-T network controller instead of PCs, because there were problems in the reliability or the network security for long continuous operation when the many PCs were used. The μITRON operating system was designed for an embedded system in all industrial fields as a real time operating system. It was achieved that the controller would make the computers become independent of the function depending on hardware like an interface board for the CAMAC crate. As a result of this replacement, the renewal of computers which will be performed in the future became easy.

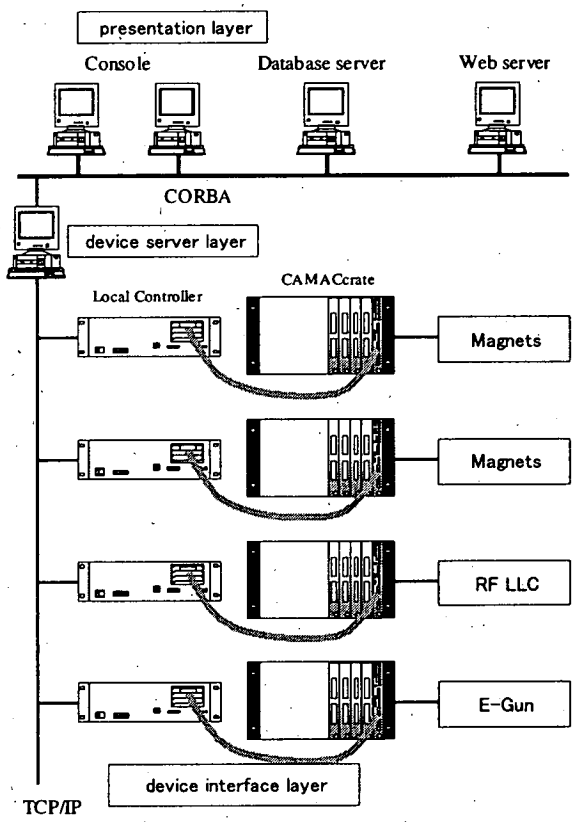

Fig.1 Hardware configuration of the JAERI ERL-FEL control system

As shown in Fig. 1, the control system is divided into three layers, a presentation layer, a device server layer and a device interface layer. The device interface layer consists of the four local controllers connected with CAMAC crates. The controller can be used as an intelligent controller and restore device settings to their former value at boot of the controller without any PCs. In order to hold the setting parameters during power off, the setting values are kept in battery backup RAM in the controller.

The device server layer manages the hardware and communicates with them via the local controllers. It is implemented as CORBA server to mediate of CORBA (Common Object Request Broker Architecture) protocol and TCP/IP protocol. The presentation layer is GUI (Graphical User Interface) applications to control the devices or to display current status. It was more effective to develop applications newly by Java language rather than studying and rewriting the very old existing Pascal code.

3. Results

The upgrade process is on its way and will continue for the next years. Since the CAMAC controller was developed, it succeeded in making the computer become independent of the function depending on hardware like an interface board. The control programs were newly developed for the control system by the Java language and CORBA.

References

1) N. Kikuzawa, Proc. of the 28th Linear Accelerator Meeting in Japan, 437, 2003 (in Japanese).
2) N. Kikuzawa, Proc. of the 14th Sympo. on Acc. Sci. and Tech., 269, 2003 (in Japanese).

4.3.3 Electrical Length Stabilization of Coaxial Cable by Cheap Temperature Regulation System

Ryoji NAGAI, Masaru SAWAMURA, Nobuyuki NISHIMORI, Ryoichi HAJIMA,
Nobuhiro KIKUZAWA and Eisuke MINEHARA

1. Introduction

To ensure high-quality beam acceleration of RF linacs, the RF phase and amplitude of the accelerator cavities are highly stabilized by each feedback controllers. The phase correlation of the cavities is ensured by an RF phase reference signal through an RF phase reference line. Therefore, the electrical length of the phase reference line should be stabilized against ambient temperature and atmospheric pressure fluctuations. At huge-scale accelerators, a phase-stabilized optical fiber (PSOF) is used for the RF phase reference line[1]. Since the PSOF system is very expensive, the PSOF system is not suite for the RF reference line of the small-scale accelerator such as the JAERI ERL-FEL. A coaxial cable reference line has electrical length fluctuation due to ambient temperature and atmospheric pressure fluctuations. Then the electrical length of the coaxial cable is stabilized by cheap temperature regulation system for the JAERI ERL-FEL. The electrical length fluctuation is suppressed sufficiently by the temperature-regulated coaxial cable operating with proper temperature.

2. Electrical length stabilization of coaxial cable

The coaxial cable electrical length is fluctuated by temperature fluctuation. The fluctuation caused by the tow effects. One is a thermal expansion of the metallic conductor of coaxial cable. Another is a thermal fluctuation of the dielectric constant of the isolator of coaxial cable. This causes a decrease in the electrical length of the coaxial cable with increase temperature. In low-loss coaxial cables with foamed polyethylene, such as Heliax-FSJ1, these two effects are similar magnitude, causing little change in the overall electrical length of the cable.

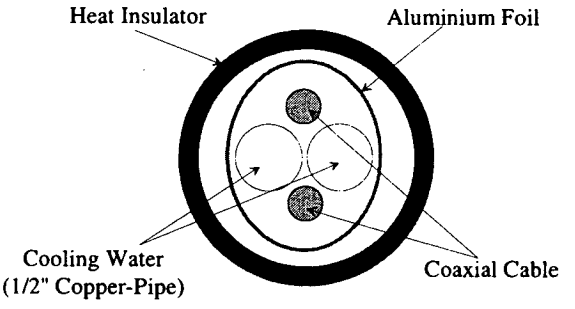

Fig.1 Cheap temperature regulation system for the coaxial reference line

The electrical length stability of the Heliax-FSJ1 is evaluated by test cable laid in the accelerator room of the JAERI ERL-FEL. In the evaluation, RF signal frequency is 499.8 MHz that is fundamental acceleration frequency of the JAERI ERL-FEL. The measured temperature coefficient of the Heliax-FSJ1 is –5 ppm/°C (-3.69×10^{-3}deg./ °C m in the frequency of 499.8 MHz). This stability is not sufficient for the reference line of the JAERI ERL-FEL because the requirement of the stability is less than ±0.1 deg. in the fluctuations of ±3 °C and the cable length of 23 m. Then a cheap temperature regulation system for the coaxial cable reference line is developed as shown in Fig. 1. In the evaluation of the developed reference line, it is found that the electrical length is fluctuated by the atmospheric pressure fluctuation. The pressure coefficient is measured as shown in Fig. 2. Fortunately, the pressure coefficient is suppressed by increasing setting temperature of the reference line. At the setting temperature of 30 °C, temperature and pressure coefficients are –0.3 ppm/°C (-1.86×10^{-4}deg./°C m) and –0.14 ppm/hPa (-1.02×10^{-4}deg./hPa m), respectively. In the result of the evaluation for the developed reference line, the requirement phase stability of the correlation of the accelerator cavities can be achieved by using the developed reference line.

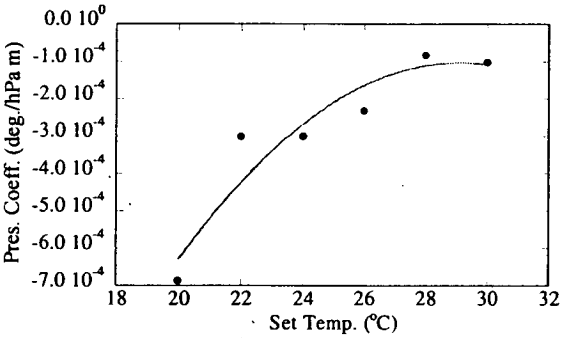

Fig.2 Pressure coefficient of the phase fluctuation of the coaxial cable in the frequency of 499.8 MHz

References

1) T. Naito, et al., Proc. of the 2000 Linear Accel. Conf. (2000) 742-744.

4.3.4 Optimization of JAERI ERL-FEL Optical Resonator

Ryoji NAGAI, Ryoichi HAJIMA, Masaru SAWAMURA, Nobuyuki NISHIMORI,
Nobuhiro KIKUZAWA and Eisuke MINEHARA

1. Introduction

An R&D program aimed at a 10-kW class ERL-FEL is in progress. This includes injector upgrades[1], HOM analysis[2], return-path optimization[3], and optical resonator optimization. The optical resonator consists of metal-coated end mirrors. This allows wide broadband operation[4] and ultrashort optical pulse generation[5]. The optical resonator has a center-hole output coupler. The output coupler introduces additional diffractive loss and expansion of the interaction mode volume due to scattering at the edge of the coupler. To ensure high-power FEL operation, the end mirror curvature and center-hole radius are optimized with a wavelength of 22 „m about the FEL efficiency through a numerical evaluation of the optical resonator by an eigenmode calculation code using the Fox-Li procedure[6].

2. Optical resonator optimization

The FEL efficiency is defined as $\eta_{fel} = \eta_{out}\,\eta_{ext}$, where η_{out} is the output coupling efficiency of the optical resonator, and η_{ext} is the FEL extraction efficiency. The output coupling efficiency is defined as $\eta_{out} = \alpha_{out} / \alpha_{loss}$, where α_{out} is the output power of the resonator, and α_{loss} is the total round-trip loss of the resonator. The total round-trip loss consists of the reflective loss of 1.2%, the diffractive loss, and output power. If the FEL is lasing in the spiking-mode, the FEL extraction efficiency is inversely proportional to square root of the round-trip loss and interaction mode volume[7]. The FEL efficiency is then represented by the following equation,

$$\eta_{fel} \propto \frac{\alpha_{out}}{\alpha_{loss}^{3/2} \cdot V^{1/2}}, \qquad (1)$$

where V is the interaction mode volume.

The optimization model contains two end mirrors, four apertures, and a center-hole output coupler as shown in Fig. 1. The effects of the undulator duct and bending magnet ducts are taken into account by the four apertures.

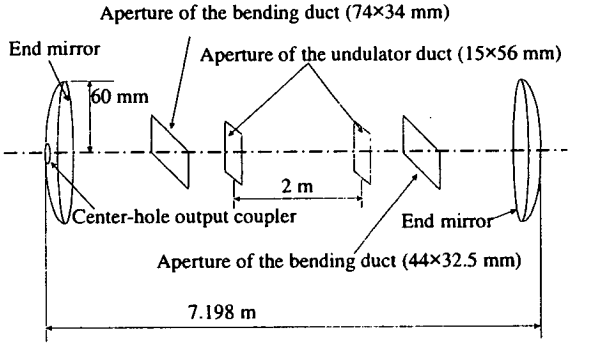

Fig.1 Optimization model of the optical resonator

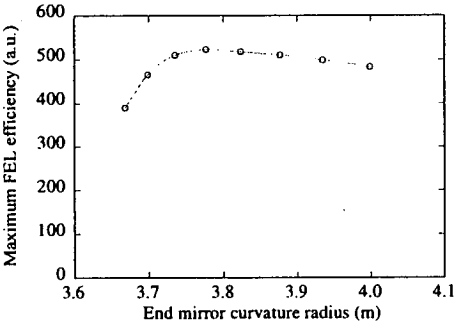

Fig.2 Maximum FEL efficiency as a function of the end mirror curvature radius

The maximum FEL efficiency as a function of mirror curvature radius is shown in Fig 2. The optimum mirror curvature radius for the JAERI ERL-FEL is 3.777 m and the FEL efficiency is almost flat in the range of 3.75 m to 3.90 m. On the other hand, the optical resonator is more stable for a large curvature radius end mirror because the optical resonator is near concentric type. Thus, the end mirror curvature radius of 3.877 m has been chosen for the JAERI ERL-FEL. This curvature radius corresponds with a Rayleigh range that is half the undulator duct length. For this end mirror curvature radius, the optimum center-hole radius is 0.8 mm.

References

1) N. Nishimori, et al., Proc. of the 28th Linear Accelerator Meeting in Japan, 159, 2003 (in Japanese).
2) M. Sawamura, et al., Proc. of the 2003 Part. Acc. Conf., 3446, 2003.
3) R. Hajima and E. Minehara, Nucl. Instr. and Meth. **A 507**, 141, 2003.
4) R. Nagai, et al., Proc. of the 13th Sympo. on Acc. Sci. and Tech., 455, 2001.
5) R. Hajima and R. Nagai, Phys. Rev. Lett. **91**, 024801, 2003.
6) R. Nagai, et al., Proc. of the 28th Linear Accelerator Meeting in Japan, 381, 2003 (in Japanese).
7) N. Piovella, et al., Phys. Rev. **E 52**, 5470, 1995.

4.3.5 Linear Analysis of CSR Effect in a Future ERL Light Source

Ryoichi HAJIMA

1. Coherent Synchrotron Radiation in an Energy Recovery Linac

Next generation light sources based on energy-recovery linacs (ERL) have been proposed. These devices will provide sub-picosecond X-ray pulses with very high brilliance, which cannot be obtained in existing X-ray light sources using electron storage rings. In the development of ERL light sources, study on coherent synchrotron radiation (CSR) is one of the critical issues, because the emittance of an electron bunch is diluted by CSR when the electron bunch travels a circular path such as a beam transport loop of an ERL.

2. Linear Analysis of CSR effects

A first-order equation of electron motion in a uniform field of a dipole magnet is

$$x'' = -\frac{x}{\rho^2} + \frac{1}{\rho}(\delta_0 + \delta_{csr} + \kappa[s - s_0]),$$

where ρ is the bending radius, δ_0 is the initial momentum deviation normalized by the reference momentum. The last two terms on the right-hand side are related with the CSR effect: δ_{csr} the normalized momentum deviation caused by CSR in the upstream path ($0 < s < s_0$), $\kappa = W/E_0$ the normalized CSR wake potential in the bending path defined by CSR wake potential W and the reference energy E_0. We can quickly solve the emittance growth along a beam transport path including CSR effects by using the above equation[1]. Emitatnce compensation methods such as envelope matching and cell-to-cell phase optimization can be also discussed by linear analysis.

The CSR-induced emittance growth in a 3GeV triple-bend achromatic cell is calculated with varying the beam envelope[2]. The beam envelope is changed by scanning Courant-Snyder parameters at the cell entrance: $-5.0 < \alpha_x < 5.0$, $\gamma_x = 0.29\ m^{-1}$. Figure 1 shows the projection emittance at the cell exit as a function of α_x. The results from the linear analysis are compared with a particle tracking code ELEGANT[3]. It can be seen that both the results show good agreement.

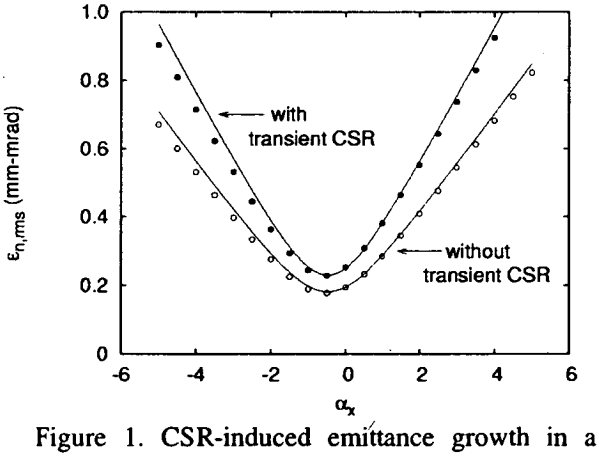

Figure 1. CSR-induced emittance growth in a 3-GeV TBA cell with scanning the beam envelope: linear analysis (solid lines) and particle tracking (dots).

References

1) R. Hajima, Jpn. J. App. Phys. 42 (2003) L974-L976.

2) R. Hajima, Proc. Asian Particle Accelerator Conference (2004).

3) M. Borland, Argonne National Laboratory Advanced Photon Source Report LS-287 (2000).

4.3.6 Analysis of an FEL oscillation at zero detuning length of an optical cavity

Nobuyuki NISHIMORI

1. Introduction

An experiment performed in JAERI FEL has clearly shown that efficiency in an FEL oscillator can reach maximum at zero detuning length of an optical cavity (dL = 0) despite the lethargy effect[1]. However, the physics responsible for the FEL at dL = 0 has not been clearly explained yet. The main difference of FELs between dL = 0 and dL < 0 is whether incident electrons interact with the field characterized by the steep intensity gradient on the leading edge, which is similar to that formed in a self-amplified spontaneous emission (SASE) FEL[2]. The analysis of the interaction between a SASE field shows that intensive energy transfer from electrons to the field at the peak of the field can account for generation of intense few cycle FELs at dL=0 .

2. Analysis of an FEL oscillation at dL=0

At dL = 0, the head of a round-trip FEL coincides with that of an incident electron pulse at the entrance to an undulator. Figure 1 shows a semi-log plot of an FEL amplitude at saturation obtained in a time dependent simulation as a function of longitudinal position in units of resonant wavelength λ. The zero is the position of the head of incident electrons at the entrance to an undulator. The position of the principal peak of the field is represented as ζ_p. The region from 0 to ζ_p is called the leading edge. The inset shows the linear plot of the amplitude. The exponential increase on the leading edge can be attributed to the lethargy, because the trailing part of the field is amplified due to the lethargy[3]. In fact, the field at the first round trip in an oscillator is identical to that of SASE. It is therefore reasonable to assume that the input field on the leading edge at the round-trip number n is the same as the SASE with FEL parameter ρ_n. The input field on the leading edge is given by $a_n(\zeta) = [|a(0)|/3] \exp[-4\pi\rho_n\zeta e^{i\pi/6}+i\phi(0)]$, where $\rho_2=\rho$. The analysis of the interaction between $a_n(\zeta)$ and the i_{th} electron leads to an asymptotical expression for the phase of the i_{th} electron at time τ, $\psi_i(\tau) = \psi_i(0) + 2|a_n[\zeta_i(\tau)]|/(4\pi\rho_n)^2 \cos[\psi_i(0)-2\pi\rho_n\zeta_i(\tau)-\pi/3]$[4].

An asymptotical expression for the field gain of $a_n(\zeta,\tau)$ due to an electron micro-bunch in units of λ, whose initial positions is around $\zeta+\tau$, are obtained by substitution of the phase for the i_{th} electron into the Maxwell equation as follows[4]: $[1/ a_n(\zeta,\tau)][d\, a_n(\zeta,\tau)/d\, \tau] = (\rho/\rho_n)^3\, (4\pi\rho_n e^{i\pi/6})$ when $2a_n(\zeta)|/(4\pi\rho_n)^2 << 1$ and $\rho_n\tau > 0.4$. This means that incident electrons lose almost the same amount of energy at ζ regardless of their initial positions, when the electrons have slipped back over the distance longer than $0.4/\rho_n$ on the leading edge. This results in an intensive energy transfer from electrons to the field at ζ_p. The intensive energy transfer is also reproduced in a time dependent simulation and can account for generation of intense few cycle FELs at dL=0.

3. Summary

An FEL interaction between incident electrons and a field with a steep intensity gradient on the leading edge is studied analytically. It is found that an intensive energy transfer, which is unique to FELs at dL = 0, occurs at the principal peak on the leading edge due to the interaction. The intensive energy transfer accounts for generation of an intense few-cycle field at dL = 0.

References

1) N. Nishimori et al., PRL **86**, 5707 (2001).
2) Kwang-Je Kim, PRL **57**, 1871 (1986).
3) G. Dattoli and A. Renieri, in *Laser Handbook*, edited by M.L. Stitch and M. Bass (North Holland, Amsterdam, 1985), Vol.4, p.75.
4) N. Nishimori, NIM A **528**, 34 (2004).

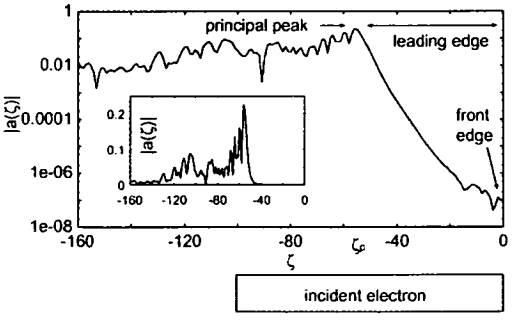

Fig. 1. Semi-log plot of an FEL amplitude at dL = 0 after saturation with respect to the longitudinal position ζ (solid line) together with an electron pulse at the entrance to an undulator. The positions of the front edge and the principal peak are 0 and ζ_p, respectively. The inset is a linear plot.

4.3.7 Chemical reaction of environmental destructive materials in IR laser irradiation calculated by Gaussian 03

Toshihiko YAMAUCHI, Seiji KOBAYASHI [a)]

a) RIST

1. Introduction

The IR lasers, free electron laser (FEL) or CO_2 laser, were irradiated to the environmental destructive materials. For example, the dioxin analogue PCB was successfully dissociated [1, 2)]. Here, it was important to choose the laser wavelength. The effective wavelengths which showed the strong absorption were determined from the results measured by FTIR spectroscope and calculated through the calculation code Gaussian 03. The results of Gaussian 03 also presented the characteristics of the vibration absorption in addition to it. The result of Gaussian 03 will present the transition process of chemical reaction, the threshold laser power of the dissociation and so on. Here, the vibration intensity was obtained in the IR wavelength (5~15 μm), which showed a good agreement with the experimental data measured by FTIR spectroscope.

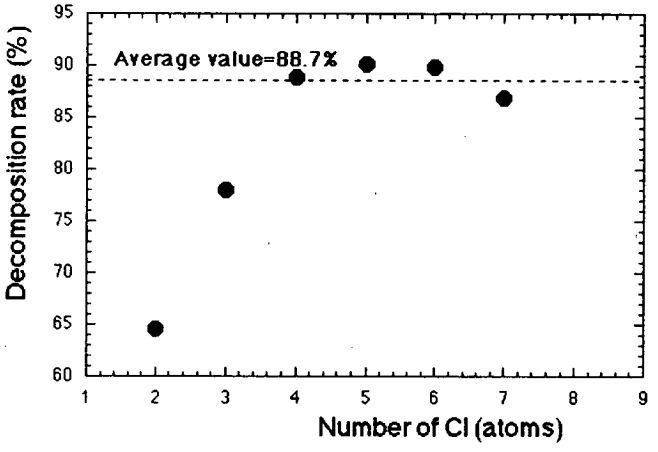

Fig.1 Decomposition rate of PCB

2. Experimental decomposition

The laser wavelengths, 7 μm and 10 μm and so on, were used to dissociate the dioxin analogues, and their wavelengths successfully made the dioxin analogues harmless. Especially the decomposition efficiency of PCB was about 90 % as shown in Fig.1[1)]. It was considered that the values 10 % was due to the reproduction of the harmful PCB, passing through the temperature of 200~300 °C after switching the laser off. These phenomena have been studied using the Gaussian 03.

3. Vibration intensity calculated by Gaussian 03

The vibration intensity of p-chrolobiphenyl molecular was preliminary calculated as shown in Fig.2 to compare the experimental absorption intensity caused by the vibration, which was measured using the FTIR spectroscope. It is understood from the results of experiment and calculation that the dissociation (dechlorination) of p-chrolobiphenyl takes place, when the vibration intensity at the wavenumber 833 cm^{-1} (12 μm in Fig.2) is reduced. This procedure is applicable to the dioxin analogues. These calculations were executed using ITBL.

4. Summary

The study of the chemical reaction interacted between laser and some environmental destructive molecules has been performed using the calculation code Gaussian 03. We will clarify the transition process of decomposition presented by T.Yamauchi[2)] using the Gaussian 03.

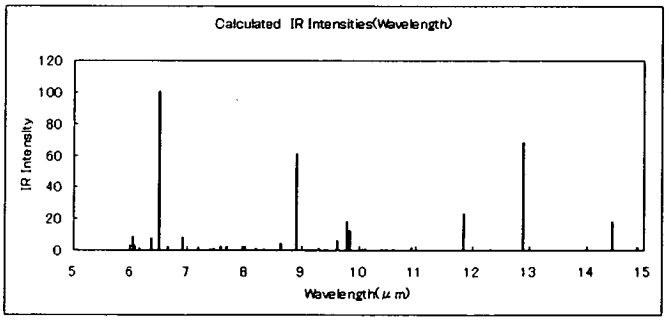

Fig.2 Vibration intensity of p-chlorobiphenyl calculated based on 6-31G(D)

References

1) T. Yamauchi *et al.*, Soc. of Environ. Sci. 13, 73, 2001.

2) T. Yamauchi, Soc. of Environ. Sci. 14, 567, 2001.

4.3.8 Evidence of nucleosynthesis process by photodisintegration reactions in supernova explosions

Takehito HAYAKAWA, Nobuyuki IWAMOTO, Toshiyuki SHIZUMA, Toshitaka KAJINO[a,b], Hideyuki UMEDA[b], Ken'ichi NOMOTO[b]

a) National Astronomical Observatory

b) Department of Astronomy, School of Science, University of Tokyo

1. Introduction

The solar system abundance ratio is important record of stellar nucleosynthesis and the chemical evolution of the Galaxy. The origin of "p-nuclei", which are rare isotopes (about 0.1~1 %) located in the neutron-deficient side in the nuclear chart, has been discussed. Many possible nuclear reactions are proposed, which are the rp-process in novae and neutron stars, the Galactic cosmic rays, the photodisintegration reactions in supernova (SN) explosions p-process[1,2] and the neutrino-induced reactions in SN explosions Our purpose is to report an empirical rule obtained from a careful analysis of the solar system abundance, which indicates that the origin of the p-nuclei is the SN p-process.

2. Analysis

There are twenty two p-nuclei associated with almost pure s-nuclei that have two more neutrons than the p-nuclei.The pure s-nuclei are dominantly synthesized by the s-process and shielded by stable isobarsagainst the beta-decay after the freezeout of the r-process. Taking the abundance ratios of the s-nucleus to the p-nucleus, N(s)/N(p), where N is each isotope abundance, we find a clear correlation between them as shown Fig.1. The ratios concentrate at a constant value of N(s)/N(p) ~ 23 in a wide mass

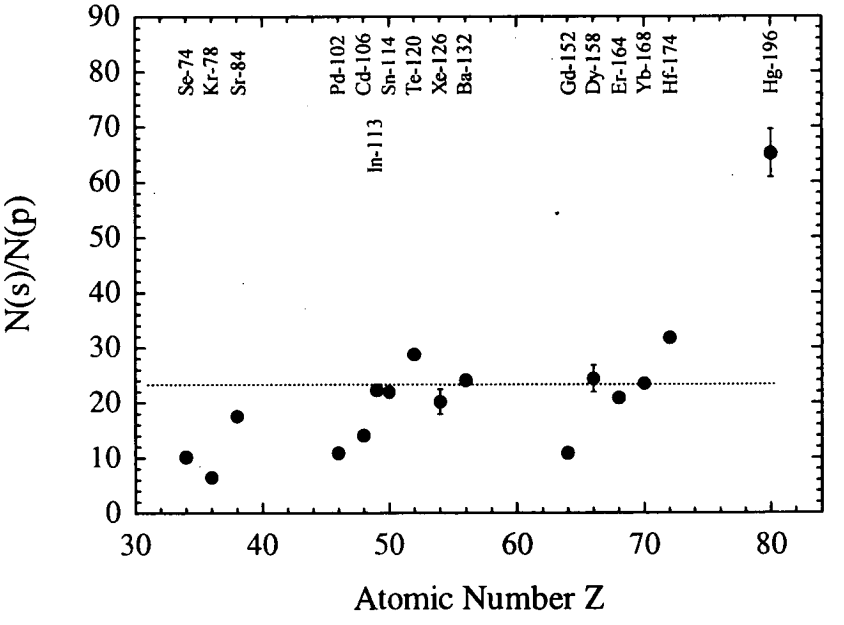

Fig.1 The ratios of p-nuclei to s-nuclei with the same atomic number in the solar system.

region. This is consistent with the previous theoretical calculations that the p-nuclei are produced by the p-process in SN explosions[1,2]: namely, the pre-existing nuclei in massive stars are affected by the s-process during the pre-supernova evolutionary stage and the p-nuclei are subsequently produced from them by photodisintegration reactions in a huge photon bath at an extremely high temperature in SN explosions. On the other hand, the other proposed processes change the proton number from the seed nuclei. Therefore this is a piece of evidence that the p-process in SN explosions is the most promising origin of the p-nuclei.

References

1) M. Arnould, Astron. Astrophys. **46**, 117, 1976

2) S.E. Woosley, W.M. Howard, Astrophys. J. Suppl. **36**, 285, 1978

4.3.9 Photoneutron cross sections on ^{187}Re and ^{188}Os

Toshiyuki SHIZUMA, Takehito HAYAKAWA, Hiroaki UTSUNOMIYA[a], Shinji GOKO[a], Ayano. MAKINAGA[a], Kaoru HARA[a], Peter MOHR[b], Hideaki OHGAKI[c], Yiu-Wing LUI[d], Stephen GORIELY[e]

a) Department of Physics, Konan University, Japan
b) Institute fur Kernphysik, Technishe Universitat Darmustadt, Germany
c) Institute of Advanced Energy, Kyoto University, Japan
d) Cyclotron Institute, Texas A&M University, USA
e) Institute d'Astronomie et d'Astrophysique, Universite Libre de Bruxelles, Belgium

1. Introduction

The ^{187}Re-^{187}Os pair is one of the best candidates for estimation of the age of our Galaxy owing to the long half-life of ^{187}Re [1]. The fact that both ^{186}Os and ^{187}Os can be produced only by s-process nucleosynthesis apart from the cosmoradiogenic yield of ^{187}Os makes this chronometer potentially reliable. The quantitative interpretation is however complicated by two major factors; the existence of s-process branchings at ^{185}W and ^{186}Re, and the importance of neutron capture by the 9.75 keV first excited state in ^{187}Os which is substantially populated in stellar plasmas [2]. These issues are related to the neutron capture cross sections for the short-living states, i.e., the ground states of ^{185}W and ^{186}Re, and the 9.75 keV state in ^{187}Os. Because of experimental limitation, direct measurements of the neutron capture cross sections on such states are very difficult. We therefore used the inverse photodisintegration reactions to estimate the neutron capture cross section on the basis of theoretical models. In this case, the (γ,n) cross sections close to the threshold energies are important to constrain the model parameters. In the present study, we have measured the photoneutron cross sections for ^{187}Re and ^{188}Os using a tunable quasi-monochromatic γ-ray beam from laser Compton scattering (LCS).

2. Experiment

The experiment was carried out at the National Institute of Advanced Industrial Science and Technology (AIST). LCS γ rays were generated by interaction of a Nd:YLF Q-switch laser in second harmonics (λ=527 nm) with a relativistic electron beam in the storage ring TERAS. The electron energy was varied from 450 to 588 MeV which allowed to produce γ-ray photons with maximum energies of 7.3 to 12.5 MeV. A 20 cm lead collimator with a 2 mmϕ hole was placed at 6 m downstream from the interaction area to form a quasi monochromatic γ-ray beam with a typical energy resolution of 10 % in FWHM. The targets consisted in enriched metallic powders of ^{187}Re and ^{188}Os, and were pressed into self-supporting tablets with a diameter of 8 mm. The tablets were then mounted into thin containers made of pure aluminum. The LCS beam energies were set below the threshold energy of ^{27}Al (E_{th}=13.1 MeV). The present measurement was therefore not affected by the ^{27}Al(γ,n) reaction. Emitted neutrons were detected by sixteen ^{3}He proportional counter embedded in double concentric (inner and outer) rings into a polyethylene moderator cube. The inner and outer rings were at 7 and 10 cm distance from the beam axis. The so-called ring ratio between the neutron counts of the inner and outer detectors was used to estimate the neutron energy.

3. Result

Figure 1 shows the photoneutron cross sections on ^{188}Os as a function of the LCS beam. The energy dependence of the photodisintegration cross section has been determined down to energies close to the neutron threshold (7.989 MeV). The previous data taken with the positron annihilation source [3] are also given in the figure for comparison. It should be noted that the non-vanishing cross section below the (γ,n) threshold energy previously reported are not confirmed in the present data.

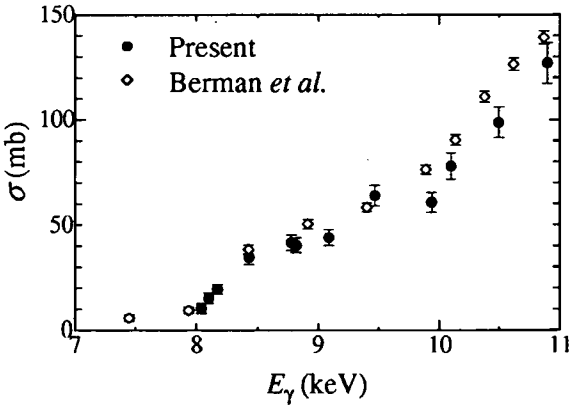

Fig.1 Photoneutron cross sections on ^{188}Os.

References

1)D.D. Clayton *et al.*, Astrophys. J. **139**, 637, 1964
2)M. Arnold *et al.*, Astron. Astrophys. **137**, 51, 1984
3)B.L. Berman *et al.*, Phys. Rev. C **19**, 1205, 1979

4.3.10 Nuclear isomer research by deep inelastic collisions

Toshiyuki SHIZUMA, Takehito HAYAKAWA, Siro MITARAI[a], Tsuneyasu MORIKAWA[a] and Hiroaki UTSUNOMIYA[b]

a) Department of Physics, Kyushu University, Japan
b) Department of Physics, Konan University, Japan

1. Introduction

Nuclei around the A=180 region have many high-Ω orbitals near the Fermi surfaces for both proton and neutron. Therefore, high-K (=ΣΩ) multi-quasiparticle states formed by stretched spin coupling of these high-Ω quasi-particles can compete with collectively excited states nearby a yrast line [1]. Transitions depopulating such states often require large K changes, low transition energies, parity change, or combination of these, making the initial state to be an isomer with a comparatively long half-life. However, high-spin studies of the heavier Hf-W-Os nuclei have been limited due to lack of suitable fusion-evaporation reactions to access to these nuclei. In order to populate high-spin excited states of such nuclei, we have employed a reaction of deep inelastic collisions (DIC). This type of reaction has been proven to be useful for population of levels of medium to high spins in heavier stable isotopes [2].

2. Experiment

A 630 MeV ^{82}Se beam derived from the tandem and booster accelerator at Japan Atomic Energy Research Institute was used to bombard a self-supporting target stacked by two ^{186}W (enriched to 98.2 %) metallic foils with a thickness of 450 μg/cm^2 each. Projectile-like fragments were detected by a silicon detector, while delayed γ rays emitted by target-like fragments were measured with four HP Ge detectors using the so-called recoil shadow method. Events were recorded on magnetic tapes when the silicon detector and one or more Ge detectors were fired in coincidence. Relative times between the silicon and γ-ray signals were also measured. The energy calibration of the Ge detectors was made by using ^{133}Ba, ^{152}Eu and ^{241}Am standard sources. Two-dimensional E_γ-E_γ matrices with various gating conditions of timing signals and silicon events were created.

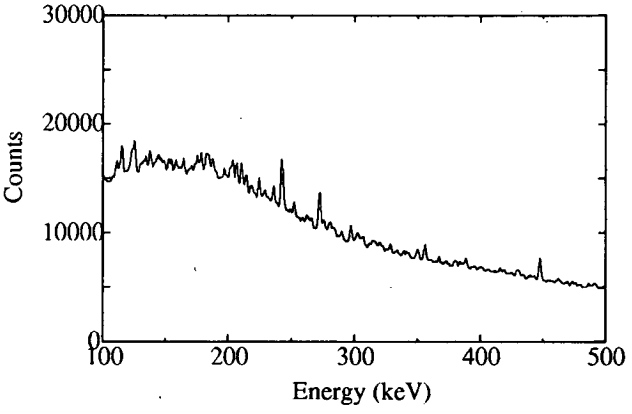

Fig.1 A projected γ-ray spectrum without any silicon gates.

3. Result

Figure 1 shows a projected γ-ray spectrum without any gates on the silicon events, while figure 2 is one obtained by gating on the the DIC events of the silicon signals. In fig. 2, known γ-ray peaks from the E_x=2124 keV isomer in ^{185}Re [1] and the E_x=1682 keV isomer in ^{187}Re [3] with half-lives of a range of 100 ns are clearly seen, exhibiting that the present experiment can be use to identify isomers with half-lives ranging nano seconds to micro seconds in neutron-rich side of nuclei. Further analysis of delayed γ-ray transitions is in progress.

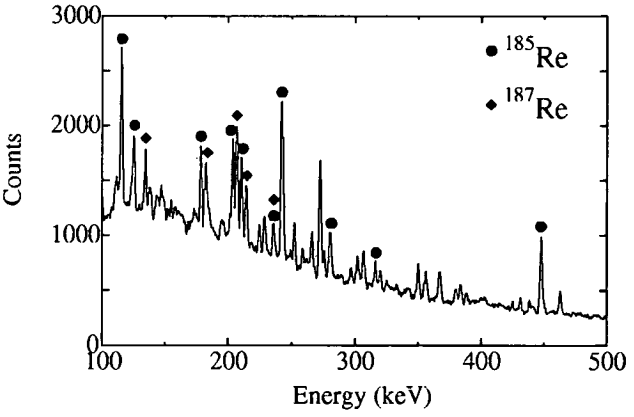

Fig.2 A projected γ-ray spectrum gated on the DIC events of silicon signals.

References

1)P.M. Walker *et al.*, Nature **399**, 35, 1999
2)C. Wheldon *et al.*, Phys. Lett. B **425**, 239, 1998
3)T. Shizuma *et al.*, Z. Phys. **A359**, 229, 1997
4)T. Shizuma *et al.*, Euro. Phys. J. A **17**, 159, 2003

4.4 Optics research and development

The Novel Optics Research Group*

* Masato KOIKE, Osamu YODA, Yuichi SHIMIZU, Akira SUGIYAMA, Masahiko ISHINO, Yasunaga NARA, Takashi IMAZONO

1. Introduction

Development of advanced lasers such as the T-cube laser and soft X-ray laser requires novel optics including laser crystals, multilayer mirrors, polarization elements, and diffraction gratings in addition to development of laser oscillation technology. The efforts of the Novel optics research group are devoted to the research and development on optical components, optical systems, and basic technologies for development and application of the advanced lasers and other soft X-ray state-of-arts sources.

2. Achievements

In the developments of laser optical elements, we have optimized the temperature of heat treatment in the Nd:YVO_4 and YVO_4 bonding process to prevent precipitates at the bonded interface. From our examination using an electron spectroscopy chemical analyzer, it was assumed that the opaque precipitates is created by the vanadic acid ($V_2O_5 \cdot nH_2O$) transformed from V_2O_5 and water inside the furnace. For the prevention, temperature adjustment less than the melting point of V_2O_5 was required. As a result, the precipitation was clearly suppressed, as shown in Fig. 1.

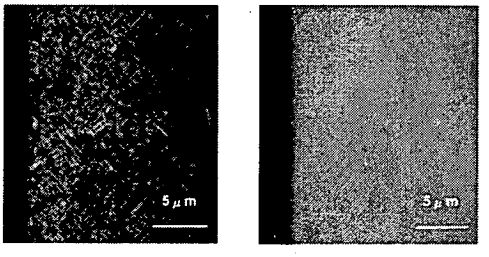

at 1373 K **at 873 K**

Fig. 1 Precipitation in the heat treatment for 50 hours

In the developments of soft x-ray optical elements, we have fabricated the multilayer mirrors consisting of oxide and nitride layers for use around the K-absorption edge of carbon (λ = 4.4 nm). We have found that the Co_3O_4/SiO_2 and the Mix/BN multilayer have uniform layer structures from the x-ray scattering measurement and the transmission electron microscopy (TEM) observation, where Mix is a mixture of Co_3O_4 and Cr_2O_3. The x-ray reflectivity curves of multilayer mirrors derived from the x-ray scattering measurements with Cu$K\alpha_1$ x-rays are shown in Fig. 2. The x-ray reflectivity curves are shifted downward successively for clarify. The x-ray reflectivity curves of the Co_3O_4/SiO_2 and the Mix/BN multilayer mirrors contain as many as four and three Bragg peaks in the measured 2θ region, respectively. The measured soft x-ray reflectivities of Co_3O_4/SiO_2 and Mix/BN multilayer mirrors are less than 2%, which are about one tenth of the theoretical values assuming perfect multilayer structures. It is thought to be due to the roughness at the interface and at the surface of the multilayer mirrors. Also we have examined a natural muscovite mica crystal having good crystallinity(Fig.3) to develop the polarization elements in the soft X-ray region of 1-2 keV. As the result of the preliminary reflection measurement of muscovite mica at the incidence of angle of around 45° using synchrotron radiation, we have confirmed that muscovite mica is promising candidate as a reflection-type polarizer. with approximately 1.4% reflectance for s-polarization around 0.9 keV.

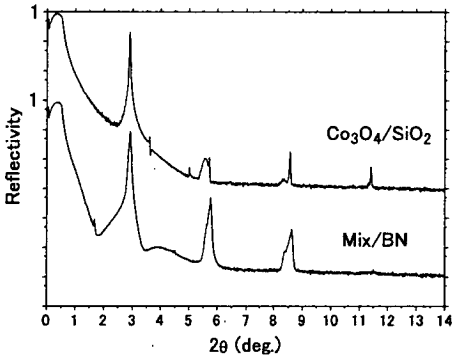

Fig.2 X-ray reflectivity curves of the Co_3O_4/SiO_2 and the Mix/BN multilayer mirrors

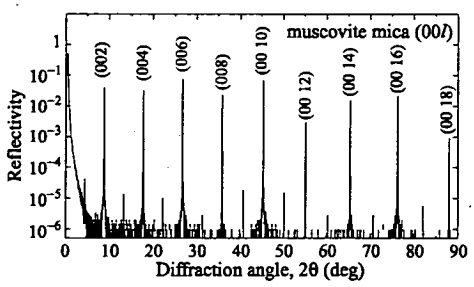

Fig. 3 X-ray reflectivity curve for a cleaved muscovite mica(00*l*)

4.4.1 Interfacial properties of a direct bonded Nd:YVO_4 and YVO_4 single crystal

Akira SUGIYAMA

1.Introduction

Laser crystal integration of Nd:YVO_4 and YVO_4 was achieved by way of our newly developed direct bonding technique[1]. In the preparation of contact, surface improvement was performed by using ion beam irradiation which is an appealing process for the extension of the bonding technique in other hygroscopic and fluoride crystals. The bonded region was evaluated from the macroscopic to the atomic level by different methods. From interferometer experiments, the wavefront distortion caused by the bonded region was assumed to be around 0.04 λ at 633 nm. Optical scattering measurements showed the number of scattering centres in the bonded region were much smaller than that of the intrinsic micro defects inside the crystal, as shown in Fig. 1. The scattering density around the bonded interface was less than 4.6×10^6 /cm^3. In addition, magnified inspection around the bonded region was also performed[2-3].

2.Experimental results

Figure 2 shows the magnified image of the bonded region. From the measured lattice constant of 0.625 nm in this photo, it is recognized that the bonded interface is parallel to the crystal c-axis. Although obscure parts of thickness 2 nm slightly appeared along the bonded interface, the atoms in the bonded region composed of two different types of crystal were well arranged with the same regularity as the bulk crystal. We attribute the obscure parts to the irregularity of the polished surfaces. In the bonding process, most of the irregularity is reduced by elastic deformation and diffusion of the atoms during the long heat treatment.

In the quantitative analysis by EDX, the four elements of neodymium, yttrium, vanadium and oxygen that compose the crystal were selected and measured in spots of 5 nm diameters around the bonded region. As a result, we recognized that Nd^{3+} ions move slightly toward the YVO_4 side, which is assumed to be driven by the Gorsky effect caused in the thermal diffusion. From the Nd^{3+} ion migration, the diffusion coefficient of Nd^{3+} ions at the bonded interface was estimated at 2.3×10^{-23} m^2/sec at 873 K. The diffusion coefficient of Nd^{3+} ions at the bonded interface of a YVO_4 crystal has not been measured by any other methods. For the estimation, we proposed the effective EDX analysis in the microscopic measurement for the bonding region of hetero materials. The measured interfacial properties suggest that the optical loss at the bonded region is insignificant and the bonded crystal is applicable for laser gain material to improve the heat transfer in case of the high power optical pumping.

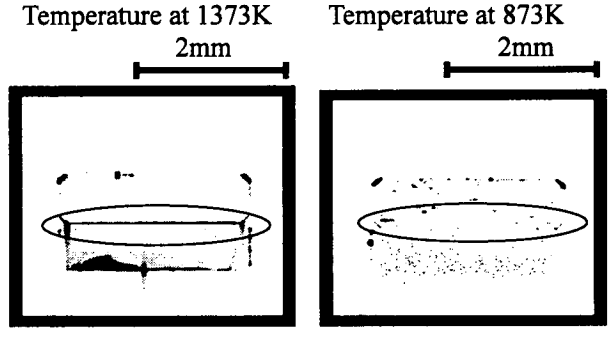

Fig. 1 Optical scattering images of the bonded crystals resulting from different heat treatment. Oval indicates the bonded region

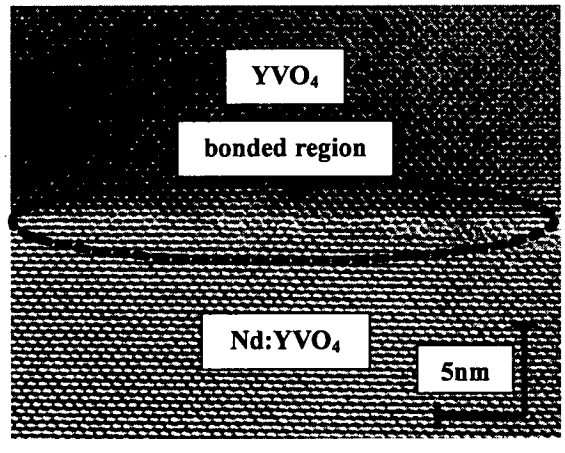

Fig. 2 Cross-sectional TEM image of the YVO_4 and Nd: YVO_4 bonded specimen

References

1) A. Sugiyama, H. Fukuyama, M. Katsumata and Y. Okada, *Proc. of SPIE.*, **4944**, 361, 2003
2) A. Sugiyama and Y. Nara, *JAERI-Research*, **2003-023**, 2003 in Japanese
3) A. Sugiyama, Y. Nara, K. Wada and H. Fukuyama, *J. of Mat. Sci. in Electron.*, 15, 607 , 2004

4.4.2 Soft x-ray reflectivity measurements of multilayer mirrors consisting of oxide and nitride layers for use around the K-absorption edge of carbon

Masahiko ISHINO, Osamu YODA, Eric M. GULLIKSON[a], and Masato KOIKE
a) Lawrence Berkley National Laboratory

1. Introduction

We have developed the multilayer mirrors for use as optical elements around the K-absorption edge of carbon (λ = 4.4 nm). We have found that the Co_3O_4/SiO_2 multilayer system has uniform layer structures, and the mixture of Co_3O_4 and Cr_2O_3 (Mix = Co_3O_4 + Cr_2O_3) is appropriate for combination with BN so that the Mix/BN multilayer system is also candidate for the soft x-ray mirror.[1] Then, we have fabricated the Co_3O_4/SiO_2 and the Mix/BN multilayer mirrors and carried out the soft x-ray reflectivity measurements.

2. Experimental

The Co_3O_4/SiO_2 and Mix/BN multilayer mirrors were fabricated by the ion beam sputtering method. Periodic lengths and the number of periods of each multilayer mirror are 3.1 nm and 201 periods (402 layers), respectively. Si-wafers were used as the substrates. The first layers on the substrates were Co_3O_4 and Mix layers and the topmost layers were SiO_2 and BN layers, respectively. The soft x-ray reflectivity measurements were carried out using the standard and calibration beamline 6.3.2 at the Advanced Light Source (ALS).[2,3]

3. Results

Figures 1(a) and 1(b) show the soft x-ray reflectivity curves of the Co_3O_4/SiO_2 and Mix/BN multilayer mirrors, respectively. The soft x-ray reflectivities are obtained by incident beams of s-polarization. The wavelengths of incident x-rays were fixed at 4.3 and 4.5 nm, and incident angles were scanned, so that the soft x-ray reflectivities are shown as a function of incident angles with respect to multilayer surface. Soft x-ray reflectivities of the Co_3O_4/SiO_2 multilayer mirror are about 1.5% for the wavelength of 4.3 nm at the incident angle around 44.5° and 2% for 4.5 nm at around 47.5°, respectively. Measured soft x-ray reflectivities of the Mix/BN multilayer mirror are smaller than those of the Co_3O_4/SiO_2 multilayer mirror. Soft x-ray reflectivities of the Mix/BN multilayer mirror are about 1% for 4.3 nm at around 45° and 2% for 4.5 nm at around 47.5°, respectively. The simulation calculation of the multilayer mirrors assuming perfect multilayer structure, i.e., uniform layer thickness and clear layer boundaries without roughness and diffusion, show the soft x-ray reflectivities of 20% and more in the K-absorption edge of carbon region at around 45°.[1] However, measured values are less than one tenth of theoretical values. The imperfect structures of multilayer mirrors such as roughness at the interface and at the surface or diffusion at the interface will decrease soft x-ray reflectivities remarkably.

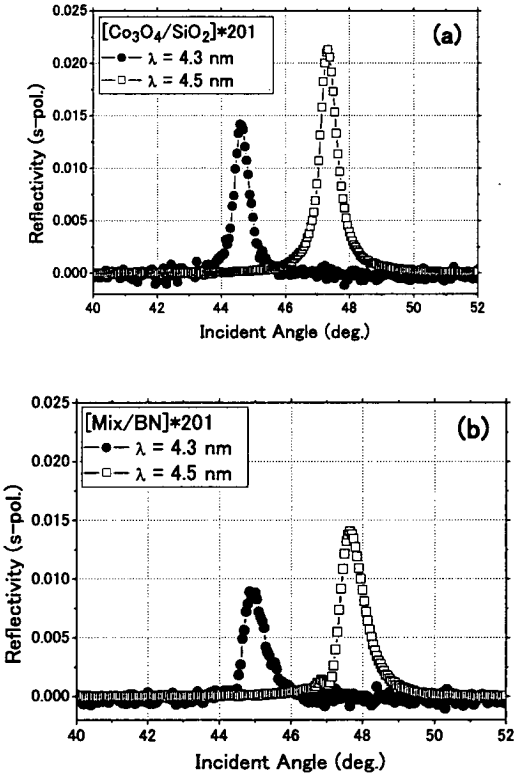

Fig. 1 Measured soft x-ray reflectivity curves of (a) the Co_3O_4/SiO_2 multilayer mirror and (b) the Mix/BN multilayer mirror

References

1) M. Ishino and O. Yoda, Appl.Opt. **43**, 1849, 2004
2) M. Koike and T. Namioka, J. Electron Spectroscopy and Related Phenomena **80**, 303, 1996
3) J. H. Underwood et al., proc. SPIE **3113**, 214, 1997

4.4.3 Conical Diffraction Monochromator Equipped with Holographic Gratings in Energy Region of 1-4keV

Masato KOIKE, Takashi NAMIOKA[a)]
a) Tohoku University

1. Introduction

The conical diffraction mounting was first discovered half a century ago and since rediscovered [1]. Recently, this mounting has attracted researchers in the field of XUV space astronomy because of its high throughput for XUV. In 1983, Cash [2] and Hettrick [3] proposed independently the use of a plane grating with radial grooves in a conical diffraction mounting. This concept was demonstrated by Windt and Cash [4] and applied to a sounding rocket-born EUV spectrograph successfully [5]. Detailed analysis of spectrographs of this type was made by Hettrick [6] and Cash [7]. While they mentioned possible use of a holographic grating in the conical diffraction mounting, they gave no analysis on it. For this reason we have analyzed the imaging property of a holographic plane grating with grooves of a radial form, which will be called holographic radial grating in this paper, in a conical diffraction mounting. This paper presents the results of the analysis together with sample monochromator designs for the 1-4 keV region and their expected performances in comparison with the ruled grating having straight radial grooves.

2. Optics

Figure 1 shows a holographic recording system and its coordinate system whose origin is at the center O of the blank of a size $W \times L$ and x axis is the blank normal at O. The points $C(x_C, y_C, z_C)$ and $D(x_D, y_D, z_D)$ are coherent point sources of wavelength λ_0. The sign of γ, δ, and $\theta_{C,D}$ are the same as that of y_C, y_D, and $z_{C,D}$, respectively.

The holographically recorded grooves are expressed by

$$n\lambda_0 = [<CP>-<DP>]-[<CO>-<DO>], \qquad (1)$$

where n is the groove number counted from the groove passing through O and takes a positive (or negative) sign when the groove intersects the y axis on its positive (or negative) side, the point $P(0,w,l)$ lies on the nth groove, and $< >$ denotes the distance between the respective points.

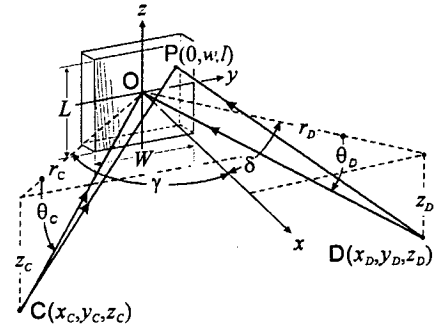

Fig. 1 Recording optics

Figure 2 shows a conical diffraction mounting that uses a holographic plane radial grating, G, in a beam of light perfectly converging to a point A_0'. G is placed in the beam so that the central ray A_0A_0' of the beam meets G (shown by the dashed lines) at its center O and its projection onto the plane of G coincides with the central groove ($n = 0$). The zero-order image is formed at a point S, the symmetric point of A_0' with respect to the plane of G.

When the grating is rotated through an angle α about the central groove, the angle, θ (> 0), between the incident principal ray A_0O and its projection onto the x-y plane remains unchanged and the zero-order image is formed at a point S', the symmetric point of A_0' with respect to the plane of G (shown by the solid lines). The principal ray of wavelength λ in mth order diffracted from O makes an angle θ' (<0) with the x-y plane and forms a spot at a point B_0 in an image plane.

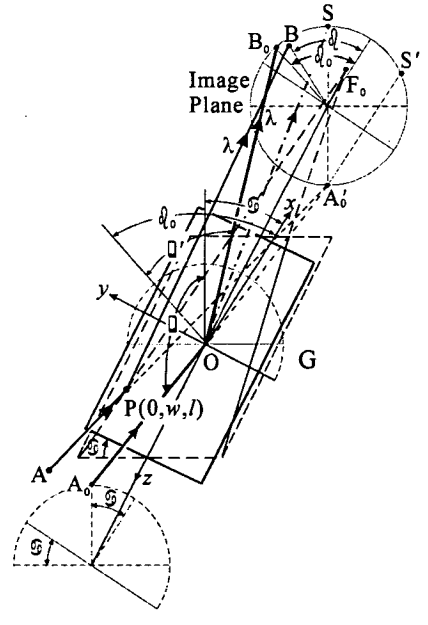

Fig. 2 Schematic diagram of a conical diffraction mounting

Since the point A_0' acts as a virtual point source, the light path function for the virtual ray $A_0'PB$ is expressed by

$$F = -<A_0'P> + <PB> + nm\lambda. \qquad (2)$$

The light path function is expanded into a power series as

$$F = F_{00} + F_{10}w + F_{01}l + F_{20}w^2 + F_{11}wl + F_{02}l^2 + F_{30}w^3 + F_{21}w^2l + F_{12}wl^2 + F_{03}l^3 + O(w^4/r^3). \qquad (3)$$

For the principal ray $A_0'OB_0$, application of Fermat's principle to the light path function F yields

$$\theta' = -\theta, \qquad \sigma\cos\theta(\sin\alpha + \sin\beta_0) = m\lambda. \qquad (4)$$

The anastigmatic condition is given by

$$\beta_0 = \alpha, \qquad r_0' = r. \tag{5}$$

This means that the anastigmatic spectral image formation is easily accomplished by the use of a Littrow-type conical diffraction (LCD) mounting.

3. Design Example

We give a sample design of holographic radial gratings for use in a LCD monochromator that covers an energy region of 1–4 keV on a low emittance synchrotron radiation beamline. The basic parameters we assumed are $\lambda_0 = 441.6$ nm, $\sigma = 1/3600$ mm, $W = 10$ mm, $L = 100$ mm, $r = r_0' = 5000$ mm, and $\theta = -\theta' = 88.6°$. The design procedure we have developed [8] yielded the following recording parameters: $r_C = r_D = 2200$mm; $z_C = z_D = -1311.741$mm; $\delta = -\gamma = 67.736271°$. The residual aberrations, $F_{30} = 1.740656\times10^{-11}$ mm^{-2} and $F_{12} = 1.214174\times10^{-10}$ mm^{-2} at $\lambda = 0.6$ nm, decrease as r_D and $|z_D|$ increase. However, the value of δ approaches rapidly to 90°. We, therefore, use this sample design for further examinations.

The performance of the holographic radial grating in an LCD monochromator was examined by ray tracing in comparison with the ruled radial grating. In doing so, we assumed a toroidal mirror M in between a source and the grating to produce a convergent beam with unit magnification. We also assumed a self-luminous entrance slit of 10 μm × 250 μm and the following values for the radii of curvature of M, R and ρ, and other parameters: R = 225112.0 mm, ρ = 134.376 mm, r_M (distance of M to the slit) = 5500.0 mm, D (distance <MG>) = 500 mm, and θ_M (angle of incidence on M) = 88.6°.

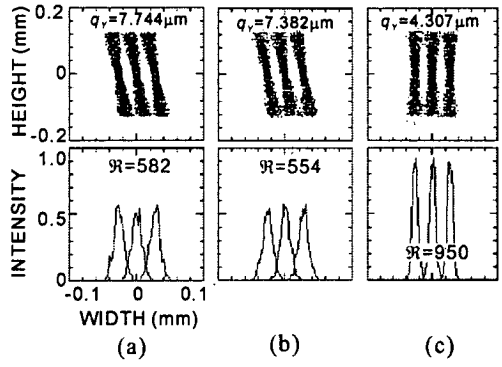

Fig. 3 Spot diagrams and line profiles

Figures 3(a) and 3(b) show the spot diagrams and line profiles constructed in an image plane perpendicular to the diffracted principal ray OS for the ruled and holographic gratings, respectively, with 1500 randomly-generated rays of $\lambda = 0.5985$, 0.6, 0.6015 nm. The separation of these three lines corresponds to a resolving power of 400 at 0.6 nm. For reference, the values of the resolving power, $\Re$, estimated from the line profiles [9] and the rms spread, q_Y, of ray-traced spots in the direction of run of the spectrum are given in the respective diagrams. These values are nearly the same for the holographic and ruled gratings. It is seen for both the gratings that the spectral images are slanted with respect to the exit slit, causing deterioration in spectral resolution. This situation can be improved by rotating the exit slit through an angle ϕ given by [10]

$$\tan\phi = 2\tan\alpha\sin\theta. \tag{6}$$

Figure 3(c) shows the spot diagrams and line profiles obtained by rotating Fig. 3(b) through 5.0557°, the value of ϕ calculated from Eq. (6). The line profiles are definitely improved and the resolving power is nearly doubled from 554 in Fig. 3(b) to 950 in Fig. 3(c), showing the necessity of synchronous slit rotation with wavelength scanning.

It is concluded from these results that, in the conical diffraction monochromator for the energy region of 1–4 keV, the holographic radial grating exhibits a resolving power equivalent to that of the ruled radial grating.

References

1) W. R. Hunter, Proc of SPIE, **503**, 78, 1984 , and the references therein.
2) W.C. Cash Jr., Appl. Opt. **22**, 3971,1983
3) M.C.Hettrick and S. Bowyer, Appl. Opt. **22**, 3921,1983
4) D.L.Windt and W.C. Cash, Proc of SPIE, **503**, 98, 1984
5) E. Wilkinson *et al.*, Astrophys. J. Supplement Series **89**, 211, 1993 and the references therein.
6) M.C. Hettrick, Appl. Opt. 23, 3221, 1984
7) W.C. Cash Jr., Appl. Opt. 30, 1749, 1991
8) M. Koike and T. Namioka, T, Proc. of The Eighth International Conference on Synchrotron Radiation Instrumentation (SRI 2003), AIP-CP (in press)
9) M. Koike and T. Namioka, Appl. Opt. **36**, 6308,1997
10) W.Cash, Appl. Opt. **21**, 710, 1982

4.4.4 Development of soft x-ray polarization elements of muscovite mica in 1-2 keV

Takashi IMAZONO

1. Introduction

It has been increasing demand for sophisticated linearly and circularly polarized lights in the soft x-ray region of 1-2 keV for the studies in the material sciences, e.g., magnetic circular dichroism measurements and the observation for three-dimensional atomic structure at absorption edges with element selectively. In spite of being very important for these studies utilizing polarized soft x-rays to acquire the information concerning the polarization state of the light source, the available soft x-ray polarization elements for polarization analysis in this energy region have not been developed so far because of the boundary aria both the crystal and artificial multilayer polarization elements. In the soft x-ray region of around 1 keV, the muscovite mica has been considered to be suitable for the polarizer due to its lattice spacing of d_{002} = 0.997 nm and excellent thermal and chemical stabilities. In order to develop the polarization elements in the soft x-ray region of around 1 keV, the polarization performances of muscovite mica have been investigated theoretically and experimentally.[1] As the results of the simulation calculations based on a conventional dynamical theory and the reflection measurement using horizontally linearly polarized synchrotron radiation, muscovite mica was found to be promising candidate as a reflection-type polarizer at around 0.9 keV.

2. Experimental

Muscovite mica used in this study is a natural product and acquired commercially. The thickness of sample is approximately 0.1 mm. The chemical formula of muscovite mica is $KAl_2(AlSi_3O_{10})(OH)_2$. The crystal structure is monoclinic, and lattice constants are a = 0.5199 nm, b = 0.9027 nm, c = 2.0106 nm, β = 95.78°. Muscovite mica has significant layer structure and it can be easily cleaved in (00l) faces. Also it has excellent thermal and chemical stabilities. At the incident energy of 879.06 eV, a symmetric Bragg reflection of (002) face satisfies ϕ_B = 45°, where ϕ_B means the Bragg angle measured from the normal of the sample surface.

The reflection measurement was carried out at BL-11 of the Synchrotron Radiation Center, Ritsumeikan University. This beamline consists of (1) prefocus system, (2) Monk-Gillieson type monochrometors[2] equipped with the varied line spacing grating and spherical focusing mirrors, (3) refocus system and (4) the evaluation system for soft X-ray optical elements.[3] The incident energy is E = 899.2 eV with energy band of approximately 1.5 eV, and then Bragg angle is ϕ_B = 45.65°.

3. Results

Figure 1 shows measured (open circle) and calculated (solid line) reflectance for s-polarization for a symmetric Bragg reflection of muscovite mica(002) of approximately 0.1 mm thickness at an incident energy of 899.2 eV, as a function of the incident angle ϕ. The Bragg angle is ϕ_B = 45.65°. The maximum reflectance for s-polarization is 1.4% at ϕ = 45.57° (open circle). Muscovite mica yields significantly higher reflectance than Au-coated mirror with 0.0005% reflectance. The reflectance for p-polarization is expected to be low enough because the incident angle is close to 45°, however, it has not been measured in this experiment. Thus this result indicates that muscovite mica has a possibility to work as a reflection-type polarizer at 889.2 eV.

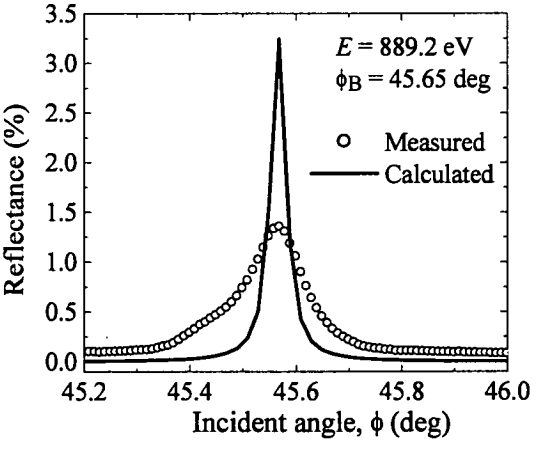

Fig. 1 Measured (open circle) and calculated (solid line) reflectances for s-polarization of muscovite mica(002)

References

1) T. Imazono, H. Soejima, K. Sano, M. Koike, JAERI-conf. 2003, in press.
2) M. Koike and T. Namioka, Appl. Opt. **36**, 6308, 1997
3) M. Koike, K. Sano, O. Yoda, Y. Harada, M. Ishino, N. Moriya, H. Sasai, H. Takenaka, E. Gullikson, S. Mrowka, M. Jinno, Y. Ueno, J. H. Underwood, T. Namioka, Rev. Sci. Instrum. **73**, 1541, 2002

4.5 Laser Driven Particle Acceleration Development

Kazuhisa NAKAJIMA, Masaki KANDO, Hideyuki KOTAKI, Shinichi MASUDA, Shuji KONDO, Shuhei KANAZAWA, Takayuki HOMMA, Izuru DAITO, Atsushi YAMAZAKI

Laser Acceleration Research Group

1. Introduction

Recently there is a great interest growing in advanced accelerator technologies based on laser and plasma acceleration mechanisms, which have attractive potential for applications to a wide range of sciences. In particular there has been a great experimental progress on the laser wakefield acceleration (LWFA) of electrons. Recent experiments have successfully demonstrated that the self-modulated LWFA mechanism is capable of generating ultrahigh accelerating gradient of the order of 1 TeV/m and of accelerating electron beams up to the high energy beyond 200 MeV[1,2] with high quality and ultrahigh current. These capabilities make it possible to realize a table-top accelerator and high energy frontier accelerators in a reasonable size and cost. High quality, ultrahigh current laser accelerated-electron beams benefit high energy accelerators and free electron lasers as an electron beam injector, and also applications to femtosecond X-ray beam generation and coherent Terahertz radiation.

Here we report the activities of Laser Acceelectron Research Group on laser wakefield acceleration experiments carried out by using 20 TW, 20 fs laser pulses. The experiments result in ultrahigh current relativistic electron beam acceleration of the order of Mega Ampere with energy spectrum characterized by a power law up to 40 MeV rather than a Maxwellian distribution.

2. Laser Acceleration Test Facility

Our laser acceleration research has been focused on electron acceleration experiments based on LWFA mechanism, aiming at high energy acceleration to achieve more than 1 GeV with plasma channel-guided scheme driven by 100 TW, 20 fs laser pulses. In order to accomplish these experiments, a high quality electron beam and high intensity laser pulses are delivered in the Laser Acceleration Test Facility (LATF) consisting of the photocathode RF gun, the 150 MeV microtron accelerator, the electron beam line and the laser transport line.

A high quality beam accelerated by the 150 MeV photocathode-microtron is utilized as a standard electron beam with 0.1% energy spread for calibrating the electron spectrometer and testing a new electron detector developed for laser acceleration experiments.

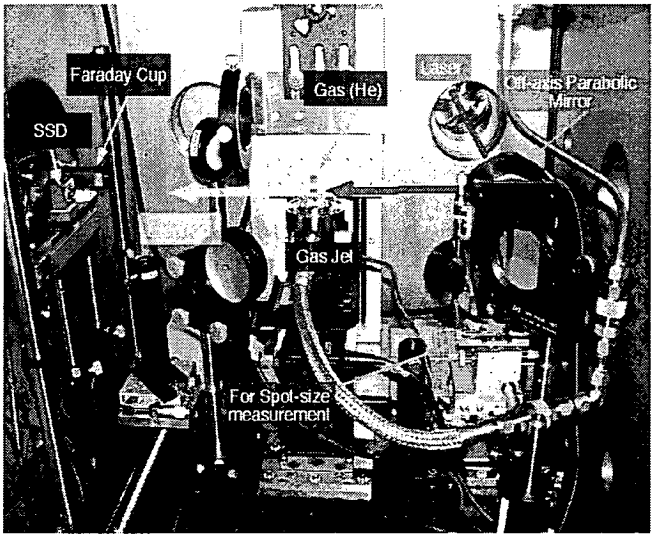

Fig. 1 An inside view of the laser plasma acceleration chamber used for ultrahigh current electron beam acceleration.

In LATF laser acceleration experiments in the use of the 100 TW laser sytem are conducted to investigate ultrahigh gradient electron acceleration by ultraintense laser pulses. In the relativistic intensity regime, nonlinear plasma dynamics evolves complex particle acceleration mechanisms. An important purpose of laser particle acceleration experiments is to elucidate relativistic particle generation and acceleration mechanisms in plasma. In addition to laser-plasma acceleration, the laser ponderomotive acceleration or the direct laser field acceleration in vacuum will be investigated by using LATF and the100 TW laser. The facility will be directed to user-oriented researches on laser particle acceleration and radiation sources under the international collaboration as a part of MEXT project on the Relativistic Engineering and Extreme Field Sciences, which has started in 2003.

3. Experiment for ultrahigh current electron beam generation

Following the preliminary laser-plasma electron acceleration experiment for 5TW, 30fs laser pulses in 2002, the electron acceleration experiments were carried out. A 100-TW Ti:Sapphire chirped pulse amplification laser system delivered a typical peak power of 20 TW and 23 fs FWHM duration which were focused onto a gas target with an off-axis parabolic mirror with a focal length of 178 mm (f/3.5) as shown in Fig.1. The electron charge of accelerated electrons was 5 nC (3 x10^{10}) per shot with emittance 0.5 π mm-mrad, which was measured over a solid angle of 0.012 sr at high plasma density of 10^{20} cm^{-3}. The total amount of the charge of accelerated electrons is inferred to be extremely as high as 50 nC, which means that a 20 % of the laser pulse energy was converted to the energetic electrons. Assuming that this electron bunch length is on the order of the plasma wavelength, the peak current of the beam may exceed 0.5 MA, which is much larger than the Alfven limit: 170 kA for 5 MeV electron beam. Since the numerical simulation indicated production of an electron bunch with ~ 0.3 fs duration[3], it is inferred that the peak current of the accelerated electron bunch was 17 MA, which is four orders of magnitude larger than that of the conventional accelerator beams.

The measured electron energy spectrum extending up to the maximum energy of 40 MeV, which are well fitted to a power law given by $E^{-3.7}$ rather than the Maxwellian distribution. It means that the acceleration mechanism for this experiment is different from the self-modulated wakefield acceleration due to a long laser pulse, of which energy spectra are dominantly characterized by the Maxwellian distribution of electrons accelerated due to both the laser field and the pure wakefield[4].

4. Applications of laser-plasma accelerated electron beams

The intense ultrashort pulse laser and plasma interactions produce high-brightness radiations with a wide range of spectrum and femtoseconds duration, which are useful for many applications in a number of scientific fields. An ultrashort pulse electron beam accelerated by wakefields can generate a well-collimated Multi-keV X-ray beam with femosecond duration through relativistic Larmor radiation or nonlinear Thomson scattering[5] and the betatron oscillation of electrons in plasma. It is known that Terahertz radiation can be generated by transition radiation from laser wakefield accelerated electron bunches[6].

Femtosecond X-ray beams with a wide range of the spectrum ranging from the soft X-ray to the hard X-ray are generated by Compton (Thomson) scattering of an intense laser pulse colliding with an ultrashort bunch electron beam accelerated by laser wakefields. A generated X-ray flux is expected to be extremely high when laser-accelerated electron beams with an ultrahigh peak current of the order of Mega Ampere interact with a Multi-TW laser pulse. As an example, assuming that a counter-propagating 20 fs laser pulse focused on a laser accelerated electron beam with the peak current of 1 MA at the intensity of 10^{20} W/cm^2, the peak X-ray flux is expected to be 10^{28} photons/s.

As an another attractive application of laser-plasma accelerated electron bunch with high charge, coherent transition radiation from electron beam accelerated by laser wake fields at a plasma-vacuum boundary generates Terahertz radiation over wavelengths longer than the electron bunch length. As an example, a 5MeV laser-accelerated electron beam with a charge of 5 nC can produce a total radiation energy of 200 mJ at the wavelength of 10 μm, which is several orders of magnitude larger than that of the state-of-the-art THz radiation sources, such as laser-triggered semiconductor THz sources.

References

[1] V. Malka et al., Science **298**, 1596 (2002).
[2] H.Dewa et al., Nucl. Instr. and Meth. in Phys. Res. **A410**, 357 (1998);
M. Kando et al., Jpn. J. Appl. Phys. **38**, L967 (1999).
[3] K. Nagashima, Y. Kishimoto, and H. Takuma, Phy. Rev. E, **59**,1263 (1999).
[4] A. Pukov and J. Meyer-Ter-Vehn, Appl. Phys. **B74**, 355 (2002).
[5] K.Ta Phuoc et al., Phys. Rev. Lett., **91**, 195001 (2003)
[6] W. P. Leemans~et al.,Phys. Rev. Lett., **91**, 074802 (2003)

4.5.1 Electron generation from a supersonic gas-jet target irradiated by 20 TW, 23 fs laser pulses

Masaki KANDO, Shinichi MASUDA*, Atsushi YAMAZAKI†, Hideyuki KOTAKI, Takayuki HOMMA, Shuji KONDO, Shuhei KANAZAWA, Kazuhisa NAKAJIMA‡, Hiromitsu KIRIYAMA, Yutaka AKAHANE, Michiaki MORI, Yukio HAYASHI, Yoshiki NAKAI, Norihiro INOUE, Hideki UEDA, Youichi YAMAMOTO, Koichi TSUJI, Alexei Zhidkov[a)], Tomonao HOSOKAI[a)], James K. KOGA, Koichi YAMAKAWA

[a)] The Nuclear Engineering Research Laboratory, The University of Tokyo

1. Introduction

Since the laser-plasma accelerator concept was invented[1], a large number of experiments of laser-plasma electron acceleration has been reported at various parameter regimes. In particular, so-called laser-plasma cathode scheme is studied extensively because of its simplicity rather than externally injection scheme and a capability of producing a high-quality electron beam. Nowadays, the maximum energy achieved in this scheme reaches to 200 MeV[2], the smallest emittance is 0.1π mm-mrad[3] and the shortest bunch duration is 50 fs[4]. However, the underlying acceleration mechanism, especillay the injection mechanism, is still open to argument. From the point of view, more experimental data are required at wide parameter spaces such as a laser pulse duration, a laser pulse energy, a contrast ratio, a plasma density, and so on. Here we report on the experimental data using the shortest laser pulse duration (23 fs) as well as the physical interpretation of its injection mechanism.

2. Experimental setup

The experimental setup is depicted in Fig.1. The experiments were performed with the JAERI 100 TW Ti:Sapphire laser that delivered, a 20 TW, 23 fs pulsed at 800 nm with a repetition rate of 10 Hz[5]. The typical intensity contrast was 10^{-6} on the nanosecond scale. The laser pulses were focused with a focal length of 178 mm(f/3.5) off-axis parabolic mirror onto a supersonic. The attenuated laser spot radius was 5 μm at $1/e^2$ intensity containing 50 % of the total laser pulse energy. This corresponds to the peak focused intensity of 2.3×10^{19} W/cm^2. A specially designed pulsed valve with a shock-wave free nozzle is used to produce a flat gas (helium) density distribution in a vacuum chamber. We varied the plasma density from 1.0×10^{19} to 1.4×10^{20} cm^{-3} by changing the stagnation pressure of the pulsed valve. Energetic electrons were monitored with a lithium doped silicon semiconductor detector (SSD) with amplifiers. To avoid exposure from the strong laser light and plasma fluorescence, the SSD is contained in a shielding box which has an entrance window covered with a 20 μm thick titanium foil. The electron spatial distribution was measured with image plates (Fuji Film, BAS-SR) placed 180 mm away the focus on laser axis. The electron charge was measured with a Faraday cup consisting of 20 × 20 mm copper block. The collected electron charge is measured by use of a CAMAC charge ADC. The electron energy distribution was measured with a magnetic spectrometer which consists of a dipole magnet and 32 channel plastic scintillators coupled with photomultipliers. To increase energy resolution, a collimator was placed in front of the dipole magnet which limited the electron beam acceptance to within ±10 mrad. The collimator was made of polyethylene and lead to reduce the amount of bremsstrahlung.

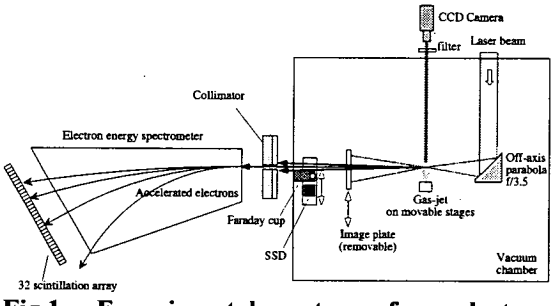

Fig.1 Experimental setup for electron generation

3. Experimental results and discussions

We have observed electron generation at a high density of 1.4×10^{20} cm^{-3} and the power of 20 TW. The electron charge was 5 nC per shot using the Faraday cup. The angular divergence of the electrons was 10 degrees rms. This leads to a calculated geometrical emittance of 0.5 π mm-mrad. The energy of

*Present address: National Institute of Advanced Industrial Science and Technology
†Also at Institute for Chemical Research, Kyoto University
‡Also at High Energy Accelerator Research Organization

electrons are shown in Fig.2. By changing the magnetic filed strength and shielding in front of the detectors, we confirm that these signals were due to high energy electrons. Exponential fit curves are also plotted, effective temperatures of which lead to 2.5 MeV and 7.8 MeV, respectively.

The present measurement are not free from laser pre-pulse effects. The laser pulse had a pre-pulse which was 10^{-6} continuing a nanosecond time scale. This pre-pulse forms a shock-wave in a plasma resulting in a formation of cavity[6]. We performed a two-dimensional PIC simulation using the moving-window technique. The plasma length was set to 2 mm, with a density gradient of length 5 μm at the edge of the gas-jet. The electron energy distribution obtained in the calculation has reproduced fairly well the experimental one as seen in Fig. 2. The two groups of electrons with different temperatures have been reproduced well. According to the spatial distribution of the electron momentum in the 2D simulation, these groups have different duration (see Fig.3). The higher temperature group constitutes a bunch with duration around 40 fs while the colder electron group has a length comparable (or may be longer) than with the simulation window which is 160 μm or 0.53 ps duration. According to the calculation, the shorter bunch is built from electrons injected at the shock-wave front and further accelerated by the plasma wake-field behind the laser pulse. The longer bunch is formed by electrons injected and accelerated by the wave-breaking of the plasma wake-field in the uniform part of the plasma. Since the latter process lasts much longer than the injection at the front of the shock wave, the duration of the corresponding bunch is also longer.

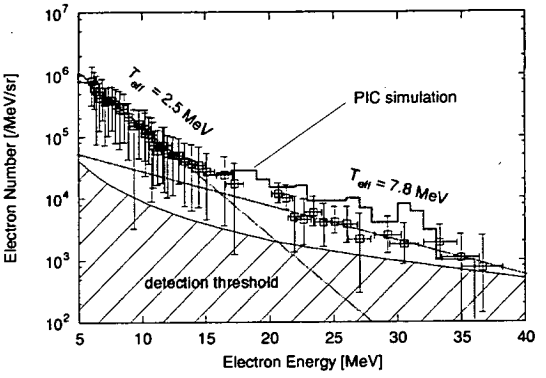

Fig. 2 Energy spectrum of electrons obtained in the experiment (open squares) and the simulation (city-space lines). The hatched line shows the detection limit.

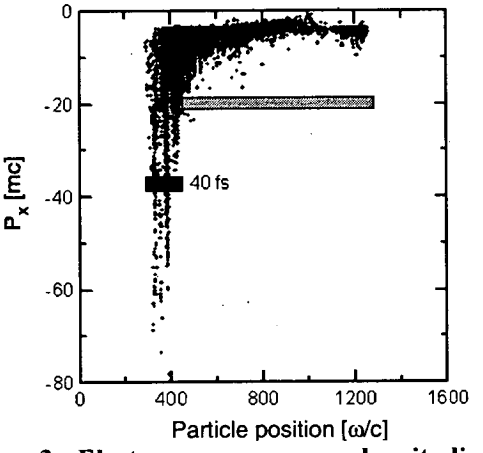

Fig. 3 Electron energy vs. longitudinal position.

4. Conclusions

We have focused an intense laser pulses with a time duration of 23 fs, which is the shortest at present, onto an underdense He plasma. A 5 nC total charge of accelerated electrons with an emittance 0.5 π mm-mrad has been detected at a high plasma density of 1.4×10^{20} cm^{-3}. Maximum electron energy extends to 35 MeV having a two temperature distribution of T_1 ~ 8 MeV and T_2 ~2.5 MeV. We attribute this to the existence of different plasma wave-breaking processes: (i) rapid wave-breaking injection at the front of the shock-wave produced by the laser pre-pulse with further electron wake-field acceleration up to high energy and (ii) slower injection originating from the wave-breaking in the uniform part of the plasma. The second group of the electrons is shown numerically to constitute a bunch with a duration of about a picosecond.

References

1) T. Tajima and J. M. Dawson, Phy. Rev. Lett. **43**, p. 267,1979.
2) V. Malka *et al.*, Science **298**, 1596, 2002.
3) S.-Y. Chen *et al.*, Phys. Plasmas **6**, 4739,1999.
4) W. P. Leemans *et al.*, Phys. Plasmas **11**, p.2899 (2004).
5) K. Yamakawa *et al.*, Opt. Lett., **23**, p.1468, 1998.
6) T. Hosokai *et al.*, Phys. Rev. E **67**, 036407, 2003.

4.5.2 Observation of fixed blueshift of focused intense laser pulses

Hideyuki KOTAKI, Masaki KANDO, James K. KOGA, Kenichi IKEDA[a)], Kazuhisa NAKAJIMA
[a)] The Graduate University for Advanced Studies

1. Introduction

The development of intense lasers has brought about a large number of experiments based on optical field ionization (OFI).[1,2] A spectral blueshift has been observed experimentally in the propagation of tightly focused intense ultrashort laser pulses through a gas medium.[3-5] This is due to the gradient of the refractive index in an ionization front at the front of the laser pulse which causes a spectral frequency shift of the short pulse laser.[6-9] This generic blueshift strongly depends on the laser intensity and the gas density. In our experiments, a different type of blueshift has been discovered.[10]

Here, we present experimental results of a fixed blueshift. The amount of shift depends on the ionic charge number and the pulse width at the focus point. We propose that the ionic charge number at the focus point can be understood from the blueshifted spectrum. Furthermore, because the amount of shift depends on the pulse width, the laser pulse width can be roughly determined from the amount of shift and we can adjust the compressor of the laser by only measuring the change of the shift.

2. Fixed blueshift of intense laser pulses

It has been shown theoretically and numerically that a short pulse laser that is propagating in a co-propagating ionization front will up-shift in frequency.[6] The frequency shift is obtained from the phase velocity gradient as photon acceleration. Assuming a linear density gradient the frequency shift, $\Delta\omega$, is written in the form

$$\frac{\Delta\omega}{\omega_0} = \frac{dv_p}{d\varsigma}\tau = \frac{c\tau}{2L_0}\frac{\omega_p^2}{\omega_0^2}, \qquad (1)$$

where where ω_0 is the initial laser frequency, ω_p the plasma frequency, v_p the phase velocity, τ the propagation time, $\zeta = z - ct$, and L_0 the scale length of the density gradient of the ionization front. The propagation distance, $c\tau$, is roughly equal to the refraction distance. The shifted laser frequency, ω_s, is given by[15]

$$\omega_s = \omega_0\left(1+\frac{\lambda_0}{2L_0}\right)^{1/2}, \qquad (2)$$

which indicates that the frequency shift is independent of the plasma density, type of gas, and laser intensity. The amount of shift just depends on λ_0 and L_0 which depends on the laser pulse length, τ_L.[15]

3. Experimental results

We measure the spectrum shift of a laser pulse with an initial spot size, D, of 45 mm for λ_0 = 795 nm and τ_L = 100 fs. The laser pulse is focused using convex lenses of various focal lengths f for the laser pulse energy, E, of 10, 20, 40, 60, and 100 mJ. Figure 1 shows the incident and the forward scattered radiation spectra. The spectra shift to 785 and 790 nm. The shifts show that L_0 is $0.5\tau_L c$ (half the pulse length), $0.85\tau_L c$ (the half width of the $1/e^2$ maximum), or a mixture of both. In the case of short (strong) focus, the incident spectrum remains in the forward scattered radiation after passing through various gases due to the short propagation distance on the outer edges of the laser pulse. Assuming a laser spot radius, ω_0, of 3f/D in units of μm at the focus point due to the defocusing of the laser pulse under the influence of ionization, the spectrum shifts to near 790 nm when the ionic charge

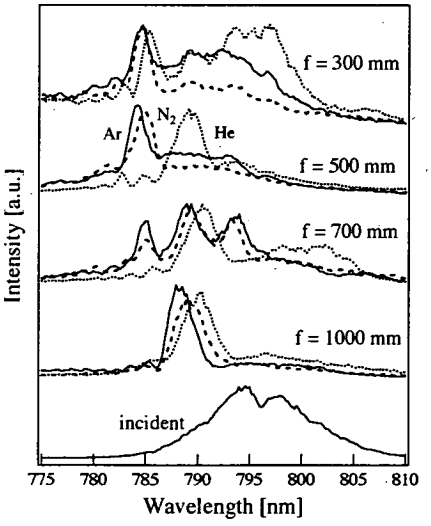

Fig.1 Forward scattered radiation spectrum after the laser pulse has focused in the gas filled chamber at 400 Torr (5.3×10^4 Pa) for E = 100 mJ. The bottom of the spectrum is the incident spectrum. For the blueshifted spectrum, the solid, the dotted, and the broken lines show the spectrum after passing through argon, nitrogen, and helium gas, respectively.

number is 2 for argon and nitrogen gas, and when the number is 1 for helium gas. The spectrum shifts to about 785 nm when the number is 3 for argon and nitrogen gas, and when the number is 2 for helium gas. When f = 700 mm, the blueshifted spectra are a mix between the 785 and 790 nm shifts for argon and nitrogen gas. This is caused by the fact that there are multiple focus points and, therefore, various focal lengths due to chromatic aberration and the loose focus. Ionic charge numbers are different at each focus point.

The measured data show that the amount of shift is independent of the pressure, and the amount of shift depends on E and f. So, the amount of shift is influenced by the intensity and the ionic charge number at the focus point. Assuming $\omega_0 = 3f/D$, in Fig. 2 we show the amount of spectrum shift with argon and helium gas. In both cases, the peak of the blueshifted spectrum strongly depends on the ionic charge number, because the gradient scale length, L_0, is the length of the ionization front of the maximum ionic charge number at the focus point. Near the ionization threshold, the spectrum shifts between 785 and 790 nm. This result might be due to the nonuniform transverse distribution of the laser pulse at the focus point. This result shows that we can determine the ionic charge number by measuring the amount of shift. Moreover, we can adjust the compressor of the laser pulse because the amount of shift depends on the ionic charge number and the pulse width.

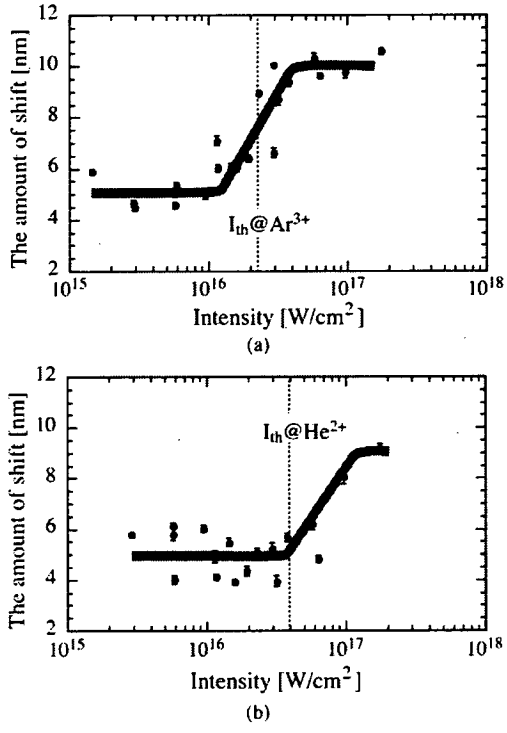

Fig.2 The amount of spectrum shift after passing through (a) argon and (b) helium gas for E = 10-100 mJ at 20-760 Torr (2.7×10^4-10^5 Pa). The vertical lines show the ionization threshold for Ar^{3+} and He^{2+}, respectively.

4. Conclusions

In this study, the mechanism of the fixed blueshift is elucidated. The forward scattered radiation spectrum shifts to a fixed value after the laser pulse has focused in gas. When the pulse is focused using a convex lens, the amount of shift depends on the pulse width and the ionic charge number at the focus point. It is expected that the ionic charge number and the laser pulse width can be measured from the blueshifted spectrum, and the compressor can be adjusted by only measurement of the amount of shift.

References

1) L. V. Keldysh, Zh. Eksp. Teor. Fiz. **47**, 1945 (1964) [Sov. Phys. JETP **20**, 1307 (1965)].
2) M. V. Ammosov, N. B. Delone, and V. P. Krainov, Zh. Eksp. Teor. Fiz. **91**, 2008 (1986), [Sov. Phys. JETP **64**, 1191 (1986)].
3) W. M. Wood, G. B. Focht, and M. C. Downer, Opt. Lett. **13**,984 (1988).
4) S. P. LeBlanc, R. Sauerbrey, S. C. Rae, and K. Burnett, J. Opt. Soc. Am. B **10**, 1801 (1993).
5) C. W. Siders, N. C. Turner III, M. C. Downer, A. Babine, A. Stepanov, and A. M. Sergeev, J. Opt. Soc. Am. B **13**, 330 (1996).
6) E. Esarey, G. Joyce, and P. Sprangle, Phys. Rev. A **44**, 3908 (1991).
7) S. C. Wilks, J. M. Dawson, W. B. Mori, T. Katsouleas, and M. E. Jones, Phys. Rev. Lett. **62**,2600 (1989).
8) B. M. Penetrante, J. N. Bardsley, W. M. Wood, C. W. Siders, and M. C. Downer, J. Opt. Soc. Am. B **9**, 2032 (1992).
9) S. C. Rae, and K. Burnett, Phys. Rev. A **46**, 1084 (1992).
10) J. K. Koga, N. Naumova, M. Kando, L. N. Tsintsadze, K. Nakajima, S. V. Bulanov, H. Dewa, H. Kotaki, and T. Tajima, Phys. Plasmas **7**, 5223 (2000).

4.5.3 Three-dimensional profile monitor for laser-accelerated electrons

Izuru DAITO, Masaki KANDO, Hideyuki KOTAKI, Shuji KONDO, Shuhei KANAZAWA, Takayuki HOMMA, Atsushi YAMAZAKI, Kazuhisa NAKAJIMA [a)]

a) JAERI Kansai and High Energy Accelerator Research Organization (KEK)

1. Introduction

Electron beam obtained with an ultra-high power laser is characterized by large energy spread[1]. In addition, total charge of electrons could be achieved up to several hundred pC in a duration of less than hundred fs. Thus it is impossible to measure its energy and position of each electron respectively. In order to monitor three-dimensional profile (2 spatial dimensions, x- and y-directions, and momentum distribution) of such kind beam, a new conceptual detection system is required.

2. Concept of detector

The profile monitor consists of many layers of scintillating fibers (SciFi) stacks as a sensitive material, and lead plates as an absorber/converter. The thickness of SciFi is 1 mm and its cross section is square. Lead plates are inserted between SciFi layers. The number of layers and the thickness of lead plates depend on a range of expected electron momentum. The spatial distribution is obtained by scintillating light distribution between fibers in each layer. The spatial resolution of 1 mm is expected since the thickness of SciFi is 1 mm. On the other hand, the information of electron energy distribution is obtained by scintillating light distribution between SciFi layers. To extract momentum distributions of the beam, at first, estimations of the detector to mono-energy electron responses by simulation is necessary. Energy deposits (= light outputs) of laser-accelerated electrons at each layer can be described by a linear combination of energy deposits of mono-energy electrons. A function F described below is a difference between measured energy deposit and a sum of estimated deposits at various monochromatic electrons.

$$F = \sum_{i=1}^{n} \left| \Delta E(i) - \sum_{j=1}^{m} C(Ej) \Delta E_i(E_j) \right| \quad ,$$

where $\Delta E(i)$ is measured energy deposit of the beam, which energy distribution is unknown, on i-th layer. $\Delta E_i(E_j)$ is calculated energy deposits of electron which energy is E_j on i-th layer, $C(E_j)$ is coefficient for incident energy E_j. By finding a combination of coefficient $C(E_j)$, which minimizes a function F, the energy distribution can be estimated, i.e., $C(E_j)$ is corresponding to the number of electrons in each energy region. The combination of the thickness of lead plates and a number of layers should be optimized to the energy distribution of the electron beam expected.

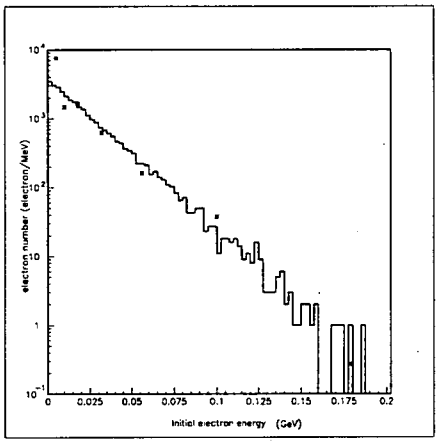

Fig 1 : One typical result of the simulation of electron energy distribution obtained by the detector (asterisk). The solid line corresponds to the incident electron energy distribution. The electron momentum distribution is assumed Maxwellian distribution.

3. Results of simulation

A result of simulation using a simulation code *GEANT3*.2.1 is shown in Fig. 1. A energy distribution of incident electrons is assumed Maxwellian distribution, $dn_e/dp_e = N_0 \exp(-p_e/p_t)$ (solid line). For 200 MeV/c of maximum electron momentum, 8 layers of SciFi are employed. The thickness of each lead plate is 0.0, 0.5, 1.0, 1.5, 1.5, 2.0 and 3.0 mm. The responses of SciFi layers from mono-energy electrons are calculated at the energies of 5, 10, 18, 32, 56, 100 and 178 MeV. The estimated energy distribution (asterisks) is good agreement with the incident electron energy distribution except low energy (less than 5 MeV) region.

References

1) M. Kando *et al.* , in this report.

4.5.4 Calibration of image plate by using electron beams from the microtron

Atsushi YAMAZAKI[a)], Masaki KANDO, Shinichi MASUDA, Hideyuki KOTAKI,
Takayuki HOMMA, Shuji KONDO, Shuhei KANAZAWA, Kazuhisa NAKAJIMA
a) JAERI-APRC and Institute for Chemical Research, Kyoto University

1. Introduction

Image plates (IPs) have come to be used as a monitor for electron profiles and energies, in laser-plasma acceleration experiments because of its high sensitivity and high dynamic range. After an irradiation of electrons, by adding a stimulated lights, an photostimulated luminescence (PSL) proportional to the deposited energy in the IP is emitted. In order to estimate a number of electrons which pass through the IP should be examined using a well-known electron source. We have calibrated a response of an IP for 150 MeV electrons from the microtron accelerator[1]. In addition the energy absorbed in the phosphor layer has been calculated with EGS4, which is a Monte Carlo simulation code for radiation transport.

2. Experimental

Image plates (Fujifilm BAS SR2025) were placed in a vacuum chamber and irradiated by electron beam from the microtron. The IPs were covered with aluminum foils to avoid exposure from room lights. Although a charge per bunch from the microtron can be reduced to 1 pC, its electron density on the IPs are still high resulting in saturation. Therefore, we used a dark current originates from field emission in a high electric field of 100 MV/m in a radio-frequency cavity of the microtron. The dark current has the charge of 0.04 pC , the energy of 150 MeV and the time duration of ~2μs. Five shots were accumulated in each IP measurement. Readout of PSL from IPs was done with an image plate reader (BAS-1800). The readout times were also recorded to compensate decay of PSL.

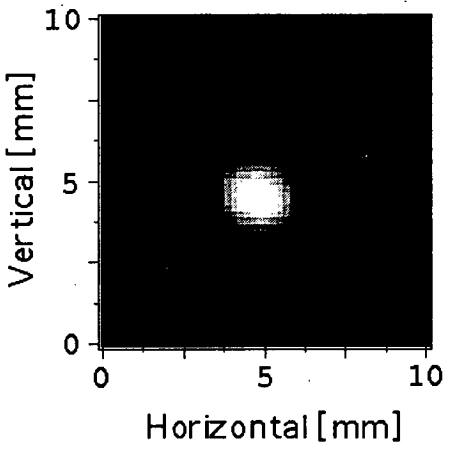

Fig 1. Dark current electron beam profiles. The intensity scale is represented in unit of PSL.

3. Results

Figure 1 shows electron beam profile accumulated over 5 shots of dark current, taken with an IP. Both the horizontal and vertical sizes of an electronic beam are about 2 mm. From the measurement, an conversion factor for a 150 MeV electron is 0.02 PSL/electron. This value is larger than the value obtained in Osaka University[2]. It is thought that this difference is due to the characteristic of a image plate reader etc. The calculation result of EGS4 is shown in Fig. 2. This result indicates that IP sensitivity has a peak around 300 keV, and nearly constant over 2MeV. By using the sensitivity curve of the IP obtained in this experiment, the number of electrons can be roughly estimated from the picture of an IP.

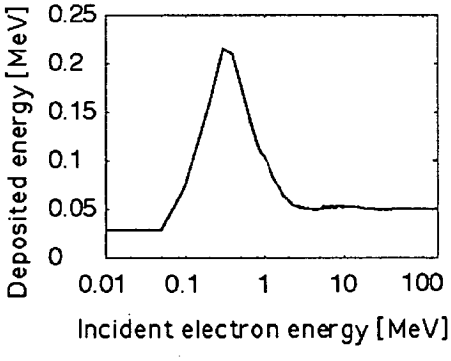

Fig 2. A response function of IP for an electron calculated with EGS4.

References

1) M. Kando et al, Proceeding of 25th Linear Accelerator Meeting in Japan, 9 - 11
2) T. Takahashi et al, Ionizing Radiation, Vol.28, No.2, 203 - 213 (2002) (in Japanese)

4.6 Advanced Photon Simulation Research

The simulation group for advanced photon science

Mitsuru YAMAGIWA, Akira SASAKI, James KOGA, Kengo MORIBAYASHI, Yutaka UESHIMA, Takayuki UTSUMI, Takao KONDOU, Kanji SAITOH, Timur ESIRKEPOV, Sergei BULANOV

Some of recent activities of the simulation group for advanced photon science are reported, in conjunction with intense laser-plasma interaction (Strong radiation reaction, Highly efficient relativistic-ion acceleration by the radiation pressure and Soliton synchrotron afterglow in a laser plasma), computational science (Data and task management for experiment and simulation and Solutions of hyperbolic equations with the CIP-BS method), and atomic process and x-ray generation (Effect of the satellite lines and opacity on the EUV spectrum of Xe and Sn and Theoretical study for the application of hollow atom production to the measurement of short-pulse high-intensity x-ray sources).

The effect of radiation damping on a single electron under the influence of a strong electromagnetic wave is examined by solving numerically the equations of motion describing the damping.

The new regime of the high density ultrashort relativistic ion beam generation from a thin foil by an ultraintense EM wave is presented. This regime is called the "Laser Piston" (LP). In contrast to previously discussed schemes, in this regime the ion beam generation is highly efficient and the ion energy per nucleon is proportional to the laser pulse energy.

Intense coherent synchrotron radiation is shown to be generated by the relativistic charge density wave rotating self-consistently inside an electromagnetic solitary wave, dwelling in a laser plasma. Solitons are formed because of the nonlinear frequency down-shift of the laser pulse; thus, their oscillation period is greater than or of the order of the Langmuir period.

The database system for the management of experimental and simulation results, which may possibly be applicable to the fields of bio and nano technology as well as advanced photon science, is described.

The Constrained Interpolation Profile - Basis Set (CIP-BS) method is generalized by introducing matrix representations and clarifying the relation with differential algebra to accommodate it to nonlinear partial differential equations. The linear and nonlinear partial differential equations are reduced to ordinary differential equations for values and spatial derivatives at the grid points. It is successfully applied to the typical hyperbolic equations.

The atomic data and atomic process codes, which have originally been developed for the study of x-ray lasers, are applied to the investigation of the complex spectrum of Xe and Sn plasmas in the extreme-ultra-violet (EUV) wavelengths. It is found that the effect of satellite lines and opacity are essential for estimating the conversion efficiency of the laser pumped Xe and Sn sources.

Theoretical study for the measurement of short-pulse high-intensity x-ray sources through the x-ray emission processes from multi-inner-shell excited states ($1s^2 2s^2 2p^k 3s^2 3p^2$, k=1~4) and hollow atoms ($1s^2 2s^2 3s^2 3p^2$) of Si is performed. The effect of weak-intensity long-pulse x-rays mixed with high-intensity short-pulse x-rays and the ratio of the x-ray emission from multi-inner-shell excited states with that from hollow atoms are discussed.

4.6.1 Strong Radiation Reaction

James KOGA, Timur ESIRKEPOV, Sergei BULANOV, Alexei ZHIDKOV[a)]
a) Nuclear Engineering Research Laboratory, Graduate School of Engineering, The University of Tokyo

1. Introduction

With the advent of petawatt level high power short pulse lasers it may become possible via strong focusing to extend the irradiance to levels close to 10^{22} W/cm^2 [1]. At such an irradiance electrons can theoretically reach high energies. Under such extreme conditions the effect of radiation damping on the electron motion in the intense wave can become large [2]. In addition by using counter-propagating laser pulses irradiances reaching the Schwinger limit, 10^{29} W/cm^2 could be achieved with current lasers [3]. Taking into account coherent radiation effects the damping could be strong even for relatively low irradiance laser pulses interacting with clusters [4]. Under most conditions here on the Earth radiation damping is usually a small perturbation. By using high irradiance lasers we can examine the dynamics of electrons under strong damping conditions. We examined the effects of radiation damping on a single electron under the influence of a strong electromagnetic wave. The equations of motion describing the damping are solved numerically.

2. Theory

The relativistically covariant form of the equation of motion of a radiating electron was first derived by Dirac, the Lorentz-Dirac equation [5]. This equation is sufficient to describe the damping of a relativistic electron interacting with an electromagnetic field. However, from a mathematical as well as numerical point of view there are difficulties. If the equations are integrated forward in time, there is an exponential blowup in the energy of the electron even if there is no electromagnetic field present. In order to avoid this problem the equations are integrated backwards in time and the acceleration is required to vanish at infinity. However, for numerical simulation purposes this is difficult as we need to know the final conditions in order to do this. If we assume that the damping is a small perturbation, then the damping force can be expressed in terms of electromagnetic fields only, the Landau-Lifshitz equation. The resulting equation can now be integrated forward in time. The Lorentz-Dirac equation is the equation of motion for a point particle. We use this equation to advance the electron forward in time. In order to check the accuracy of the Landau-Lifshitz equation we integrate backwards in time with the the Lorentz-Dirac equation using the final solution of the Landau-Lifshtz equations as an initial condition.

3. Results

Fig. 1 shows the interaction of a laser pulse of irradiance 5×10^{22} W/cm^2 with a wavelength of $\lambda_0 = 1\mu$m and pulse width of 20fs counter propagating with an electron of energy 150 MeV. In the figure γ is plotted versus x/λ_0. These are parameters similar to those in previous one dimensional simulations[2]. The laser pulse is propagating from the left to the right and the electron, which starts at x/λ_0 equals zero, is propagating from the right to the left. The figure shows the trace of the electron's trajectory with damping (solid line) and without damping (dotted line). It can be seen that that the electron is losing energy as it propagates due to radiation damping. We can see that in the case of damping more than 80% of the

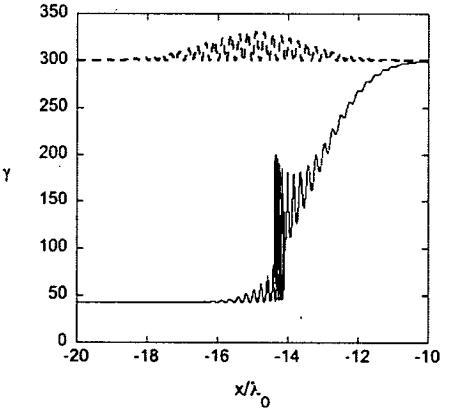

Fig. 1 Trace of the electron motion in the x-γ plane where the electron is propagating to the left and the laser is propagating to the right. The solid line is for damping and the dotted line is no damping.

electron 's energy is lost in the form of radiation. However, when we compare the difference between the Landau-Lifshitz and Lorentz-Dirac backward integrations the differences between the particle motion are insignificant. This can be attributed to the fact that the Doppler shifted wavelength of the laser is large compared to the classical electron radius. The higher order corrections to the radiation reaction force are smaller than the first order terms by a factor of the classical electron radius and, therefore, only for very short wavelengths do differences appear [6]. This is in the quantum regime where both equations of motion are of questionable validity.

References

1) M. Aoyama, K. Yamakawa, Y. Akahane, *et. al.*, Optics Lett. 28, 1594 (2003)
2) A. Zhidkov, J. Koga, A. Sasaki, and M. Uesaka, Phys. Rev. Lett. 88, 185002 (2002)
3) S. V. Bulanov, T. Esirkepov, and T. Tajima, Phys. Rev. Lett. 91, 085001 (2003)
4) S. V. Bulanov, T. Esirkepov, J. Koga, and T. Tajima, Plasma Phys. Rep. 30, 196 (2004)
5) P. A. M. Dirac, Proc. Roy. Soc. London Ser. A 167, 148 (1938).
6) J. Koga, IFSA 2003 Conf. Proc. (2004)

4.6.2 Highly efficient relativistic-ion acceleration by the radiation pressure

Sergei V. BULANOV, Timur ESIRKEPOV, Toshiki TAJIMA

1. Introduction

Today the laser drive of relativistic ions is an attractive goal of the intense laser-matter interaction physics. Direct laser acceleration of protons to relativistic energies requires intensity $I_p \approx 4.6\times10^{24}$ W/cm$^2\times(1\ \mu m/\lambda)^2$, corresponding to the dimensionless amplitude $a=eE/m_e\omega c=m_p/m_e\approx1836$, where E, λ, and ω are the electric field, wavelength, and frequency of the electromagnetic (EM) wave, e and m_e are the electron charge and mass, and m_p is the proton mass. In a plasma, because of collective effects, protons can gain relativistic energies at much less intensity, about 10^{21} W/cm$^2\times(1\ \mu m/\lambda)^2$, as is exemplified in the theory of the strongly nonlinear hybrid electron-ion wakefield induced by a short EM wave packet with the dimensionless amplitude a greater than $(m_p/m_e)^{1/2}\approx43$ and the Coulomb explosion of an overdense plasma region with the size of a few microns when a relativistically strong EM wave sweeps all the electrons away[1]. In general, the laser-driven ion acceleration arises from charge separation caused by the EM wave.

Here we present the new regime of the high density ultrashort relativistic ion beam generation from a thin foil by an ultraintense EM wave. We call this regime the "Laser Piston" (LP). In contrast to previously discussed schemes, in this regime the ion beam generation is highly efficient and the ion energy per nucleon is proportional to the laser pulse energy.

2. Laser Piston mechanism

A relativistically strong laser pulse irradiates a thin foil with thickness l and electron density n_e. The laser pulse waist is sufficiently wide, so the quasi-one-dimensional geometry is in effect. The laser intensity is so high that the radiation pressure is the dominating effect of the plasma dynamics. Thus the foil accelerates as a whole in the direction of the laser pulse. It can be regarded as a relativistic plasma mirror co-propagating with the laser pulse. Assume that the laser pulse is perfectly reflected from this mirror. According to the Einstein formula, the reflected pulse energy is $(c+v)/(c-v)\approx4\gamma^2$ times less than the incident pulse energy $\mathcal{E}_L$. Here v is the mirror velocity, $\gamma=(1-v^2/c^2)^{-1/2}$ is the corresponding Lorentz factor. The rest of the pulse energy, i. e. $(1-1/4\gamma^2)\mathcal{E}_L$, is transferred to the plasma mirror. At this stage the plasma (the electrons and, hence, ions) is accelerated due to the radiation pressure. The radiation momentum is transferred to ions through the charge separation field, and the "longitudinal" kinetic energy of ions is much greater than that of electrons. We notice a connection with a mechanism of the ion acceleration proposed by Veksler[2]. We note that the specified intensity is close to the limit where individual electrons undergo a substantial radiation friction effect. However, when the foil is accelerated up to relativistic energy, this effect becomes weaker because its strength measure, $4\pi r_e/3a^3\lambda$, is reduced by 2γ in the foil reference frame ($r_e=e^2/m_ec^2$ is the classical electron radius).

3. Three-dimensional Particle-in-Cell simulation

In order to examine the present scheme in three-dimensional geometry, whose effects may play a crucial role in the dynamics and stability of the plasma layer under the action of a relativistically strong laser pulse, we carried out 3D PIC simulations with the code REMP. In the simulations the laser pulse is linearly polarized along the z axis; it propagates along the x axis. Its dimensionless amplitude is $a=316$ corresponding to the peak intensity $I=1.37\times10^{23}$ W/cm$^2\times(1\ \mu m/\lambda)^2$. The laser pulse is almost Gaussian with FWHM size $8\lambda\times25\lambda\times25\lambda$, its energy is $\mathcal{E}_L=10$ kJ$\times(\lambda/1\ \mu m)$. The target is a 1λ thick plasma slab with density $n_e=5.5\times10^{22}$ cm$^{-3}\times(1\ \mu m/\lambda)^2$, which corresponds to the Langmuir frequency $\omega_{pe}=7\omega$. For $\lambda\approx1\ \mu m$ the laser pulse electric field is strong enough to strip even high-Z atoms in much shorter time than the laser wave period; thus, we assume that the plasma is fully ionized. The ions and electrons have the same absolute charge, and their mass ratio is $m_i/m_e=1836$. The simulation box size is $100\lambda\times72\lambda\times72\lambda$ corresponding to the grid size 2500×1800×1800, so the mesh size is 0.04λ. The total number of quasi-particles is 4.37×10^9. The boundary conditions are periodic along the y and z axes and absorbing along the x axis for both the EM radiation and the quasi-particles. Simulation results are shown in Figs. 1–2, where the space and time units are the laser wavelength λ and period $2\pi/\omega$. Figure 1 shows the ion density and x component of the EM energy flux density (the Poynting vector). We see that the region of the foil corresponding to the size of the laser focal spot is pushed forward. Although the plasma in the foil is overcritical, it is initially transparent for the laser pulse due to the effect of relativistic transparency. Therefore a portion of the laser pulse passes through the foil. Eventually it accelerates electrons and, as a

result of the charge separation, a longitudinal electric field is induced. The dimensionless amplitude of the longitudinal field is $a_{\|}$=150 corresponding to $E_{\|}$=4.8×10^{14} V/m×(1 μm/λ). The typical distance of the charge separation is comparable with the initial thickness of the foil and is much less than the transverse size of the region being pushed. The ion layer is accelerated by this longitudinal field. As the foil moves more and more rapidly, in its proper frame the incident wavelength increases; thus, the accelerating foil becomes less transparent with time.

As seen in the cross section of the Poynting vector in Fig. 1, the thickness of the stripes, corresponding to half of the radiation wave length, increases from left to right (along the x axis). The increase is weaker at the periphery (in the transverse direction); correspondingly, we see distinctive phase curves. This "anisotropic redshift" results from the relativistic Doppler effect when the laser pulse is reflected from the co-propagating accelerating and deforming relativistic mirror. The redshift testifies that the laser pulse is expending its energy for the acceleration of the plasma mirror, as specified above in the LP mechanism. The foil is transformed into a "cocoon" where the laser pulse is almost confined. The accelerated ions form a nearly flat thin plate with high density. Figure 2 shows the ion maximum energy versus time and the ion phase space plot. The dependence is initially linear; at later times it scales as $t^{1/3}$. The number of ions in the plate is N_i=2×10^{12}, their energies are from 1.4 to 3.2 GeV. The efficiency of the energy transformation from laser to ions is greater than 40%. The ion bunch density is 3×10^{21} cm^{-3}, its duration is 20 fs, its transverse emittance is less than 0.1π mm mrad.

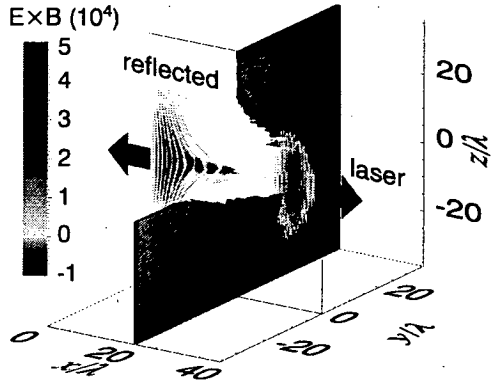

Fig. 1 The ion density isosurface for n_i=8n_{cr} (a quarter removed to reveal the interior) and the x component of the Poynting vector at t=40.

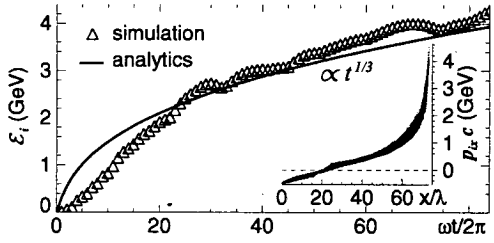

Fig. 2 The maximum ion kinetic energy versus time and the ion phase space projection (x,p_x) at t=80.

4. Conclusion

The Laser Piston regime of ultra-intense laser plasma interaction can be employed in a laser-driven heavy ion collider. In the collision of two ion bunches the number of reactions with cross section σ is $N=\sigma N_i^2/s$, where s is the bunch sectional area. Adopting the presented simulation parameters, we obtain $N=2\times10^{30}\sigma/\mathrm{cm}^2$. Provided that the energy is high enough so that $\sigma=10^{-24}$ cm^2, we can get about a million events in a few femtosecond shot. As suggested by Tajima and Mourou[3], one can get a short multi-exawatt laser pulse with sufficient contrast ratio (10^{-12}) using the megajoule NIF facility and present-day technology. Then the resulting ion bunch energy can be over 100 GeV per nucleon, which is suitable for the quark-gluon plasma studies[4]. The laser piston regime, being one of the examples of what we call the relativistic engineering, can give us a promising and unique tool for nuclear physics research.

More details can be found in Ref. 5).

References

1) T. Zh. Esirkepov et al., JETP Lett. **70**, 82, 1999; S.V. Bulanov et al., Plasma Phys. Rep. **25**, 701, 1999; S.V. Bulanov et al., JETP Lett. **71**, 407, 2000; K. Nishihara et al., Nucl. Instrum. Methods Phys. Res., Sect. A **464**, 98, 2001.

2) V. I. Veksler, in Proceedings of CERN Symposium on High Energy Accelerators and Pion Physics, Geneva, 1956 (European Organization for Nuclear Research, Geneva, 1956), Vol. **1**, p. 80; At. Energy **2**, 427, 1957.

3) T. Tajima and G. Mourou, Phys. Rev. ST Accel. Beams **5**, 031301, 2002.

4) T. Ludlam and L. McLerran, Phys. Today **56**, No. 10, 48, 2003.

5) T. Esirkepov, M. Borghesi, S.V. Bulanov, G. Mourou, T. Tajima, Phys. Rev. Lett. **92**, 175003, 2004.

4.6.3 Soliton synchrotron afterglow in a laser plasma

Timur ESIRKEPOV, Sergei V. BULANOV, Toshiki TAJIMA

1. Introduction

One of the most fundamental results of classical electrodynamics is that a relativistic charged particle, rotating in a circle, emits an electromagnetic (EM) wave. In the particle rotation plane this EM wave has a spiral shape, and it is commonly called synchrotron radiation[1]. At a remote distance it is seen as a sequence of bursts passing through the point of observation. The interval between the bursts is the particle rotation period. The width of each burst is less than the interval between the bursts by a factor of the order of the cube of the particle Lorentz factor. A rotating compact bunch of charged particles, when the bunch size is less than the burst width, emits almost coherent EM radiation, whose power is proportional to the square of the number of particles in the bunch. The synchrotron radiation plays a very important role in cyclic accelerators of high-energy electrons and storage rings. It affects the charged particle dynamics, e.g., the radiation energy loss and the betatron oscillation decay.

Here we show that intense coherent synchrotron radiation can be generated by the relativistic charge density wave rotating self-consistently inside an electromagnetic solitary wave, dwelling in a laser plasma.

The relativistically strong laser pulse can generate relativistic EM subcycle solitary waves in a plasma, as was indicated by particle-in-cell (PIC) simulations in one-, two-, and three-dimensional (1D, 2D, and 3D) geometries[2]. Solitons are formed because of the nonlinear frequency down-shift of the laser pulse; thus, their oscillation period is greater than or of the order of the Langmuir period.

2. Three-dimensional Particle-in-Cell simulation

We performed 3D PIC simulations of a short relativistically strong laser pulse interaction with underdense plasma. We use the REMP code. In a series of simulations with different initial parameters, groups of solitons with different frequencies were observed, and their emission (spiral wave) frequency corresponded to their frequency. Here we present the simulation with the following parameters. The laser pulse propagates along the x axis; it is circularly polarized, and its peak intensity is $I=7.7\times10^{18}$ W/cm$^2\times(1\ \mu\text{m}/\lambda)^2$, corresponding to the dimensionless amplitude $a=eE/m_e\omega c=2$, where λ and ω are the laser wavelength and frequency, respectively. Here and below to obtain dimensional values one must substitute a specific laser wavelength, e.g., $\lambda=1\ \mu$m. The laser pulse is Gaussian, its duration is approximately 10 fs, and its FWHM size is $3\lambda\times5\lambda\times5\lambda$, which gives the pulse energy 7 mJ$\times(\lambda/1\ \mu\text{m})$. Its focal plane is placed in front of the plasma slab at the distance of 5λ. The length of the plasma slab is 60λ. The plasma density is $n_e=0.11n_{cr}=5.5\times10^{22}$ cm$^{-3}\times(1\ \mu\text{m}/\lambda)^2$, and the corresponding Langmuir frequency is $\omega_{pe}=\omega/3$. We make ions an immobile neutralizing background. This approximation eliminates an ion response; thus, it allows us to distinguish the soliton lifetime limitation due to high frequency radiation, in contrast to a limitation due to postsoliton formation[3]. In the simulations the boundary conditions are periodic along the y and z axes and absorbing along the x axis for both the EM radiation and the quasiparticles. The simulations were performed on 720 processors of the HP Alpha Server SC ES40 at JAERI-Kansai. We used $2112\times630\times648$ grids with mesh size $\lambda/32$ and 5.23×10^9 quasiparticles. The simulation result is shown in Fig. 1, where the time unit is the period of the incident EM radiation $2\pi/\omega$. The laser pulse is introduced into the simulation box at $t=0$.

After a long time after the laser pulse propagation, we see several positively charged (on the time average) regions in the pulse wake. These regions correspond to almost spherical cavities in the electron density surrounded by walls of overdense plasma. The typical size of the cavities is approximately 2λ. Besides the electrostatic component, in these cavities we see the oscillating transverse component of the trapped electromagnetic field. The period of the transverse component oscillations is $T_S\approx3.4\times2\pi/\omega$, which is 13% greater than the period of the Langmuir wave in an unperturbed plasma, in agreement with the soliton generation scenario. The typical lifetime of the oscillations is of the order of 20–30 plasma periods. These coherent entities can be regarded as 3D circularly polarized relativistic EM subcycle solitons.

The cross section of the z component of the magnetic field in the plane (x, y, $z=0$) reveals well pronounced outgoing spiral EM wave, Fig. 1. At $t=T_S/4$ just after emission the magnitude of this wave is of the order of 3.7 MG$\times(1\ \mu\text{m}/\lambda)$ or $eB_z/m_e\omega c=0.035$ in dimensionless units. The spiral wave is also seen in the cross sections of electric field components. The distance between adjacent spiral arcs corresponds to the soliton oscillation period T_S. The emission of the spiral wave correlates to the rotation of the electron density hump in the cavity wall (in Fig. 1 it is counterclockwise). The density hump consists of

approximately $N_h=2\times10^6\times(\lambda/1\ \mu m)$ electrons. The hump gyrates in a circle with radius $\approx0.46\lambda$, and the period of revolution is exactly equal to T_S. The spiral wave burst width is much smaller than the distance between the spiral arcs and approximately equal to $T_b\approx T_S\gamma_h^{-3}$, where $\gamma_h\approx1.89$ is the Lorentz factor of the electron density hump in the cavity wall. The polarization of the spiral wave corresponds to well known synchrotron radiation[1]. We found that the magnitude of the spiral wave in the simulation is N_h^2 times greater than that of the single rotating electron emission defined analytically by the Liénard-Wiechert potentials, so the density hump emission is coherent.

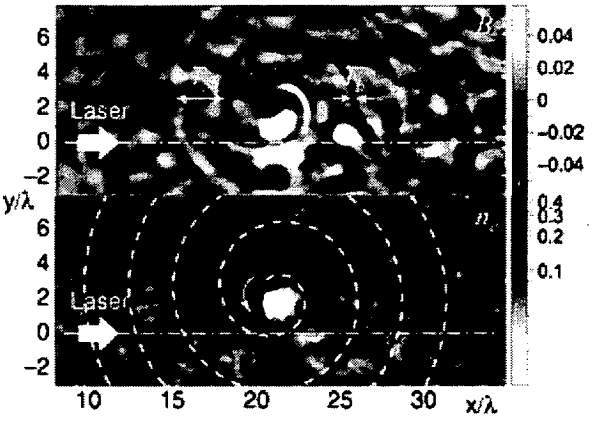

Fig. 1 Cross-sections of the magnetic field component $eB_z/m_e\omega c$ (upper frame, linear color scale) and electron density n_e/n_{cr} (bottom frame, logarithmic color scale) in the plane $(x,y,z=0)$ at t=82. The dashed line in the bottom frame repeats the spiral pattern of the outgoing wave. The dash-dotted line shows the initial laser pulse axis.

This soliton synchrotron radiation cannot be attributed to the motion of relativistic electrons due to the quasistatic magnetic field generated by the laser pulse. The time-averaged magnetic field in the laser pulse wake is localized mainly in the electron density cavities, its magnitude is $e|\boldsymbol{B}_{max}|/m_e\omega c=0.07$. This field is too weak to induce the rotation of the electron density hump, because the corresponding cyclotron frequency $e|\boldsymbol{B}_{max}|/\gamma_e m_e c=0.07\omega/\gamma_e$ is much less than the frequency of revolution $\Omega_S=2\pi/T_S=0.29\omega$. It is important that the maximum Lorentz factor of individual electrons $\gamma_{e,max}=1.12$ is significantly less than the Lorentz factor of the electron density hump.

From the analysis of simulation results we conclude that the outgoing spiral EM wave is induced by the electron density hump self-consistently rotating in the soliton cavity. Such a motion can be regarded as the surface charge density wave in the soliton cavity wall.

4. Conclusion

We show that a relativistically strong circularly polarized laser pulse can generate circularly polarized relativistic EM solitary waves. They look like a rotating principal mode of EM fields in a cavity. The oscillating EM field is associated with a surface density wave in the cavity wall in the form of a relativistic rotating electric charge density hump, which is significantly faster than individual electrons composing it. This hump emits a spiral high-frequency EM wave that can be identified as the coherent synchrotron radiation. This radiation contains harmonics of the order of $\gamma_h^3\Omega_S$, and its intensity is proportional to the square of the number of charges in the hump. This provides a new mechanism of the high harmonic generation, as distinct from the well known mechanisms such as the nonlinear Thomson scattering, the "relativistic oscillating mirror", and the stimulated scattering of relativistically strong electromagnetic radiation. The discovered effect demonstrates basic properties of nonlinear plasma electrodynamics. It can be responsible for long-persisting high-frequency afterglow in the wake of relativistically strong EM pulse in plasmas, since the solitons can stay in a plasma for tens of Langmuir periods. Thus, it is important to consider this effect in plasma diagnostics in terawatt laser experiments and in the interpretation of astrophysical observations. More details can be found in Ref. 4).

References

1) A. A. Sokolov and I.M. Ternov, Synchrotron Radiation (Pergamon Press, New York, 1968); V. L. Ginzburg, Applications of Electrodynamics in Theoretical Physics and Astrophysics (Gordon and Breach, New York, 1989); V. S. Berezinskii et al., Astrophysics of Cosmic Rays (Elsevier, Amsterdam, 1990).

2) S.V. Bulanov et al., Phys. Fluids B **4**, 1935, 1992; S.V. Bulanov et al., Plasma Phys. Rep. **21**, 550, 1995; S.V. Bulanov et al., Phys. Rev. Lett. **82**, 3440, 1999; Y. Sentoku et al., Phys. Rev. Lett. **83**, 3434, 1999; S.V. Bulanov et al., Physica (Amsterdam) **152–153**D, 682, 2001; T. Esirkepov et al., Phys. Rev. Lett. **89**, 275002, 2002.

3) N.M. Naumova et al., Phys. Rev. Lett. **87**, 185004, 2001; M. Borghesi et al., Phys. Rev. Lett. **88**, 135002, 2002.

4) T. Esirkepov, S. V. Bulanov, K. Nishihara, T. Tajima, Phys. Rev. Lett. **92**, 255001, 2004.

4.6.4 Data and task management for experiment and simulation

Yutaka UESHIMA, Kanji SAITOH, Daisuke WAKABAYASHI[a)], Yukimasa MATSUDA[b)],
Yasuhiro TAKEDA[c)], Tomoaki TATSU[d)], Ryusuke KIMURA[d)] and Hirofumi SHIMOHARA[d)]

a) Research Organization for Information Science and Technology
b) Mitsubishi Space Software Co. Ltd.
c) Fujitsu Tokushima System Engineering Co. Ltd.
d) Oyogijutu System Engineering Co. Ltd.

1. Introduction

Recently a lot of data are being produced because it has become easy to digitize and create large data after the IT revolution. Since the accuracy of generated data and analysis methods are advancing, experiments and simulations in the field of bio, nano, and photon technology with quick progress in speed are opening up new windows of research opportunities. Nuclear engineering, space science and accelerator physics which are forefront research areas were of large science research style. In these, the control system of the whole equipment or format of data analysis is planed in the research, and the database system based on the research plans is developed in the process of design of the research equipment.

It is difficult to store data in a database with experimental and simulation results, because the cycle of change is short in the fields of bio, nano, and photon technology. We have developed a database system by which research data can be stored and used easily in the fields.

2. Data and Task Management for Experiment and Simulation

In quickly progressing research the most important things required of a database system are the following three points.

1) Storing of a lot of unstructured and unsteady data
2) Easily reproducing results and changing of procedures
3) Ease of preservation and reference of data

The developed components to achieve these demands are explained. The problem of "storing of a lot of unstructured and unsteady data" was solved by developing the database with high flexibility using XML (Extended Markup Language) and RDB (Relational Data Base) technology. In this database system, a request is described by the XML format in the application portion, and is changed into SQL in the database portion. Moreover, the file storing, the backup of data, and the file attribute management functions were assigned to independent servers, respectively for large data storage.

Although the problem of "the reproducibility as a result of analysis and visualization portion" is the most difficult, we have solved it with collaborative operation of the database. Our system guarantees reproducibility not only by the case of automatic visualization and analysis at the time of data registration but also in the case of interactive visualization. Moreover, the batch processing mechanism which enables the same analysis of a lot of data was also developed. The problem of "the change ease of procedure" was solved by developing a workflow control tool by the JAVA language. Moreover, those tools can describe various workflows under distributed environment easily, and the workflow operation can be supervised.

The problem of "the preservation of data" is solved by transmitting a data file to the file server automatically at the time of data registration. Furthermore, the system which can cooperate with backup tape equipment was developed so that data restoration could be performed at the time of trouble, and guarantee of data preservation is strengthened. The trouble in the database itself is also protected by the backup restoration function by the same structure.

The platform dependability which poses a problem of "ease of access" was decreased by using the TOMCAT, JAVA, SOAP, etc. which are the standard technology of the Web service. Moreover, the communication mechanism by SSH and SCP was prepared so that the supercomputer and file server which are not provided with Web service could also be included in our system. Moreover, even when the data of a file server disappeared due to a trouble etc., data was automatically restored from the backup tape at the time of reference. It can be called the pseudo HSM function.

3. Design Free Database

The highly efficient and stable database software increase recently and a database system can be individually built now cheaply. However, most databases are not suitable for the handling of atypical and unsteady data by the RDB. In construction of a standard of RDB, the modelling of data and their relation are analyzed first. Next, the table structure of a data base is decided by data structure. Therefore, changing the design of a data base will occur, when a data structure changes. That is, a RDB treating irregular and uneasy data is the weakest. There is an object-oriented database and an object-oriented XML database which are databases good at processing of irregular and uneasy data. However, the introduction cost of the high performance and quality object-oriented database system is not small.

We developed a database which can deal with irregular and uneasy data. It applies the XML technology to the PostgreSQL which is the high performance RDB in the open source database software. The data for the management of users, security, project types, and projects have the same structure independent of the type of research. Therefore, a structure of the management data was fixed and the data was treated in the domain of relational database, i.e., table structure portion. The reliability of the database was kept by this structure. The detailed data structure not only changes with the methods and types of the experiment and simulation, but may change as research progresses. Therefore, the table structure can not correspond to the data structure. Therefore, the XML technology was used in one simple table, and the data structure was embedded to the inside of the table. The concrete field of the table is made very general-purpose as follows.

Table1. Fields of the XML table embedded data structure

Field name	Self ID	XMLtag ID	Project series ID	Parent ID	Value	Unit code
Numeric	Numeric	Numeric	Numeric	Numeric	Varchar	Numeric
Relation	PK	FK1	FK2			FK3

PK(primary key):identical number of this table
FK(foreign key):identical number of another table related with this table

Since the portion which should be built on a relational 2-dimensional table is used as a 1-dimensional single table so that this database has the flexibility for storing atypical and unsteady data, the reference speed becomes slow and is an important problem. In order to solve this problem, we developed a function for some improvement in the speed. At first, the CUT-OFF function which removes unnecessary trees at an early stage at the time of reference was developed. Next, when the number of reference hits was narrowed down hierarchically, the DROP-OFF function to search only a respectively required tree of data was also developed. Moreover, an index table was created in order to discover the branch of the data tree at high speed in the table which stores data. The speed of reference is shown in the following table.

Table2. Speed of reference in our developed database

Record No.	123940	247880	495760	991520
Image No.	2470	4960	9920	19840
Time[sec]	19	35	59	100

Additionally, in the PostgresSQL, since it has a function which analyzes the data structure and optimizing data access, it is good to execute the "vacuumdb" command for employing these functions for database efficiently at the time of new creation, restoration, and large renewal of data. For example, in our developed database, reference speed accelerated 30 to 50 times by enforcement of the "vacuumdb" command.

4. Future Works

If the number of data increases, reference speed of our database will become slow linearly. However, since the number of the storing tables of real data is one, it is easy to perform parallelization of reference. Next year, we are scheduled to advance level data distribution by server extension using the distributed database (PostgresForest) developed in IPA in 2003.

4.6.5 Solutions of hyperbolic equations with the CIP-BS method

Takayuki UTSUMI, James KOGA, Mitsuru YAMAGIWA, Takashi YABE[a)], Takayuki AOKI[a)]
a) Tokyo Institute of Technology

1. Introduction

During the past three decades. there has been significant progress in numerical analysis for hyperbolic equations, especially for hydrodynamic equations. However, nowadays, it is widely recognized that more robust and efficient methods must be developed to trace sharp discontinuities of physical quantities such as shock waves or interfaces between different materials.

As far as incorporating only the values at grid points, it seems difficult to improve grid methods which exemplify the spectral method's accuracy. Recently, a new numerical method, the CIP-Basis Set (CIP-BS) method[1)], has been proposed by generalizing the concept of the Constrained Interpolation Profile (CIP) method[2)] from the viewpoint of the basis set. The idea of the CIP method is that not only values but also their first derivatives are treated as independent variables associated with the grid point. Although the CIP method is formulated without a matrix form equation, methods using matrix operations are more advantageous because a number of numerical methods for large, sparse systems can be adopted. With this view, the CIP-BS method has introduced the polynomial basis set, by which physical quantities are approximated with their values and derivatives associated with grid points. The governing equations are discretized into matrix form equations requiring the residuals to be orthogonal to the basis functions via the same procedure as the Galerkin method. The CIP-BS method, in which the local polynomial basis functions corresponding to the values and spatial derivatives at each grid point belong to the complete set and the C^K class, is called the CIP-BS^K method.

Here we present the CIP-BS method can be extended for nonlinear operations on functions in the framework of differential algebra, can be a universal solver for hyperbolic equations.

2. Numerical solutions

We consider shock tube problems by the hydrodynamic equations. Since the CIP-BS method has low diffusion some artificial viscosity must be included. However, those introduced by Von Neumann is not convenient for our purpose due to their non-differentialble property. Therefore, we have introduced small real viscosity in the hydrodynamic equation. The value of viscosity is determined so that the thickness of the shock becomes some multiple of the grid interval. Figure 1shows the results for a shock problem with the initial conditions: $\rho=1$, $u=0$, $p=1$for $0 < x < 1$, and $\rho=0.125$, $u=0$, $p=0.1$ for $1 < x < 2$. Figure 2 shows the results for a shock collision problem with the initial conditions: $\rho=1$, $u=0$, $p=2/3$ for $x < 40$, $\rho=0.5$, $u=0$, $p= 5\ 10^{-5}$ for $40<x<280$ and $\rho=1.5$, $u=0$, $p=1$ for $280 < x < 400$. Our numerical simulations show that the CIP-BS method gives fairly good agreement with the analytical results, in particular, the correct shock speed and well resolved shock front.

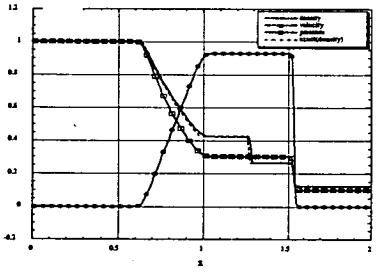

Fig. 1 Shock wave

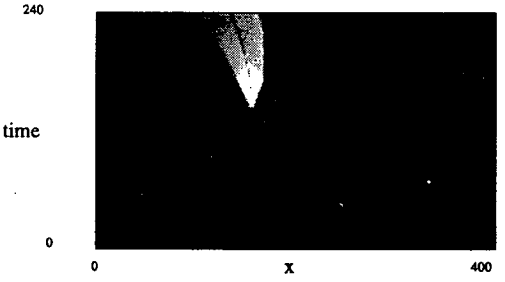

Fig. 2 Collision of shock waves

3. Conclusions

We have generalized the CIP-BS method by introducing matrix representations and clarifying the relation with differential algebra to accommodate it to nonlinear partial differential equations. The linear and nonlinear partial differential equations are uniquely reduced to ordinary differential equations for values and spatial derivatives at the grid points. It is successfully applied to typical hyperbolic equations.

References

[1] T. Utsumi, J. Koga, T. Yabe , T. Aoki, M. Sekine, Comput. Phys. Comm.**157**, 121 2004
[2] T. Yabe and T. Aoki, Computer Phys. Comm. **66**, 219, 1991

4.6.6 Effect of the satellite lines and opacity on the EUV spectrum of Xe and Sn

Akira Sasaki

1. Introduction

The atomic data and atomic process codes, which have originally been developed for the study of x-ray lasers, are applied to the investigation of the complex spectrum of Xe and Sn plasmas in the extreme-ultra-violet (EUV) wavelengths. It is found that the effect of satellite lines and opacity is essential for estimating the conversion efficiency of the laser pumped Xe and Sn sources.

2. Emission mechanism

Figure 1 shows the experimental[1] and theoretical emission spectrum of Xe. The observed spectrum shows a predominant peak near 11nm, which originates from 4d-4f resonance lines of Xe^{8-11+}. Weak peaks at 13.5, 14.5 and 16nm are attributed to 4d-5p transitions of Xe^{10+}, Xe^{9+} and Xe^{8+}, respectively. However, emission in the 13.5nm band is rather dominated by an unidentified broad structure, which could not be explained by any existing model[2].

It is found from detailed investigation of the emission lines using the HULLAC[3] code that millions of fine structure transitions overlaps each other to produce the broad spectrum. In the high density laser produced plasmas ($n_e>10^{20}/cm^3$), the population in the plasma approaches to LTE, leading the doubly- and inner shell- excited configuration to have considerable population, which contribute to the emission of satellite lines. In particular, as the opacity of the plasma increases, the intensity of resonance lines saturates, and the intensity of the satellite lines may become comparable to the resonance lines. Figure 1(b) and 1(c) show calculated radiation intensity and opacity of the Xe plasma, with T_e=25eV, and $n_e=10^{21}/cm^3$. Uniform plasma sphere with a radius r=10μm and LTE population is assumed. It is found that calculated spectrum shows reasonable agreement with experiment in Fig. 1(a). It is also found that the satellite lines of the 4d-5p transition of Xe^{9+} and Xe^{10+}, and 4p-4d transition of Xe^{8-10+} contribute the emission in the 13.5nm band.

3. Conclusions

The present model also reproduce Sn spectra. This implies that similar mechanism of emission based on the effect of satellite lines and opacity apply both Xe and Sn. In the case of Sn , the strongest peak appears near 13nm, therefore the spectral efficiency from total emission to the in-band emission (13.5nm 2%BW) is 3% , whereas it is 1% with Xe. The emissivity and opacity of the plasma calculated using the present model will be applied to the coupled radiation hydrodynamics simulation for the optimization of the efficiency of the EUV source.

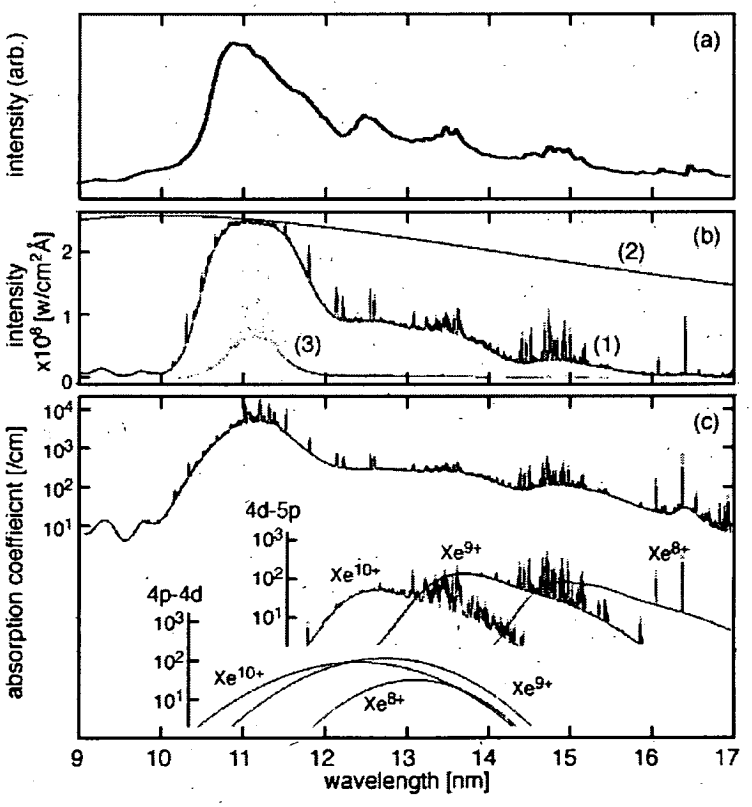

Fig .1 (a) Typical EUV spectrum from a laser produced plasma. Calculated emission intensity (b) , where (1) the Planckian intensity (2), and relative emissivity (3) are shown, and absorption coefficient (c).

References

[1] H.Komori, et al., J. Vac. Sci. Technol. **B21**, 2843 (2003).
[2] N.Böwering, et al, J. Appl. Phys. **95**, 16 (2004).
[3] M.Klapisch et al., J. Quant. Spectrosc. Radiat. Transf. **58**, 687 (1997).

4.6.7 Theoretical study for the application of hollow atom production to the measurement of short-pulse high-intensity x-ray sources

Kengo MORIBAYASHI, Takashi KAGAWA[a)] and Dong Eon KIM[b)]

a) Department of Physics, Nara Women's University

b)POSTECH, Korea

1. Introduction

Recent rapid progress in high intensity laser pulse technology has made possible new high-intensity short-pulse (~ fs) x-ray sources such as from Larmor radiation[1)] or radiation damping[2)] due to the high intensity laser field. These x-ray sources are useful for (i) inner-shell ionization x-ray lasers[3-5)], (ii) the measurement of ultrafast processes[6-8)] and (iii) the production of photo-ionized plasma[9,10)]. However, it is difficult to characterize the fs pulse x-ray sources because they are mixed with weak-intensity long-pulse x-ray emission processes such as bremsstrahlung.

Moribayashi *et al.*[3)] have found a new characteristic for the production of inner-shell excited states (IES) and hollow atoms (HA) by high-intensity short-pulse x-rays. They have devised a new x-ray laser scheme using hollow atoms, which originate from inner-shell ionization x-ray lasers pumped by very high intensity x-rays. In this case, inner-shell ionization processes surpass any other atomic processes such as auto-ionization and radiation transition processes. As a result, multi-inner-shell ionizations predominate, leading to the formation of HAs. On the contrary, for an ordinary x-ray source, since auto-ionization, or radiation transition processes are much faster than photo-ionized processes, further inner-shell ionizations from IES seldom occur. From this characteristic, we predict that x-ray emissions from HA inform us of the x-ray intensities of high intensity x-ray sources. In this paper, we discuss their application to the measurement of short-pulse x-ray sources.

2. Atomic processes

We study x-ray spectra emitted from IES($1s^2 2s^2 2p^5 3s^2 3p^2$), multi inner-shell excited states (MIES) ($1s^2 2s^2 2p^k 3s^2 3p^2$, k=1~4), and HA ($1s^2 2s^2 3s^2 3p^2$) of Si produced by high-intensity short-pulse x-rays theoretically. The initial state is the ground state of the Si atom. We consider photo-ionization (*PI*), radiative transition (*Ar*), and auto-ionization (*Aa*) processes. With these atomic rates, the population dynamics of the various atomic states may be investigated by the following rate equations:

$$\frac{dN_k}{dt} = -\alpha_k N_k + \sum_{m(>k)} \beta_{mk} N_m, \qquad (1)$$

where N_k, α_k and β_{mk} are the population, decay constant in the k state, and the transition rate from the m state to k state, respectively. The photon number is given by

$$P_k = \int_0^\infty N_k A r dt, \qquad (2)$$

where Ar is the radiative transition probability from the IES, MIES, and HA.

3. Results and discussions

We study the effect of weak-intensity long-pulse x-rays mixed with high-intensity short-pulse x-rays on the production of IES, MIES and HA. We consider x-rays for a pulse of 20 fs and an intensity of 10^{16} W/cm^2 and for pulses of 1 ps and 10 ps and an intensity of

$$I_L = n \times I_s, \qquad (3)$$

where I_S and I_L are the intensities of high-intensity short-pulse and weak-intensity long-pulse x-rays, respectively. Figure 1 shows the effect of the weak-intensity long-pulse x-rays on the production of the IES, MIES, and HA as a function of n (n=0.001-0.1). In order to show this effect, we introduce the parameter R defined by

$$R = \frac{(Y - Y_S)}{Y_S} \times 100, \qquad (4)$$

where Y and Y_S correspond to the photon numbers with and without weak-intensity long-pulse x-rays, that

is, R increases in accordance with the effect of the weak-intensity long-pulse x-rays. Figure 1 corresponds to t_2= 1 ps, where t_2 is the pulse length of the weak-intensity long-pulse x-rays. For small n, $n \leq 0.01$, the values of R for IES are larger than those for MIES and HA. Furthermore, the effect of weak-intensity long-pulse x-rays on the production of MIES and HA may be ignored because R has small values (< 1 %) and is almost the same for t_2=1~10 ps (not shown here). Therefore, it is found that the x-rays from MIES and HA are better for the measurement of ultrafast processes than those from IES.

Figure 2 shows the ratio of the x-ray number from the $1s^2 2s^2 2p 3s^2 3p^2$ with those from $1s^2 2s^2 3s^2 3p^2$ as a function of pulse duration for various x-ray intensities of x-ray sources. The ratio remains almost constant for pulses (>20 fs) and depends strongly on the x-ray intensities. Namely, we may deduce the measurement of the x-ray intensities of high-intensity short-pulse x-ray sources by using the ratio.

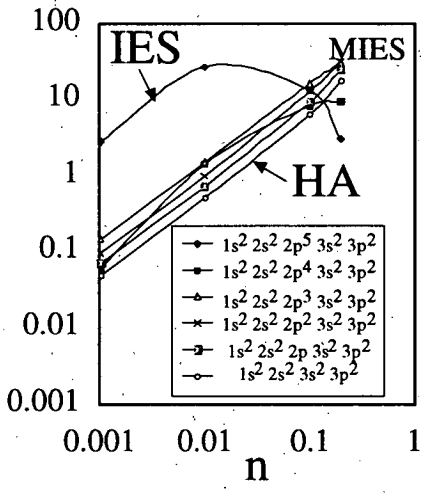

Fig.1 R vs. n for IES, MIES, and HA, where n and R are defined in Eqs.(3) and (4), respectively.

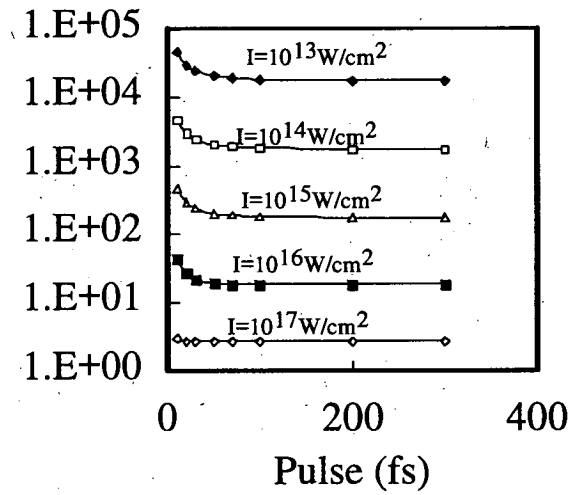

Fig.2 The ratio of the x-ray number from the $1s^2 2s^2 2p 3s^2 3p^2$ state with those from $1s^2 2s^2 3s^2 3p^2$ vs. pulse for various x-ray intensities (I).

4. Conclusions

We have found that the x-rays, which are emitted from MIES and HA of Si ions excited by high intensity x-ray sources, are greatly affected by high-intensity short-pulse x-rays and little by weak-intensity long-pulse x-rays. The ratio of the x-ray intensity from HA to that from the MIES becomes almost independent of the pulses and dependent on the intensities of the x-ray sources. These ratios may be used for the measurement of intensities of high-intensity short-pulse x-ray sources.

Acknowledgements

We wish to thank to Prof. T. Tajima and Drs. J. Koga, and M. Yamagiwa for their useful discussions.

References

1) Y. Ueshima *et al.*, Laser and Particle Beam **17**, 45, 1999
2) A. Zhidkov *et al.*, Phys. Rev. Lett. **88**, 185002, 2002
3)K. Moribayashi, A .Sasaki, and T. Tajima, Phys.Rev.A **58**, 2007, 1998
4)K. Moribayashi, A. Sasaki, and T. Tajima, Phys.Rev.A **59**, 2732, 1999
5) D. Kim *et al.*, Phys. Rev. A **63** 023806, 2001
6) T. Guo *et al.* Proc. SPIE **3157**, 84, 1997
7) H. Kandori *et al.*, *J.Am.Chem.Soc.* **118**, 320, 1996
8) S. Akimoto *et al.*, Chem. Phys. Lett, **260**, 147, 1996
9)R F. Paerels, *et al.*, Astrophysical J. **553**, L135, 2000
10)D.A, Liedahl and R.F. Paerels, Astrophysical J. **468**, L33, 1996

4.7 High power laser applications

Hiroyuki Daido

We are investigating the ultra-high intensity laser-matter interaction physics especially for the relativistic plasma phenomena such as a few tens of MeV x-ray and particle generation and their applications. During this fiscal year, we have performed the experiments on energetic particle generation by a Ti Sapphire laser at the intensity of ~10^{18}W/cm^2. Observed plasmas have been characterized with x-ray spectroscopic techniques as well as optical probing techniques. We have also performed rather low intensity femto second laser applications such as an ultra-fast spectroscopic study, fabrication of nano-crystals by a femto-second laser pulse. Theoretical study on quantum control of materials by a coherence controlled high quality laser, have also been performed.

Figure 1 shows the direction of ultra high peak power laser development which is going into higher and higher intensity with shorter and shorter pulse duration. This flow is quite natural like a water flow from the higher place towards the lower place. Applications of such sources are quite important to accelerate the laser developments themselves. Therefore from place to place, we have to construct dams to reduce the speed of the water flow to absorb other technologies and it should be mixed with each other for making a really attractive technology for human life.

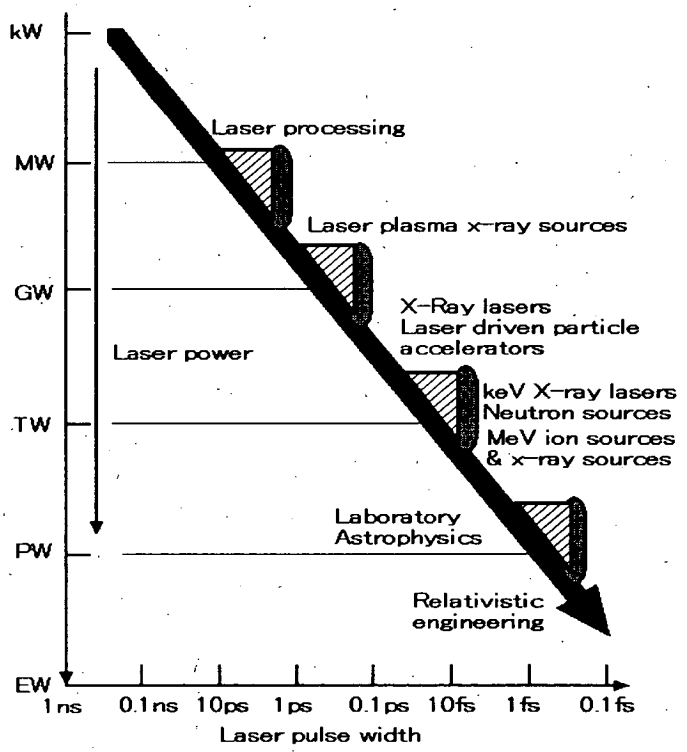

Fig.1 Direction of the high power laser development and its applications.

4.7.1 Development of laser-driven ion source for compact cancer therapy accelerator

Atsushi FUKUMI[a)], Hiroyuki DAIDO, Koji MATSUKADO[a)], Zhong LI[a)], Yukio HAYASHI, Mamiko NISHIUCHI, Satoshi ORIMO, Akito SAGISAKA, Koichi OGURA, Michiaki MORI, Hisanao HAZAMA, Kenichi TAKAGAKI, Takayuki UTSUMI, Sergei BULANOV, Timur ESIRKEPOV, Akira NODA[b)], Yoshihisa IWASHITA[b)], Toshiyuki SHIRAI[b)], Shu NAKAMURA[b)], Atsushi YAMAZAKI[b)],

a) National Institute of Radiological Sciences

b) Institute for Chemical Research, Kyoto University

1. Introduction

Cancer therapies using charged particles such as a proton or heavy ion are recently paid attention. Many medical facilities using proton or heavy ion accelerators have been working all over the world. A laser-driven ion source can play a role of compact ion injector and enables us to reduce the size of the accelerator[1)]. This would contribute to the wider spread of cancer therapy facilities. We have then started a project for developing a compact ion accelerator for cancer therapy.

It is well known that energetic ions are emitted from a target irradiated by an ultra-intense laser pulse. Several studies have been reported in the last decade[2-5)]. A table-top terawatt laser system is rather compact while it can deliver an intense pulse. Thus it is a possible candidate for the compact ion injector of a synchrotron without a pre-accelerator or a tandem accelerator.

When an ultra-intense laser irradiates a foil target, suppression of a pre-pulse becomes serious. Increasing the intensity, the pre-pulse becomes so intense as to destroy the thin foil target before the arrival of the main pulse. One of the ways for solving this problem is to put the pre-pulse to good use for efficient acceleration of electrons leading to the ion generation[6-7)]. In our previous work[8)], we presented experiments and simulations for testing a model in which the pre-pulse forms a layer of underdense plasma (pre-formed plasma)[9)] before the arrival of the main pulse. The main pulse consequently interacts with this pre-formed plasma. The simulated results were in good agreement with the experimental results.

As the first step for developing laser-plasma ion source, we have performed an experiment for generating the energetic ions by using a laser pulse accompanying a pre-pulse. This also gives us a lot of information concerning the acceleration mechanism of ions.

2. Experimental setup

The experiments were performed with a Ti:sapphire laser system, which provided a laser pulse at a repetition rate of 10 Hz with a wavelength centered at 800 nm. The pulse duration of 50 fs (FWHM) was measured with an autocorrelator. An s-polarized laser pulse was delivered to a target chamber with 200 mJ after mechanically decreasing the repetition rate to 1 Hz. The laser pulse was normally focused onto the target with *F*/6.5 off-axis parabolic mirror. Thin foil targets used were tantalum foils with the thickness of 1, 3 and 5 μm. The focal spot diameter was 13×18 μm (FWHM) including 44% of total energy. This yielded the peak intensity of 1×10^{18} W/cm^2. A temporal structures of the laser pulse in ns- and ps-regions were measured with a PIN photodiode and the third order crosscorrelator, respectively. The pre-pulse caused by a leakage of the switch out from regenerative amplifier at 12.5 ns before the main pulse was measured with a PIN photodiode. The contrast ratio was less than 10^{-4}. The contrast ratio of amplified spontaneous emission (ASE) in the range of ±100 ps from the main pulse was determined to be 10^{-6} with the third order crosscorrelator. A pedestal level around 3 ps after the peak of the main pulse was ~10^{-3}.

To obtain the ion energy spectra and to resolve the ion species, a Thomson parabola ion analyzer (B=0.16 T, E=4×10^5

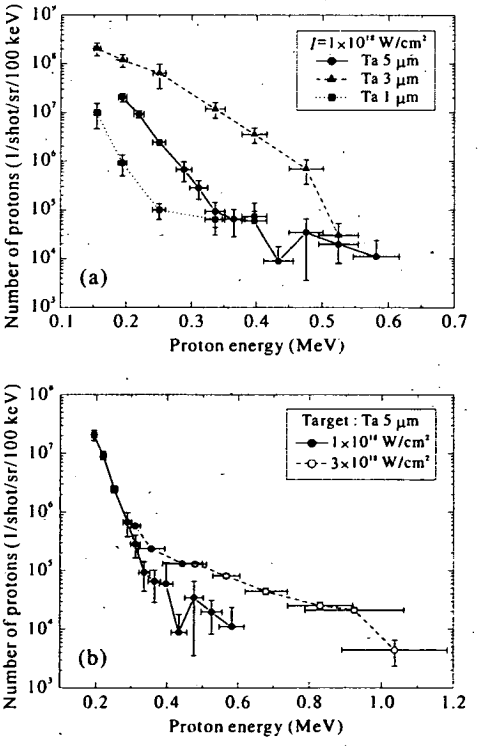

Fig. 1 Energy spectra of protons
(a) Dependency on target thickness
(b) Dependency on laser intensity

V/m) was placed 180 mm behind the target along the target normal direction. The angular distribution of ions was measured with CR-39 track detectors with a 0.8-μm thick alminum range filter, which stops the protons with the energies smaller than 100 keV. The CR-39 track detectors surrounded the laser-target interaction point at the distance of 500 mm. The degree of vacuum was kept about 10^{-5} Torr during the measurements. About 400 shots were accumulated for each measurment. A pump-probe measurement with an interferometer was also carried out to observe a time evolution of a preformed plasma profile[10].

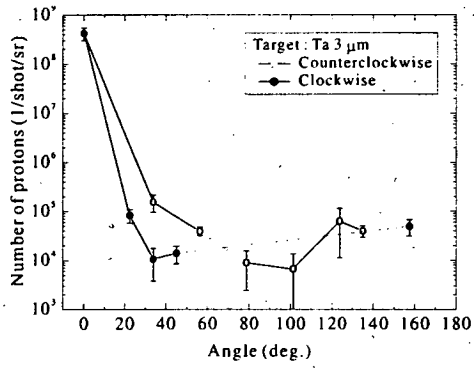

Fig. 2 Angular distribution of ion emission

3. Results

The ions obtained in the experiments were identified to be protons using Thomson parabola ion analyzer. They are attributed to contaminations of hydrogen layer on the target. The proton energy spectra obtained are shown in Fig. 1. Figure 1 (a) represents a dependency of the energy spectra on target thickness. The maximum energies for these targets are similar to each other while the maximum flux of protons is obtained with a 3-μm thick tantalum foil. In Fig. 1 (b), the previous data with the intensity of 3×10^{18} W/cm^2 [8] are presented for comparison. We find that the maximum energies with the intensities of 1×10^{18} W/cm^2 and 3×10^{18} W/cm^2 reach 600 keV and 1 MeV, respectively. Figure 2 shows an angular distribution of protons. The propagation direction of the laser pulse is defined as an angle of 0°. A collimated proton beam is obtained in the forward direction. Using the interferometer, we confirmed the existence of pre-formed plasma before the arrival of the main pulse (see Sec. 4.7.3).

In our previous work[8], we presented a novel scaling depending on two parameters; a dimensionless amplitude of laser pulse and a normalized density integrated along the laser axis. This scaling predicted several parameters such as maximum ion energy and conversion efficiency from laser pulse into ions. According to the scaling, the maximum proton energies predicted were consistent with the experimental ones.

References

1) S.V. Bulanov and V.S. Khoroshkov, Plasma Phys. Rep. **28**, 453, 2002
2) E.L. Clark, K. Krushelnick, M. Zepf, F.N. Beg, M. Tatarakis, A. Machacek, M.I.K. Santala, I. Watts, P.A. Norreys and A.E. Dangor, Phys. Rev. Lett. **85**, 1654, 2000
3) A. Maksimchuk, S. Gu, K. Flippo and D. Umstadter, Phys. Rev. Lett. **84**, 4108, 2000
4) M. Hegelich, S. Karsch, G. Pretzler, D. Habs, K. Witte, W. Guenther, M. Allen, A. Blazevic, J. Fuchs, J.C. Gauthier, M. Geissel, P. Audebert, T. Cowan and M. Roth, Phys. Rev. Lett. **89** 085002, 2002
5) I. Spencer, K.W.D. Ledingham, P. McKenna, T. McCanny, R.P. Singhal, P.S. Foster, D. Neely, A.J. Langley, E.J. Divall, C.J. Hooker, R.J. Clarke, P.A. Norreys, E.L. Clark, K. Krushelnick and J.R. Davies, Phys. Rev. E **67**, 046402, 2003
6) Wei Yu, V. Bychenkov, Y. Sentoku, M.Y. Yu, Z.M. Sheng and K. Mima, Phys. Rev. Lett. **85**, 570, 2000
7) Y. Sentoku, V.Y. Bychenkov, K. Flippo, A. Maksimchuk, K. Mima, G. Mourou, Z.M. Sheng and D. Umstadter, Appl. Phys. B **74**, 207, 2002
8) K. Matsukado, T. Esirkepov, K. Kinoshita, H. Daido, T. Utsumi, Z. Li, A. Fukumi, Y. Hayashi, S. Orimo, M. Nishiuchi, S. V. Bulanov, T. Tajima, A. Noda, Y. Iwashita, T. Shirai, T. Takeuchi, S. Nakamura, A. Yamazaki, M. Ikegami, T. Mihara, A. Morita, M. Uesaka, K. Yoshii, T. Watanabe, T. Hosokai, A. Zhidkov, A. Ogata, Y. Wada and T. Kubota, Phys. Rev. Lett. **91**, 215001, 2003
9) T. Ustumi, K. Matsukado, H. Daido, T.Z. Esirkepov and S.V. Bulanov, App. Phys. A **79**, 1185, 2004
10) A. Sagisaka, H. Daido, K. Ogura, S. Orimo, Y. Hayashi, M. Nishiuchi, M. Mori, K. Matsukado, A. Fukumi, Z. Li, S. Nakamura, K. Takagaki, H. Hazama, M. Suzuki, T. Utsumi, S. V. Bulanov and T. Esirkepov, Appl. Phys. B **78**, 919, 2004

4.7.2 Laser Produced Ion Beam Transportation by PMQs (Permanent-Magnet Quadrupole)

Shu NAKAMURA[a)], Yoshihisa IWASHITA[a)], Akira NODA[a)], Shinji SHIBUYA[b)], Koji NODA[b)], Atsushi FUKUMI[b)], Koji MATSUKADO[c)], Hiroyuki DAIDO

a) Institute for Chemical Research, Kyoto University

b) National Institute of Radiological Sciences

c) Research Foundation for Opto-Science and Technology

1. Introduction

We could obtain energetic protons by irradiation of an ultrashort intense laser on thin foils[1)]. A tabletop laser system with the peak power of 3 TW and the pulse duration of 50 fs is used. The laser pulse with peak intensity 6×10^{18} W/cm^2 is incident at right angles onto the 5 μm thick Ta foil targets. Protons with energies up to 1MeV are detected with a Thomson parabola ion energy spectrometer. An emission angle of produced ions is 10 ° (FWHM). For the purpose of application of laser-produced ions, it needs to transfer ions from a focus spot where ions are produced to the place of real usage. Consequently, we plan to collect ions that have divergence within ± 5° by PMQs (Permanent Magnet Quadrupole)[2)] installed in the vacuum vessel for laser irradiation on the target.

2. Simulation

We perform a TRACE 3-D[3)] simulation code using a transfer matrix. Magnetic fields in PMQs are optimized to make a proton beam at 500keV and an angle within ± 5° be parallel beam. The result of the simulation is presented in Fig.1. The parallel, focus and defocus lines show the proton beam envelope at 500keV, 475keV and 525keV. Comparing a triplet PMQ (see in Fig 1-(a)) with a quartet PMQ (see in Fig 1-(b)), we propose that the quartet PMQ be better than the triplet PMQ from the view of creating axially symmetric beam. The diameter of the parallel beam in the quartet PMQ is about 3cm. This is small enough for injector for ion accelerators.

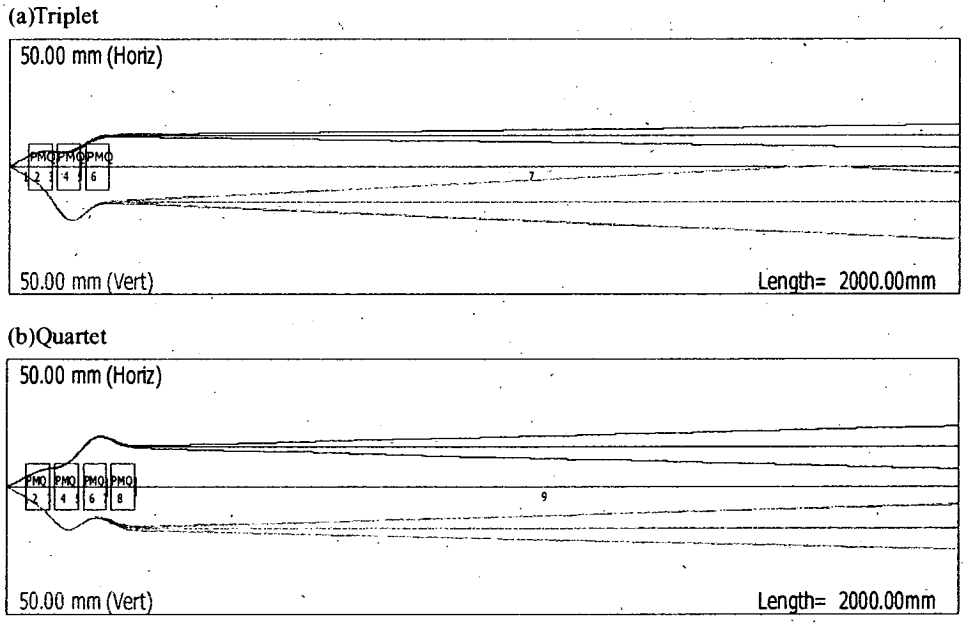

Fig. 1 The result of the TRACE3-D simulation
The upper side shows a horizontal envelope and the lower side shows a vertical envelope.

References

1) K. Matsukado *et al.*, Phys. Rev. Lett. **91**, 215001, 2003
2) K.Halbach, Nucl. Instr. and Meth. **169**, 1, 1980
3) http://laacg1.lanl.gov/laacg/c-on-line/descriptions/trace3d.html

4.7.3 Observation of preformed plasma of metal foil target for laser-plasma interaction

Akito SAGISAKA, Hiroyuki DAIDO, Koji MATSUKADO [a)], Atsushi FUKUMI [a)], Zhong LI [a)],
Koichi OGURA, Satoshi ORIMO, Yukio HAYASHI, Mamiko NISHIUCHI, Michiaki MORI,
Shu NAKAMURA [b)], Kenichi TAKAGAKI, Hisanao HAZAMA, Masayuki SUZUKI [c)],
Takayuki UTSUMI, Sergei BULANOV, and Timur ESIRKEPOV,
a) National Institute of Radiological Science, Japan
b) Institute for Chemical Research, Kyoto University
c) Institute for Solid State Physics, University of Tokyo, Japan

1. Introduction

High-energy x-rays, electrons, and ions from a high-intensity laser-produced plasma have been observed. Matsukado et al. reported the production of high-energy protons with a Ta plasma by using the high-intensity Ti:sapphire laser[1]. To interpret the experimental results, they proposed the ion generation in the preformed plasma slab created by a prepulse. The experimental results indicated that the characterization of preformed plasma was essentially important.

In this experiment, we measured the preformed plasmas of a Ta foil target produced by a high-intensity Ti:sapphire laser.

2. Experiment

A linearly polarized commercial Ti:sapphire laser was used at the wavelength of 800 nm. The pulse duration of 50 fs (FWHM) was measured by an auto-correlator. The temporal shape of the laser pulse was composed of prepulses such as the leakage of the switch out from the regenerative amplifier, continuous nanosecond duration pulse came from the amplified spontaneous emission (ASE), and the picosecond pedestal component. In this laser system, the contrast ratio of a prepulse at ~12 ns before the main pulse was $\sim 10^{-4}$. The contrast ratio of the ASE and the picosecond pedestal component were $\sim 10^{-6}$ and $\sim 10^{-3}$, respectively. The laser beam was divided into pump and probe beams. The pump beam was focused by an off-axis parabolic mirror, giving the peak intensity of 10^{18} W/cm^2. On the other hand, the probe beam was used for interferogram. The interference fringes were produced by using a Fresnel biprism and detected by a CCD camera[2].

3. Results

Figure 1 shows the interferogram with a preformed plasma of a 3 μm thick Ta foil target. It was taken at the time of ~20 ps before the main laser pulse arrived. The arrow shows the direction of the laser pulse propagation. The target surface corresponds to the left-side edge of the figure. In this case, the intensity of the main pulse is $\sim 1 \times 10^{18}$ W/cm^2 and the prepulse intensity is $\sim 1 \times 10^{14}$ W/cm^2. The preformed plasma size of ~150 μm is larger than the x-ray image size observed by a pinhole camera filtered with an 0.8 μm thick Al. We also detected the electrons with energies up to ~2 MeV and the protons with energies of ~0.5 MeV in this preformed plasma condition. The preformed plasma definitely plays an important role for laser-matter interactions such as x-ray and particle generations. We will characterize the electron density distribution of the preformed plasma.

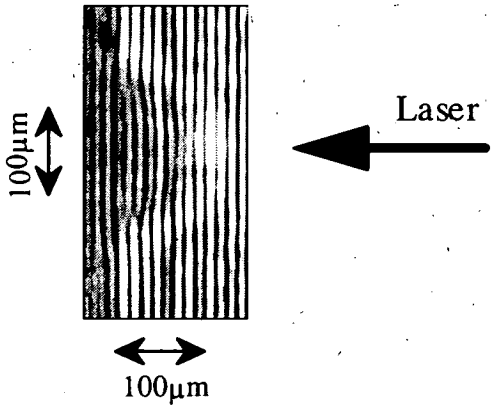

Fig. 1 Interferogram of the preformed plasma for a 3 μm thick Ta foil target.

References

1) K. Matsukado *et al.*, Phys. Rev. Lett. **91**, 215001 (2003).
2) A. Sagisaka *et al.*, Appl. Phys. B **78**, 919 (2004).

4.7.4 Simple method to estimate the radiation dose generated by high field science

Yukio HAYASHI, Atushi FUKUMI[a)], Koji MATSUKADO[a),*)], Kouichi OGURA, Michiaki MORI, Mamiko NISHIUCHI, Masataka KADO, Akito SAGISAKA, Satoshi ORIMO, Zhong LI[a)], Hiroyuki DAIDO, Hideyuki KOTAKI, Masaki KANDO, Shuji KONDO, Shuhei KANAZAWA and Izuru DAITO

a) National Institute of Radiological Sciences

1. Introduction

Recently new techniques of the short laser pulse generation and development of high quality crystal for lasers enable the construction of high power short pulse laser system. These laser systems have been applied for generating the high-energy particles. The electrons with energy higher than 1MeV were observed by use of these lasers. Kmetec et al. [1] detected high-energy photons > 1MeV generated with these lasers. The phenomenon is due to the interaction between the target and the high power short laser pulses.

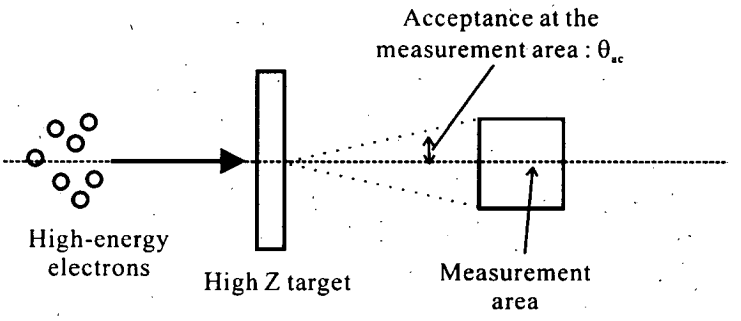

Fig.1 The geometry of the electrons and the target

These high-energy particles have a very short pulse width. For example, the pulse width of photons is shorter than 1ns (sometimes shorter than 10ps). This pulse width is suitable for a radiation source to study ultra fast phenomena [2] and it is applicable to various fields. The high power short pulse laser with a target is regarded as a new type of radiation source. However little discussion has been made on the photon dose generated by a high power laser. This paper introduces calculation method of photon dose generated by a high power laser plasma interaction and its applicability to radiation safety.

2. The dose calculation

2.1 The calculation model for the dose

We consider the photon dose it the case that the energy spectrum of the electrons can be approximated as the relativistic Maxwell Boltzmann distribution with the electron temperature T_h (MeV). We also assume the photon dose is due to the electromagnetic interaction between the target and the electrons. Geometry of the calculation model is as follows: the incident electrons are injected into the normal direction for Ta target surface and the target thickness is equal to the electron range with mean energy. The dose was estimated in the forward direction within the acceptance angle θ_{ac}. This model is illustrated in Fig.1.

2.2 The dose estimation by modified well-known formula

First, the photon dose formula in the forward direction proposed by Swanson [3] was used. This equation was obtained by the experimental results on photons produced by the interaction between mono energetic electrons and a target.

Thus the equation was modified for the electrons, which had the relativistic Maxwell Boltzmann energy distribution. Then following equation was obtained:

$$H(T_h) = 4.6\times10^{-1} P/(T_h^{\,3}\times R^2)$$
$$\times[-\exp(-20.0/T_h)(1.6\times10^4 + 6.4\times10^3 T_h$$
$$+1.76\times10^3 T_h^{\,2} + 3.36\times10^2 T_h^{\,3} + 40.8T_h^{\,4} + 2.4T_h^{\,5}) + 2.4T_h^{\,5}], \quad (1)$$

where $H(T_h)$ is the photon dose in Sv, P is the total energy in J and R is the distance from the target in cm. This is the simple method to calculate the photon dose.

When the electron temperature is very high (T_h>5MeV), the photon dose can be written as simpler form as follows:

$$H(T_h) = (5.33\times10^{-13} P/R^2)\times T_h, \quad (2)$$

This has been obtained from equation (1) with Taylar expansion. The equation (2) shows that the photon dose is proportional to the electron temperature, when the electron temperature is high enough. The relation between the electron temperature T_h and the photon dose is plotted in Fig. 1 at P=1J and R= 100cm. At the temperature higher than ~ 5MeV, the photon dose can be estimated by the equation (2). The equation (1) and (2) are plotted in Fig.2.

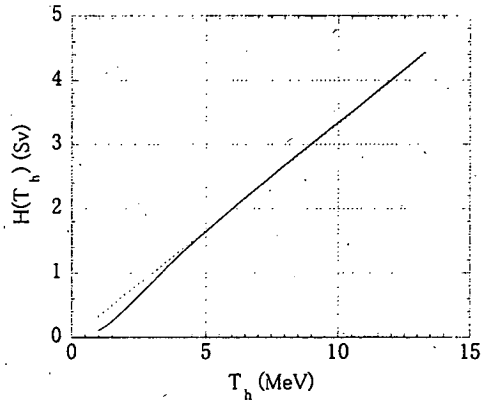

Fig.2 The equation (1) is represented as the solid line and the equation (2) as the broken line.

2.3 The dose estimation by Monte Carlo simulation code EGS4.0

We also have performed the calculation with Monte Carlo Simulation code EGS4.0 [4] to obtain much more information and to cheek the result obtained in the previous section. The acceptance angle θ_{ac} is shown in Fig.1 and it is described as

$$\theta_{ac} = (180.0/\pi) \times (m_e / E_{e,mean}) \quad \text{deg}, \qquad (3)$$

where m_e is the rest mass of the electron and $E_{e,mean}$ is the mean energy of the electron. The angle corresponds to the critical angle [**] for the mean energy of electron $E_{e,mean}$. The result of photon dose calculated by EGS4.0 and the equation (1) are shown in Table 1.

Table.1 The calculations have been performed under the condition of P=1J and R=100cm.

Th (MeV)	1.0	3.0	5.0	8.0	10.0
Dose H(T_h) with EGS4.0 (mSv)	0.16	0.98	2.17	4.42	5.97
Dose H(T_h) with equation (1) (mSv)	0.11	0.86	1.64	2.67	3.34

3. Summary

We have obtained the simple formula for dose calculation of high intensity laser-matter interaction. We found that the photon dose was proportional to the electron temperature T_h, when T_h was higher than 5MeV. The result of the formula has a similar dependence to the result obtained by EGS4.0, although the latter is a little higher (1.8 times at the maximum) than the former. The dose calculated by EGS4.0 is a factor <2 larger. Probably because the dose calculated by empirical formula is based on the experimental results with larger acceptance angle, which includes smaller dose components in the emission solid angle. We confirm that the formula with safety factor 1.8 is acceptable to calculate the photon dose generated by high intensity laser-matter interaction.

References

1) J.D.Kmetec et al. Phys. Rev. Lett. 68,1527 (1992).
2) C.Rose-Petruck et al. Nature 398, 310(1999).
3) W.P.Swanson. Radiological safety aspects of the operation of electron linear accelerators. IAEA Technical Report Series 188 (1979).
4) W.R.Nelson, H.Hirayama and D.W.O.Rodgers. The EGS4 Code system. SLAC Report 265, Stanford Linear Accelerator Center (1985).

*) Present address: Research Foundation for Opto-Science and Technology

**) Critical angle is defined that the divergence angle of the emitted x-ray from a target.

4.7.5 Measurement of Energy Spectrum of Positron

Zhong LI[a)], Hiroyuki DAIDO, Koji MATSUKADO[a)], Atsushi FUKUMI[a)], Yukio HAYASHI
Satoshi ORIMO, Akito SAGISAKA, Koichi OGURA, Hisanao HAZAMA, Kenichi TAKAGAKI
Mamiko NISHIUCHI, Michiaki MORI
a) National Institute of Radiological Sciences, 4-9-1, Anagawa, Inage, Chiba, 265-8555, Japan

The positron source has applications in physics research, material science, and biophysics *etc.* It can be produced from radioactive or through pair creation in high-Z target by high energy gamma rays or electron beam. It is known that an intense high energy electron beam can be produced from a plasma irradiated by an ultra-intense short laser pulse. The intense electron beam can bring out bright positron beam via pair creation in heavy atomic number target. It provides a simple way to produce bright positron beam and promotes the applications of positron. The cross section of the pair creation depends on the energy of the electron. An energy spectrometer to determine the energy spectra for both of electrons and positrons can study the pair creation driven by an intense energetic electron beam from laser-plasma interaction. We improved our electron energy spectrometer to determine the energy spectra of both electrons and positrons for this goal. The improved energy spectrometer was tested and calibrated with a ^{22}Na positron radioactive source.

The ^{22}Na positron radioactive source is packaged in a cylinder with a diameter of 20mm for active area. The activity of the source is 0.118 MBq after time calibration. The energy spectrometer is a magnetic energy spectrometer. The magnetic field is induced by a pair of permanent magnets. The magnetic field at the center of the magnetic cavity is 1200Gauss. The detector is an imaging plate typed BAS-SR2025 produced by Fujifilm Co. Ltd., which is placed under the magnets with a distance of 20mm to the axis of the collimator. The measurable energy range for positron with a 100mm long imaging plate is from 150keV to 8MeV. There is a collimator with a length of 460mm and a diameter of 5mm before the magnetic field. The ^{22}Na positron radioactive source was fixed at the front terminal of the collimator. The solid radian of the energy spectrometer to the radio source is 7.38×10^{-6}Sr. The positron flux entered the energy spectrometer is $5.42\times10^{-2}e^{+}$/s.

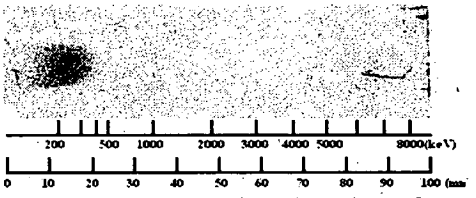

Fig.1 Shadow on imaging plate of positrons from a ^{22}Na radioactive source.

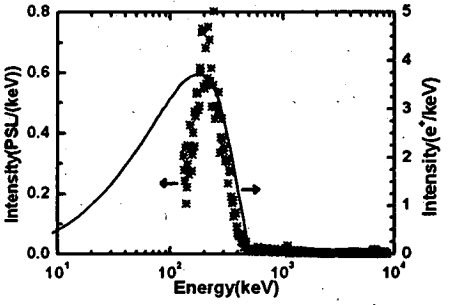

Fig.2 Energy spectrum of positrons from a ^{22}Na radioactive source described in the text.

The positron trace on the imaging plate exposed 6 hours is shown in Fig.1. The energy spectrum after time calibration (star mark) is given in Fig.2 together with an ideal energy spectrum (solid line). The sensitivity of the imaging plate to the positron has a maximum value around 0.16PSL/e^{+} at 200keV. It goes down rapidly at low energy side and slowly at high energy side. The energy spectrum of the electrons from ^{90}Sr-^{90}Y source exposed 5 hours at the same condition is given in Fig.3 with the same marks as in Fig.2 for comparing the sensitivities of the imaging plate to electrons and positrons. We can find the sensitivity of the imaging plate for positrons is similar to that for electrons. The sensitivity of the imaging plate for electrons also has a peak around 0.09PSL/e^{-} at 200keV, which is lower than that for positrons. While a positron injects into the imaging plate, it will produce gamma rays in the imaging plate and deposit more energy in the imaging plate in contrast to an electron with the same kinetic energy. It causes that the imaging plate has a higher sensitivity for positrons than that for electrons.

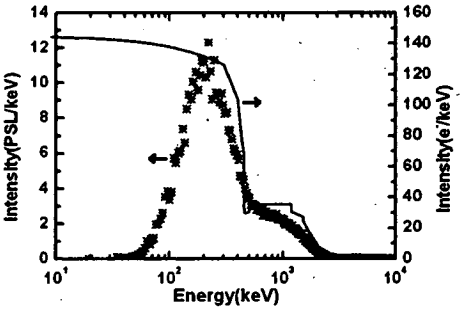

Fig.3 Energy spectrum of electrons from a ^{90}Sr-^{90}Y „ source described in the text.

The experimental result confirms that the imaging plate can be applied to detect the positron. Our energy spectrometer can determine the energy spectra of electron and positron to study the pair creation by high energy electron driven by an ultra-intense short laser pulse.

4.7.6 Production of fast electrons accelerated by the ponderomotive pressure

Michiaki MORI, Hiroyuki DAIDO, Yuji FUKUDA, Koichi OGURA, Yukio HAYASHI, Masaki KANDO, Shinichi MASUDA, Takayuki HONMA, Yutaka AKAHANE, Hiromitsu KIRIYAMA, Norihiro INOUE, Hideki UEDA, Koichi TSUJI, Yoshiki NAKAI, Youichi YAMAMOTO, Hideyuki KOTAKI, Shuji KONDO, Shuhei KANAZAWA, and Koichi YAMAKAWA

1. Introduction

In production of energetic electrons by using ultra-high intensity laser-plasma interactions, ponderomotive acceleration process is important role above intensity of 10^{17} W/cm^2. We report on the experiment of the ponderomotive acceleration in APRC.

2. Ponderomotive acceleration

At non-relativistic intensity (i.e. normalized vector potential: $a_0<1$) and continuous wave in time and space, a motion of the electron driven by electro-magnetic wave is almost linear in lab frame. However, at relativistic intensity (i.e. $a_0>1$), the relativistic effect and **vxB** acceleration effect cannot be ignorable. Moreover, the spatial profile of the laser plays an important role to define the trajectory of electron (i.e. ponderomotive force). From these reasons, trajectory of electrons has a forward component to the laser propagation. Many papers[1-3] were discussed energetic electron generation by the ponderomotive acceleration process in several conditions. From these predictions, accelerated electrons strongly depended on the laser intensity, focus, or the pulse duration of the laser. This research is interesting not only for the ultra-high laser-plasma interaction studies but also particle accelerator studies. So, we have experimentally studied on ponderomotive acceleration since this fiscal year.

A schematic of the experimental apparatus is shown in Fig. 1. The experiment was performed with Ti:Sapphire CPA laser system delivering pulses with a duration of 23fs, a repetition rate 10 Hz, and an energy of 400mJ. A laser pulse was focused to be 10 micron in diameter with an f/3 off axis parabolic mirror in vacuum. Then the peak intensity in vacuum was estimated to be 2×10^{19} W/cm^2. The gas jet (HFC-152a gas) was produced by a pulsed gas valve in the target chamber. The pulsed gas valve has a 1-mm-diameter orifice. The backing pressure was fixed to be 5 atm in absolute unit (Then the average atomic density was estimated to be 10^{19} cm^{-3}). A prepulse ratio was 10^{-6}. Accelerated electrons were observed via stacked imaging plate (Fuji Film, SR2025) placed behind the interaction point. In Fig. 2, it is shown observed accelerated electron image (E>25keV) under such condition. A ring shape pattern was observed. It is in good agreement with theoretical predictions of the relativistic ponderomotive acceleration. However, at secondary imaging plate (E>400keV), it was no observed signals in such experimental condition. Therefore, we observed electrons energy with <400keV predominantly.

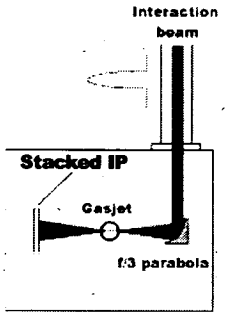

Fig. 1. Schematic of experimental setup.

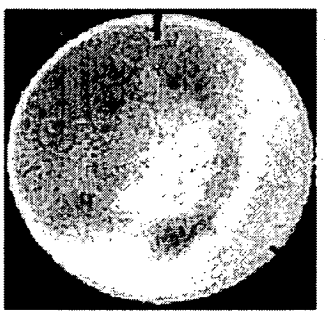

Fig. 2. Image of accelerated electrons (E>25keV).

References

1. F. V. Hartmann et. al, Phys. Rev. E **51**, 4833 (1995).
2. P. X. Wang et. al, J. Appl. Phys. **91**, 856 (2002).
3. F. He et. al, Phys. Rev. E **68**, 046407 (2003).

4.7.7 Soft X-ray Emission in the Water Window from a Double-stream Gas-puff Target Irradiated with Nd:YAG Laser

Koichi OGURA, Hisanao HAZAMA, Kenichi TAKAGAKI, Etsuya YANASE,
Sadao HUJII, Henryk FIEDOROWICZ and Hiroyuki DAIDO

1. Introduction

The soft x-ray in the water window spectrum (2.3~4.3nm) is an area where carbon absorbs more x-ray than water. Thus one can clearly take images of protein in a water. Such an x-ray can be produced by high-power laser irradiation of a solid target. When the solid target is irradiated, the debris is generated. The debris causes the degradation of the x-ray optical elements and the reduction of the efficiency of focusing optics. Therefore it is necessary to develop a target which will not generate any debris. Though a gas-puff target dose not generate debris, the intensity of the x-ray is smaller than that of the solid targets. Recently, the double-stream gas-puff target, which produces a high plasma in comparison with that produced by the single nozzle gas puff target, has been developed. Fiedorwicz *et al.* investigated the x-ray emission in the 1.0 to 3.5 nm wavelength range from N_2 or Ar gas target irradiated by focusing a 1 ns Nd:glass laser pulse with an energy up to 10 J[1]. Suzuki *et al.* investigated the water window x-ray from a double-stream gas target created using Ar, Xe, Kr, and N_2 irradiated by focusing a 8 ns laser pulse energy up to 0.7 J produced with a commercial Nd:YAG laser[2]. In their experiments, x-ray intensity of the water window was much lower than that from a solid carbon target. The intensity of the emission in the water window was only about 2 times higher for the double-stream target than for the single nozzle gas target.

Here, it was demonstrated that the intensity of the x-ray in the water window from a double-stream gas-puff target was enhanced about 7 times as high as that from the single nozzle gas target using a commercial Nd:YAG laser.

2. Experimental

The valve system consists of two combined solenoid valves and a double-nozzle setup. The nozzle setup consists of two coaxial nozzles. The outer nozzle in the form of a ring with outer/inner diameter of 1500 and 700 mm, respectively, produces a hollow cylinder of a low-Z gas (He). The inner nozzle is a circular orifice of 500 mm in diameter, through which high-Z gas (Xe, Ar, Kr, N_2) is injected into the outer gas stream. The gas backing pressure in both valves was 10 atom. The diameter of the orifice of the inner nozzle was 1.25 times larger than that in Suzuki's experiment so that the mass-density along the axis of the nozzle is about 1.6 times higher than that in Suzuki's experiment. The target was irradiated by a 2 ns commercial Nd:YAG laser pulse with energy up to 250 mJ at 1.06 μm wavelength.

3. Results

Typical spectra for an Ar/He target and a Kr/He target are shown in fig.1(a) and (b), respectively. For comparison spectra from an ordinary Ar and Kr targets are also shown in fig.1. The enhancement of the x-ray in the water window have been observed for the double-stream target compared to the single nozzle target. The spectra from Kr target is broad as compared with that from an Ar target. To compare the x-ray produced from a double-stream target with an emission from a solid target, spectra from Au (100μm) irradiated under the same condition and measured same spectrometer are shown in fig.1. These results show that the laser irradiated double-stream gas-puff target is effecticient debris-free x-ray source in the water window which is applicable to for a microscope and other applications.

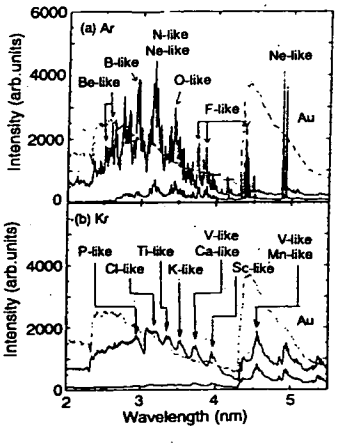

Figure 1. Spectra from Ar/He and Kr/He double-stream target and spectra from Au target (broken line).

References

1) H. Fiedrowicz *et al.*, Scientific Report, Institute of Optoelectronics,, Military University of Technology , Warsaw, Poland , 2003.

2) M.Suzuki, Dr.Thesis, Osaka University, Suita, Osaka, 2003.

4.7.8 Development of a laser plasma x-ray microscope for live biological specimens

Masataka KADO and Hiroyuki DAIDO

1. Introduction

Investigating the structure and the function of life object performing advanced life activity becomes important. In order to investigate the life object, it is necessary to observe living specimens with high spatial resolution and high temporal resolution. Since laser plasma x-ray source has high brightness and short pulse duration, x-ray microscope with the laser plasma x-ray source makes possible to observe living specimens. Such as chromosomes, macrophages[1], bacterium[2)3)], and so on have been observed by contact x-ray microscopy. The x-ray images obtained by indirect measurements such as the contact x-ray microscopy have difficulty to avoid artificial effect such as irregular due to developing process. Development of an x-ray microscope with laser plasma x-ray source is necessary to avoid such defects.

2. Design of the x-ray microscope

The x-ray microscope is consisted of a laser plasma x-ray source, a spherical multilayered x-ray mirror as a condenser lens, a micro zone plate as an objective lens, a specimen holder to keep wet specimens in vacuum, and a back illuminated x-ray CCD camera. Shown in Figure 1 is the schematic view of the laser plasma x-ray microscope. An Yttrium target is irradiated with a laser pulse produced by a Nd:glass laser system. The x-ray emitted from the laser plasma is focused with the condenser lens on to the specimen. The x-ray image of the specimen is magnified with objective lens to the x-ray CCD camera. The x-ray source size is 50μm in diameter. The magnification of the condenser lens is 2 and the magnification of the objective lens is 200. Since the Pixel size of the x-ray CCD camera is 13μm and pixel number is 1000 x 1000, the field of view of the microscope is 60μm. The specimen holder is consisted of two Silicon Nitride thin films and sandwich the wet specimen to avoid the wet specimen to be exposed to vacuum.

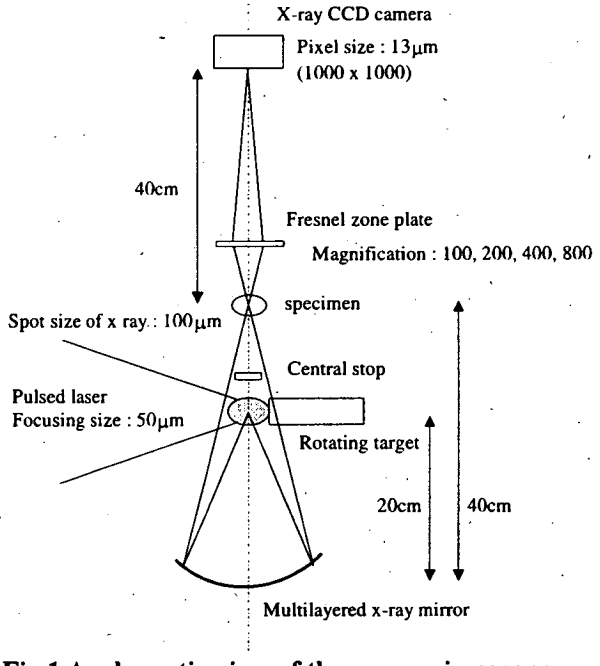

Fig.1 A schematic view of the x-ray microscope

3. Calculation of the photon margin

The laser energy to be focused onto the Yttrium target is 6J at 527nm in wavelength, which is the second harmonics of Nd:glass laser. The laser intensity on the target is going to be $3x10^{14}W/cm^2$ since the laser focusing size is 50μm in diameter. The x-ray conversion efficiency into the so-called "water window" x ray (2.3-4.4nm) is about 10%. The spherical multilayered x-ray mirror is placed 20cm away from the x-ray source and the diameter of the mirror is 1.6cm, which gives a solid angle of $1.6x10^{-3}$str. Since the spectral width of the multilayered x-ray mirror at 300eV is about 0.08nm with 50 layer pairs and the reflectivity at 300eV is about 10%, the photon number at the specimens is calculated to be $7.62x10^{10}$ photons. The x-ray photons are attenuated by 25% with two Silicon Nitride films with thickness of 100nm and 12% with water layer of 5μm. The x-ray photons are also attenuated by 40% with a Titanium filter with thickness of 0.4μm which blocks visible light. Since the efficiency of the micro zone plate is about 20% the photon number at the x-ray CCD camera is about $1.83x10^8$ photons and the photon number at each pixel of the x-ray CCD camera is about 77.3 photons/pixel, which will make clean images of the living specimens.

References

1) M. Kado, M. C. Richardson, Y. Yamamoto, et al., Proc. of Exp. Biology and Medicine **220**, 21, 1999.
2) J. M. Rajyaguru, M. Kado, M. C. Richardson, et al., Biophysical Journal **72**, 1521, 1997.
3) J. M. Rajyaguru, M. Kado, K. Nekula, M. C. Richardson, et al., Microbiology **143**, 733, 1997.

4.7.9 Selective excitation of atoms by quantum control methods

Yoshiaki TERANISHI

1. Introduction

Recently, there has been a growing interest, both experimental and theoretical, in controlling atomic and molecular processes by laser fields. This is basically due to the fact that the recent remarkable progress in laser technology has opened new possibilities of realizing it. Utilizing the coherence of laser field together with the quantum property of the target, more effective and precise control is expected.

In this study, we discuss excitation processes of Cs atom by phase-locked pulse pairs. Due to the quantum effect, it is made possible to select the final state out of the closely-lying spin-orbit states which splitting is much smaller than the bandwidth of the light source. Our theoretical results are compared to relevant experimental results.

2. Control scheme

We apply a phase-locked laser pulse pair (center wavelength = 770 nm, bandwidth = 380 cm^{-1}) to Cs atoms in their ground states ($6S_{1/2}$). From the spectroscopic point of view, Cs atom can be excited into both $7D_{5/2}$ and $7D_{3/2}$ states. For the selective excitation, we have to adjust the phase difference of the pulse pair to wipe out the amplitude of the wave function in either excited state. In order to simulate this process, we solved time-dependent coupled channel equations including 18 states from 6S to 9S for Cs atom.

3. Results

We calculated excitation probabilities as functions of the laser intensity, time delay, and the phase difference of irradiated pulse pair. Figure 1 shows the calculated excitation probabilities induced by a pulse pair (intensity = 0.1 GW/cm2, delay =300 fs) with various phase difference. In Fig.1, experimental results[1] are also shown for comparison. As shown in the figure, our results agree well with the experimental results, and excitation into either state is almost completely suppressed, which means selective excitation is realized with high accuracy. It should be pointed out that the absolute values of the excitation probability are very small (~ 10^{-5}).

In order to obtain much higher probability, we have to increase the peak intensity. The selectivity, however, becomes worth due to the nonlinear effect. Figure 2 shows an example of high intensity case ($15GW/cm^2$). Excitation probability is high while suppression is not complete. This nonlinear effect can be surmounted by applying chirped pulses[2].

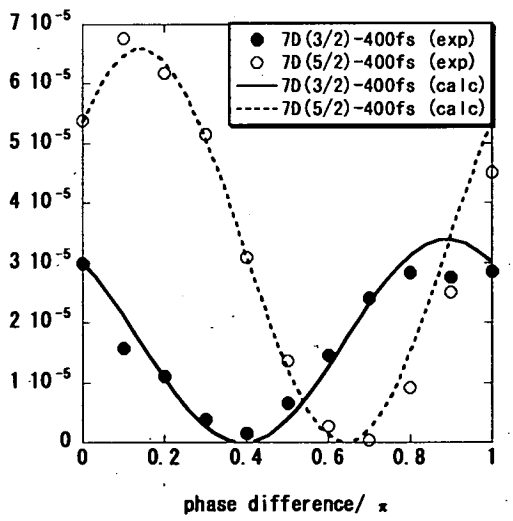

Fig.1 Excitation probabilities as functions of phase difference

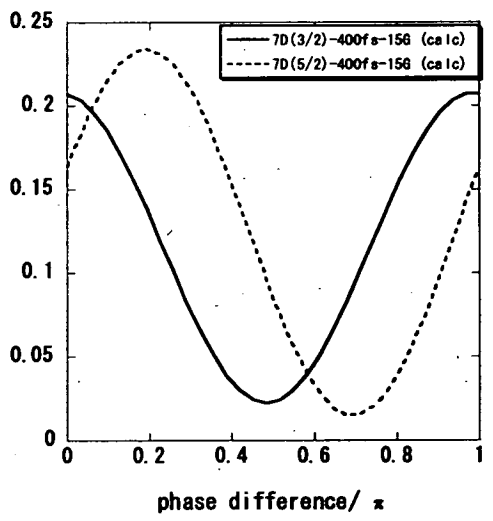

Fig.2 Calculated excitation probabilities in the case of high intensity ($15GW/cm^2$)

References

1) H. Yamada *et al.*, (to be published).
2) Y. Teranishi and H. Nakamura, J. Chem. Phys. **111**, 1415 1999.

4.7.10 Reflection of a high intensity laser pulse at the plasma-vacuum interface: Generation of attosecond pulses

Alexander PIROZHKOV, Hiroyuki DAIDO, Sergei BULANOV

1. Introduction

Recently[1-4], the method of attosecond pulse generation using several high-order harmonics of a laser radiation[5] was experimentally fulfilled using noble gases as generating media. The energy of harmonics generated in gases was rather low. The energy of harmonics of a relativistic laser pulse reflected from a solid target, in contrast, can be as high as several mJ in the 10-30 nm region (2π sr)[6]. For this reason, use of high-order harmonics from solid targets for the generation of attosecond pulses is of considerable interest.

One of the models accounting for the emission of high-order harmonics during the reflection of a relativistic laser pulse from a solid target or a thin foil is a model of oscillating mirror[7]. In this model, the target is represented by a thin layer of electrons, which oscillates as a whole under the influence of the incident laser pulse. Such collective behaviour of electrons is justified by PIC simulations[7,8]. Due to the relativistic intensity of the laser pulse, electrons oscillate not only in the plane of the layer, but also along the direction of a wave vector[9]. This oscillation leads to a Doppler up- and down shift of a frequency of a reflected electromagnetic wave. This model is applicable when the influence of ions and the back reaction of the reflected radiation are negligible, so the normalized plasma density $\varepsilon_0 = \omega_p^2 l/(2\omega_0 c) << 1$. Here, ω_0 is the laser frequency, c is the speed of light, $\omega_p = (4\pi n e^2/m)^{1/2}$ is the plasma frequency, n is the electron density, e is the electron charge, m is the electron mass, and l is the thickness of the plasma layer. Generation of attosecond pulses in the case of an underdense plasma with $\varepsilon_0<1$ was considered in Ref. 10. We consider the reverse case of an overdense plasma with $\varepsilon_0>1$.

2. Nonlinear boundary conditions for the laser pulse reflection at the thin plasma layer

We adopt the model of the electron layer with a constant density. In the case of an overdense plasma considered here, the electron layer cannot be separated from the immobile ion layer, therefore electrons cannot move in the direction perpendicular to the plasma layer. However, electrons can move along the layer.

We consider a plane electromagnetic wave with a wave vector $\boldsymbol{k}_0 = \{\omega_0/c\cos\theta, \omega_0/c\sin\theta, 0\}$ obliquely incident on the foil located at $x = 0$. Here, θ is the incidence angle. We perform the Lorentz transform from the laboratory reference frame into the reference frame moving along the y axis with a velocity $V = c\sin\theta$. In the boosted reference frame, the field amplitude is $E_0' = E_0\cos\theta$, the frequency is $\omega_0' = \omega_0\cos\theta$, the wave vector is $\boldsymbol{k}_0' = \{\omega_0/c\cos\theta, 0, 0\}$ and therefore the wave propagates along the normal to the foil[11]. A prime denotes quantities in the boosted reference frame.

The dimensionless vector potential $\boldsymbol{a}'(t')$ taken at the foil position $x = 0$ can be found from equation[8]

$$\dot{\boldsymbol{a}}'(t') + \varepsilon_0\left\{[\boldsymbol{p}_0 + \boldsymbol{a}'(t')]\sqrt{\frac{1+\boldsymbol{p}_0^2}{1+[\boldsymbol{p}_0+\boldsymbol{a}'(t')]^2}} - \boldsymbol{p}_0\right\} = \dot{\boldsymbol{a}}_0'(t') \qquad (1)$$

Here, $\boldsymbol{a}_0'(t')$ is a vector potential of the incident pulse at the foil position, $\boldsymbol{p}_0 = \{0, -\tan\theta, 0\}$ is the electron momentum in the absence of the electromagnetic field in the boosted reference frame, and t' is measured in the units of $1/\omega_0$. We use dimensionless units, where velocities are normalized to c, momenta to mc, fields to $mc\omega_0/e$, and vector potentials to mc^2/e. The electric field of the reflected wave is

$$\boldsymbol{E}'(x,t') = \varepsilon_0\left\{[\boldsymbol{p}_0 + \boldsymbol{a}'(t'+x)]\sqrt{\frac{1+\boldsymbol{p}_0^2}{1+[\boldsymbol{p}_0+\boldsymbol{a}'(t'+x)]^2}} - \boldsymbol{p}_0\right\}. \qquad (2)$$

3. Generation of high-order harmonics

Equation (1) was numerically integrated for the case of a p-polarized laser pulse with its amplitude $a = eE_0/(mc\omega_0) = 8.8$, duration $\tau_0 = 15/\omega_0$ (we use FWHM pulse durations), the incidence angle $\theta = 28.6°$. If $\lambda_0 = 800$ nm, this corresponds to the intensity of about $1.6\cdot10^{20}$ W/cm^2 and to the pulse duration of 6.3 fs. Reflected pulse spectra calculated in the laboratory reference frame are shown in Figure 1. The normalized plasma density in the layer is $\varepsilon_0 = 8.8$ (curves 1 and 2) and 13.2 (curve 3). The high-order harmonic intensity decreases with plasma density. Note that in the high-frequency part spectra do not longer consist of individual harmonics. They rather resemble a descending supercontinuum. Such behavior is characteristic for short pulses. Longer pulses produce spectra with a pronounced harmonic structure.

Furthermore, in the case of a short pulse the shape of the spectrum of the reflected pulse depends on the carrier-envelope phase, so that changing this phase it is possible to obtain spectra with or without harmonic structure (Figure 1, curves 1 and 2). The similar effect in the completely different regime of non relativistic harmonics generation was experimentally observed in Refs. 12, 13, where high-order harmonics from a gas target were generated by using 5-6 fs laser pulses focused to the intensity below 10^{15} W/cm^2.

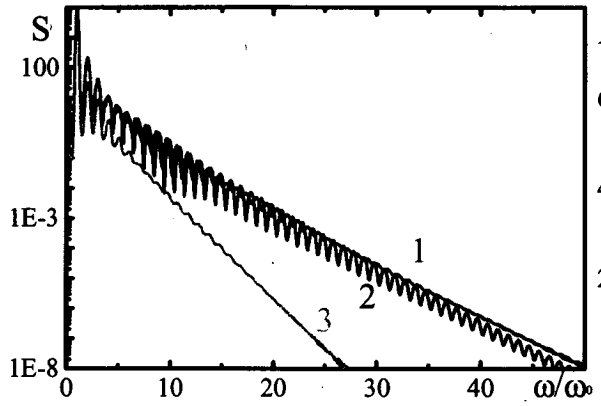

Fig. 1. Spectra of reflected pulses
(1): $\varepsilon_0 = 8.8$, cosine-like pulse.
(2): $\varepsilon_0 = 8.8$, sine-like pulse.
(3): $\varepsilon_0 = 13.2$, cosine-like pulse.

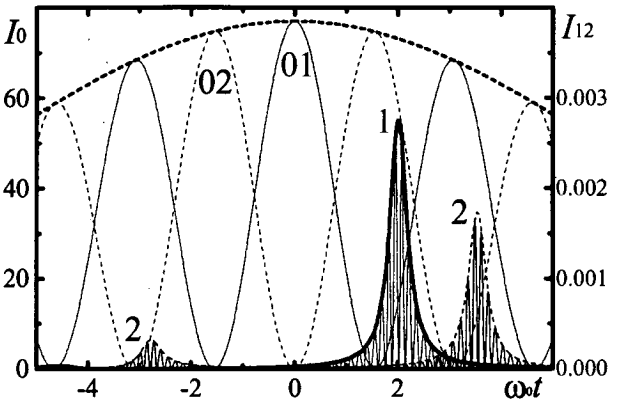

Fig. 2. Intensities of the incident (01, 02) and spectrally filtered ($21\omega_0 - 47\omega_0$) reflected pulses (1, 2) ($\varepsilon_0 = 8.8$)
(1): cosine-like incident pulse, $\tau = 0.41/\omega_0$
(2): sine-like pulse. $\tau = 0.44/\omega_0$.

4. Generation of attosecond pulses

In order to obtain the attosecond pulse from the reflected electromagnetic wave, we need to select a certain frequency band[1-5]. Figure 2 shows intensities of reflected pulses that pass through a bandpass spectral filter $21\omega_0 - 47\omega_0$ (curve 1: cosine-like incident pulse, curve 2: sine-like pulse). The carrier-envelope phase influences the form of the reflected attosecond pulse. In the case of a cosine-like laser pulse, the reflected pulse is shorter, has higher energy and no satellite pulses. The reflected pulse (Figure 2, curve 1) has a duration of $0.41/\omega_0$ (0.17 fs for $\lambda_0 = 800$ nm), the conversion efficiency is $1.4 \cdot 10^{-6}$.

5. Conclusion

In the model where the overdense plasma was represented by the thin electron layer, the motion of electrons in the direction perpendicular to the plasma surface was negligible. Using this model, we calculated high-order harmonics generated during the reflection of the high intensity laser pulse. We demonstrated that these high-order harmonics were phase-locked and formed attosecond pulses if one sums several harmonics. We showed that cosine-like laser pulses generated attosecond pulses with higher energy and shorter duration than sine-like ones.

References

1) R. Kienberger *et al.*, Nature **427**, 817, 2004
2) Y. Mairesse *et al.*, Science **302**, 1540, 2003
3) S. A. Aseyev, Y. Ni, L. J. Frasinski, H. G. Muller, M. J. J. Vrakking, Phys. Rev. Lett. **91**, 223902, 2003
4) P. Tzallas, D. Charalambidis, N. A. Papadogiannis, K. Witte and G. D. Tsakiris, Nature **426**, 267, 2003
5) Gy. Farkas and Cs. Tóth, Phys. Lett. A **168**, 447, 1992
6) M. Zepf *et al.*, presented on Jan. 6, 2004 at the REEFS workshop, APRC-JAERI, Kyoto, Japan.
7) S. V. Bulanov, N. M. Naumova, F. Pegoraro, Phys. Plasmas **1**, 745, 1994
8) V. A. Vshivkov, N. M. Naumova, F. Pegoraro, S. V. Bulanov, Phys. Plasmas **5**, 2727, 1998
9) L. D. Landau, E. M. Lifshitz, The Classical Theory of Fields, Pergamon, Oxford, 1983
10) N. M. Naumova, J. A. Nees, I. V. Sokolov, B. Hou, G. A. Mourou, Phys. Rev. Lett. **92**, 063902, 2004
11) A. Bourdier, Phys. Fluids **26**, 1804, 1983
12) A. Baltuska *et al.*, Nature **421**, 611, 2003
13) M. Nisoli *et al.*, Phys. Rev. Lett. **91**, 213905, 2003

4.7.11 Design of multilayer mirrors for the reflection of attosecond XUV pulses

Alexander PIROZHKOV, Hiroyuki DAIDO, Sergei BULANOV, Michiaki MORI, Eugene RAGOZIN [a)]
a) Division of Optics, P. N. Lebedev Physical Institute of the Russian Academy of Sciences

1. Introduction

Recent progress in the generation and characterization of sub-femtosecond pulses in the XUV spectral region[1-2)] calls for the development of suitable optical elements. Among the most efficient XUV optical elements are multilayer mirrors. Up to now, only periodic multilayer mirrors were used for the reflection of sub-fs pulses. The shortest generated pulse[1)] had the duration of 0.25 fs which was almost limited by the bandwidth of the multilayer used (9 eV). This means that further decrease in the pulse duration is impossible without a broadband aperiodic multilayer mirrors. The first broadband aperiodic XUV multilayer mirrors for the 12.5-25 nm spectral range were successfully synthesized and used as focusing elements of the imaging XUV spectrograph in Refs. 3, 4. Evidently, for the reflection of ultrashort pulses an increased attention should be paid to the dispersive (or phase) properties of multilayer structures. We extended the method of calculation of aperiodic multilayer mirrors for the reflection of ultrashort pulses and designed mirrors for the compression of chirped pulses and the simultaneous reflection of several high-order harmonics.

2. Calculation of aperiodic multilayer structures for the reflection of ultrashort pulses

The inverse problem of XUV multilayer optics – that is, the problem of calculation of an aperiodic multilayer structure that gives an extremum of a prescribed merit function – was first stated in Ref. 5. Later this problem was solved with different methods by many authors[6-10)]. We used a specially designed genetic algorithm for the optimization of aperiodic multilayer structures. Optimization parameters were thicknesses of all layers. In contrast to the previous papers, the merit function was taken in the form of I_{max}/τ, where I_{max} is the peak intensity of the reflected pulse, $\tau = \int \tilde{I}(t)dt/I_{max}$ is the effective duration of the reflected pulse, $\tilde{I}(t)$ is the intensity envelope. Note that FWHM durations of pulses presented here are somewhat shorter.

In calculations, we assumed that multilayer structures consist of two alternating layers with ideal interfaces. We used the method of recurrent relations for calculation of the complex reflectivity amplitude of structures[11)]. Optical constants of materials were taken from Ref. 12.

3. Compression of chirped XUV pulses

Intense chirped XUV pulses can be generated in the process of reflection and focusing of a source laser pulse from a flying plasma mirror[13)]. The chirp of the XUV pulse can be controlled by the chirp of the source laser. Another possibility is to use a plasma with a density gradient as the speed of the flying plasma mirror depends on density. Due to a relatively small diameter of the flying mirror (<1 mm for a 17 J driver pulse), the focal spot would be relatively large at the practical focusing length. In contrast, multilayer mirrors with the diameter of several centimeters are readily available. It means that the intensity of the XUV pulse generated by the flying mirror and focused by a multilayer mirror can be 2-3 orders of magnitude higher.

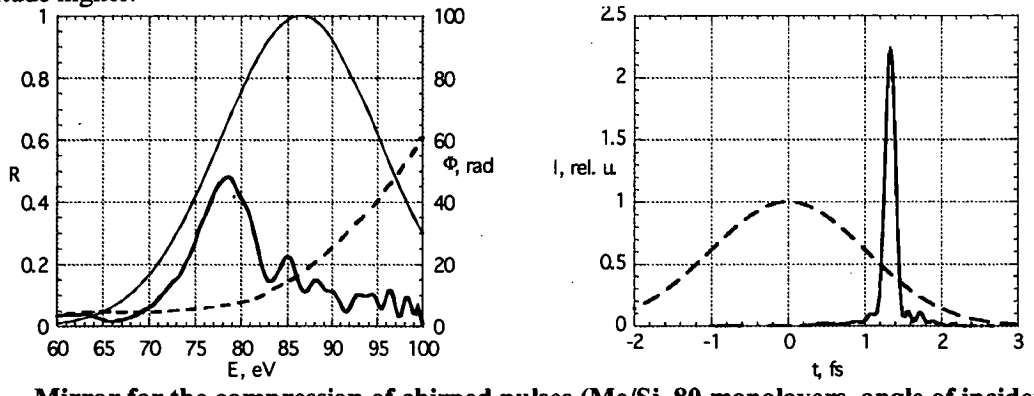

Fig. 1. Mirror for the compression of chirped pulses (Mo/Si, 80 monolayers, angle of incidence 5°) Left: mirror reflectivity (thick line) and spectral phase (dashed line). Thin line – spectrum of the chirped incident pulse ($\hbar\omega_0$ = 86 eV, τ_0 = 2.5 fs, b = -6.5 fs^{-2}). Right: intensity envelopes of the incident (dashed line) and reflected (solid line) pulses. τ = 0.19 fs, energy reflectivity 0.17.

In the calculation, the incident pulse had a Gaussian form with the duration $\tau_0 = 2.5$ fs and the chirp parameter $b = -6.5$ fs^{-2}. The chirp was negative, so the leading part of the pulse had a higher frequency. This was consistent with the natural trend of a deeper penetration (hence, a longer delay) of the higher-frequency radiation into the mirror structure. The results of calculation are shown in Figure 1. The aperiodic mirror performed a 13-fold temporal compression with an energy reflectivity of 0.17. The peak intensity of the reflected pulse was more than twice the intensity of the incident pulse.

4. Simultaneous reflection of several high-order harmonics

It was shown recently that high-order harmonics of the laser radiation were not completely phased[2]. For harmonics generated by a Ti:Sapphire laser in Ar gas the emission time difference between two neighboring harmonics was measured to be $\Delta t = t_e(q+2) - t_e(q) = 33$ as. It is important to note that higher harmonics were emitted after lower ones. This means the positive chirp of the incident pulse, which is not consistent with the above-mentioned natural trend.

To calculate mirrors for the simultaneous reflection of several harmonics, we set the incident train of pulses in the form $E_0(t) = \sum a_q \cos(\omega_q t - \omega_q^2 \Delta t / 4\omega_L)$, where $\omega_q = q\omega_L$, so that the group delay was $t_g = \omega_q \Delta t/(2\omega_L) = q\Delta t/2$. We calculated a mirror for the reflection of odd harmonics 25-69. Harmonic amplitudes a_q decreased exponentially with order from 1 to 0.1 (intensities from 1 to 0.01). The results of calculation are shown in Figure 2. The mirror performed a two-fold compression of the incident pulse.

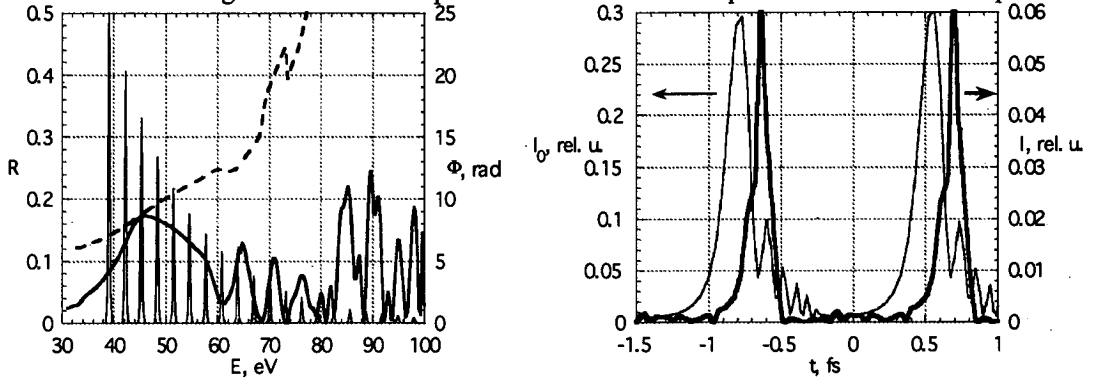

Fig. 2. Mirror for the simultaneous reflection of 25-to-69-order odd harmonics ($\lambda_0 = 800$ nm) with an emission time difference of 33 as (Mo/Si, 80 monolayers, angle of incidence 5°)
Left: mirror reflectivity (thick line) and spectral phase (dashed line). Thin line – spectrum of the incident pulse. Right: intensity envelopes of the incident (thin line) and reflected pulses (thick lines, scaled (x5) for convenience). $\tau_0 = 0.27$ fs, $\tau = 0.13$ fs, energy reflectivity 0.11.

5. Conclusion

We made a theoretical investigation of aperiodic multilayer mirrors for the reflection of ultrashort XUV pulses. We designed aperiodic structures for the 13-fold compression of negatively chirped XUV pulses and for the reflection of several high-order harmonics with different emission times. Use of aperiodic multilayer structures is indispensable for further decrease in the pulse duration and increase in the focused pulse intensity in the XUV spectral region.

References

1) R. Kienberger *et al.*, Nature **427**, 817, 2004
2) Y. Mairesse *et al.*, Science **302**, 1540, 2003
3) V.G.Kapralov, R.Korde, V.E.Levashov, A.S.Pirozhkov, E.N.Ragozin, Quantum Electron. **32**,149, 2002
4) V. E. Levashov, K. N. Mednikov, A. S. Pirozhkov, E. N. Ragozin, Plas. Phys. Reports **30**, 149, 2004
5) J. F. Meekins, R. G. Cruddace, H. Gursky, Appl. Opt. **25**, 2757, 1986; *ibid* **26**, 990, 1987
6) K. D. Joensen, Proc. SPIE **3113**, 500, 1997
7) E.Ziegler, I.N.Bukreeva, I.V.Kozhevnikov, A.S.Pirozhkov, E.N.Ragozin, Proc. SPIE **3737**, 386, 1999
8) N. N. Kolachevsky, A. S. Pirozhkov, E. N. Ragozin, Quantum Electron. **30**, 428 2000
9) I. L. Beigman, A. S. Pirozhkov, E. N. Ragozin, JETP Lett. **74**, 149, 2001
10) I. L. Beigman, A. S. Pirozhkov, and E. N. Ragozin, J. Opt. A: Pure Appl. Opt., **4**, 433, 2002
11) A. V. Vinogradov, ed., X-Ray Mirror Optics, Leningrad: Mashinostroenie, 1989
12) R. Soufli and E. M. Gullikson, Proc. SPIE **3113**, 222, 1997, http://cindy.lbl.gov/optical_constants/
13) S. V. Bulanov, T. Esirkepov, T. Tajima, Phys. Rev. Lett. **91**, 085001, 2003

4.7.12 Generation of silicon tadpoles by fs high intensity laser ablation

Hirozumi AZUMA[a)], Hiroyuki DAIDO, Nobuo KAMIYA[a)]. Tadashi ITO[a)], Michiaki MORI, Kouichi OGURA, Akito SAGISAKA, Satoshi ORIMO, Akihiro TAKEUCHI[a)], Noritomo SUZUKI[a)], Yukio HAYASHI, Hisanao HAZAMA, Koji MATSUKADO[b)], and Atsushi FUKUMI[b)]

[a)]TOYOTA Central Research and Development Lab. [b)]National Institute of Radiological Sciences

1. Introduction

It is well-known that different mechanisms of pulsed laser ablation of materials are realized at different laser pulse duration[1)]. For ns laser ablation, amorphous silicon films have been introduced to be piled on the substrate by laser ablation in many papers[2)]. Surface modifications under fs laser irradiation of bulk silicon have been also analyzed for laser pulse duration from 5 to 400 fs, but a few information of ablators has been obtained[3,4)]. On the other hand, by using silicon substrates in the oven at more than 800K, silicon nano-wire has been created successfully[5)]. However the growth rate of silicon nano-wire is not high. The industrial production of silicon nanofibers or nanotubes has been expected as high efficiency photo-voltaic devices, emitter devices, and LSI devices.

2. Experimental

High purity silicon wafers were used as silicon targets. The pulsed laser of 800 nm wavelength, the pulse duration of 50 fs, the repetition rate of 10 Hz, and the energy of 10 mJ, delivered from the Ti-Sapphire laser system were used. The focused laser beam on the silicon target was about 20 μm-spot in diameter by the off-axis parabola mirror mounted in the vacuum chamber. Irradiated intensity of the laser beam on the target was estimated to be approximately $8x10^{16}$ W/cm^2. Scattered ablated particles were collected by the copper mesh and the copper mesh with carbon thin films mounted in the vacuum chamber under $2.6x10^{-4}$ Pa. Scattered ablated particles on the silicone substrate were collected by the replica method. The distance between the target and the copper mesh was about 130 mm. Ablated particles or fibers were observed by the transmittance electron microscope (TEM).

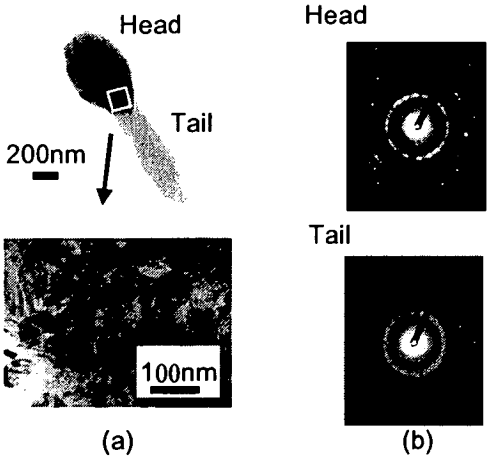

Fig. 1 A TEM image(a) and diffraction patterns(b) of the silicon tadpol

3. Results

In the ablated particles on the silicon substrate, many particles like tadpoles were observed, while in the ablated particles on the carbon thin films, smaller sized fibers than those on the silicon substrate were observed. On the other hand, the head of the tadpole was about a few hundred nm in the diameter and the tail was 200 nm in the width and more than a few hundred nm in the length. Clear grain images were observed in the head of the tadpole but not in the tail (Fig. 1(a)). In the electron diffraction pattern (Fig. 1(b)) at the head of the tadpole, many clear diffraction spots, caused by multi-crystalline structure, were observed. Each spacing of lattice plane calculated from this diffraction pattern was correspondent to the d-value of silicon plane of (111), (220), and (311). In the electron diffraction pattern at the tail of the tadpole, two diffuse diffraction rings, caused by amorphous or micro-crystal structure, were observed.

References and Notes

1) J. Kruger et al., Appl. Surf. Sci. **129**, 892, 1998
2) M. K. Spyridaki et al., Appl. Phys. Lett. **83**, 1474, 2003
3) G. Dumitru et al., Appl. Surf. Sci. **222**, 226, 2004
4) S. Amoruso et al., Appl. Phys. Lett. **84**, 4502, 2004
5) D. T. Colbert et al., Science **266**, 1218, 1994

4.7.13 Research using an ultrafast spectroscopy: derivation of the time-resolved fluorescence spectrum at t=0 of a solution and so on

Hiroshi Murakami

The purpose of our research is to develop ultrashort pulsed sources in the wavelength range from X-ray to THz using a high peak femtosecond laser and to study the dynamics in complex condensed systems such as solutions and proteins by a pump-probe spectroscopy using those sources. What we have done this year is as follows:

1. We have set up CPA laser systems in experimental rooms 222 and 202. The performances obtained are ~0.5mJ/pulse and ~200 fs (FWHM) at the central wavelength of 800 nm and at 1 kHz repetition for the system in room 222, and ~2 mJ/pulse and ~60 fs (FWHM) at 790 nm and 10 Hz repetition for the system in room 202. These laser systems will be used for developing new pump-probe systems.
2. We have developed a system for 100 ps-time-resolved fluorescence measurement using a time-correlated single-photon counting method to make us measure fluorescence spectra up to a microsecond time region.
3. We have obtained the time-resolved fluorescence (TRF) spectrum at t=0, i.e., just after an optical pulse excitation, of a coumarin dye in an ethanol/methanol mixture.

Here, we describe the result of the last part in the above list. In the preceding years, we have developed a fluorescence up-conversion system combined with a vibrating cryostat using liquid nitrogen and applied it to dye solutions [1]. Although the TRF spectrum of such systems provides information on the energy relaxation in the electronic excited state of the solute molecule, it is necessary to obtain the TRF spectrum at t=0 in order to discuss the energy relaxation process quantitatively. However, even if a deconvolution procedure is done successfully with the instrumental response function of the experimental system and the TRF spectrum at t=0 is derived formally, it is difficult to determine whether the spectrum is valid or not, because the fluorescence up-conversion system used has a temporal resolution of ~150fs. Hence, we need other landmark for determining it, and so employed a method proposed by Fee et al.[2]. This method needs no time-resolved measurements, but is based on steady state ones. The TRF spectrum at t=0, $F(\nu)$, of a solute molecule dissolved in a polar liquid such as a dye molecule in alcohol is calculated from $F(\nu) = \int g(\nu_{ex} - \delta)p(\delta)f(\nu - \delta)d\delta$ as a line-shape function, where $g(\nu)$ and $f(\nu)$ are the line-shape functions of the steady-state absorption and fluorescence spectra of a free solute molecule without any interaction with the others, respectively, $p(\delta)$ the site-energy distribution function, and ν_{ex} the excitation energy. Since the steady-state absorption spectrum of the polar solution, $A(\nu)$, is expressed as $A(\nu) = \int g(\nu - \delta)p(\delta)d\delta$, $p(\delta)$ is obtained through this expression by measuring $A(\nu)$. In this method, the absorption and fluorescence spectra of a free molecule without any interaction are replaced with those of the molecule dissolved in a non-polar solvent, because the interaction between a solute and solvents responsible for the time-dependent change of the TRF spectrum, which starts after an abrupt change of the electronic configuration of the solute molecule due to light irradiation, is largely a dipole-dipole interaction. The TRF spectrum at t=0 of a coumarin dye in an ethanol/methanol mixture at 296 K is shown as a typical example in Fig.1, together with $A(\nu)$, $g(\nu)$, $f(\nu)$ and $p(\delta)$. Isopentane was used as a non-polar solvent. It has been found from this method in the temperature range from 296 K to 170 K that the peak energy of the TRF spectrum at t=0 shows almost no temperature dependence if the same excitation energy is employed, and is nearly the same with that obtained from the TRF measurement. Therefore, the deconvolution procedure is considered to go well in this case. Since we can measure the TRF spectrum at $t = \infty$, i.e., in the thermal equilibrium in the electronic excited state, by the system described in the second part in the above list now, we will discuss the energy relaxation in detail [3].

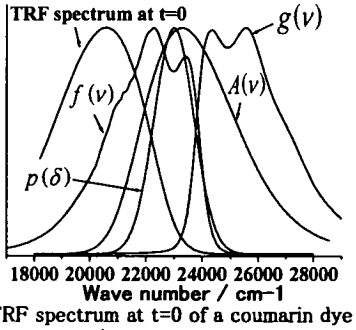

Fig.1. TRF spectrum at t=0 of a coumarin dye in an ethanol/methanol mixture at 296 K

References

1) H. Murakami, J. Mol. Liq. **89**, 33, 2000 ; J. Lumin. **102**, 295, 2003.

2) R. S. Fee and M. Maroncelli, Chem. Phys. **183**, 235, 1994.

3) H. Murakami and M. Tanaka, Slow Dynamics in Complex Systems: 3rd International Symposium, ed. by M. Tokuyama and I. Oppenheim, 739, 2004.

5. Synchrotron Radiation Science

Jun'ichiro MIZUKI

The following 6 research fields and an experimental facility development field were studied in FY2003 in the Synchrotron Radiation Research Center.

In the experimental facility development field, we developed a muti-crystal switching system on a cryogenically cooled monochromator to endure the energy range from 6 keV to about 70 keV at BL-11XU. We installed a monochromator stabilization system, so called MOSTAB, at BL-22XU to keep the beam intensity and the position constant as good as possible.

In the materials science at high pressure, a single crystal synthesis of GaN under high pressure and high temperature has been progressed. The phase diagram of GaN for a pressure and temperature range of 0-10 GPa and 300-2550 K was determined by in-situ X-ray diffraction study. This reveals that GaN melts above 6GPa and 2500 K without decomposition. Other metal nitride, such as $Al_XGa_{1-X}N$, also becomes a target to synthesize by the same idea. Structural studies on a Ca-Yb 1/1 approximate crystal and CoS_2 under pressure and low temperature were carried out, and new structural phase transitions were found for the first time in these systems. The multi-anvil apparatus for high pressure study was installed at BL-22XU, which was constructed in 2002. This press is capable of generating pressures up to 12 GPa and temperatures up to 1,500℃, with which X-ray radiography and angle-dispersive X-ray diffraction can be carried out.

In the field of the structural physics in materials, the surface structure of GaAs(001) under MBE crystal growth condition were studied at various temperatures to elucidate the growth mechanism in atomic level. The local structural change of Pd-containing perovskite catalyst was investigated under a real automobile engine condition by an energy dispersive XAFS technique. The reversible structure change, which corresponds to the movement of Pd, was observed to occur within a few seconds. TiO_2 known as a photocatalyst was found to show the catalytic activity also by irradiation of X-rays. The phonon properties of high temperature superconducting copper oxides were studied as a function of hole doping level in $La_{2-x}Sr_xCuO_4$ by inelastic X-ray scattering with about 6 meV energy resolution. Clear one-to-one correspondence between the LO- bond stretching phonon anomaly and the T_C was observed. The domain controlled $BaTiO_3$ of a ferroelectric material was suited by X-ray topography to reveal domain-domain correlation.

In the research field of surface chemical reaction the oxidation process of Cu and Si were studied by in-situ X-ray photoemission spectroscopy with a hyperthermal O_2 molecular beam and O_2 gas. Also oxidation reaction dynamics on several materials were studied as a nanotechnology research project. Hexagonal BN was grown epitaxially on Si(111), and the electronic properties were investigated by near edge X-ray absorption structure spectroscopy. Ultra-thin SiC film was synthesized, and its electronic properties and structure were investigated by X-ray photoelectron spectra and near edge X-ray absorption spectra.

In the field of heavy element materials, we developed a pulsed magnet up to 30 Tesla for studying the strongly correlated electron systems under magnetic fields by X-ray diffraction and spectroscopic methods at BL-22XU. The charge gap excitations of the high T_C superconductor, $YBa_2CuO_{7-\delta}$ were observed by resonant inelastic X-ray scattering, and compared with those of other high T_C families to discuss the relation between superconductivity and charge excitation. The speckle diffraction for studying the dynamics of nano-scaled domains was observed successfully. This promises the future progress for investigation of the nano-domain dynamics. $UNiGa_5$ was studied by resonant X-ray diffraction to investigate the magnetic and electronic properties. The scanning type synchrotron radiation Moessbauer microscope was much improved by upgrade of the optics.

In the research field of electronic materials science, the electronic structure of $CuIr_2S_4$ was investigated by a photoemission spectroscopy to understand the mechanism of a metal-insulator transition from the electronic structure point of view. Uranium compound $UFeGa_5$ was studied by an angle-resolved photoemission spectroscopy to reveal the 5-f state in this compound. Mn-doped GaAs, which is a candidate material for spintronic devices, and perpendicular magnetic film (Co/Pd)n were studied by an XMCD spectroscopy to reveal the Mn electronic states and the role of the Co electronic state, respectively. Pulsed Laser Deposition (PLD) system was installed in the side station at BL-23SU to study the various oxides thin film with smooth and clean surface. Soft X-ray emission spectroscopy was applied to polycyclic aromatic hydrocarbons to extract the information on the chemical bonding states.

In the field of synchrotron radiation simulation research, in order to clarify the origin of the magnetic resonance X-ray diffraction intensity in UGa_3 observed in the experiment, a band structure calculation based on the density functional theory was done. The theoretical analysis of the resonant inelastic X-ray scattering in insulating cuprates was performed and was able to reproduce the characteristic spectral properties observed experimentally.

5.1 Beamline and Experimental Facilities Development

Taikan HARAMI

In the experimental facility development field, we operated four JAERI beamlines and continued to upgrade them in order to carry out the synchrotron radiation research of JAERI items. BL22XU for the quantum structure physics started to be operated for the experiments. To measure the beam vibration which originates from the temperature change in the circulating liquid nitrogen for cooling the crystal of the optics, the MOSTAB was installed to feedback the beam intensity and the beam position to the optical crystal angle. The variation of the intensity and the position change succeeded to suppress less than 0.1% and less than 1μm, respectively. In the material science beamline BL11XU, the cryogenically cooling system for the monochromator crystal was introduced instead of the water cooled diamond crystal. The monochromator crystal has a multi-crystal switching system which is composed of Si(111) and Si(311) diffraction plane crystals which cover at least the energy range of 6～70keV. The intensity increased by 3～4 times than before and it could take only 30 minutes to switch the crystal diffraction plane. In the material science bending beamline BL14B1 and BL11XU, MOSTAB is under consideration to be installed. In the heavy element science beamline BL23SU, the performance the optical device decreased due to the carbon contamination in the long use. The grating monochromator and mirrors were washed in the surface and installed again. The intensity and resolution was recovered.

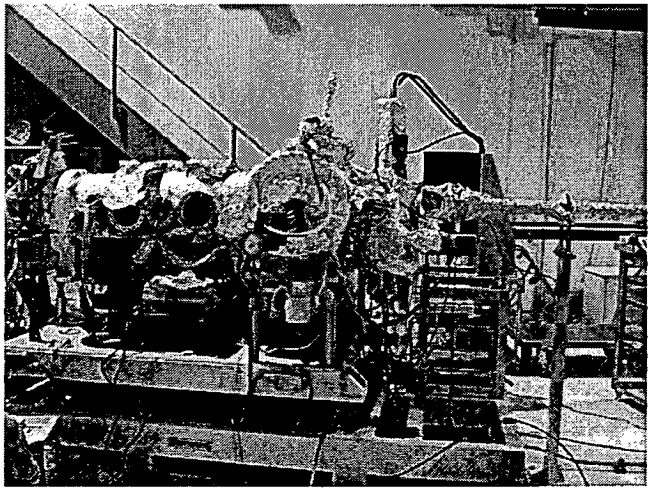

Fig. 1 The grating monochromator of BL23SU in which the contaminated carbon was washed away.

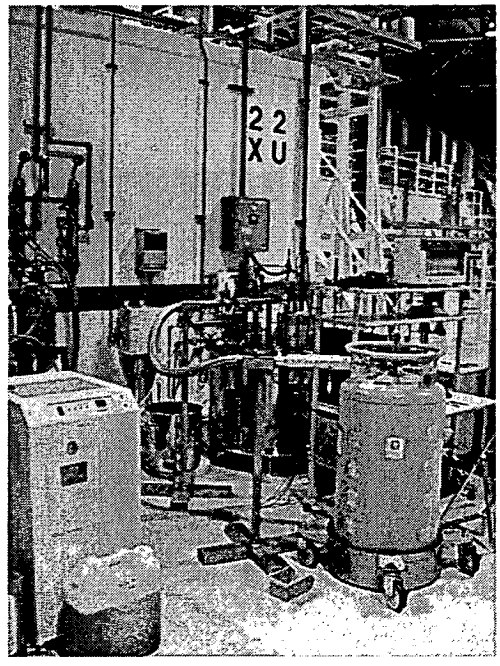

Fig. 2 The liquid nitrogen cooling system for the bouble crystal monocromators in which the MOSTAB systems were installed.

5.1.1 Performances of the multi-crystal switching system on the cryogenically cooled monochromator on BL11XU at SPring-8

Hideaki SHIWAKU, Takaya MITSUI, Kazukiyo TOZAWA* and Koji KIRIYAMA
*present address: Ishikawajima-Harima Heavy Industries Co.,Ltd. (IHI)

1. Introduction

We introduced a cryogenically cooling system for a monochromator and developed a multi-crystal switching system on a cryogenically cooled monochromator of the JAERI materials science beamline, BL11XU at SPring-8[1-2]. In order to make progress in our science, it is necessary to ensure at least the energy range of 6 ~ 70 keV which is achieved by employing Si(111) and Si(311) crystals.

2. Multi-crystal switching system

The principle of the crystal switching system is shown in Fig. 1. Two crystals are arranged side by side, and they are translated in the horizontal direction for exchanging the crystals.

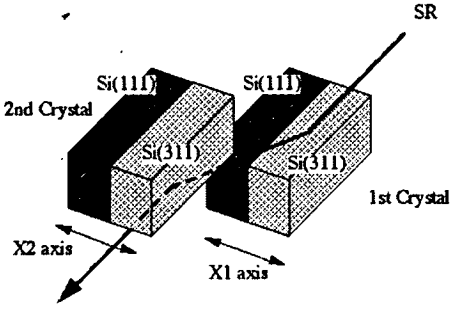

Fig. 1 A principle layout of the multi-crystal switching system

3. Performances

In order to check that ±20 mm movement of the X-axis stage does not affect the center of gravity of the 1st crystal unit, the straightness of the Y-axis translation stage was measured, as shown in Fig. 2. The pitching and yawing of Y-axis translation stage were 5 seconds, respectively. The influence by the movement of the X-axis stage cannot be found.

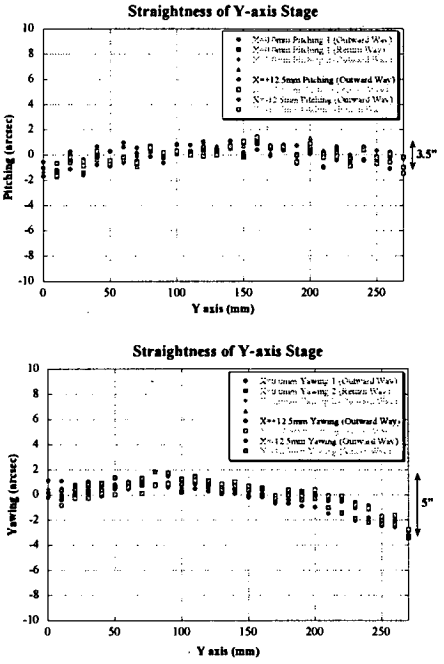

Fig. 2 Straightness of Y-axis translation stage

Figure 3 shows a relationship between FWHM and Energy. FWHM of the Si (111) crystal agrees well with theoretical value. But, FWHM of the Si (311) crystal was extended by 1.1 ~ 1.5 arcsecond than the theoretical value. According to observation of the x-ray intensity after the monochromator, it turned out that the intensity vibrated in the cycles of about 15 seconds and in a cycle of several minutes. It is considered that the crystal can be vibrating due to the flow of liquid nitrogen. It is necessary to remove the relative large periodic vibration and to stabilize x-ray intensity.

In comparison with a previous indirect water-cooling diamond (111) crystal monochromator, this monochromator provides 7.4 times higher flux intensity at 14.4 keV. It takes only 5 minutes to exchange and adjust the crystals. The stabilization of the x-ray from the monochromator is expected.

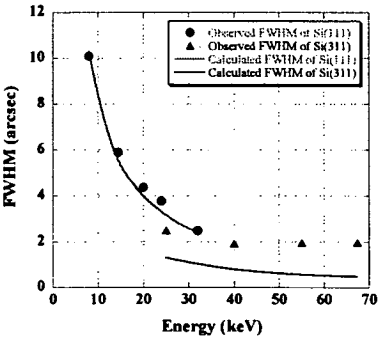

Fig. 3 FWHM vs. Energy

References

1) H. Shiwaku, T. Mitsui et al., AIP Conference Proc. #705, 659 (2004)
2) K. Tozawa, H. Shiwaku et al., AIP Conference Proc. #705, 671 (2004)

5.1.2 Beam Stabilization by using MOSTAB System at BL22XU in SPring-8

Takahisa SHOBU and Hiroyuki KONISHI

The position and intensity of the monochromatized beam introduced in the experimental hutch of a beamline may fluctuate over the negligible range by the thermal fluctuation and the mechanical vibration of optical devices, for example, monochromator crystals or mirrors. The former arises from the thermal instability of cooling systems for optical devices, and the latter arises from the mechanical vibration of some beamline components, vacuum pumps, compressors of cooling systems etc. It is important to make effort in order to remove the origin of the beam fluctuation, but it is impossible to achieve that perfectly. MOSTAB (Monochromator Stabilization) is the force system to stabilize the beam intensity or position and is used in some beamlines of SPring-8 recently. This is a feed-back system to retune the monochromator automatically by using a piezo actuator monitoring the position or intensity of the monochromatized beam. We also apply the system at JAERI undulator beamlines with liquid-nitrogen cooled monochromators, BL11XU and BL22XU. In this section, we will introduce the present performance of MOSTAB at BL22XU.

MOSTAB is used only for the beam intensity stabilization at BL22XU at present. An ion chamber set in an experimental hutch is usually utilized to monitor the intensity of the monochromatized beam. But in this case, when a down stream shutter (DSS) is closed and it is impossible to monitor the beam intensity, MOSTAB system may lose the stabilization condition. Then we must stop and restart the MOSTAB system before and after the DSS operation. A new type of the monitor equipment was installed at between the monochromator and the DSS to avoid the cumbersome procedure. A beryllium plate can be supported on the monochromatized beam path in vacuum within the equipment containing a PIN detector. Monitoring the intensity is possible by counting the photons scattered from the beryllium plate with the PIN detector.

Plotting the intensity of the beam monochromatized by the double crystal monochromator versus the output voltage to the piezo actuator controlled the MOSTAB, that is equivalent to the deviation of the parallelism between the two monochromator crystals, the graph exhibits the so-called rocking curve with single maximum point. As the MOSTAB system are monitoring the first deviation of the rocking curve by using a lock-in amplifier, the peak of the rocking curve can be set as the objective intensity for the intensity stabilization. Almost of the modulus of the MOSTAB system are put on the roof deck of the optics hutch. They can be controlled by way of beamline network from each of experimental hutches. The MOSTAB system can be operated by using a friendly GUI (Fig. 1).

The performance of the MOSTAB system is shown in Fig. 2. The measured energy was 25keV and it was the top-up operation of the SPring-8 storage ring. The long-time stability of the monochromatized beam intensity is established with the MOSTAB system.

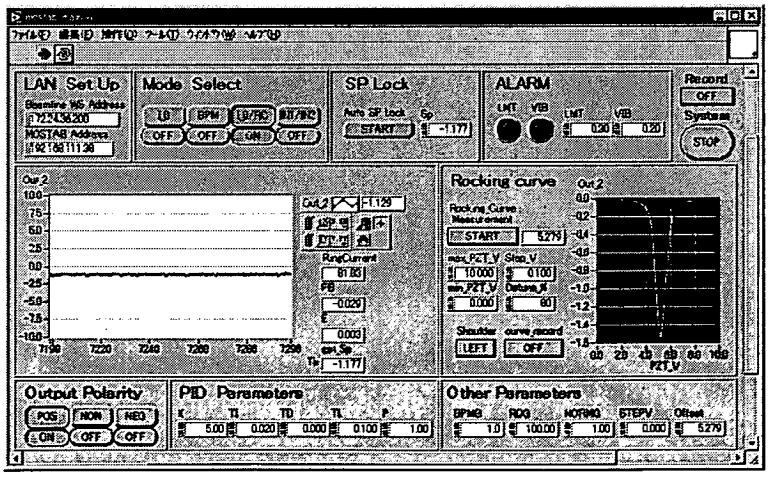

Fig. 1 Graphical user interface (GUI) on the personal computer for the MOSTAB control

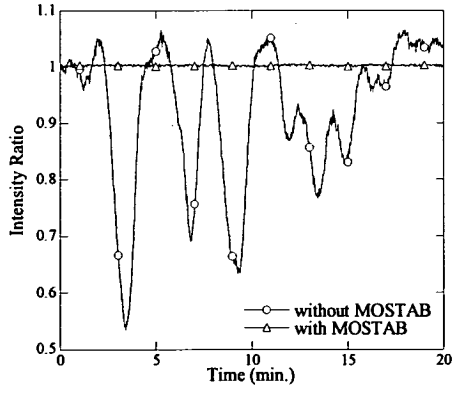

Fig. 2 The long-time fluctuation of the beam intensity with and without MOSTAB

References

1) T. Kudo et al.:J. Jpn. Soc. Synchrotron Rad. Res., 16(2003) 173-177

5.2 High Pressure Science

Katsutoshi AOKI

X-ray diffraction and radiography experiments have been carried out to explore new materials and phenomena at high pressure and high temperature using brilliant light from synchrotron radiation at SPring-8. Synthesis of GaN crystal has been initiated on the basis of our accumulated high-pressure and high-temperature techniques. This challenging research has greatly advanced through this fiscal year and widely impacted on the related research field. The first-order transition in phosphorus has been confirmed more definitely by in-situ image observation of the coexistence state of the two liquid phases. A new concept has been proposed for the nature of liquid.

The phase diagram of GaN has been determined for a pressure and temperature span of 0-10 GPa and 300-2550 K. The crystalline GaN decomposes into Ga metal and N_2 gas by heating at pressures below 6 GPa. At pressure above 6 GPa the crystal melts at 2500 K without decomposition. Single crystals prepared by cooling the melt slowly were found to have high quality in crystallinity from x-ray diffraction and Raman scattering measurements.

X-ray diffractometer was upgraded for precise measurement of high pressure structures and phase transition process with a diamond-anvil type high-pressure cell. Diffraction measurements were made for single crystal of Cd_6Yb alloy and powder sample of CoS_2 for a temperature rang of 4-300 K and a pressure range of 0-20 GPa, revealing structural transformation with lowering symmetry by detecting weak diffraction peaks due to rearrangement crystalline lattices with slight displacement of constituted elements.

X-ray radiography measurement has revealed that the liquid-liquid transition in phosphorous observed at about 1300 K and 1 GPa is well characterized in terms of first-order transition. The phase separation between the low and high density liquids indicates clearly the nature of this transition, suggesting a large difference in density between them in agreement with the previous density measurement.

The experimental results described above have partly been published in major journals, for instance, Nature Materials 2, 735 (2003)、Jpn. J. Appl. Phys. 43, L981(2004) etc.

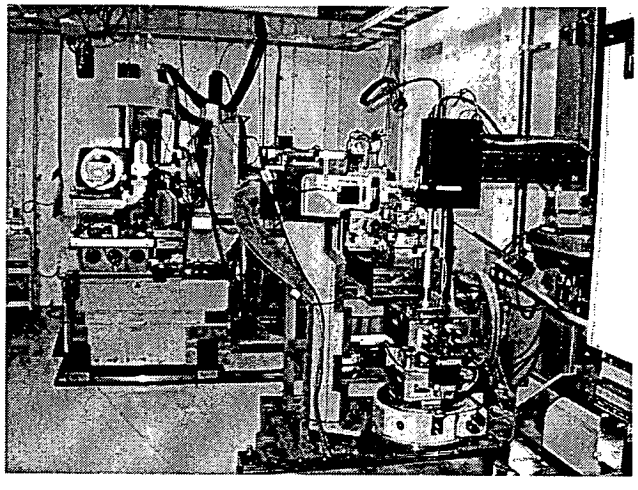

High Pressure Apparatuses at BL22XU
Front: Diffractometer for low temperature and high pressure diffraction measurement with a diamond anvil cell.
Rear: Cubic press for large volume experiment at high temperature and high pressure.

5.2.1 Congruent Melting of GaN at High Pressures and its Application to Single Crystal Growth

Wataru UTSUMI, Hiroyuki SAITOH and Katsutoshi AOKI

1. Introduction

Gallium nitride (GaN) is a very important material in optoelectronic devices for blue light-emitting diodes and lasers. These devices are usually fabricated by epitaxial growth on sapphire substrates because large GaN single crystals are unavailable. There is a large mismatch in the lattice constants of sapphire and GaN, which causes high-density dislocations in the deposited layer and is a major obstacle for improving device quality. Hence, the large single crystals of GaN suitable for substrates are strongly desired. However, such single crystals are difficult to grow because GaN usually decomposes into Ga and N_2 before melting at ambient pressure. Several studies have attempted to alleviate this problem, but have all been unsuccessful in growing large single crystals suitable for the substrates of optoelectronic devices. If high pressure is effective in suppressing the decomposition and meting of GaN at high temperatures, a new method for the single crystal growth of GaN is expected to be developed. In order to clarify the decomposition and melting behaviors of GaN under high pressures and temperatures, in situ X-ray diffraction experiments were carried out. The congruent melting of GaN, which occurred above 6.0 GPa and 2215° C, was confirmed for the first time.

2. Experimental

The experiments were performed using a multi-anvil high-pressure apparatus installed on beamline BL14B1 at the SPring-8. The pressure was initially increased at room temperature and then the temperature was increased under a constant applied load. The in situ powder X-ray diffraction profiles of GaN were obtained for each pressure/temperature condition by the energy-dispersive method using a white synchrotron radiation beam.

3. Results

Figure 1 summarizes the decomposition and melting behaviors of GaN determined by the present study in the pressure-temperature diagram. At pressures less than 5.5 GPa, GaN decomposed into Ga and N_2 gas, and the decomposition temperature almost linearly increased with pressure (solid circles). In contrast, at pressures higher than 6.0 GPa, congruent melting occurred at around 2220°C (solid triangles), and its pressure dependence is very small.

This result leads to a new method of providing bulk single crystals of GaN by slow cooling of its stoichiometric melt under high pressures. Single crystals of GaN with a diameter of 100 μm have been obtained successfully from 6.8 GPa and 2400°C. The X-ray rocking curve and the Raman spectrum of the specimens indicate that they are high-quality single crystals with very low dislocation density.

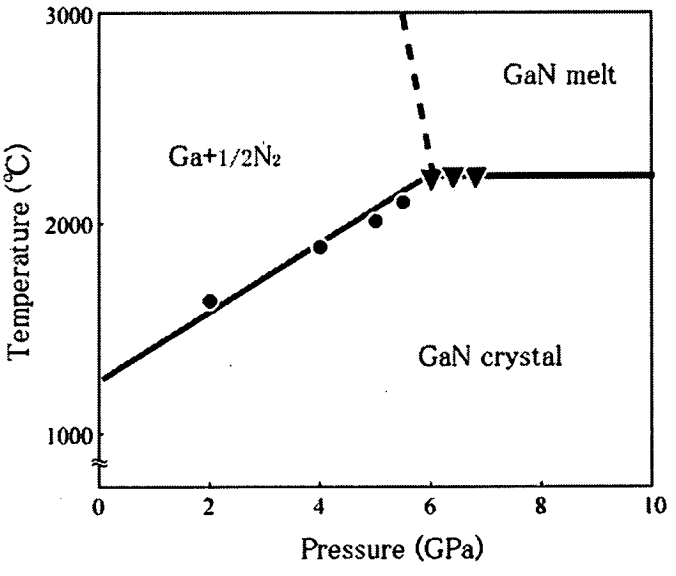

Fig. 1 The phase diagram of GaN under high pressure and temperature
Solid circles and triangles denote the pressure/temperature conditions where GaN decomposed and congruent melting occurred, respectively.

Reference

W. Utsumi et al., Nature Materials 2, 735 (2003)

5.2.2 Synthesis of polycrystalline $Al_xGa_{1-x}N$ under high pressure

Hiroyuki SAITOH, Wataru UTSUMI and Katsutoshi AOKI

1. Introduction

$Al_xGa_{1-x}N$ semiconducting alloy is an indispensable material for ultraviolet light-emitting diodes and lasers due to its wide direct band gap energy, which can be changed from 3.4 to 6.4 eV with variation of the atomic composition. However only thin films of $Al_xGa_{1-x}N$ are available and no bulk specimens are obtained. This is because GaN decomposes into gallium metal and nitrogen gas at high temperature. In our previous study, we found that applying high pressure prevents the decomposition[1]. It is also expected that high pressure is potential technique for synthesizing bulk $Al_xGa_{1-x}N$ alloys[2].

2. Experimental

Experiments were carried out using a DIA type high-pressure apparatus (SMAP2) installed on the beam line BL14B1 at SPring-8. Highly pure, fine powders of GaN and AlN were used as the starting materials. These powders were blended for suitable compositions (x=0.0, 0.2, 0.4, 0.6, 0.8, 1.0, for $Al_xGa_{1-x}N$) and compacted in disk shapes (1.0 mm in diameter and 1.0 mm in height). A disk sample was put into a capsule made of polycrystalline hexagonal boron-nitride. The capsule was then placed in a cubic pyrophillite pressure medium along with a graphite heater.

3. Results

Figure 1 shows *in-situ* x-ray diffraction profiles of powdered mixture of AlN and GaN (x=0.6) at 6.0 GPa with increasing temperature. The dashed lines show the peak positions of pure GaN at 6.0 GPa and 600°C. At 600°C, pairs of peaks form AlN and GaN with the same Millar indices appeared side by side. When the temperature increased to 1000 and further to 1200°C, the GaN peaks shifted to higher energies, and at 1400°C the pairs of peaks became single peaks. Alloying process was completed and solid-solution was formed.

The lattice constants of recovered polycrystalline samples were measured by an x-ray micro diffractometer. Figure 2 shows the relationship between the nominal concentration x and the lattice constants of the samples. Both lattice constants "a" and "c" continuously varied with the mixing ratio. This implies that the solid solution of AlN and GaN was formed over the whole atomic composition.

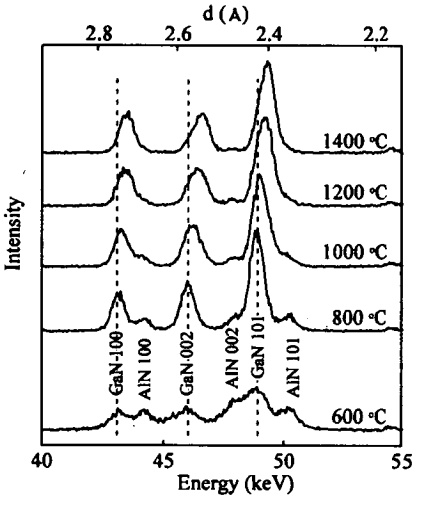

Fig. 1 A series of x-ray diffraction profiles of AlN and GaN with increasing temperature at 6.0 GPa

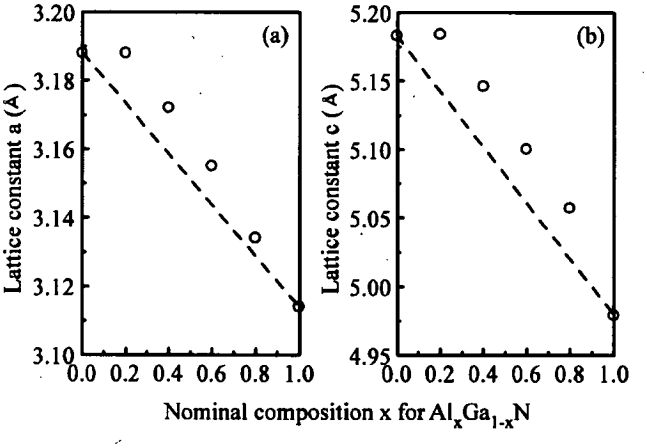

Fig. 2 Nominal composition versus lattice constant of "a" (a) and "c" (b) at ambient conditions

References

1) W. Utsumi, H. Saitoh, H. Kaneko, T. Watanuki, K. Aoki and O. Shimomura, Nature Materials **2**, 735, 2003

2) H. Saitoh, W. Utsumi, H. Kaneko and K. Aoki, Jpn. J. Appl. Phys. **43**, L981, 2004

5.2.3 Various pressure-induced phases of Cd-Yb 1/1 approximant

Tetsu WATANUKI, Akihiko MACHIDA, Tomohiro IKEDA, Katsutoshi AOKI,
Taku J. SATO[a)] and An Pang TSAI[a)]
a) NIMS

1. Introduction

Cd-Yb 1/1 approximant crystal has a cluster-like local structure which is also found in Cd-Yb icosahedral quasicrystal. Recently, Tamura et al. have revealed that this approximant crystal (bcc structure) undergoes a structural phase transition at low temperature of 110 K [1]. It is considered that an ordered state about the orientation of the cluster-like structure is formed in the low temperature phase. We considered that compressing this low temperature phase would create other new ordered states, because applying pressure can change the correlation between the cluster-like structures. So, we searched pressure induced new structural phase by means of single crystal X-ray diffraction experiments under pressure.

2. Experimental

We carried out single crystal X-ray diffraction experiments of Cd-Yb 1/1 approximant crystal under pressure up to 5.2 GPa in the temperature region between 50 – 300 K at SPring-8 BL22XU. The sample was sealed in a diamond anvil cell (DAC) with a methanol/ethanol pressure medium. X-ray oscillation photographs, recorded on an imaging plate, were taken at each pressure-temperature point by changing temperature under constant pressure condition. Applying pressure was changed only at 300 K in order to avoid the compression in a solidified pressure medium.

3. Results

Figure 1 shows the phase diagram of Cd-Yb 1/1 approximant crystal which is determined by analyzing the pattern of super-lattice reflections. We found 4 or 5 new pressure induced phases up to 5.2 GPa where the lattice shrinks only by 3%, which indicates that the arrangement of the cluster-like structures forms various ordered states even by slight change of the atomic packing. Some of these phases form distorted cubic lattice structure, so, now, we consider that the occurrence of such various phases is caused by the combination of orientation order of cluster-like structures and the distortion effect of the cubic lattice.

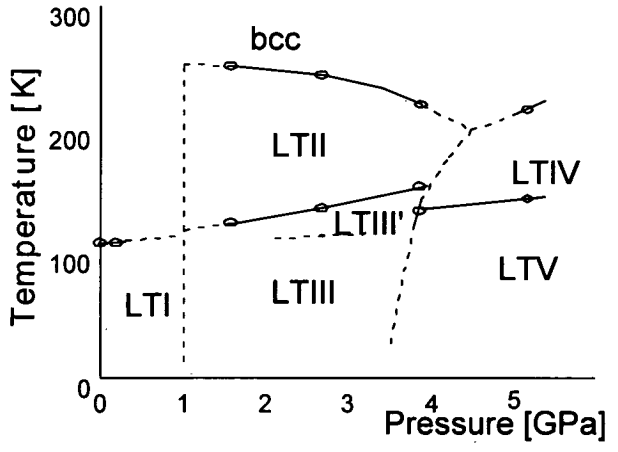

Fig. 1 Pressure-temperature phase diagram of Cd-Yb 1/1 approximant crystal

References

1) R. Tamura et al., Jpn. J. Apple. Phys. 41 (2002) L524

5.2.4 Structural property of pyrite type CoS_2 under high pressure and low temperature

Akihiko MACHIDA, Tetsu WATANUKI, Tomohiro IKEDA, Katsutoshi AOKI, Yutaka MORITOMO[a)]
a) Department of Applied Physics, Nagoya University

1. Introduction

Pyrite type cobalt disulfide CoS_2 shows transition into ferromagnetic state at low temperature below T_C~120 K. The transition is not accompanied by volume change and hence characterized as second-order one. At high pressures above ~0.4 GPa, the nature of transition was found to change from second-order to first-order[1)]. We have measured x-ray powder diffraction patterns under high pressure and low temperature using synchrotron radiation (SR) to investigate the relation between the crystal structure and the nature of magnetic transition.

2. Experimental

Single crystals of CoS_2 synthesized by the flux method were crushed into fine powder for high pressure x-ray diffraction measurement. The powder was loaded into the sample chamber of a diamond anvil cell (DAC) with methanol/ethanol (4:1) mixture used as pressure medium. Pressure was determined by the ruby fluorescence method. X-ray powder diffraction patterns were recorded with an imaging plate detector mounted on a diffractometer constracted for high pressure measurement with DAC at SPring-8 BL22XU. The incident x-ray beam monochromaitized with Si(111) double crystals to a wavelength of 0.496 A (E~25 keV) was emploied. For high pressure and low temperature experiments, the gas driven DAC was cooled in a closed-cycle He-gas refrigerator and the sample pressure was chaned outside by controlling He gas. We measurd diffraction paterns across the magnetic transition along isbar lines at ~2 GPa and ~4 GPa, and an isothermal line at 50 K.

3. Results

Obtained powder patterns were analyzed with a cubic structure (*Pa*-3; *Z*=4) by RIETAN-2000 program[3)]. Figure 1 shows the temperature dependence of the lattice constant at ~2 GPa. Downward arrow indicates the Curie temperature T_C determined by Goto *et al.*[1)]. With decreasing temperature, the lattice constant decreases initially and then increases abruptly at ~110 K. The lattice constant measured at ~4 GPa showed a similar variation with temperature at ~90 K. It is considered that the anomaly in the lattice constant is caused by the magneto-volume effect accompanied with the ferromagnetic transition.

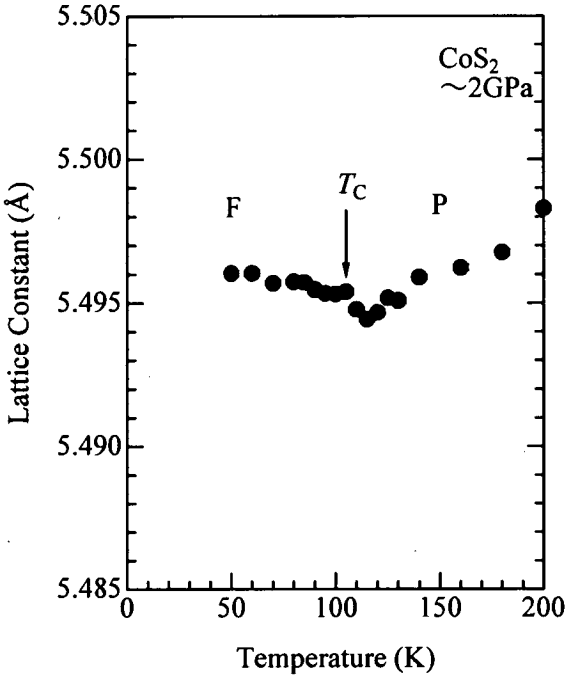

Fig. 1 The temperature dependence of the lattice constant of CoS_2 at ~2 GPa
Downward arrow indicates the Curie temperature T_C. F and P represent ferromagnetic and paramagnetic regions, respectively.

References

1) T. Goto, Y. Shindo, H. Takahashi, and S. Ogawa, Phys. Rev. B **56**, 14019, 1997
2) A. Machida *et al.*, unpublished
3) F. Izumi *et al.*, Mater. Sci. Forum **321-324**, 198, 2000

5.2.5 Installation of a cubic-type multi-anvil press on BL22XU

Yoshinori KATAYAMA, Yasuhiro INAMURA, Kazuhiko TSUJI[a)], Takanori HATTORI[a)],
Satoru URAKAWA[b)], Osamu OHTAKA[c)]

a) Department of Physics, Faculty of Science and Technoroly, Keio University
b) Department of Earth Sciences, Faculty of Science, Okayama University
c) Department of Earth and Space Science, Faculty of Science, Osaka University

1. Introduction

Construction of a new beamline, BL22XU JAERI Actinide Science II, was completed in 2002. The beamline has a high-pressure station in the experimental hall in addition to a station in the RI laboratory. The high-pressure station is shared by two diffractomators, one for diamond anvil cells and the other for a cubic-type multi-anvil apparatus. Here we report the installation of the multi-anvil apparatus.

2. Equipments

BL22XU is an undulator line, which equips two sets of double-crystal monochromator with different tunable energy range. The high-energy monochromator provides x-rays up to 70 keV. The high-energy x-ray is useful to collect diffraction data of non-crystalline materials in wide wave-vector range. It is also useful for studies of heavy elements that strongly absorb low-energy x-ray. The cubic-type multi-anvil apparatus, SMAP180 (SPring-8 Multi-Anvil Press with maximum load of 180 ton), was moved from BL11XU. This press is capable to generate pressures up to 12 GPa and temperatures up to 1500°C. With this press, angle-dispersive x-ray diffraction (ADX) measurements and density measurements by means of x-ray absorption are possible. The ADX method has the advantage of accuracy and resolution over energy-dispersive x-ray diffraction method, which is commonly used for multi-anvil presses. However it has disadvantage of very long data acquisition time. Bright x-ray from the undulator source greatly reduces measuring time and makes ADX method practical. A radial slit system which consists of a set of 35 collimators further improved the efficiency[2)]. A new radial slit system with micrometers was installed and it reduced the time for the adjustment. Diffraction pattern is collected using an imaging plate (IP). For real-time observation, a CCD camera with an x-ray image intensifier can be used. For absorption measurements, two ionization chambers are used.

3. Results

Figure 1 shows diffraction pattern of SiO_2 glass, 2.0mm in diameter, inserted in pressure-transmitting medium made of mixuture of boron and epoxy. The measurements were carried out at room temperature and 1 bar. The energy of the x-ray is 68.5 keV. The pattern (a) was measured without the radial slit system and the pattern (b) was measured with it. It is clear that the radial slit system successfully eliminates background x-rays except for those at low-angle region. Thanks to the high-energy x-ray, the wave-vector region is extended to about 16 $Å^{-1}$. Using this system, diffraction studies of liquid II-VI and I-VII compounds under high pressure and density measurements of glassy silicate were carried out in 2003.

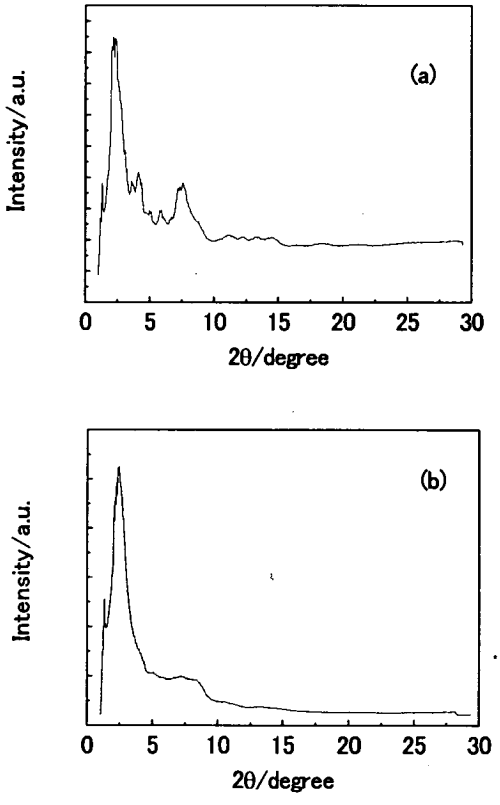

Fig. 1 Diffraction data of SiO_2 glass
(a) without radial slit system
(b) with radial slit system.

References

1) K. Yaoita, et al., Rev. Sci. Instrum. **68** (1997) 2106.
2) Y. Katayama, et al., J. Synchrotron Rad., **5** (1998) 1023.

5.3 Structural Physics Research

Structural Physics Group
Group leader
Jun'ichiro MIZUKI

The major research purpose of the structural Physics Group is to investigate (1)structural aspects of relevant surfaces and interfaces, where one encounters crystal growth of compound semiconductors by MBE, and electrochemistry, (2)close relation between structures and catalytic activities, (3)dynamics of transition metal oxides, in which the interplay between spin, charge and orbital degrees of freedom is the key ingredient underlying the physics, (4)micro-domain structures in ferroelectronic materials. Also, since exploiting the full potential of the SPring-8 remains a permanent challenge for the experimentalist, we have been working on the focusing monochrometer crystal/system for the bending magnet beamline. Thus, a final goal of our group is to make the rational design of new materials with specific properties by investigating the relationship between the static and dynamical structure of the materials and their properties.

In this chapter, we will show the recent results regarding to (1) ~ (4). As surface and interface researches, crystal growth study under non-equilibrium condition will be presented. The present work is concerning to the surface structure of GaAs(001) under MBE crystal growth condition. As the study of the structure- catalytic activity relationship, we focus on a perovskite catalyst as an automotive emission control and a photocatalyst to investigate photo electrochemical reaction based on electronic and atomic structure information. Last year we found the mechanism of the long live activity of $LaFe_{0.57}Co_{0.38}Pd_{0.05}O_3$, which is a Pd-containing perovskite catalyst, by ex situ XAFS experiment. Here, in order to know the real world for the catalyst, we will show how the structure changes with reduction and oxidation fluctuation by using the energy dispersive XAFS technique. TiO_2 as a photocatalyst is newly found as a high energy radiation catalyst. We will show the anodic current under X-ray irradiation to TiO_2 in the present report. As an example of (3), inelastic X-ray scattering was carried out to study the phonon properties of high T_C superconducting copper oxides. The evolution of phonon anomaly as a function of hole doping level in $La_{2-X}Sr_XCuO_4$ will be presented, and discuss this with relation to the superconductivity. As an example of (4) a ferroelectric material, $BaTiO_3$, with micro-domains was studied by X-ray topography to investigate domain-domain correlation.

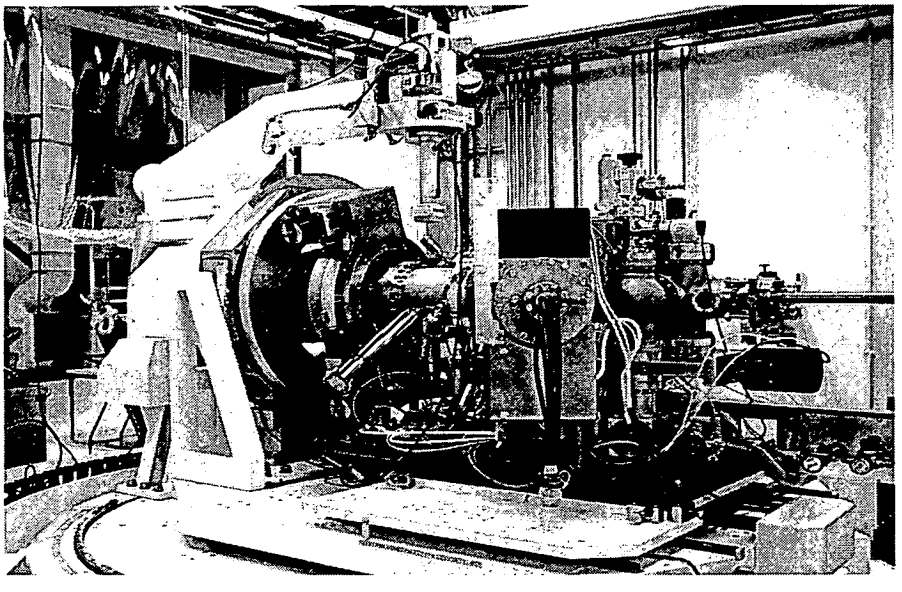

***In situ* X-ray diffractometer with the Molecular beam epitaxy (MBE) chamber system in BL11XU**

5.3.1 Crystal structure of Pd-perovskite catalyst in redox fluctuating atmosphere V

Yasuo NISHIHATA, Jun'ichiro MIZUKI, Hirohisa TANAKA[a)], Mari UENISHI[a)], Masashi TANIGUCHI[a)], Kazuo KATO[b)] and Tomoya URUGA[b)]

a) Materials R&D Div., Technical Center, Daihatsu Motor Co., Ltd.

b) Japan Synchrotron Radiation Research Institute

1. Introduction

Pd-containing perovskite oxides are applied to control automotive emissions as three-way catalysis. We already demonstrated using x-ray anomalous diffraction (XAS) and x-ray absorption fine structure (XAFS) techniques that the Pd-perovskites have self-regeneration function due to the structural responses to the redox fluctuation in exhaust-gas composition: Pd reversibly moves into and out of the perovskite lattice to suppress the metallic particle growth[1,2]. The catalytic activity hardly deteriorates for a long use. However, previous x-ray measurements were not conducted *in situ*. The samples were alternatively exposed oxidative and reductive atmospheres for a period of 1 hour. This period was much longer than for a real engine. The inherent redox fluctuation usually occurs in the frequency of 1-4Hz. Here, we present new experimental results with time resolution of 1 sec by using the energy dispersive XAFS optics.

2. Experiments

The sample was pressed to form into pellets to be uniform and was put in a quartz-glass tube. The atmosphere varied by alternating oxidative gas (O_2 50% balanced with N_2) and reductive gas (H_2 50-100% balanced with N_2). XAFS spectra at the Pd K-edge (24.35keV) were measured with Si(422) crystal polychromator in transmission geometry at BL28B2, SPring-8. The sample in a glass tube was located at the focus of the dispersed x-ray and was heated by an infrared furnace. The x-ray intensity was accumulated with a phosphor-lens coupling optics and a two-dimensional CCD detector.

3. Results

Figure 1 shows time dependence of XANES spectra, which were consecutively measured every 1 sec at 400°C. A shift of the absorption edge towards the lower energies implies reduction of Pd ion, which initially occupied the B-site (6-fold coordination) of the perovskite lattice. The edge position of the perovskite did not reach that of the Pd-metal, after rapid edge shift for about 3 sec. Figure 2 shows radial structure functions, which calculated as the magnitude of Fourier transform of k^3-weighted EXAFS (extended x-ray absorption fine structure) oscillations. The peak height of Pd-O bond decreases, while the peak height of Pd-Pd bond increases as time elapsed. This implies that Pd segregated out from the B-site of the perovskite lattice, and that Pd metal particles agglomerated and grew. The reversible change was also observed by switching atmosphere from reductive gas to oxidative one. We have found that the reversible movement of Pd really occurred within a few seconds to ensure the self-regeneration phenomenon in the real world.

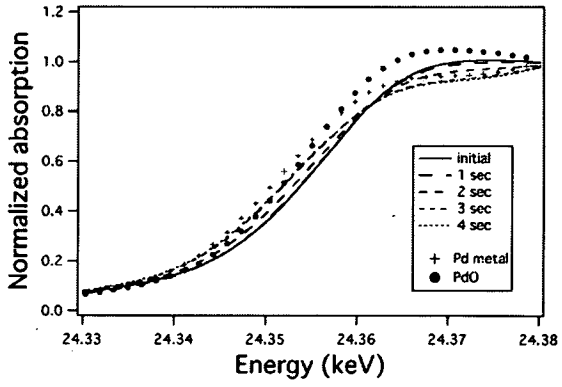

Fig. 1 Time dependence of XANES spectra at the Pd K-edge for $LaFe_{0.9}Pd_{0.1}O_3$ after the atmosphere switched from the oxidative gas to the reductive one (400°C)

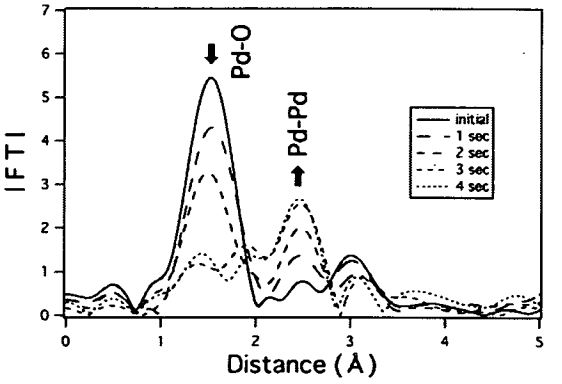

Fig. 2 Time dependence of radial structure functions around Pd after the atmosphere switching from the oxidative gas to the reductive one

References

1) Y. Nishihata, *et al. Nature* **418**, 164-167 (2002).
2) Y. Nishihata, *et al. J. Phys. Chem. Solids* (in press).

5.3.2 Fundamental studies of x-ray induced photocatalytic reaction on TiO_2

Kazuhisa TAMURA, Yoshihisa OHKO[a], Tetsu TATSUMA[b] and Jun'ichiro MIZUKI
a) PREST, b) Inst. of Ind., Sci., University of Tokyo

1. Introduction

TiO_2 is a very stable n-type semiconductor and possesses a wide band gap of 3 eV. These two features give TiO_2 quite high oxidative reactivity under UV illumination. The mechanism of photocatalytic reaction has been widely investigated in terms of electrochemical reaction, surface reaction, electronic structure, and so on. Recently, it has been recognized that high reactive radials, e.g., OH· play an important role in photocatalytic reactions. These studies are carried out under UV illumination because the sun light and fluorescence tubes contain UV light, however, the excitation source can be high energy source, like x-ray and γ-ray, which have much energy than 3 eV. If high energy light sources can be used as excitation sources, TiO_2 can be utilized for medical treatments and processing of nuclear wastes. However, systematic studies of photo electrochemical reaction induced by high energy light source haven't been done yet. Recently, we have observed anodic current under x-ray irradiation and figured out it was photocurrent due to electron-hole separation. In the present report, we present fundamental features of x-ray induced photocatalytic reaction and its mechanism.

2. Experimental

TiO_2 was prepared by thermal oxidation of Ti sheet and set to an electrochemical cell, which has an x-ray window. The electrolyte was 0.1 M Na_2SO_4 prepared by Milli-Q water. The reference electrode was Ag/AgCl and the counter electrode was a Pt wire. X-ray irradiation measurements were carried out at SPring-8, BL22.

3. Results

Figure 1 shows a cyclic voltammogram of TiO_2 in 0.1 M Na_2SO_4 under x-ray irradiation. The x-ray energy was 5.02 keV, which is above Ti-K absorption edge, 4.965 keV. When x-ray shutter was opened, anodic current was clearly observed in both anodic and cathodic scans. To elucidate the origin of the observed anodic current, a photopotential measurement was carried out. It is not shown in this report; however, the rest potential of TiO_2 showed negative shifts under x-ray irradiation and showed positive shifts under dark condition. Photopotential is due to accumulating of electrons, which are generated by electron-hole pair separation. Thus, the observed negative shift and anodic current prove that electron-hole pair separations followed by photocatalytic reactions occur under x-ray irradiation.

To examine features of photocurrent under x-ray irradiation, energy dependence measurements were carried out. Figure 2 shows x-ray energy dependencies of photocurrent, photopotential, and fluorescence intensity. A rutile crystal was used for the x-ray fluorescence measurement. Both photocurrent and photopotential showed energy dependence and they followed the x-ray fluorescence spectrum. It indicates that electron-hole pair separation is related to inner shell excitation.

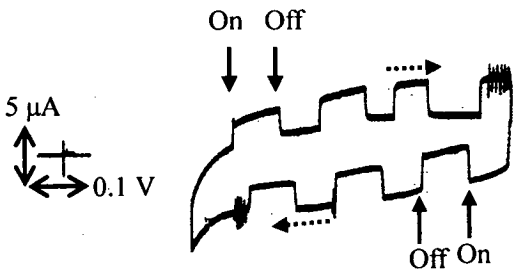

Fig. 1 Cyclic voltammogram under x-ray irradiation
X-ray energy was 5.02 keV. X-ray shutter was opened and closed at the signs of "on" and "off", respectively. Scan rate: 10 mV s^{-1}

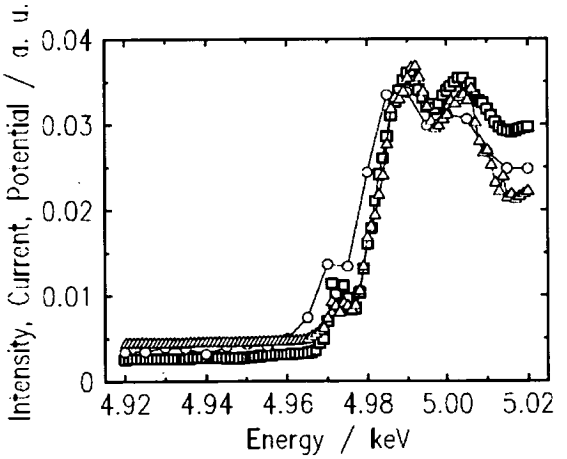

Fig. 2 X-ray energy dependencies of photocurrent (triangles), rest potential (circles), fluorescence intensity (squares)

5.3.3 X-ray diffraction study on GaAs(001)-(2x4) surfaces under molecular-beam epitaxy condition

Masamitsu TAKAHASI, Yasuhiro YONEDA and Jun'ichiro MIZUKI

Because of its importance in the molecular-beam-epitaxy (MBE) growth of III-V group semiconductor devices, the As-stabilized GaAs(001)-(2x4) surface has been intensively studied by many experimental techniques and theoretical calculations. As a result, it has been established that the most stable is the β2(2x4) structure consisting of a pair of As dimers in the topmost layer and of a single As dimer in the third layer. However, actual surfaces under MBE conditions are more complicated because of flexibility in the surface stoicheometry. Depending on the substrate temperature and As overpressure, reflection high-energy electron diffraction (RHEED) gives the three distinctive 2x4 patterns called α, β and γ phases. Recently, we have found by surface X-ray diffraction (SXRD) that, in the α and γ phases, the 2x4 domains are separated by the antiphase domain boundaries characteristic to each phase[1]. By the presence of the antiphase domain boundaries, the α and γ phases can be distinguished from the β phase, which is stable over a range of about 100 K. However, it is still questionable whether only the β2 structure prevails in such a wide temperature range because very few in situ studies have been reported on the β phase under MBE conditions. In the present work, we have investigated the β phase of GaAs(001)-(2x4) at various temperatures in a constant As flux by SXRD [2].

The experiments were performed on the synchrotron radiation beamline 11XU at SPring-8, Japan, with an X-ray wavelength of 1.24 using a surface X-ray diffractometer directly coupled to an MBE chamber [3]. X-ray measurements were carried out in the grazing-incidence geometry with the incoming and outgoing angles set at the critical angle for total reflection.

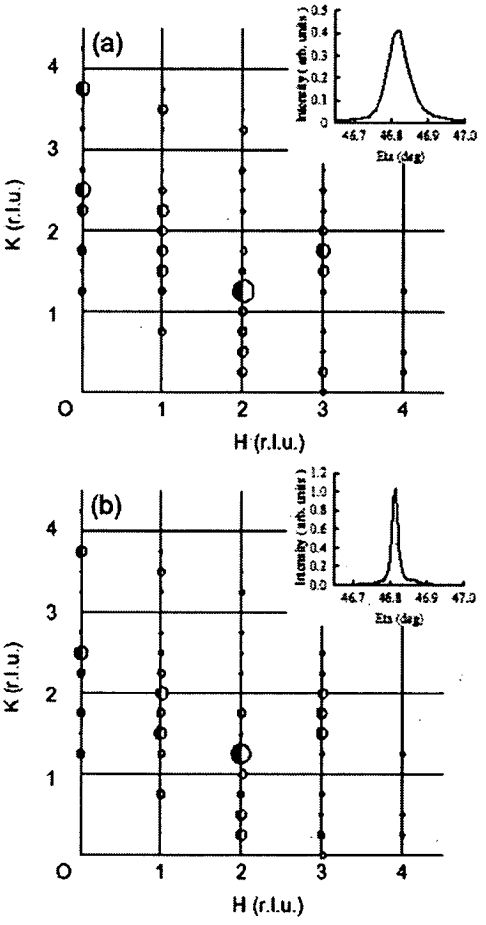

Fig. 1 X-ray diffraction patterns at 545°C (a) and 585°C (b) under an As flux of $5x10^{-7}$ Torr
The open circles represent the observed structure factors and the filed circles show the calculation based on the best fit model. The insets are the rocking curves at (0, 1.25).

Figure 1 shows a comparison between inplane X-ray diffraction patterns at 585°C and 545°C within the β phase. Reflection indices, H and K, are described on the basis of the surface 1x1 unit cell defined by [1-10] and [110]. The open and filled semicircles represent the observed and calculated structure factors, respectively. The radii of the semicircles are proportional to the amplitude of the structure factors. While the X-ray diffraction pattern observed at 545°C agrees well to the β2(2x4) surface, the X-ray pattern at 585°C can be explained by a mixture of two structures called α2 and β2. This structural change is interpreted in terms of partial As-dimer desorption from the β2(2x4) surface.

References

1) M. Takahasi , Y. Yoneda and J. Mizuki, Phys. Rev. B 68 (2003) 085321.

2) M. Takahasi, Y. Yoneda and J. Mizuki, Appl. surf. Sci., to be published.

3) M. Takahasi , Y. Yoneda, H. Inoue, N. Yamamoto and J. Mizuki, Jpn. J. Appl. Phys. 41 (2002) 6247.

5.3.4 Inelastic x-ray scattering studies of phonons in $La_{2-x}Sr_xCuO_4$

Tatsuo FUKUDA, Jun'ichiro MIZUKI, Kazuhiko IKEUCHI[a], Kazuyoshi YAMADA[a], Alfred Q.R. BARON[b], Satoshi TSUTSUI[b]
a) Institute for Materials Research, Tohoku Univ. b) JASRI, SPring-8

1. Introduction

Since a kink structure in the dispersion of electron quasiparticles was observed by angle-resolved photoemission measurements in hole-doped high-T_c superconductors (HTSC)[1], the role of electron-phonon coupling in the HTSC has attracted much interest. This is because one explanation of this kink structure is the interactions with electron quasiparticles with an in-plane bond-stretching longitudinal optical (LO) phonon mode. This highest energy LO phonon shows softening along <100> direction when the holes are doped[2]. However, samples only below optimum hole concentration have been investigated so far mainly by inelastic neutron scattering studies, because the crystal growth becomes difficult as hole concentration increases. Therefore, we carried out phonon measurements on one of typical HTSCs, $La_{2-x}Sr_xCuO_4$ (LSCO), by inelastic x-ray scattering, which enables the measurements with a small sample. The LSCO has a single CuO_2 layered structure. In addition, the doping concentration (x) can be easily controlled from the non-doped Mott insulator to the overdoped normal metal in this system, so the doping dependence can be investigated precisely.

2. Experiments

The single crystals of LSCO were grown at Kyoto and Tohoku University using the traveling-solvent floating-zone method. The experiments were performed at BL35XU of SPring-8. A silicon (888) reflection backscattering monochromator was used to provide an incident x-ray beam, whose energy was 15.816 keV. The scattered photons were analyzed using 4 independent spherical crystal analyzers in a horizontal scattering geometry. The total energy and momentum resolutions were 6.0~6.2 meV and about 0.076 $Å^{-1}$, respectively. The measurements were carried out with a reflection mode (Bragg geometry) at low temperature to reduce tails of low energy phonons.

3. Results

We measured the bond-stretching phonon mode along <100> direction, and defined the amplitude of the softening (A) by fitting the dispersion curve using a phenomenological function $0.5A\cos(2\pi\zeta) + B$, where A and B are constants. The x dependence of the softening determined by present work was shown in Fig. 1 together with the x dependence of the T_c. In general, a screened Coulomb interaction causes a phonon softening, whose x dependence is expected to be linear. In our result, an anomalous enhancement (hatched part; $x \sim 0.15$) of the phonon-softening was observed in the superconducting region. The present observation of precise x dependence of the phonon softening will evoke further discussions and studies to elucidate the reason for the anomalous phonon softening in the HTSC.

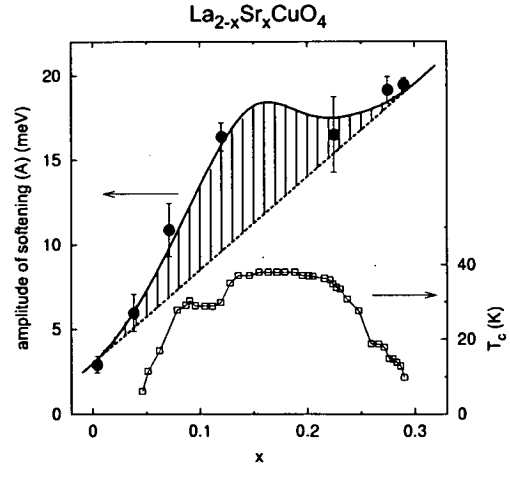

Fig. 1 x dependences of the softening in the bond-stretching vibration along [100] and T_c

References

1) A. Lanzara *et al.*, Nature **412** 510, 2001.
2) L. Pintschovius *et al.*, Physica B **174**, 323, 1991.; R.J. McQueeney *et al.*, Phys. Rev. Lett. **82**, 628, 1999; L. Pintschovius *et al.*, Phys. Rev. B **60**, R15 039, 1999.; private communication.

5.3.5 X-ray absorption and neutron diffraction study of $CaMn_{0.6}Ru_{0.4}O_3$

Kenji YOSHII, Akio NAKAMURA[a)], Masaichiro MIZUMAKI[b)], Hajime TANIDA[b)], Naomi KAWAMURA[b)], Hideki ABE[c)], Yoshinobu ISHII[a)], Yutaka SHIMOJO[a)], Yukio MORII[a)]
a) Advanced Science Research Center, JAERI, Tokai, Ibaraki 319-1195, Japan
b) Japan Synchrotron Radiation Research Institute (JASRI), Mikazuki, Hyogo 679-5198, Japan
c) National Institute for Materials Scienc (NIMS), Tsukuba, Ibaraki 305-0047, Japan

1. Introduction

Perovskite manganese oxides have attracted renewed attention in this decade because of their intriguing properties such as colossal magnetoresistance and real-space charge-order. One of the compounds, $CaMnO_3$, have an orthorhombic crystal structure (*Pnma*) and is an insulating antiferromagnet below ~150 K. Recently, it was reported that ferromagnetism and metallicity are developed for $CaMn_{1-x}Ru_xO_3$ where Mn is partially substituted by Ru. [1,2] $CaRuO_3$ (x=1) has the same *Pnma* structure and exhibits metallic conductivity with a tendency toward magnetic order at low temperatures. The Curie temperature was found to reach a maximum value of 210 K at x=0.4. In this work, X-ray abasorption and neutron diffraction measurements were carried out to obtain further information about crystal, magnetic and electronic structures of $CaMn_{0.6}Ru_{0.4}O_3$.

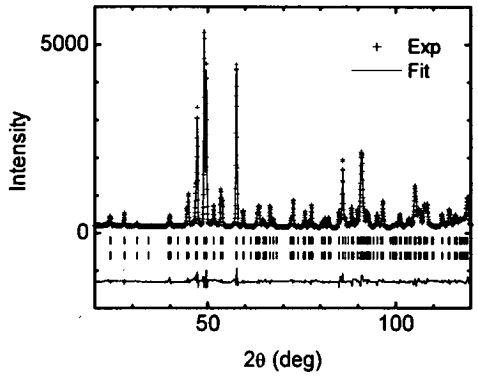

Fig. 1 Neutron diffraction patterns at 4 K (Space group $P2_1/n$)

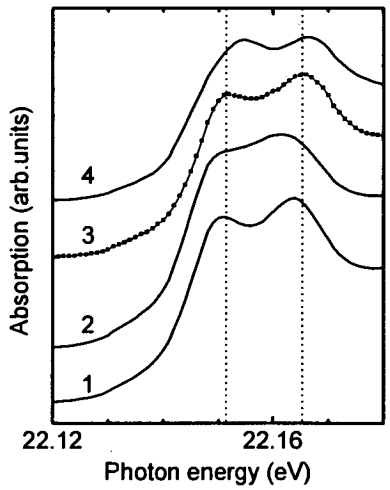

Fig. 2 X-ray absorption spectra for the four ruthenates
The spectra 1, 2, 3 and 4 stand for those of $CaRuO_3$, $SrRuO_3$, $CaMn_{0.6}Ru_{0.4}O_3$ and $Pb_2Ru_2O_{6.5}$, respectively.

2. Experimental

The samples were prepared by the same method as noted in Ref. 1. Neutron diffraction patterns were measured at 300 K and 4 K using high resolution powder diffractometer (HRPD) at the JRR-3 nuclear reactor of JAERI. The patterns were fitted by the Rietveld method using the program RIETAN-2000. [3] X-ray absorption measurements were done at the Bl01B1 beamline of SPring-8.

3. Results

Figure 1 shows the neutron diffraction patterns at 4 K. The experimental pattern could be fitted on the assumption of the coexistence of ferro- and antiferromagnetic domains, which was proposed previously. [1] The ordered moments in the former and the latter phases were 2.7 and 1.2 μ_B/unit formula, respectively. Figure 2 shows that the absorption peaks for $CaMn_{0.6}Ru_{0.4}O_3$ are located at the photon energies between those of $ARuO_3$ (A=Ca and Sr; Ru^{4+}) and $Pb_2Ru_2O_{6.5}$ ($Ru^{4.5+}$). [4] Thus, the average valence of the Ru ion in the present system is higher than 4+. The plausible existence of Ru^{5+} supports the proposed valency effect, i.e., the substitution of Ru^{5+} generates the Mn^{3+} species and leads to ferromagnetic double-exchange interactions between Mn^{3+} and Mn^{4+}. [1]

References

1) A. Maignan *et al*, Solid State Commun., **117**, 377, 2001.
2) V. Markovich *et al*, Phys. Rev. B**70**, 024403, 2004, and references therein.
3) F. Izumi, T. Ikeda, Mater. Sci. Forum **321-324**, 198, 2000.
4) K. Yoshii *et al*, J. Alloys Compd., **348**, 236, 2003.

5.3.6 X-ray topography on domain-controlled $BaTiO_3$ crystals

Yasuhiro YONEDA, Yoshiki KOHMURA[a)], Yoshio SUZUKI[b)],
Shin'ichi HAMAZAKI[c)], Masaaki TAKASHIGE[d)] and Jun'ichirou MIZUKI
a) Institute of Physical and Chemical Research (RIKEN),
b) Japan Synchrotron Radiation Research Institute (JASRI),
c) Fukushima National College of Technology d) Iwaki Meisei University

1. Introduction

Minituarization of ferroelectric components is the present endeavor in the micro electric industry. Consequently the study of size-depend properties with micro-domain configuration is important to elucidate the micro-structural characteristics of the ferroelectric components. The local strain around the domain boundary should be spread on the whole crystal by minimizing and by uniforming the domain size. In such configuration, the domain-size effect will be evident, especially in crystal structure.

The $BaTiO_3$ crystal with micro-domains was prepared by substituting strontium for barium. The ferroelectric domains were restricted by the impurities of strontium, and consisted square-net pattern. We observed this domain-controlled $BaTiO_3$ and normal butterfly $BaTiO_3$ crystals by using synchrotron X-ray, including X-ray topography.Traditionally, X-ray topography has been used for the samples with high-crystal quality like silicon. Most ferroelectrics has not been performed X-ray topography because of their poor crystal quality. However, recently, some ferroelectric materials were investigated with high-resolution synchrotron X-ray topography for revealing domain-domain correlation rather than for evaluating crystal quality.

2. Results

The topographic image and polarizing microscope observation of square-net domain $BaTiO_3$ are shown in Fig. 1 (a) and (b), respectively. In the rocking curve observation, the microscopic symmetry of the square-net domain $BaTiO_3$ was pseudo-cubic rather than tetragonal structure. If the $BaTiO_3$ crystal shows the cubic symmetry, the whole area is diffracted. In this case, only three narrow lines were recorded in the CCD. The Sr-doped crystal was not perfect cubic symmetry but slightly strained tetragonal symmetry. The periodicity in Fig. 1(a) is the same as that in optical microscope, as shown in Fig. 1(b).

In the case of the tetragonal $BaTiO_3$, the lattice strain causes the fluctuation of the surface bending mode and tilting of the polar direction. However, the moire-related pattern was not observed in the X-ray topography.[1)] The moire-related sharp lines as shown in Fig. 1(a) are characteristic of uniform and small domain configuration.

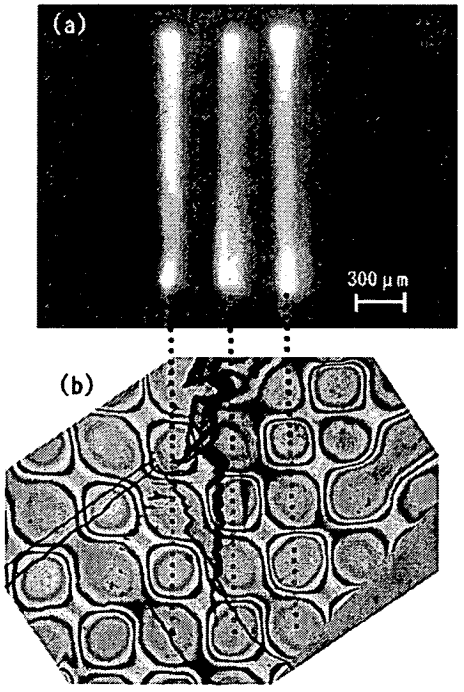

Fig. 1 (a) X-ray diffraction topography images and (b) polarization microscope image of 0.5%-Sr-substituted $BaTiO_3$ crystal at room temperature.

References

1) Y. Yoneda, Y. Kohmura, Y. Suzuki, S. Hamazaki and M. Takashige, J. of Phys. Soc. of Jpn. **73**, 1050, 2004.

5.4 Surface Chemistry Research

Surface Chemistry Research Group
Yuji BABA

Surface of solid is chemically active compared with the inside of solid. Such active properties also show up in low-dimensional materials e.g., one-dimensional wires and two-dimensional ultrathin films. The active property of a solid surface and low-dimensional material is applied to various functional devices such adsorbent, gas sensor and catalysis. In order to contribute to the development of new surface functional devices, it is of great importance to elucidate the dynamics of surface chemical reaction as well as to clarify the electronic structures of low-dimensional materials at mono-layer and mono-atomic scale.

The main objectives of Surface Chemistry Research Group are, 1) to clarify the dynamics of gas-solid reaction at mono-layer and mono-atomic scale using synchrotron radiation, 2) to search new low-dimensional materials and elucidate their electronic and geometrical structures, and 3) to control surface chemical reaction by core-level photoexcitation using linearly polarized synchrotron radiation.

In this chapter, seven recent highlights from the above topics are presented. First and second reports (5.4.1 and 5.4.2) deal with the dynamics of chemical reaction at metal and semiconductor surfaces probed by high resolution X-ray photoelectron spectroscopy installed at the BL-23SU SPring-8. The third report (5.4.3) is the summary of nanotechnology researches performed in this half year at the surface chemistry experimental station in the BL23SU of SPring-8. The following three reports (5.4.4, 5.4.5 and 5.4.6) present the electronic and geometrical structures of two-dimensional materials, probed by X-ray absorption spectra using linearly polarized synchrotron beams. These three works were performed at the beamlines in the Photon Factory of the High Energy Accelerator Research Organization. The last report (5.4.7) presents the in-situ observations on photo-induced decomposition of DNA components. This work is now being conducted in cooperation with the Advanced Science Research Center, JAERI.

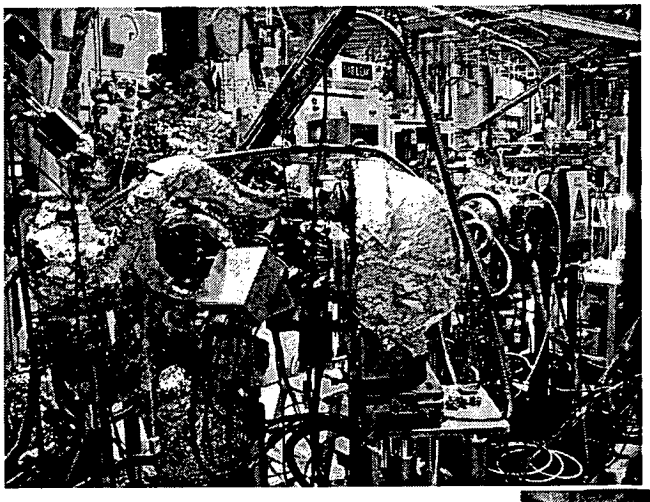

Fig. 1 Fast neutral beam irradiation system and electron energy analyzer with 64-channel detector installed at the BL23SU, SPring-8

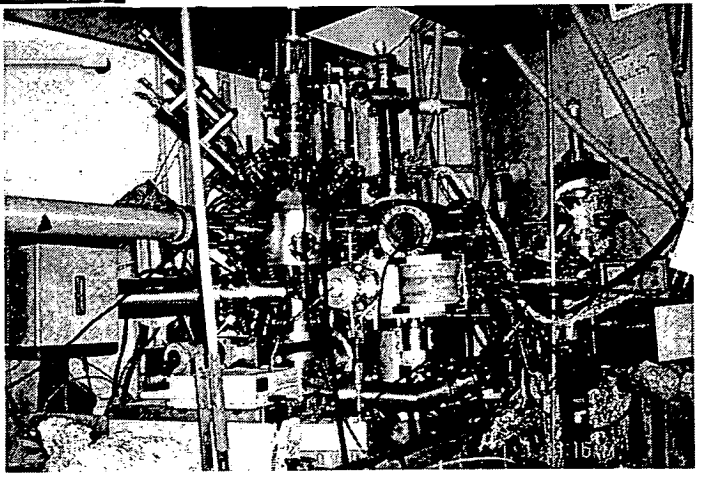

Fig. 2 Surface analysis system installed at the BL-27A in the Photon Factory, KEK for the analysis of low-dimensional material and photon-stimulated desorption

5.4.1 Oxygen adsorption and reconstruction on Cu(111) induced by translational energy of oxygen

Kousuke MORITANI, Akitaka YOSHIGOE, Yuden TERAOKA, Michio OKADA[a], Toshio KASAI[a]
a) Graduate School of Science, Osaka University

1. Introduction

The oxidation of Cu has been of great interest because of the important role of Cu oxides in material science, for example, high T_c superconductors of cuprates and solar cells. Thus, many experimental and theoretical studies have been performed to understand the oxidation of Cu. Despite these considerable efforts, the oxidation processes accompanied by complex surface reconstructions are not fully understood[1]. Copper oxide thin films grown on a Cu (111) surface are frequently reported as well-ordered, but several different types of surface ordered structures were found depending on the surface preparation conditions: the '29 - $(\sqrt{13}R46.1° \times 7R21.8°)$ and the '49 - $(\sqrt{73}R5.8° \times \sqrt{21}R-10.9°)$ structures[2-4]. These structures consist of three O and two Cu layers on the surface, which are quite similar to the bulk Cu_2O structure. Moreover, Judd *et al.* reported another structure at a high O_2 exposure, ~10^6 L, where the Cu(111) surface reconstructed to a slightly distorted Cu(100)-$(\sqrt{2} \times \sqrt{2})R45°$-O layer with O atoms[5]. We studied the oxidation process of Cu(111) accompanied by reconstruction with a hyperthermal O_2 molecular beam (HOMB) using X-ray photoemission spectroscopy (XPS) in conjunction with a synchrotron radiation (SR) source.

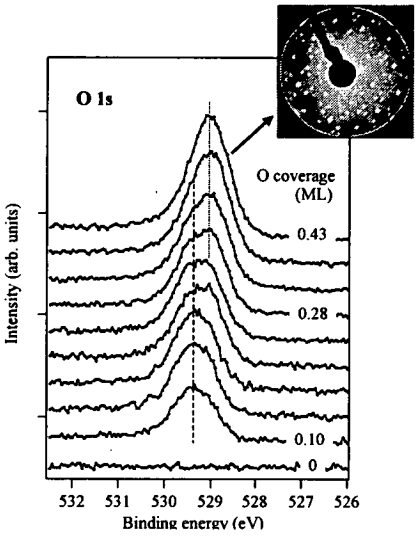

Fig. 1 The evolution of O-1s-XPS spectra during 0.5-eV O_2 molecular beam irradiation on Cu(111) surface and the LEED pattern at oxygen coverage of 0.43 ML

2. Experimental

All experiments were performed using a surface reaction analysis apparatus (SUREAC 2000) constructed in BL23SU at SPring-8. Cu(111) samples were cleaned by repeated sputtering with 1-keV Ar^+ and annealing at 870 K. The sample was exposed to HOMB seeded in Ar and/or He. Changing the seeding ratio controlled the kinetic energy of HOMB. After exposing to a proper amount of thermal O_2 or HOMB, the O-1s XPS spectra were measured in the surface-normal direction. All experiments were performed at a sample temperature of ~300 K.

3. Results

Figure 1 shows evolution of O-1s XPS spectra during 0.5-eV-HOMB irradiation and a LEED pattern, which is consistent with a slightly distorted Cu(100)-$(\sqrt{2} \times \sqrt{2})R45°$-O layer on Cu(111) surface. At ~0.3 ML, another peak which corresponds to distorted Cu(100)-$(\sqrt{2} \times \sqrt{2})R45°$-O grows at the low binding energy side, while symmetric single peak grow at first. Such oxygen adsorption accompanied with reconstruction to Cu(100)-$(\sqrt{2} \times \sqrt{2})R45°$-O above ~0.3 ML is induced by 0.5-eV HOMB as shown in Fig. 2.

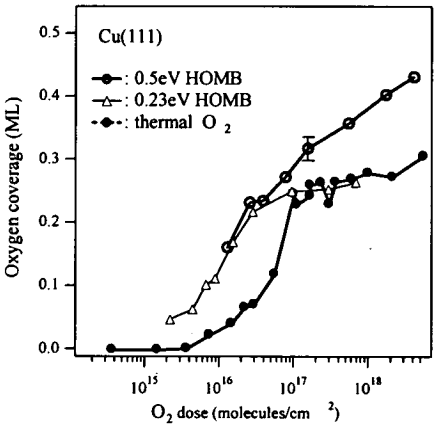

Fig. 2 Oxygen uptake curves for hyperthermal O_2 molecular beam irradiation and thermal gas dose on Cu(111).

References

1) D. P. Woodruff, J. Phys.: Condens. Matter **6**, 6067, 1994.
2) F. Jensen, F. Besebacher, E. Laegsgaard and I. Stensgaard, **259**, L774, 1991
3) F. Jensen, F. Besebacher and I. Stensgaard, **269/270**, 400, 1992.
4) T. Matsumoto, R. A. Bennett, P. Stone, T. Yamada, K. Domen and M. Bowker, Surf. Sci. **471**, 225, 2001.
5) R. W. Judd, P. Hollins, and J. Pritchard, Surf. Sci. **171**, 643, 1986.

5.4.2 Real-time *in-situ* photoemission spectroscopy using synchrotron radiation for thermal oxidation on Si(001) at high temperature

Akitaka YOSHIGOE, Kousuke MORITANI, Syunsuke HACHIUE and Yuden TERAOKA

1. Introduction

Thermal oxidation processes on Si(001) surface is important to form well-controlled gate-oxide thin films of metal-oxide-semiconductor field-effect-transistors (MOS-FETs). With decreasing the sizes of the ultra-large scale integrated (ULSI) devices, it is essential to understand and control the chemical compositions and the film thickness in the nanometer scale. Furthermore, it is also interesting from the viewpoints of the surface chemistry as a basic science, because the oxidation includes many surface processes, such as adsorption of oxygen molecules, migration and desorption of not only adatoms but also products. In order to realize the reaction mechanisms of thermal oxidation on Si(001) surfaces, we investigated the time evolution of Si oxidation states (Si^{1+}, Si^{2+}, Si^{3+}, Si^{4+}) by means of real-time *in-situ* photoemission spectroscopy using synchrotron radiation [1].

2. Experimental

All experiments were performed at the surface reaction analysis apparatus (SUREAC2000) of the BL23SU in SPring-8. The surface temperature was 1000 K and the O_2 gas was fed into the reaction chamber at $1x10^{-4}$Pa through a variable leak valve. Real-time *in-situ* photoemission spectroscopy using synchrotron radiation was performed during oxidation. The photon energies were 409eV for Si-2p, and 830eV for O-1s photoemission spectra, respectively. It took 30 s and 5 s to measure one Si-2p and O-1s spectra, respectively.

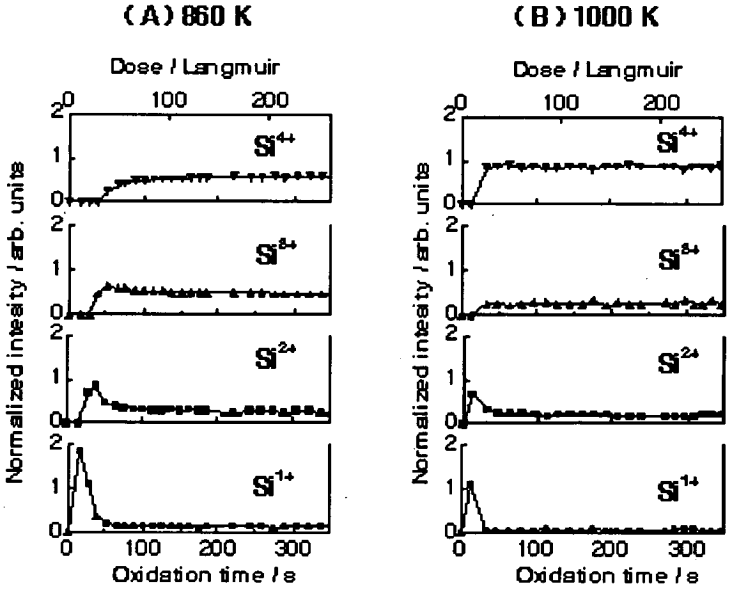

Fig. 1 Time evolution of Si oxidation states obtained by real-time Si-2p photoemission spectroscopy using synchrotron radiation at (A) 860K and (B) 1000K
The pressure of O_2 gas is $1x10^{-4}$Pa.

3. Results

The oxygen uptake curve measured by the real-time *in-situ* O-1s photoemission spectroscopy showed the typical Langmuir-type adsorption at 860K and two-dimensional island growth at 1000K, respectively. Figure 1 shows the time evolution of Si oxidation states derived from the real-time *in-situ* Si-2p photoemission spectra. The Si^{2+} species relating to the backbond oxidation at the topmost Si dimers appeared in conjunction with Si^{1+} species in the initial oxidation stage at 1000K in the case of the two-dimensional island growth condition. We clarified that the topmost Si atoms bonding to two oxygen atoms play an important role as an initial adsorbate to progress the oxidation. Since Si oxidation states with higher oxidation number, such as Si^{4+} and Si^{3+}, appeared in the early oxidation states as well, we concluded that SiO_2 adsorbates constructed with the Si^{4+} species was preferentially formed on Si(001) surface at 1000K.

Reference

1) Akitaka Yoshige, Kousuke Moritani and Yuden Teraoka, Surf. Sci. (in press).

5.4.3 Nanotechnology researches supported at the surface chemistry experimental station in the BL23SU of SPring-8

Yuden TERAOKA, Akitaka YOSHIGOE, Kousuke MORITANI

1. Introduction

JAERI is supporting researches concerning nanotechnology by applying its four beamlines. The research support subject at the BL23SU is "Formation of ultra-thin metal oxide layer and its photoemission spectroscopic analyses". The surface chemistry experimental station is also used for the research supports. By using the station, an ultra-thin oxide layer can be formed at surfaces of various kinds of metals and semiconductors using supersonic molecular beam techniques. Therefore, surface reaction dynamics of incident molecules can be also studied. The high brilliance and high energy resolution synchrotron radiation contributes to real-time in-situ photoemission spectroscopy for the observation of the initial formation processes of ultra-thin oxide layer. In 2003, the following three subjects were accepted for the research supports. First, "The real-time in-situ XPS analysis of the ultra-thin oxide-layer formation processes at the Ti(0001) surface" by Tohoku University group, second, "The oxidation reaction dynamics at the Si(111) surface" by AIST group, and finally "Trial of Au(111) oxidation by a supersonic O_2 molecular beam" by Osaka University group.

2. Experimental

All experiments were performed at the surface reaction analysis apparatus (SUREAC2000) in the BL23SU. The surface oxidation was done in the O_2 gas ambient or by irradiating the supersonic O_2 beam. The translational kinetic energy of O_2 molecules can be controlled up to 2.3 eV. The oxidized surfaces were analyzed via in-situ photoemission spectroscopy with soft x-rays. Owing to the high energy resolution and high brilliance synchrotron radiation, real-time XPS measurements can be also performed.

3. Results

3.1 Ti(0001) oxidation[1,2)]

Ti oxide is important as a photo-catalyst and also a passivation layer of vacuum material. In order to make clear the oxidation mechanisms, the Ti(0001) surface was oxidized by O_2 molecules and the oxide layer was analyzed by real-time in-situ XPS. The initial reaction probability decreased with increasing incident energy. This implies that the O_2 molecule dissociates at the Ti(0001) surface via a trapping-mediated mechanism. The oxide-layer thickness reached to be 5 nm even at room temperature in the O_2 ambiance condition. The thickness in the case of 2.3 eV-O_2-beam irradiation was thinner than that of O_2 ambiance. Nevertheless, Ti was well oxidized up to TiO_2 rather than TiO by the action of O_2 incident energy.

3.2 Si(111) oxidation

The incident O_2 energy dependence for the initial oxidation processes was investigated by using the supersonic O_2 beam. The O-1s photoemission showed that the oxygen amount at the saturation increased with increasing O_2 incident energy. This implies that the oxide-layer thickness is controllable with a nanometer scale not only by temperature but also by the incident energy. The Si-2p peak de-convolution showed that the SiO_2 (Si^{4+}) component was dominant with increasing O_2 incident energy. Consequently, the incident energy has effects of promoting the oxide-layer thickness and the silicon oxidation number.

3.3 Au(111) oxidation

A gold surface is known as inert chemically. However, the Au(111) surface was expected to be oxidized by the supersonic O_2 beam. The threshold energy was estimated to be 1.8 eV by theoretical calculations. No evidence, however, for oxidation was found even by the use of O_2 beam with the incident energy of 2.3 eV although oxygen ion beams with 1 keV energy were effective for oxidation.

References

1) Y. Takakuwa, S. Ishidzuka, A. Yoshigoe, Y. Teraoka, K. Moritani, S. Ogawa, Y. Mizuno, H. Tonda and T. Homma, J. Vac. Soc. Jpn. **47**, 457, 2004 (in Japanese)

2) Y. Takakuwa, S. Ishidzuka, A. Yoshigoe, Y. Teraoka, Y. Mizuno, H. Tonda and T. Honma, J. Surf. Sci. Soc. Jpn. **24**, 500, 2003 (in Japanese)

5.4.4 Formation of hexagonal boron nitride ultrathin film on Si(111)

Iwao SHIMOYAMA, Yuji BABA, Tetsuhiro SEKIGUCHI and Krishna G. NATH

1. Introduction

Due to the wide band gap property and graphite-like structure, hexagonal boron nitride (*h*-BN) is an attractive material as a candidate of ultrathin insulator. So far, epitaxial *h*-BN monolayer has been formed on a few single crystal surfaces of transition metals by chemical vapor deposition (CVD) method with borazine ($B_3N_3H_6$) gas [1]. However, semiconductor surfaces have not been used as substrates for the *h*-BN epitaxial monolayer. Then, we attempted to form *h*-BN ultrathin film on Si(111) with same method. In this study, the electronic structure and orientation of the thin film formed on Si substrate was investigated by near edge X-ray absorption fine structure (NEXAFS) spectroscopy.

2. Experimental

The experiments were performed at the BL-11A of the Photon Factory in the High Energy Accelerator Research Organization. After Ar^+ sputtering and annealing procedures, Si(111) surface was exposed to borazine gas (10^{-4}~10^{-3} Pa) at high temperature in an ultra high vacuum chamber. Substrate temperature and borazine dose were changed as synthesis parameters. The thickness and composition ratio of the thin films were estimated by X-ray photoelectron spectroscopy (XPS) measurements with monochromatic X-ray (*hv*=450eV). NEXAFS spectra were measured by total electron yield method. We also investigated electronic structures of bulk *h*-BN and *h*-BN ultrathin film on Ni(111) substrate for comparison with NEXAFS spectroscopy.

3. Results and discussion

Figure 1 shows the thickness of the films as functions of substrate temperature and borazine dose. The thickness reached to 6.5 Å at 1000 °C and 10^4 L. This thickness corresponds to two monolayers of *h*-BN. In the case of *h*-BN/Ni(111), we obtained same thickness at 800 °C and 180 L [2]. [B]/[N] ratio was larger than unity for thin films (< 3 Å), however this ratio was almost unity for thick films (>3 Å). This suggests B-rich film was formed in the initial stage and stoichiometric BN ultrathin film finally grew.

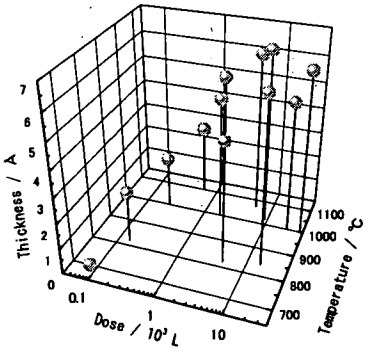

Fig. 1 Thickness of *h*-BN thin films deposited on Si(111) for various substrate-temperatures and borazine doses

Figure 2 shows B K-edge NEXAFS spectra of the BN films. Top spectrum shows result for the thin film prepared at 1000 °C and 5.4×10^3 L. Middle and bottom spectra show the results for bulk *h*-BN and *h*-BN/Ni(111), respectively. Here, magic angle is chosen for incidence angle of X-ray to cancel out the polarization dependence. The spectrum of the BN thin film is similar to that of bulk *h*-BN. Furthermore, the spectra of the film showed graphite-like polarization dependence. The sharp peak around 192 eV, which is assigned to B 1s→π^* transition, was enhanced at grazing incidence and suppressed at normal incidence. This gives clear evidence for formation of *h*-BN on Si(111). In the spectrum of *h*-BN/Ni(111), new π^* peak appears which originates from hybridisation between π^* orbital of *h*-BN and Ni atomic orbitals. However, the spectrum of *h*-BN/Si(111) does not show such modification of π^* state. This indicates that the interaction between Si(111) and *h*-BN is weak and *h*-BN ultrathin film would keep intrinsic insulating property on Si(111).

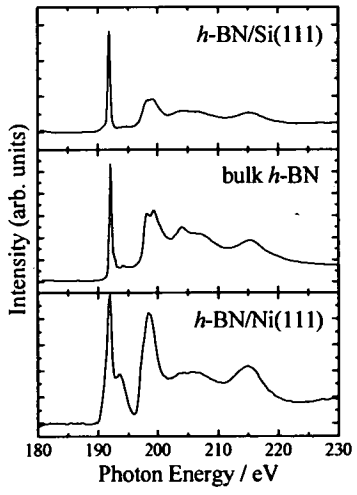

Fig. 2 K-edge NEXAFS spectra of *h*-BN/Si(111) (top), bulk h-BN (middle), and *h*-BN/Ni(111) (bottom) at magic angle

References

1) A. Nagashima et al., Phys. Rev. Lett. 75, 3918 (1995).
2) I. Shimoyama et al., J. Elec. Spec. Relat. Phenom. 137-140, 573 (2004).

5.4.5 Structure of ultra-thin SiC studied by X-ray photoelectron spectroscopy and polarization-dependent near-edge X-ray absorption fine structure

Yuji BABA, Tetsuhiro SEKIGUCHI, Iwao SHIMOYAMA, Krishna G. NATH

1. Introduction

The discovery of carbon nanotube has stimulated the search for new low-dimensional materials composed of carbon atoms. The versatility of carbon allotrope originates from the stability of both sp^2 and sp^3 configurations in C-C bonds. Recently some of new hetero-atomic low-dimensional materials of which configurations are similar to those of graphite, fullerene and carbon nanotube were synthesized. For example, B-N nanotubes, B-C-N nanotubes, Si and SiC nano-wires, and SiO_x nano-flowers were synthesized. Among them, SiC-based low-dimensional materials have attracted particular attention as a wide-gap electronic and optoelectronic material, because it has excellent properties such as high thermal conductivity and chemical stability. In this report, we present the electronic and geometrical structures of ultra-thin SiC films synthesized by low-energy ion-beam deposition and post-annealing using organic silicon compounds as source materials.

2. Experimental

The experiments were performed at the BL-27A station in the Photon Factory of the High Energy Accelerator Research Organization (KEK-PF). The X-ray beam was linearly polarized in the horizontal direction. A single crystal of highly oriented pyrolitic graphite (HOPG) was used as a substrate. High-purity tetramethylsilane (TMS) was used as a source gas. The ions were bombarded on HOPG at about 10 eV. The monolayered SiC was synthesized by 1) ion-beam deposition at 1.1×10^{15} ions/cm^2, and 2) annealing at 850℃ by YAG laser.

3. Results and discussion

X-ray photoelectron spectra show that the binding energy of Si 1s peak for monolayered SiC is higher by 2.8 eV than that for bulk SiC, suggesting that the silicon atoms in monolayered SiC films are more positively charged than those in the bulk-SiC. Figure 1 shows the polarization-dependent near-edge X-ray absorption fine structure (NEXAFS) spectra for monolayered SiC film. For comparison, NEXAFS spectra for bulk Si(100) and β-SiC are shown in the upper figure. Sharp peaks (marked A) are clearly seen at 1840 eV in the spectra at 10° and 30° incidences. It should be noted that the energy of this new peak is lower than that for β-SiC. Such a low-energy peak has never been reported for any silicon-containing materials. Inferred from the C K-edge NEXAFS for carbon-containing compounds[1], the low-energy and sharp features of the peak A suggests the existence of π^*-like orbitals around Si atom. A remarkable polarization dependence is observed; The intensity of the peak A decreases with the increase in the incident angles, and it almost disappears at nearly normal incidence (θ=80°) From this polarization dependence, we can suppose that the final state orbitals represented by the peak A is perpendicular to the surface. The result suggests that Si atoms are located as one of the six-membered aromatic ring in graphite-like configuration. It is concluded that the obtained monolayered SiC film has flat-lying two-dimensional structure of which configuration is similar to a single sheet of graphite.

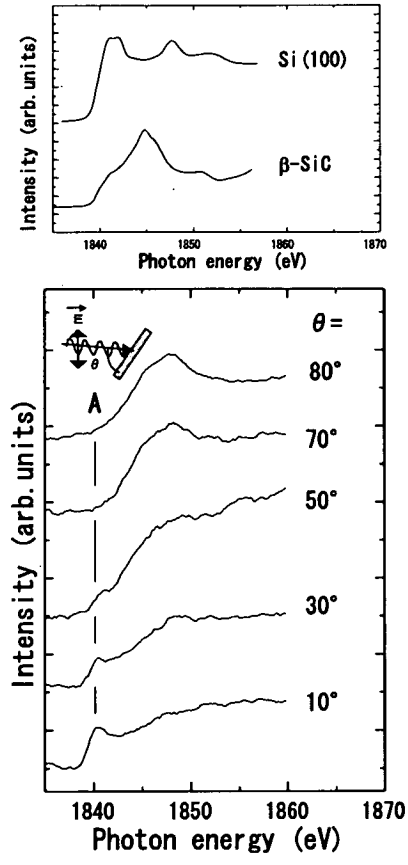

Fig. 1 Polarization dependence of NEXAFS spectra at the silicon *K*-edge for monolayered SiC
For comparison, NEXAFS spectra for standard materials of Si(100) and β-SiC are shown in the upper figure.

References

1) R.A. Rosenberg *et al.*, Phys. Rev. B **33**, 4034, 1986

5.4.6 Local bonding states of ion-irradiated graphite investigated by photon-stimulated desorption (PSD) technique

Tetsuhiro SEKIGUCHI, Yuji BABA, Iwao SHIMOYAMA and Krishna G. NATH

1. Introduction

The local bonding states of ion-irradiated graphite have been investigated by photon-stimulated ion-desorption (PSID) technique that is incorporates polarized with NEXAFS spectroscopy. Graphite is one of candidate materials for the first wall of fusion reactors. The damage effect of the graphite surface by deuterium-ion irradiation is thus key subject in fusion research. Irradiation products show a variety of complex formation of carbon-hydrogenous (C-H, C-D) bonds. Commonly used surface analyzing techniques such as X-ray photoelectron spectroscopy (XPS) and Auger electron spectroscopy (AES) are, however, not sensitive to hydrogen. Experiments with a time-of-flight mass-spectrometer (TOF-MS) using pulsed synchrotron radiation have therefore been designed to isolate individual bond.

2. Experimental

The experiments were performed at BL13C station. The dependence of fragment-ion yields on photon incidence angles were measured using a rotatable TOF-MS[1,2] that was developed in our laboratory. TOF measurements were done using pulsed soft X-rays during the single bunched operation. Polarized NEXAFS was measured by recording carbon-KVV Auger electron yields (AEY). The sample was prepared by irradiation of D_2^+ ions into highly oriented pyrolitic graphite (HOPG) single crystal.

3. Results and discussion

In Fig. 1 we compare the carbon K-*edge* (a)H^+-PSID and (c)AEY-NEXAFS spectra of D^+-irradiated HOPG for various polarization angles (θ). Broken lines show the assignments of resonances. In θ=45°, H^+ curve is similar to AEY. In θ=10°, however, H^+ yields are enhanced in a resonance characteristic of C=C-H site. This resonance is most probably of C1s→σ*(C-H). It is noteworthy that the enhancement of H^+ yields depends on polarization angles. This is an evidence for the mechanism of direct desorption; namely, core excitation directly follows C-H bond-braking and H^+ desorption. The mechanism of indirect desorption induced through collision excitation by secondary electrons is ruled out in σ*(C-H) state.

In analogous with H^+ ions, D^+ yields (Fig. 1(b)) are enhanced in σ*(C-D) state characteristic of C=C-D site. Another interesting fact is that D^+ yields show very strong enhancement in σ*(C=C) state which is characteristic of C=C bonds. Very high D^+ yields in the σ*(C=C) state suggest that de-excitation processes are not prominent. It comes to the conclusion that graphite basal planes are decomposed owing to ion irradiation and fragmented planes bonded to D atoms are smaller sized compared with those bonded to H atoms.

A tilt angle (α) between transition dipole moment for C1s→σ*(C-D) and the surface normal can be calculated based on polarization dependence of D^+ yields. Fig .1(d) shows spectra simulated with the best fitted α, 36°. The results suggest that small-sized carbon planes with C-D bonds are tilted up from the substrate plane. This surface modification was induced by ion irradiation.

In summary, the results demonstrate that the present technique enables one to measure partial X-ray absorption cross section relevant to each bond and to obtain insights into local structure such as a bond orientation.

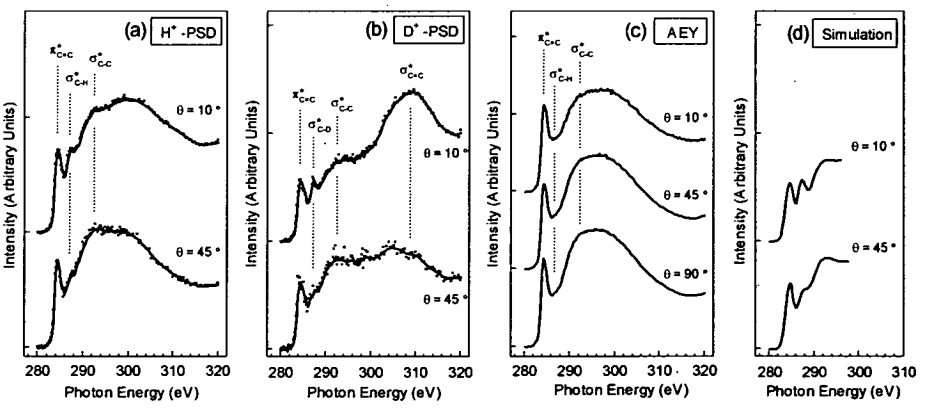

Fig. 1 C K-*edge* (a) H^+, (b) D^+, (c) AEY, and (d) simulated NEXAFS spectra of D^+-irradiated HOPG for various polarization angles (θ) The "θ" shows the incidence angles of X-ray beam. The E vector of polarized light and the surface normal has an angle of θ.

References

1) T. Sekiguchi et al., Surface Science, **532-535**, 1079 (2003); ibid **528**, 242 (2003).
2) S. Wada and T. Sekiguchi et al., Nucl. Instr. Meth. Phys. Res., **B199**, 361(2003).

5.4.7 Decomposition of 2-deoxy-*D*-ribose by irradiation with 0.6 keV electrons and by 0.5 keV soft X-rays

Kentaro FUJII, Ken AKAMATSU[a)] and Akinari YOKOYA
[a)] Radiation Risk Analysis Laboratory

1. Introduction

To understand the mechanism of the molecular lesions in DNA induced by ionizing radiation, we have studied photo-decomposition of DNA components using a quadrupole mass spectrometer (QMS) installed in a soft X-ray undulator beamline in SPring-8[1,2]. In our recent study, we revealed that the sugar moiety is one of the most fragile site in DNA molecule by measuring the desorbed ions from DNA components[2]. This study showed that not only the primary photoabsorption process, but also subsequent process induced by the resulting secondary electrons such as Auger electrons, largely contribute to the desorption of fragment ion species from the sugar residue. In the present study, we have attempted to reveal which process in the main contribute to the degradation of DNA components by comparing the desorbed ion spectra of 0.6 keV low-energy electron and 0.5 keV soft X-ray photon irradiations.

2. Experimental

Measurement of the desorbed positive ions was performed using the soft X-ray beamline (BL23SU) in SPring-8. The desorbed ions were detected by a QMS analyzer positioned ~30 mm from the sample thin film. The low-energy electron beam from the electron source was inclined at 45° to the soft X-rays.

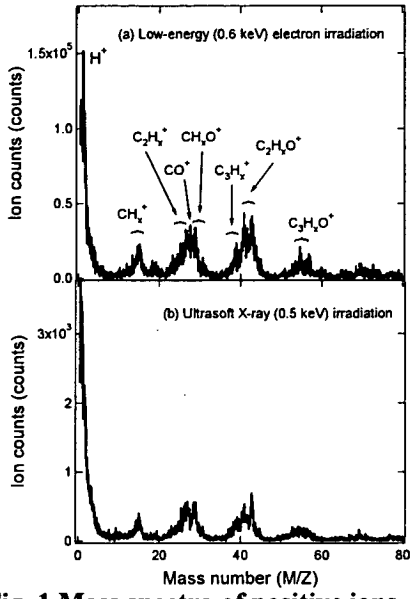

Fig. 1 Mass spectra of positive ions obtained from a 2-deoxy-*D*-ribose thin film due to (a) low-energy electron (0.6 keV) irradiation and (b) soft X-ray (0.5 keV) irradiation

3. Results and discussion

The desorbed ion spectra induced by irradiation with low-energy electrons (0.6 keV) and soft X-rays (0.5 keV) are shown in Fig. 1. The ions that were desorbed from 2-deoxy-*D*-ribose due to electron irradiation were mainly H^+, CH_x^+, $C_2H_x^+$, CO^+, CH_xO^+, $C_3H_x^+$, $C_2H_xO^+$ and $C_3H_xO^+$ (x= 1, 2, and 3) ions. These ions were the same as those observed in desorption due to soft X-ray irradiation. Therefore, it is inferred that these products are primarily produced by secondary electrons (less than several hundreds of eV). The changes induced in the X-ray absorption near edge structures (XANES) spectrum by the low-energy electron irradiation are shown in Fig. 2. The π* peak, at around 532 eV, increased with increasing electron irradiation dose. On the other hand, the intensity of the σ* peak, at around 538 eV, decreased. This result showed C-O bond cleavage in the molecule and C=O bond formation in the surface residues. The energies of the two peaks (531.4 eV and 532.4 eV) coincide with the excitation energies of the π*(C=O) of formaldehyde and the π*(C=O) of acetone, respectively. These results indicated that aldehyde-type and ketone-type products are formed as residues by the 0.6 keV electron irradiation as well as the positive ions observed above.

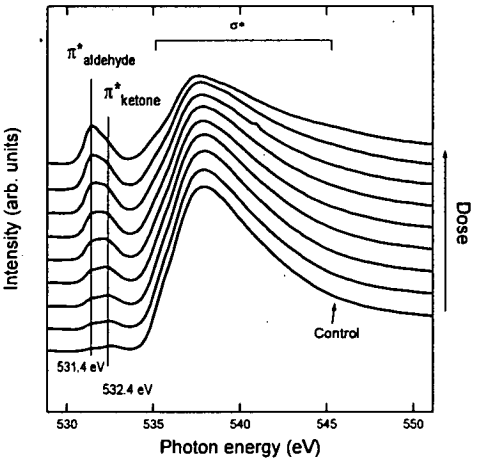

Fig. 2 X-ray absorption near edge structures (XANES) spectra of 2-deoxy-*D*-ribose obtained after irradiation with the low-energy (0.6 keV) electrons

References

1) K. Fujii, K. Akamatsu and A. Yokoya, *Surf. Sci.*, **528** (2003) 249-254.
2) K. Fujii, K. Akamatsu and A. Yokoya, *Radiat. Res.*, **161** (2004) 435-441.

5.5 Heavy Atom Science

Youichi MURAKAMI

The aim of our research is to elucidate the electronic ordering and the dynamics in the strongly correlated electron systems. The electronic ordering is characterized by the three degrees of freedom, that is, charge, spin and orbital. However, it is not so easy task to detect the ordering of these degrees of freedom by the normal x-ray diffraction. For that purpose we have developed the experimental technique of the resonant x-ray scattering (RXS) to detect these ordering. The RXS is a powerful tool to detect the charge, spin, and orbital ordering. Our station of the beamline BL22XU is dedicated to the RXS experiments of the transition metal K-edge, the rare-earth L-edge, and the actinide M-edge energy. The characteristics of this station are the capability of the RXS at the low x-ray energy down to 3.0 keV. The uranium compound (M4-edge: 3.73keV, M5-edge: 3.55 keV) is a good target to investigate the charge, spin, and orbital ordering. The high brilliance of this station also make it possible to measure the ordering under extreme conditions, such as high magnetic field, high pressure in low temperature. This year we have developed the technique of the diffraction experiment using pulse magnet. In order to study the dynamics we have constructed the spectrometer for resonant inelastic x-ray scattering (RIXS) in a station of the beamline BL11XU. Recently we have started to investigate the dynamics of high Tc cupper compounds.

In this chapter, we will present the following researches including the development of the experimental technique:

(1) the applicaiton of pulsed magnetic field up to H = 30 T,
(2) the charge gap excitation of a high Tc cupper compound by RIXS,
(3) the development of the coherent x-ray diffraction,
(4) the observation of the RXS from the magnetic ordering in a uranium compound,
(5) Mössbauer microspectroscopy of corrosion material.

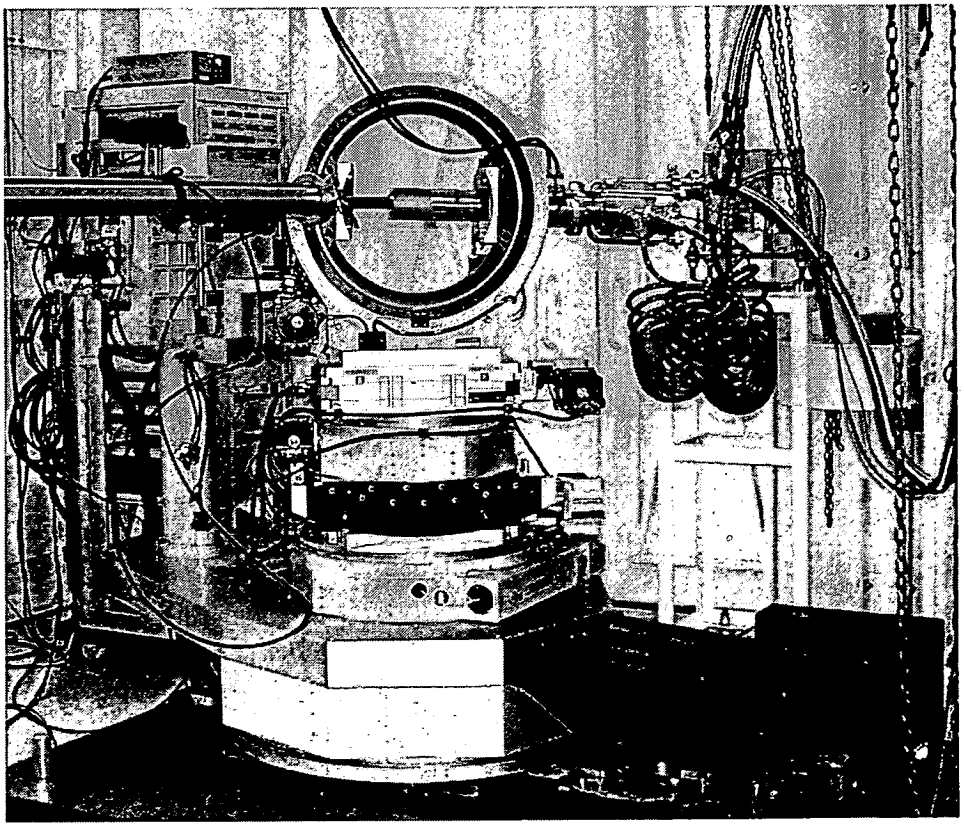

Fig. 1 Two-axis diffractometer in BL22XU during the experiment on Uranium compounds

5.5.1 Application of pulsed magnetic fields to synchrotron x-ray diffraction experiments

Toshiya INAMI, Kenji OHWADA, Y. H. MATSUDA[a)], Y. UEDA[a)], H. NOJIRI[a)],
Y. MURAKAMI[b)], T. ARIMA[c)] and K. YOSHIMURA[d)]
[a)]Okayama University, [b)]Tohoku University, [c)]University of Tsukuba, [d)]Kyoto University

1. Introduction

A magnetic field is one of important external parameters, such as temperature, pressure and electric fields, which control phase transitions. However, magnetic field is a rather weak field and thus a magnetic field required in order to cause a phase transition readily exceeds twenty or thirty Tesla. Nevertheless, usually x-ray diffraction experiments under strong magnetic fields are performed using a superconducting magnet, and recent maximum fields are only 15 T. A pulsed magnet is one of methods which overcome this limitation. Recently, we have constructed an x-ray diffraction system combined with a pulsed magnet [1)]. Here, we shortly describe particular features of the system and show the results of demonstration experiments.

2. X-ray diffractometer with pulsed magnet

A key technique in this system is that we employed a small pulsed magnet. A small magnet produces little heat. Hence the magnet can be cooled down by using a conventional closed cycle He refrigerator and is readily included in a conventional x-ray diffraction system. The diameter of the magnet coil is only 20 mm; the length is 25 mm and the bore size is 3 mm. However, the maximum magnetic field of this coil is more than 30 T. The pulse duration is about 1 msec. For data acquisition, we employed time-resolved measurements. Using a multi-channel scalar, the diffracted intensity is counted every 10 μsec. In order to deal with diffracted x-rays about 10^7 counts/sec, we used an avalanche photo diode as a detector [2)].

3. Results

We first measured the field-induced structural phase transition of $Pr_{0.6}Ca_{0.4}MnO_3$. $Pr_{0.6}Ca_{0.4}MnO_3$ undergoes a transition from an antiferromagnetic insulator to a ferromagnetic metal around 8T at low temperatures, which is accompanied by a huge orthorhombic-orthorhombic structural change. We set the diffractometer at the top of the 202 reflection and applied a pulsed magnetic field. The diffracted intensity was recorded as a function of time. It showed a steep fall at around 9T and increased again when the field was decreased below 2T. Similar temporal developments were measured at several reciprocal lattice points along the radial direction, and the change of the θ-2θ profiles as a function of magnetic fields was obtained.

The second example is the valence transition of $YbInCu_4$. At high temperatures, the Yb ion is trivalent, whereas below 42K the valence is reduced to approximately 2.9. Simultaneously the lattice volume increases about 0.5%. This low-temperature metallic phase is also broken by the application of the magnetic field. We applied pulsed magnetic fields up to about 30T, and observed the intensity change of the 220 reflection. In Fig. 1, the reconstructed θ-2θ profiles are shown as a function of the magnetic field. The volume expansions at high fields are clearly observed.

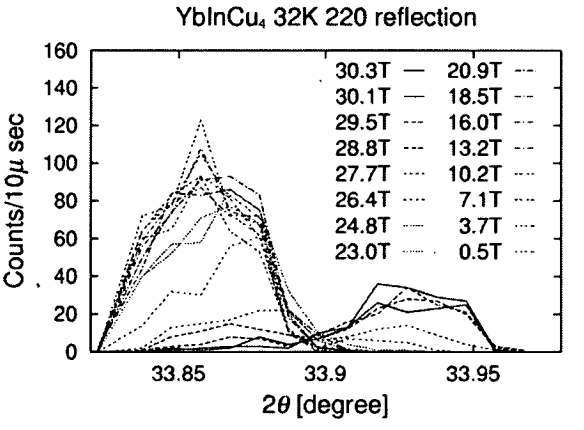

Fig. 1 θ-2θ profiles of the 220 reflection as a function of magnetic fields
The lattice shrinks in the high-field phase.

References

1) Y. H. Matsuda et al., Physica B **346-347**, 519 (2004)
2) S. Kishimoto, Rev. Sci. Instrum. **63**, 824, (1992)

5.5.2 Charge gap excitation of optimally doped $YBa_2Cu_3O_{7-\delta}$ studied by resonant inelastic x-ray scattering

Kenji ISHII, Toshiya INAMI, Kenji OHWADA, Kaori KUZUSHITA, Youichi MURAKAMI, Jun'ichiro MIZUKI, Yasuo ENDOH [a], Kenji TSUTSUI [b], Takami TOHYAMA [b], Sadamichi MAEKAWA [b], Takahiko MASUI [c], Setsuko TAJIMA [c]

a) Institute of Advanced Studies, b) IMR, Tohoku Univ., c) ISTEC

1. Introduction

Strongly correlated electron systems have been an attractive issue in recent condensed matter physics. Strong on-site Coulomb interaction separates a partially filled band into the occupied lower Hubbard band (LHB) and the unoccupied upper Hubbard band (UHB), and it produces a charge gap, known as the Mott gap, which has quite different character from the usual band gap due to the Pauli's exclusion principle. The measurement of the whole Brillouin zone using a momentum-resolved experimental technique is indispensable for understanding of the electronic structure of these systems. Angle-resolved photoemission spectroscopy (ARPES) provides a plenty of information of the LHB with momentum resolution[1]. On the other hand, resonant inelastic x-ray scattering (RIXS) can elucidate nature of the charge gap, which reflects both the LHB and the UHB. Here, we report the RIXS experiment on the high-T_c superconductor, $YBa_2Cu_3O_{7-\delta}$ at the optimal doping (T_c = 93 K). In $YBa_2Cu_3O_{7-\delta}$, there are two crystallographycally inequivalent Cu atoms. One forms a CuO_2 plane which is a playground of the superconductivity, and the other is in the CuO chain along the b-axis.

2. Experimental

The RIXS spectra of $YBa_2Cu_3O_{7-\delta}$ single crystal were measured at beam line 11XU at SPring-8. Overall energy resolution is about 400 meV. The c-axis of the crystal was kept perpendicular to the scattering plane.

3. Results and Discussion

First we measured spectra varying the energy of incident x-ray to determine the resonant energy. The excitation at 2-3 eV, corresponding to the charge gap excitation, is resonantly enhanced at 8990 eV. Figures 1 show the momentum dependence of RIXS spectra of $YBa_2Cu_3O_{7-\delta}$. We found two characteristics in the low energy region. One is an excitation at 2 eV which is prominent at the zone boundary of b^*-direction, that is, the intensity is enhanced near $(0,\pi)$, as indicated by the arrow in the figure. The other is an excitation at 3 eV which can be seen clearly in the spectra along [100] direction. Clear momentum dependence along the b^*-axis of 2 eV peak is a direct evidence that this is the excitation between the Mott gap of the chain, because the excitation along the b^*-axis should be equivalent to that along the a^*-axis in the plane. On the other hand, the excitation from CuO_2 plane is around 3 eV and the dispersion is small, as clearly seen in the spectra of q//[100]. These characters are well reproduced by a theoretical calculation based on the one-dimensional Hubbard model for the chain and two-dimensional one for the plane, where the lower Hubbard band is regarded as the Zhang-Rice band (ZRB). Our results demonstrate for the first time that the charge gap in the plane is smaller than that in the plane. Furthermore the dispersion of the excitation in the plane is almost flat in contrast to the case in undoped $Ca_2CuO_2Cl_2$[2] and La_2CuO_4[3], in which the dispersion of the order of 1 eV was observed in the low energy excitation. The smaller dispersion in the hole-doped CuO_2 plane is predicted in theory, and it is discussed in relation to the antiferromagnetic correlation[4].

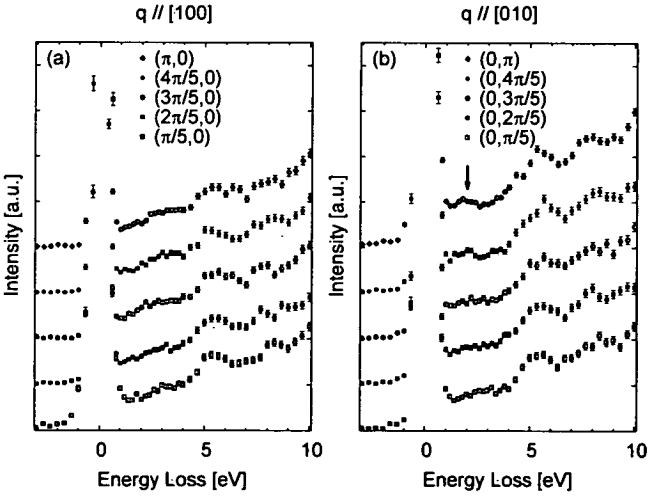

Fig. 1 RIXS spectra of $YBa_2Cu_3O_{7-\delta}$
The values in the legend represent the reduced momentum transfer in the *ab*-plane.

References

1) A. Damascelli *et al.*, Rev. Mod. Phys. **75**, 473 (2003).
2) M. Z. Hasan *et al.*, Science **288**, 1811 (2000).
3) Y. J. Kim *et al.*, Phys. Rev. Lett. **89**, 177403 (2002).
4) K. Tsutsui *et al.*, Phys. Rev. Lett. **91**, 117001 (2003).

5.5.3 Development of a setup for the coherent x-ray diffraction at BL22XU

Kenji OHWADA, Toshiya INAMI, Tetsu WATANUKI, Youichi MURAKAMI
Susumu SHIMOMURA[a)], Naoshi IKEDA[b)]
a) Department of Physics, Keio University b) Japan Synchrotron Radiation Research Institute

1. Introduction

In recent advances of the third generation synchrotron sources such as SPring-8, the use of the coherent x-ray beam becomes familiar. When a coherent x-ray illuminates a disordered material, the fine structure of the Bragg scattering can be observed, called speckle pattern. The speckle pattern contains information of the higher order structure of the material larger than a unit cell, so-called nano-scaled-domain. When the domains fluctuate by a certain perturbation, the speckle pattern also fluctuates. The intensity fluctuation provide the correlation time of the domain dynamics. Thus, the coherent x-ray diffraction (CXD) is a candidate of the new technique for observing the dynamics of such nano-scaled-domains. To know the possibility of realization of the CXD at BL22XU, we developed some setups and evaluated them.

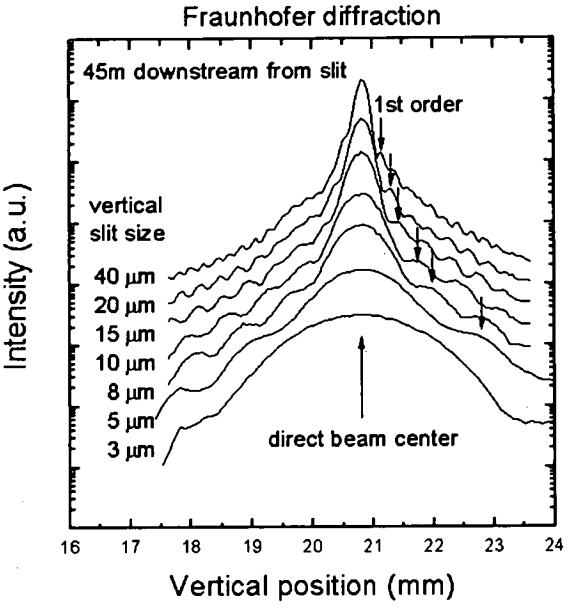

Fig. 1 Fraunhofer diffraction patterns

2. Experimental

BL22XU is one of beam lines of JAERI. Firstly, we studied the coherence of the x-rays by the Fraunhofer diffraction through a slit. The width was varied from 3 to 40 μm and the outgoing x-ray was detected at 45 m downstream from the slit. Then, we put a small pin-hole having a diameter of 20 μm just above upstream from the standard sample Cu_3Au, which has static nano-scaled-domain (generally called anti-phase domain)[1)], within near-field range. We observed the speckle pattern by using the detection pin-hole which also have a diameter of 10 μm and is put at 1.2 m downstream from the sample. 8 keV x-rays were used for all experiments.

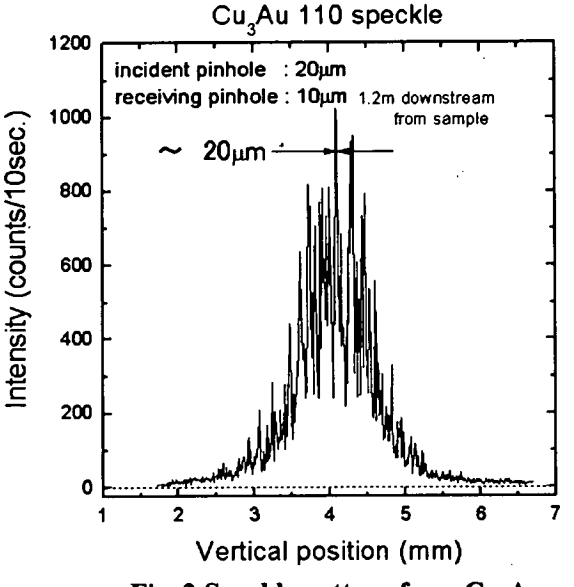

Fig. 2 Speckle pattern from Cu_3Au

3. Results

Figure 1 shows the Fraunfoher diffraction profiles as a function of slit width. The distance between fringes increases as the slit narrows; it is one of the characters of Fraunhofer diffraction. These observations well represent that the incident x-ray is coherent (> 40 μm vertical). Figure 2 shows the speckle pattern at 110 Bragg diffraction from Cu_3Au. The speckle size (ξ) is about 20 μm and consistent with the value derived from the present setup $\xi = \lambda R/D = 18.6\mu m$, where λ is the wavelength (1.55Å), R is the distance from the sample to the pinhole (1.2m) and D is the size of the incident pinhole (10 μm). Here, we present the coherence of the incident x-rays of BL22XU and demonstrate the speckle pattern from Cu_3Au which has static domains. We will refine the setup of BL22XU and study the domain dynamics in the near future.

Reference

1) M. Sutton et al. Nature, **352**, 608 (1991)

5.5.4 Observation of resonant x-ray magnetic scattering in $UNiGa_5$

Kaori KUZUSHITA[a)], Kenji ISHII[a)], Kenji OHWADA[a)], Youichi MURAKAMI[a, b)], Koji KANEKO[c)], Naoto METOKI[c, b)], Yoshinori HAGA[c)], Shugo IKEDA[c, d)], Yoshichika ÔNUKI[d)], Gerry H. LANDER[e)]

a) Synchrotron Radiation Research Center, JAERI, b) Graduate School of Science, Tohoku Univ.
c) Advanced Science Research Center, JAERI, d) Graduate School of Science, Osaka Univ.
e) European Commission, JRC, Institute for Transuranium Elements

1. Introduction

$UNiGa_5$ shows antiferromagnetic ordering below T_N = 86 K[1)], and the antiferromagnetic propagation vector in $UNiGa_5$ is [1/2 1/2 1/2] and uranium moments with 0.75 μ_B orient along c-axis[2)]. The band calculation shows that the U-5f bands around E_F are hybridized the Ga-4p bands[3)]. Therefore, It is easily expected that the Ga-4p bands may receive some effects of spin and orbital polarization of U-5f bands. Resonant x-ray scattering is a useful experiment to select an element and an electron shell specifically. Namely, the information of the intermediate level is obtained by using the specific absorption edge. We performed resonant magnetic scattering measurements of $UNiGa_5$ using x-ray tuned near both absorption edges (U M_4-edge and Ga K-edge).

2. Experimental

The experiments were performed at BL22XU of SPring-8. The single crystal of $UNiGa_5$ were grown by Ga self-flux method[4)], and mounted on a closed-cycle refrigerator. We collected the intensities of magnetic reflections of $UNiGa_5$ at incident photon energies near U M_4-edge (3.728 keV) and Ga K-edge (10.367 keV).

3. Results

Figure 1(a) shows energy dependence near U M_4-edge of the intensities at the peak of the (1/2 1/2 1/2) reflections at 6 K. It is the first data of resonant peak obtained by using M_4-edge at BL22XU. The huge enhancement was observed due to the spin polarized 5f state contributing to the excitation process of M_4-edge. The absorption correction is not enough because the absorption of low energy x-ray by the sample is especially large at the energy of peak of the fluorescence yield spectrum, so the energy dependence looks double peaks.

We also obtained the intensities of the (5/2 5/2 5/2) reflections near Ga K-edge. Normally Ga is considered as a nonmagnetic element, however the energy dependence shows a large enhancement at the absorption edge as shown in Fig. 1(b). We observed the reflections at nonresonant energy (10.32 keV), the intensity was about 2 cps (at 100 mA synchrotron current), and then the enhancement at K-edge show about 300 in $UNiGa_5$. It was observed the enhancement at the energy of Ga K-edge in UGa_3[5)]. This resonant process is explained through a band theoretical approach that the origin of the magnetic resonant scattering intensity is the Ga-4p orbital polarization induced by the 5f orbital polarization of the neighboring U atom[6)]. We consider that the same mechanism applied to $UNiGa_5$.

There is no difference in the temperature dependence of the intensity of the reflections between U M_4-edge and Ga K-edge.

From above results, it is concluded that we observed the Ga-4p orbital polarization induced by the 5f orbital polarization in $UNiGa_5$.

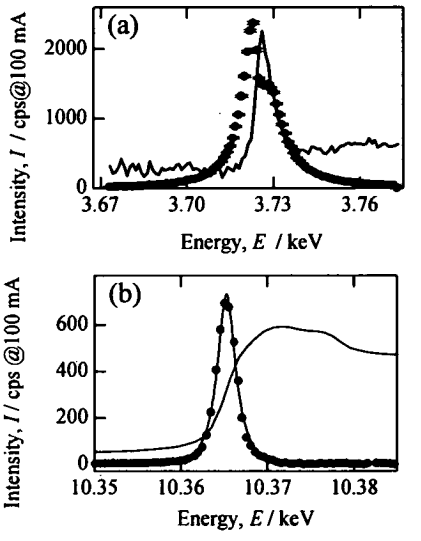

Fig. 1 Incident photon energy dependence of the intensity of magnetic reflection at 6 K (a) (1/2 1/2 1/2) at U M_4-edge, (b) (5/2 5/2 5/2) at Ga K-edge
The dashed lines show the fluorescence yield spectra.

References

1) S. Noguchi *et al.*, J. Magn. & Magn. Mater. **104-107**, 57, 1992
2) Y. Tokiwa *et al.*, Soc. Jpn. **71**, 725, 2002
3) H. Yamagami, Acta Phys. Polonica B, **34**, 1201 2003
4) Y. Tokiwa *et al.*, J. Phys. Soc. Jpn. **70**, 1744, 2001
5) D. Mannix *et al.*, Phys. Rev. Lett., **86**, 4128, 2001
6) M. Usuda *et al.*, Phys. Rev. B, **69**, 224402, 2004

5.5.5 Synchrotron Radiation Mössbauer Microspectroscopy of Corrosion Material

Takaya MITSUI and Makoto SETO [a)]
a) Research Reactor Institute, Kyoto University, Noda, Kumatori-cho, Sennan-gun, Osaka 590-0494, Japan

1. Introduction

Scanning type synchrotron radiation Mössbauer microscope (SSRMM) has been developed and improved at the BL11XU (JAERI) of SPring-8 [1]. As the two main upgrades of x-ray optics, we installed a Liquid-N_2-cooled Si (111) double crystal pre-monochrometer and a compact cylindrical x-ray focusing mirror [2,3]. As the result, the performance of SSRMM is improved remarkably. As a typical application experiment, we performed the line scanning measurement of nuclear forward scattering from the rust layer formed on the weathering steel.

2. Sample and Measurements

Weathering steel is a popular steel alloy widely used for structural purpose. It contains Cr, Cu, P, Ni etc slightly. When atmospherically exposed for several years, the steel corrodes at rates dependent on the environment. Than, the weathering steel develops an adherent corrosion coating that protects the steel from further corrosion. The latest report indicates that the rust layer is composed of the ultra-fine particles of Cr substituted goethite [4].

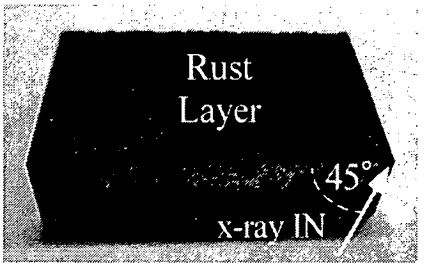

Chemical Components (wt/%)		
C	Si	Mn
0.11	0.2	0.66
P	S	Cu
0.014	0.01	0.3
Cr	Ni	Nb
0.51	0.13	-

Fig. 1 Photograph and chemical components of our measured corroded weathering steel

In our experiments, the measured weathering steel has been exposed in the atmosphere for 17 years under the girder of Yokkaichi-city-bridge in JAPAN. The monitored environmental conditions were 0.041mgNaCl/100cm^2/day and 0.109mgSO_3/100cm^2/day. Since the site is chlorine-rarefied area, protective corrosion coating layer formed on the steel surface firmly. Figure 1 shows the outside view and the chemical components of our measured sample. To avoid the extreme x-ray absorption, Mössbauer time spectra were measured at the edge part by a line scanning of the sample (See Fig.1.).

3. Results

The line scan micro Mössbauer time spectra using focusing beam of ϕ18μm were recorded from the coating surface inward toward the steel. Here the depth from the surface is expressed in the parameter L. Figures 5(a), (b), (c) and (d) show the time spectra at different four irradiation positions of L=38μm, 25μm, 18μm and 8μm respectively. As the results, a gradual decrease of the visibility of quantum beats pattern in the time spectra was observed as the line scan proceeded from the inner layer lying close the steel substrate to the outer surface layer. These results indicate that the outer layer was composed of mainly of a nano-phase goethite enough to show the super paramagnetic relaxation. In further research, if a more detailed analysis is performed, we will be able to decide the distribution of the particle size of nano-phase goethite at local parts of the sample.

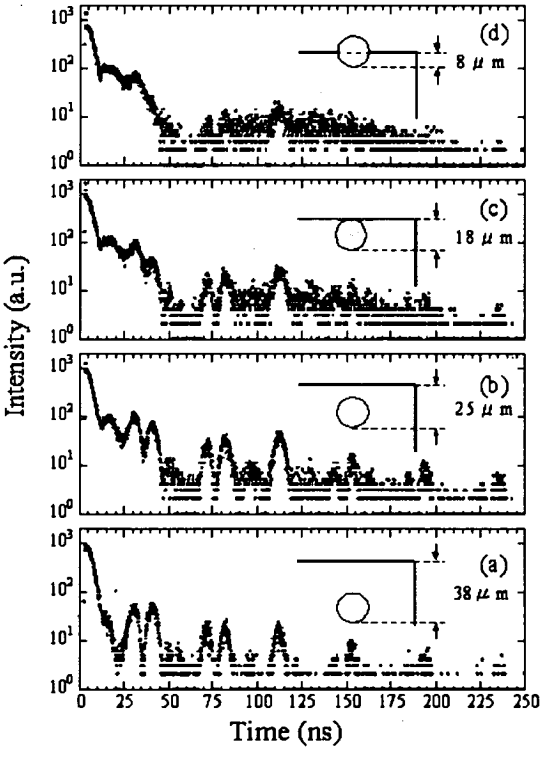

Fig. 2 Mössbauer time spectra measured at the depth parameter L of (a)38μm, (b) 25μm, (c) 18μm, and (d) 8μm

References

1) T.Mitsui et al., JJAP. **43**, No1, (2004)389.
2) H. Shiwaku et al., API. Conference proceedings, 705, (2004)659.
3) K. Tozawa et al., API. Conference proceedings, 705, (2004)671.
4) M.Yamashita et al., Corros. Sci. **45**, (2003)381.

5.6 Electronic Material Science

Yasuji MURAMATSU

The electronic material science group has constructed a soft x-ray beam line (BL23SU), in collaboration with the surface chemistry research group dating to 1997. We have developed a novel control system for the double-array APPLE-2 undulator (ID23) and a high-resolution beamline system which is mainly composed of a varied-line-spacing plane grating (VLSPG) monochromator. Two experimental stations for high-resolution photoemission spectroscopy (PES) and soft x-ray magnetic circular dichroism (MCD) spectroscopy have been installed in the radioisotope (RI) experimental hall, which is located downstream of the BL23SU. These stations perform research on strongly correlated electron systems and various functional materials.

In 2003, we have improved the optical performance of the beamline by cleaning the carbon-contaminated mirrors and re-alignment of optical elements, which provides approximately ten-times higher photon flux than in 2002 and the high energy resolution of 85 meV for PES measurements at the Au4f Fermi edge. Figure 1 demonstrates the improved photon flux. Experimental stations have also been further improved. For the MCD station, incident photon helicity can be switched at every scanning photon energy by the newly developed MCD control software, which enables the highly accurate MCD measurements. The pulsed laser deposition (PLD) system was connected to the PES station, which enable the clean surface PES measurements of various nano-structured thin films. By a transportable vacuum chamber of the PLD system, clean surface MCD measurements can also be achieved in the MCD station. Figure 2 shows the PES/MCD/PLD system in the RI experimental hall. Using this system, we have investigated electronic structure of the spinel-type chalcogenide, $CuIr_2S_4$, by high-resolution PES and diluted magnetic semiconductor, GaMnAs, by MCD. Feasibility of angle-resolved photoemission spectroscopy (ARPES) in the soft x-ray region of uranium compounds has also been successfully confirmed. In addition, electronic-structure/chemical-state analysis of light element materials has been proceeded by using the Advanced Light Source (ALS) at Lawrence Berkeley National Laboratory (LBNL). Soft x-ray emission spectra of polycyclic aromatic hydrocarbons can provide the structural information of nano-graphite.

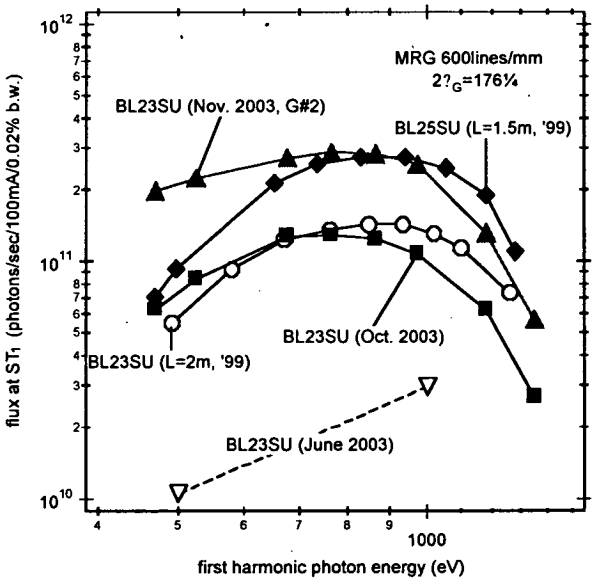

Fig. 1 Improved photon flux of BL23SU

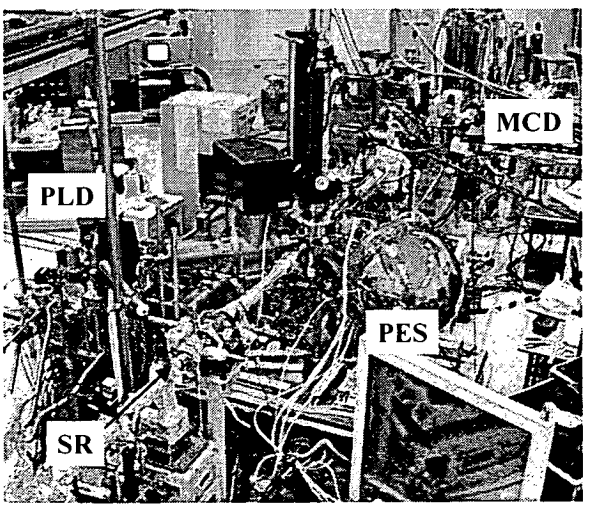

Fig. 2 PES/MCD/PLD system installed in the RI experimental hall of BL23SU

5.6.1 Photoemission spectroscopy of spinel-type compound $CuIr_2S_4$

Tetsuo OKANE, Shin-ichi FUJIMORI, Kazutoshi MAMIYA, Jun OKAMOTO, Yasuji MURAMATSU, Atsushi FUJIMORI[a], Hiroyuki SUZUKI[b], Takehiko MATSUMOTO[b], Takao FURUBAYASHI[b], Masaaki ISOBE[b] and Shoichi NAGATA[c]

a) Department of Complexity Science and Engineering, University of Tokyo

b) National Institute for Materials Science

c) Department of Materials Science and Engineering, Muroran Institute of Technology

1. Introduction

Spinel-type chalcogenide $CuIr_2S_4$ exhibits a metal-insulator transition (MIT) at the temperature T_{MI} ~ 230 K from the high-temperature metallic phase to the low-temperature insulating phase[1]. The transition is accompanied by a change of the crystal structure: the cubic spinel structure in the metallic phase turns to triclinic in the insulating phase [2]. The Cu ion was found to be in the monovalent state [3], and thus the probable ionic configuration is $Cu^{1+}Ir^{3+}Ir^{4+}(S^{2-})_4$. One possible explanation for the nature of the insulating phase is the charge ordering of Ir^{3+} and Ir^{4+} ions, accompanied by the dimerization of Ir^{4+} ions to cancel the spin moment[4]. However, the charge differentiation of Ir has not been experimentally confirmed yet. To clarify the electronic structure variation at MIT of $CuIr_2S_4$, we have performed temperature-dependent photoemission spectroscopy (PES) measurements using bulk-sensitive soft x-ray synchrotron radiation.

2. Experimental

Polycrystalline samples of $CuIr_2S_4$ were prepared by the solid-state reaction method. PES measurements were carried out using synchrotron radiation at beamline BL23SU of SPring-8. The excitation energy was 700 eV. The overall energy resolution was ~ 150 meV.

3. Results

Figure 1 shows Ir 4*f* core-level spectra of $CuIr_2S_4$ measured at the sample temperature of 250, 200 and 15 K. Across the transition temperature T_{MI} ~ 230 K, the line shape varied dramatically. First, the energy position of the $4f_{7/2}$ peak was shifted from 60.7 eV to 61.1 eV in going from 250 K to 200 K. Second, while the overall line-shape is highly asymmetric in the metallic phase, it becomes almost symmetric in the insulating phase. The spectrum remained almost identical between 200 and 15 K. The behavior should be associated with the variation of Ir 5*d* electron states across the metal-insulator transition. The broadness of the spectrum in the insulating phase may be a sign of two spin-orbit components due to charge separation, peaking at the different energy positions. To clarify what the temperature-dependent variation indicates, theoretical analysis should be necessary and is in progress.

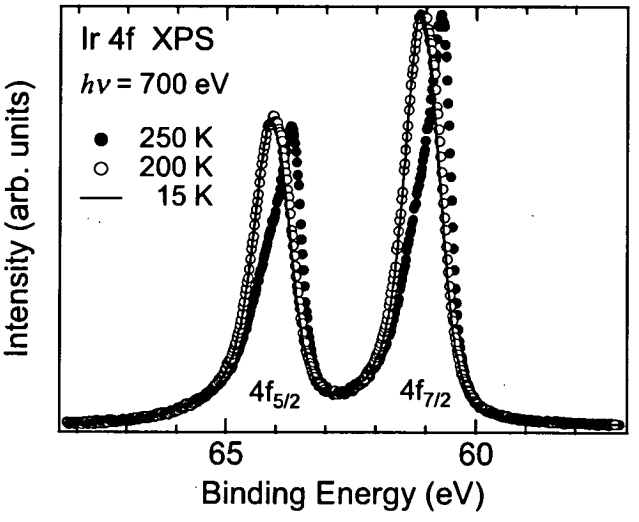

Fig. 1 Ir 4*f* core-level PES spectra measured at 250, 200 and 15 K

References

1) S. Nagata et al., Physica B **194-196**, 1077 (1994)
2) T. Furubayashi et al., J. Phys. Soc. Jpn. **63**, 3333 (1994)
3) J. Matsuno et al., Phys. Rev. B **55**, R15979 (1997)
4) P.G. Radaelli et al., Nature **416**, 155 (2002)

5.6.2 Soft X-ray angle-resolved photoemission study of $UFeGa_5$

Shin-ichi FUJIMORI, Kota TERAI, Koji TAKEDA, Tetsuo OKANE, Yuji SAITOH, Yasuji MURAMATSU, Atsushi FUJIMORI[a], Hiroshi YAMAGAMI[b], Yoshifumi TOKIWA[c], Shugo IKEDA[c], Tatsuma MATSUDA[c], Yoshinori HAGA[d], Etuji YAMAMOTO[d] and Yoshichika ŌNUKI[c,d]

a) Department of Complexity Science and Engineering, University of Tokyo
b) Department of Physics, Faculty of Science, Kyoto Sangyo University
c) Department of Physics, Graduate School of Science, Osaka University
d) Advanced Science Research Center, Japan Atomic Energy Research Institute

1. Introduction

Uranium compounds exhibit a rich variety of electrical and magnetic properties due to their peculiar behaviors of the U 5*f* states. Numbers of photoemission studies have been made on these compounds. However, it is still unclear which of two approaches, of the localized U 5*f* electrons or of the itinerant U 5*f* electrons, supplies a better basis for the description of these compounds. An essential question is whether the band structure calculation can be a good starting point for a description of their U 5*f* states. To understand this point, the photoemission experiments have been performed for many uranium compounds, and the obtained spectra have been compared with the results of the band structure calculations. Especially, angle-resolved photoelectron spectroscopy (ARPES) experiments are powerful tool to reveal the band structure of materials. The ARPES experiments for uranium compounds are generally done with the experimental He discharge lamp ($h\nu$ = 21.2 eV). One of the problems in these experiments is that the lower photoemission cross-section for U 5*f* states compared with ligand *s*, *p*, and *d* states. Therefore, the obtained band dispersions do not represent 5*f* states. In the present study, we have performed ARPES experiments for paramagnetic uranium compound $UFeGa_5$ with the soft X-ray synchrotron radiation ($h\nu$=500 eV) from BL23SU of SPring-8. In this photon energy, the relative cross section to U 5*f* states is large enough to distinguish from other states. Moreover, the spectra are relatively bulk-sensitive compared with the experiments with He discharge lamp.

2. Results

Figure 1 shows the Soft X-ray ARPES (SX-ARPES) spectra of $UFeGa_5$ measured along Γ-X direction. The photon energy used was $h\nu$=500 eV. The energy resolution was about 100 meV. In the spectra, some dispersive features were clearly observed. Especially, there is a dispersive band around Γ point in the energy region of 0.4 eV to E_F. From the photon energy dependence of the valence band spectra, it is found that the contribution from U 5*f* states is distributed at around 0.3 eV to Fermi level. Therefore, the energy dispersions in this region can be attributed to the itinerant U 5*f* states in this compound. Some bands cross the Fermi level, suggesting that U 5*f* states are forming the Fermi surface of this compound. The quasi-two-dimensional Fermi surface, which was observed in the dHvA experiments were observed by this photoemission experiment also. We believe that this is the first direct observation of the U 5*f* dispersions by the photoemission experiment. We have compared these results with the result of the band structure calculation. Some experimental bands are reproduced by the calculation, supporting that the itinerant description can describe some aspects of U 5*f* electrons in this compound.

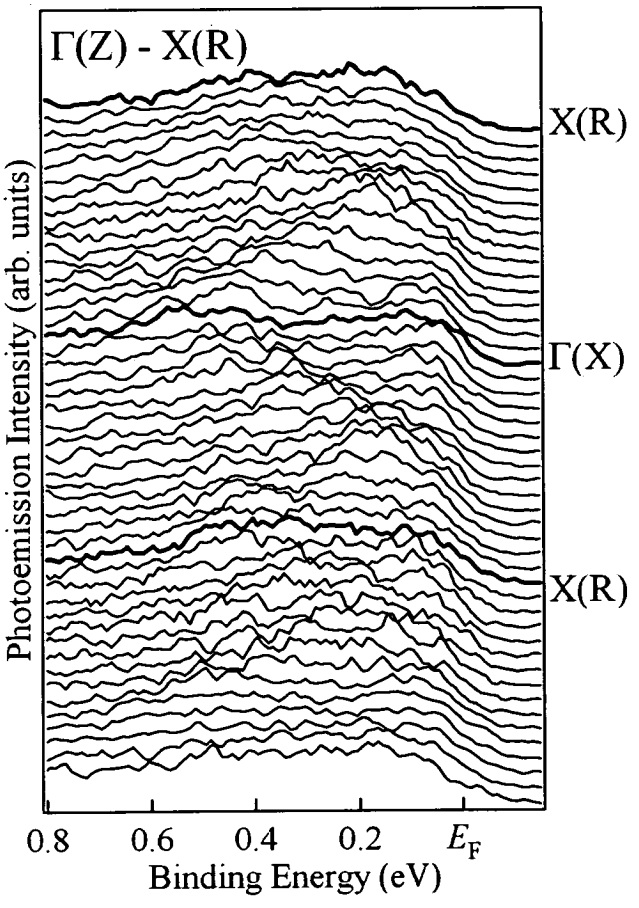

Fig. 1 SX-ARPES spectra of $UFeGa_5$

5.6.3 Magnetic field dependence of XMCD of GaMnAs

Yukiharu TAKEDA, Jun OKAMOTO [a)], Tetsuo OKANE, Shin-ichi FUJIMORI, Yuji SAITOH, Yasuji MURAMATSU, Atushi FUJIMORI [b)], Jun OKABAYASHI [c)], Masaharu OSHIMA [c)], Shinobu OHYA [c)] and Masaaki TANAKA [c)]
a) NSRRC
b) Faculty of Frontier Sciences, Univ. of Tokyo,
c) Faculty of Engineering, Univ. of Tokyo

Mn – doped GaAs has received the most attention due to the possibility of new functionality for future electronic devices [1)]. Because the MBE synthesis is made under thermal non-equilibrium condition, it is difficult to avoid the formation of various kinds of defects. Part of the doped – Mn atoms become paramagnetic rather than ferromagnetic [2)], meaning that those Mn atoms are in a different chemical environment than the substitutional Ga site. In order to obtain information about the different Mn atoms, we have applied the core-level magnetic circular dichroism (MCD) technique to Ga0.922Mn0.078As, which has the Curie temperature (TC) ~ 40 K. In order to separate signals from Mn atoms in different magnetic states, we utilized the fact that the paramagnetic and ferromagnetic moments respond differently to the magnetic field. That is, ferromagnetic moments saturate already at a low magnetic field whereas paramagnetic moments linearly increases up to high magnetic fields. The experiment was done at beamline BL23SU of SPring-8, where MCD measuring system with a superconducting magnet (up to 10 T) is established.

Figure 1 shows the Mn 2p core-level MCD spectra of a ferromagnetic Ga0.922Mn0.078As sample. Above TC (top panel), the entire MCD signal increases almost linearly with increasing magnetic field. Below TC (bottom panel), part of the MCD signal (the peak at hn ~ 638.5 eV) rapidly increases and then saturates already at 1 – 2 T whereas the remaining part (the peak at hn ~ 640 eV) slowly increases as the field increases up to 6 T. We therefore attribute the peaks at ~683.5 eV and ~640 eV to ferromagnetic and paramagnetic Mn atoms, respectively. The decomposed MCD spectra (not shown) indicate subtle differences in their multiplet structures, which probably originate from different As coordinations for the different Mn atoms.

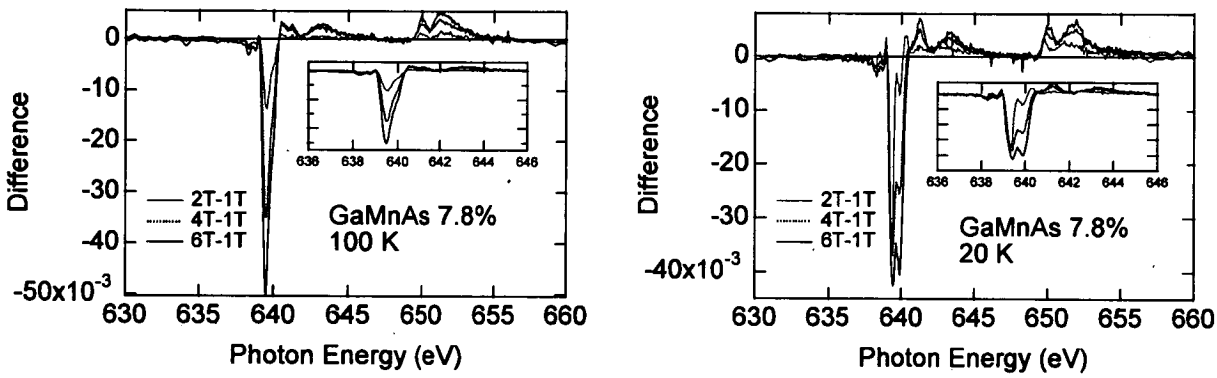

Fig. 1 Mn 2p core-level MCD of Ga0.922Mn0.078As with TC = 40 K
Plotted are the difference spectra from those taken at H = 1 T. Right: Paramagnetic phase above TC; Left: Ferromagnetic phase below TC.

References

1) H. Ohno, Science **281**, 951 (1998).
2) A. Oiwa, S. Katsumoto, A, Endo, M. Hirasawa, Y. Iye, H. Ohno, F. Matsukura, A. Shen, Y. Sugawara, Solid State Commun. **103**, 209 (1997).

5.6.4 Pulsed laser deposition (PLD) system

Kota TERAI, Tetsuo OKANE, Yukiharu TAKEDA, Shinichi FUJIMORI, Yuji SAITOH, Yasuji MURAMATSU, Jun OKAMOTO[a)] and Atsushi FUJIMORI[b)]
a) National Synchrotron Radiation Research Center Taiwan
b) Department of Complexity Science and Engineering, University of Tokyo

Perovskite transition-metal oxide materials have interesting properties such as superconductive and colossal magnetic resistance. Understanding of these properties is a challenging thesis for the exploitation of physics and applications. To investigate the electronic structure of these strongly correlated electron systems, experimental stations for high-resolution photoelectron spectroscopy (PES) and x-ray magnetic circular dichroism[1)] (XMCD) have been developed in soft x-ray beamline, BL23SU. These soft x-ray spectroscopic measurements often have some limitations on samples; Atomically smooth and clean surface should be required for the measurement samples.

Pulsed laser deposition (PLD) is a powerful technique to fabricate thin films which have smooth and clean surface. In addition, the PLD method is attracting a lot of interest to find new functional materials. We have therefore developed the PLS system which is combined with the PES and MCD experimental stations in BL23SU.

Figure 1 shows the PES/MCD/PLD system in BL23SU. This system achieves in-vacuum sample transfer between the PLD and PES/MCD experimental stations. to avoid surface contamination. Figure 2 shows a schematic image of the sample transferring. The samples prepared in the PLD system can be directly transferred to the PES chamber. The samples can also be transferred to the XMCD chamber using a transportable tiny vacuum chamber. This transportable chamber is equipped with an ion pump driven by a portable battery. This PLD system equips two lasers. One is a semiconductor laser for heating sample substrates. This laser can control temperature up to the 1000 °C in high oxygen atmosphere. Another is a Nd:YAG laser (355nm) for ablation. Morphology of the sample surface can be *in-situ* monitored by a refraction high energy electron diffraction (RHEED) method during the sample deposition.

We are now preparing some transition metal oxide thin films to demonstrate the capability of this PES/MCD/PLD system.

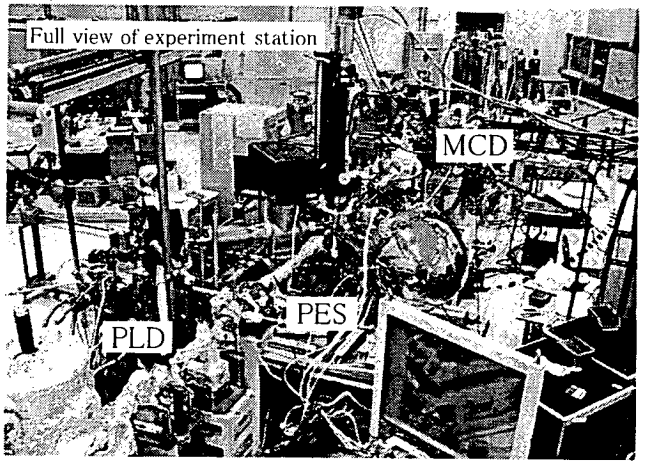

Fig. 1 Overview of the PES/MCD/PLD system in BL23SU

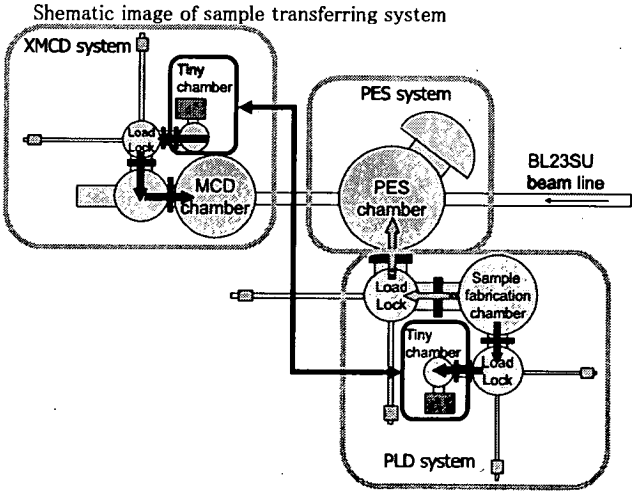

Fig. 2 Schematic view of the sample transferring system between the PLD system and the PES/MCD experimental stations

Reference

1) J. Okamoto *et al.*, The Eighth International Conference on Synchrotron Radiation Instrumentation **705**, 1110, 2004

5.6.5 Measurement of orbit fluctuation depending on the phase position of APPLE-2 undulator and the direction of its phase motion

Takeshi NAKATANI, Akane AGUI, Akitaka YOSHIGOE, Tomohiro MATSUSHITA[a)], Masaru TAKAO[a)], Masao TAKEUCHI[a)], Hideki AOYAGI[a)] and Hitoshi TANAKA[a)]

a) Japan Synchrotron Radiation Research Institute (JASRI)

1. Introduction

In the third generation facility, such as SPring-8, many insertion devices (IDs) are installed to generate brilliant synchrotron radiation light of which energy range is from ultra-violet to X-ray region. Since the electron beam is spatially sharp in this kind of light source, the fluctuation of electron beam orbits should be kept smaller than the submicron level to make the most of its high brilliance. There are many kinds of perturbation sources of closed orbit distortion (COD) and especially an error field of ID is one of the most serious sources. In general, this error field is usually corrected with a feed-forward correction algorithm, because the error field changes as the ID parameters (such as the gap distance, the phase shift, etc.) are changed. The strengths of steering magnets (STMs) are thus determined as a function of the ID gap distance and phase shift to cancel out the induced COD assuming (1) small background noise and (2) small eddy current effects without rapid field change.

On the other hand, a beam position monitor (BPM) in the SPring-8 storage ring takes about 30 seconds to measure the beam position distribution along the ring. Owing to this long period, the measured beam positions contain not only the contribution from the target perturbation but also that from the other sources, e.g., the chamber vibration, current ripple of magnet power-supply, etc. This means that by the usual BPM system, we can not measure the COD caused by the variation of the ID gap and phase precisely. Furthermore, some IDs in SPring-8 are used to quickly switch the polarization of emitted light. The fast polarization switching is performed by the fast field change of an ID which induces unexpected eddy current. Therefore, it is inadequate to apply the conventional method to the correction of error field of all kinds of ID.

In order to overcome this problem, it is necessary to develop the new method based on synchronized real-time measurement to extract only the orbit fluctuation caused by the error field of the ID. We report the detailed method and an application to obtain the effects of ID23 error field.

2. Concept

We developed the method with the real-time measurement system [1)] to investigate the influence of the perturbation source. When the perturbation source is changed periodically by changing the ID parameters, this operation modulates the orbit fluctuation with same periodicity. To rigorously relate between the perturbation source condition represented by the ID parameters and the orbit fluctuation, the real-time measurement requires synchronizing with the change of perturbation source. The periodical fluctuation can be extracted by removing no periodical components caused by ordinary perturbation sources.

The orbit fluctuation caused by the variation of the ID parameters is composed of two components. One is caused by the static error field of ID (static term) and the other is by eddy current effects due to a rapid field change (dynamic term). When the boundary condition of an eddy current is symmetric to a center of ID, the eddy current effect in one direction is completely cancelled out by addition to the effect in another direction. This means that the dynamic term is cancelled out by summing up a couple of dynamical changes of ID parameters with moving opposite directions, for example, open / close in the gap motion and coming / going in the phase motion, etc. The static and dynamic terms are distinguished by two steps. By this cancellation, only the static term can be extracted firstly and precisely and consequently corrected. Then, after removing the static term, the dynamic term is main component and can be investigated. We can obtain the static and dynamic terms of the orbit fluctuation separately.

3. Result

We apply the method to the extraction of the orbit fluctuation caused by the error field related to the phase motion of APPLE-2 type undulator installed in BL23SU (ID23) [2)]. We measure the orbit fluctuation in synchronization with ID23 phase motion of which speed is 30mm/sec. The periodical pattern of the phase motion is modified triangular, in which the phase position is halted for 1 second when the driving

direction is turned (0mm→+60mm→ -60mm→+60mm→0mm) (see Fig. 1 (a) upper line). The periodical pattern was optimized for the Wavelet Transform so that the reference of the orbit fluctuation is zero.

The middle line in Fig. 1 (a) shows the horizontal fluctuations observed at BPM15 and the bottom line shows the extracted fluctuation with the Wavelet Transform filter. Figure 1 (b) shows each data (Fig. 1 (a) bottom line) in the range of -60mm→60mm at the phase. In the figure, we set the origin of the time axis to the time when the phase position is at -60mm. The accuracy of this method is evaluated to be 3 - 4 microns from the variation of each line.

Here, we extract the static term and the dynamic term caused by ID23 phase motion. The crosses in Fig. 2 (a) indicate the average of the orbit fluctuations during coming and going in the phase motion without the feed-forward correction. The electron orbit fluctuation of about 150 μ m is observed in the region of the phase motion (from -60mm to 60mm). We correct the averaged fluctuation as shown the open circles in Fig. 2 (a) and compare the fluctuation during the phase motion from -60mm to 60mm (crosses) with that from 60mm to -60mm (open circles) as shown in Fig. 2 (b). Even after the correction of the averaged fluctuation, the electron orbit fluctuation of about 20 μ m remains, which is caused by the eddy current effect on the ID23 chamber. And also, the fluctuation in each driving direction (-60mm→60mm and 60mm→-60mm) shows the symmetric pattern as expected. Figure 2 (b) actually shows that the static and dynamic terms are obtained by our method separately.

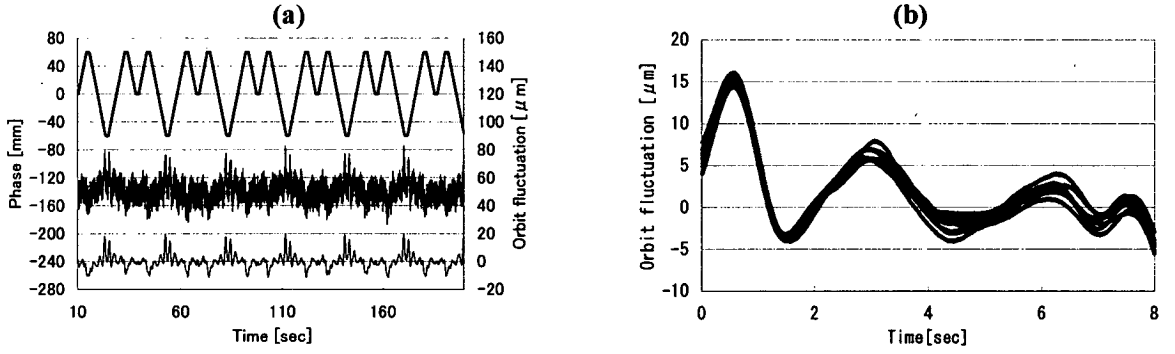

Fig. 1 The horizontal fluctuations caused by ID23 phase motion measured at BPM15. (a): The upper line shows the ID23 phase position, the middle is the observed orbit fluctuation and the bottom is the orbit fluctuation filtered by the Wavelet Transform. (b): The orbit fluctuation (Fig. 1 (a) bottom line) in the range of -60mm→60mm at the phase.

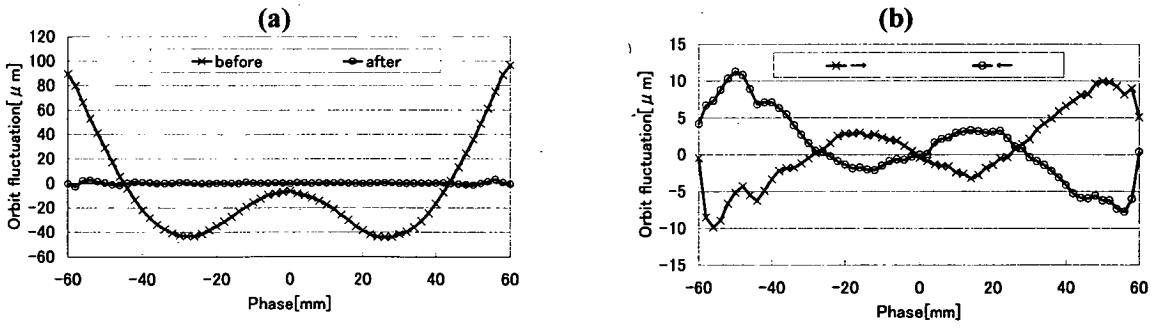

Fig. 2 The horizontal fluctuations caused by ID23 phase motion measured at BPM15. (a): The crosses and circles show the static term of the orbit fluctuation before and after the correction, respectively. (b): The crosses (circles) mean the data measured during changing ID23 phase from -60mm to 60mm (60mm to -60mm).

References

1) Nakatani, T. et al., "Applications of PC Based Off-The-Shelf Measurement System", Proc. of PCaPAC2002, Frascati, Italy.

2) Sasaki, S., Kakuna, K., Takada, T., Shimada, T., Yanagida, K., Miyahara, Y., Nucl. Instrum. Methods Phys. Res. A331,763(1993)

5.6.6 Soft x-ray emission spectroscopy of polycyclic aromatic hydrocarbons

Yasuji MURAMATSU, Kana TOMIZAWA[a)], Jonathan D. DENLINGER[b)] and Rupert C. C. PERERA[b)]
a) Himeji Institute of Technology
b) Lawrence Berkeley National Laboratory

1. Introduction

Soft x-ray emission spectroscopy with highly brilliant synchrotron radiation recently has been utilized to characterize various carbon materials. However, many organic carbon materials usually exhibit broad structures in x-ray emission spectra. To extract useful information on the chemical-bonding-states of carbon materials from the soft x-ray emission spectra, we have measured C*K* x-ray emission spectra of various polycyclic aromatic hydrocarbon (PAH) compounds, which can be regarded as components of important industrial carbon materials, such as carbon black and carbon nanotubes, and compared their spectral features.

2. Experiments

Commercially available PAH compounds (*p*-terphenyl, anthracene, naphthacene, pentacene, triphenylene, pyrene, perylene, coronene), and highly oriented pyrolytic graphite (HOPG) were used for the spectroscopic measurements. The molecular structure of the PAH compounds will be described later in Figure 1. Soft x-ray emission spectra in the C*K* region were measured using a grating x-ray spectrometer installed in the undulator beamline, BL-8.0.1 at the Advanced Light Source (ALS).

3. Results and Discussion

Figure 1 shows the C*K* x-ray emission spectra of the PAH compounds and HOPG. In the broad main peak features of the PAH compounds, however, the peak energy shift depends on the molecular structure. To obtain quantitative information on PAH compounds from the spectra, the main peak features in the region between the 276.9 eV and 278.2 eV were approximated with linear functions. The slopes of the linear functions on the PAH compounds are described in the upper panel of Figure 2. The slopes are plotted in the lower panel as a function of the percentage of hydrogenated outer carbons. The data of PAH compounds, except for HOPG, can be approximated by linear functions, represented in the Figure by a solid line. This linear relation between the slopes of PAH and the percentage of hydrogenated outer carbon atoms can be expanded to HOPG. This finding means that we may easily extract the degree of hydrogenation in PAH-based carbon materials.

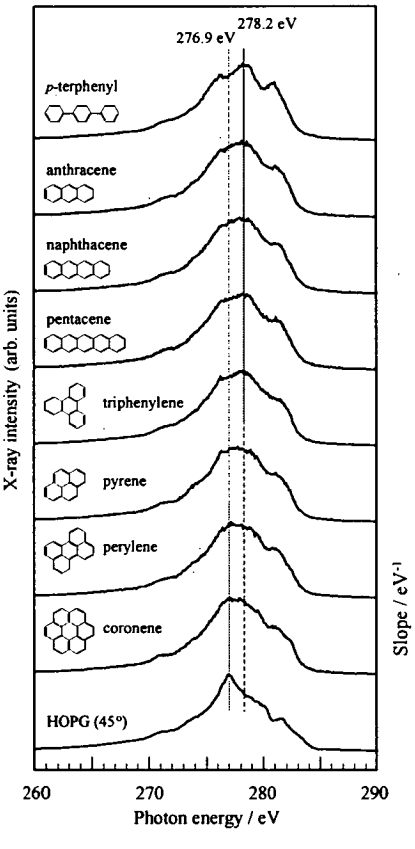

Fig. 1 C*K* x-ray emission spectra of PAH compounds

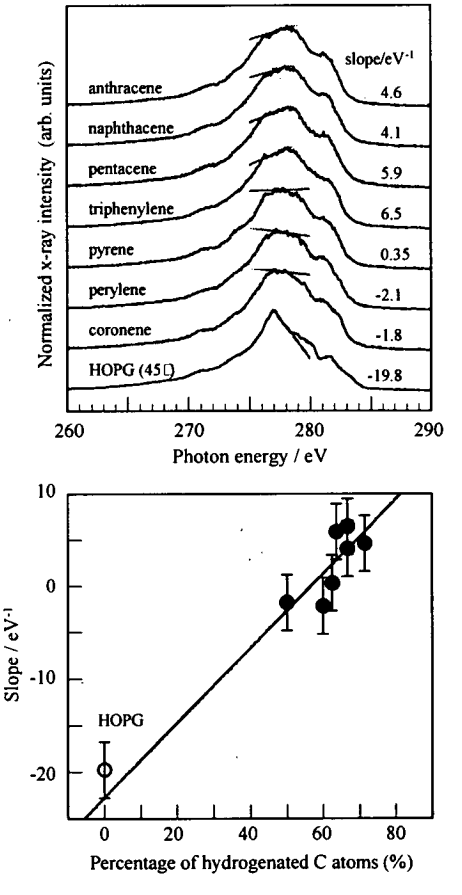

Fig. 2 Approximated slopes near the main peaks (upper) and the relation between the slopes and the percentage of hydrogenated outer carbon atoms (lower)

5.6.7 Soft X-ray MCD Measurement of [Co/Pd]n Perpendicular Magnetic Films

Akane AGUI, Masaichiro MIZUMAKI[a)], Tomohiro MATSUSHITA[a)], Toru ASAHI[b)], Jun KAWAJI[b)], Junichi SAYAMA[b)] and Tetsuya OSAKA[b)]

a) Japan Synchrotron Radiation Research Institute

b) Waseda University

1. Introduction

Perpendicular magnetic recording has been recognized as a technology indispensable for magnetic recording of an area density over 100 Gbits/inch^2 [1)]. In recent years, a sputter-deposited multilayered film $[Co/Pd]_n$ (n is the lamination number of the Co and Pd layers) has attracted much attention as a perpendicular magnetic recording medium for high-density magnetic recording. To improve the performance of the $[Co/Pd]_n$ film as medium, a number of investigations for developing a suitable seedlayer have been carried out[2)], and the most effective seedlayer is still requested

The selectivity of soft X-ray absorption and magnetic circular dichroism spectroscopy (XAS and MCD) allows us to investigate the magnetic and electronic states of a selected orbital of a target element. We report that the electronic and spin states of [Co/Pd] multilayered perpendicular magnetic films with various seedlayers by means of XAS and MCD at the Co $L_{2,3}$-edges.

2. Experimental

The $[Co/Pd]_n$ perpendicular magnetization film consisting of n=20 or 10 bi-layers of Co (0.2 nm) and Pd (0.8 nm) was deposited on a C, Si, or Pd/Si seedlayer with dc magnetron sputtering. The values of macroscopic magnetic properties, such as the saturation magnetization (M_s), perpendicular coercivity (H_c) and anisotropy constant (K_u), change 50-60% by seedlayers[3,4)]. A 5 nm-thick C overcoat layer was deposited on the Co top layer of the $[Co/Pd]_n$ film to avoid oxidation of the sample.

The XAS and MCD spectra at the Co $L_{2,3}$-edges of the $[Co/Pd]_n$ perpendicular magnetization films were measured using synchrotron radiation at soft X-ray beamline BL23SU at SPring-8, Japan[5)].

3. Results

Figure 1 shows XAS spectra of the Co $L_{2,3}$-edges of the $[Co/Pd]_n$ films with various seedlayers, where the seedlayer is described under each spectrum. The XAS of the Co $L_{2,3}$-edges mainly shows the Co 3*d* unoccupied electronic state in the upper part of the $[Co/Pd]_n$ film. The spectral shape is similar to each other.

The expected value of the microscopic total magnetic moment ($\langle L_z \rangle + 2\langle S_z \rangle$) of Co 3*d* was estimated by applying so-called "sum rule" [6)] to Iiso and IMCD ($\langle L_z \rangle$: the orbital magnetic moment, $\langle S_z \rangle$: the spin magnetic moment). The expected values were found to be about 1 mB, in spite of the fact the macroscopic property (*e.g.* M_s) changed with seedlayer condition. We concluded that the seedlayer changes macroscopic magnetic properties of the [Co/Pd] multilayered films without affecting the electronic and spin states of the upper layers of Co[7)].

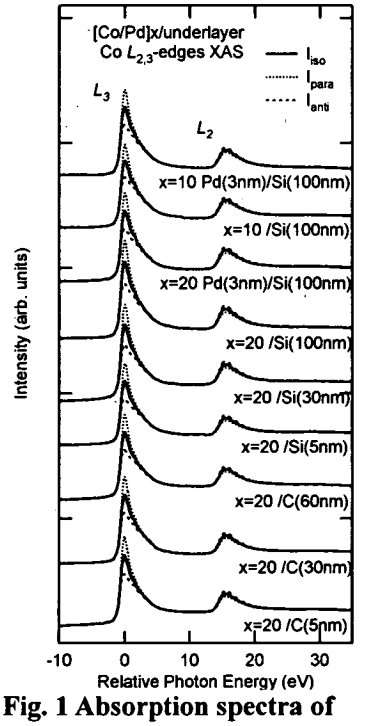

Fig. 1 Absorption spectra of films with various seedlayer near the Co $L_{2,3}$-edges
The photon energy of the Co L_3 peak was set at 0 eV.

References

1) R. Wood, IEEE Trans. Magn. 36, (2000) 36.
2) For instance, H. Ohmori and A. Maesaka, J. Magn. Magn. Mater. 235 45 (2001).
3) T. Onoue, *et.al.*, J. Magn. Magn. Mater. 235, 82 (2001).
4) J. Kawaji *et al.*, J. Magn. Mang. Mater. 251 (2001) 220.
5) A. Agui *et al.*, Rev. Sci. Inst. 72 (2001) 3191.
6) B. T. Thole et al., Phys. Rev. B 32 (1985) 5107.
7) A. Agui, M. Mizumaki and T. Matsushita, T. Asahi, J. Kawaji, J. Sayama and T. Osaka, Journal Applied Physics, 95 (2004) 7825.

5.7 Synchrotron Radiation Simulation Research

5.7.1 Magnetic resonant x-ray scattering at the Ga *K* edge in UGa_3

Manabu USUDA, Jun-ichi IGARASHI, Akio KODAMA[a)]
a) Fuji Research Institute Corporation

1. Introduction

In transition metals, the 4*p* states compose a part of unoccupied states. The 4*p* states usually attract only minor interest because they do not contribute to magnetic or orbital orders. However, understanding 4*p* states has become important with the development of x-ray spectroscopy using *K* edges of transition metals, in which the 1s core electrons are excited to the 4*p* states through the dipolar transition. Recently a magnetic resonant x-ray scattering (MRXS) experiment was carried out on the *K* edge of Ga in UGa_3. [1)] In the experiment a relatively large resonant intensity was observed, though the Ga atom is usually considered as a nonmagnetic ion. The purpose of this study is to clarify the origin of the MRXS intensity in UGa_3, on the basis of a band-structure calculation.

2. Results

The calculation is based on the density-functional theory within the local-density approximation (LDA). Relativistic effects except for the spin-orbit interaction (SOI) are included within the scalar-relativistic approximation, while for the valence states we include the SOI approximated as $\propto(1/r)(dV/dr)L_zS_z$ at each variational step. We found that the exchange splitting in the Ga 4*p* states is quite small compared with that in the U 5*f* states, while there is a small difference between the Ga 4*p* DOS for $m = +1$ and $m = -1$ orbitals. The difference (the orbital polarization of the Ga 4*p* states) appears from approximately -0.2 eV to 2 eV and becomes the largest at 1 eV. This difference is essential to give rise to the MRXS intensity, as shown below.

Figure 1 shows the calculated MRXS spectrum on the $\sigma-\pi'$ channel for $\mathbf{G}=(7/2, 7/2, 7/2)_c$ as a function of photon energy. The experimental data are taken from Ref. 1. A resonant peak is found at 10.365 keV. The peak position is in agreement with that of the experiment, while the peak width is much underestimated in the calculation. It may be important to consider the effect of the multiplet interaction of the U 5*f* states as well as of band hybridization.

In order to clarify how the Ga 4*p* orbital polarization is induced, we calculate the spectra by turning the SOI off separately on the Ga 4*p* states and the U 5*f* states, respectively. The results are summarized in Fig. 2. It is found that the MRXS intensity largely diminished when the SOI on the U 5*f* states is turned off (the dotted line in Fig. 2), while slightly reduced when the SOI on the Ga 4*p* orbital is turned off (the long dashed line in Fig. 2). This indicates that the Ga 4*p* orbital polarization originates mainly from the large 5*f* orbital polarizations at neighboring U atoms through the Ga 4*p* and U 5*f* hybridization.

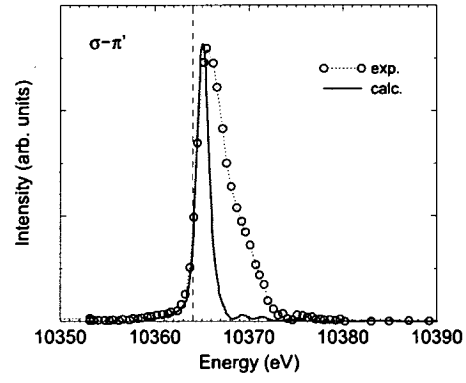

Fig. 1 MRXS spectra in the $\sigma-\pi'$ channel for $\mathbf{G}=(7/2, 7/2, 7/2)_c$ as a function of photon energy in comparison with the experimental spectra
The vertical line indicates the Fermi level.

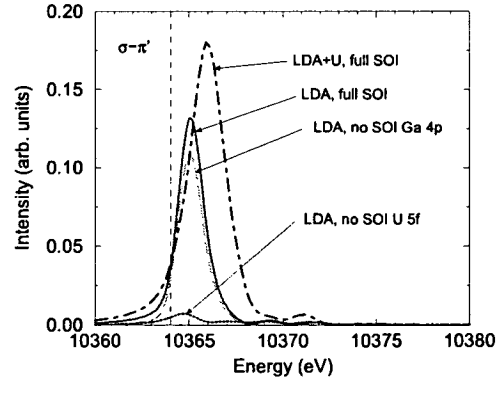

Fig. 2 MRXS spectra in the LDA with turning the SOI off separately on the Ga 4p states and U 5f states, respectively
The MRXS spectra in the LDA and LDA+U (U_{eff}= 2 eV) with full SOI are also shown.

Reference

1) D. Mannix, A. Stunault, N. Bernhoeft, L. Paolasini, G.H. Lander, C. Vettier, F. de Bergevin, D. Kaczorowski, and A. Czopnik, Phys. Rev. Lett. **86**, 4128 (2001).

5.7.2 Theoretical analysis of Cu-K edge resonant X-ray scattering in insulating cuprates

Takuji NOMURA and Jun-ichi IGARASHI

1. Introduction

Resonant inelastic x-ray scattering (RIXS) in the hard x-ray regime is recently becoming a promising and powerful tool to clarify the momentum-resolved charge excitation properties of solids in the relatively high-energy range, owing to highly brilliant synchrotron radiation. Actually they have succeeded in obtaining momentum-resolved charge excitation spectra in some materials. Among them, the RIXS utilizing the Cu-K edge in Cu oxides attracts much attention. Cu-K edge RIXS experiments were performed for La_2CuO_4 [1] and quasi-one-dimensional (Q1D) copper oxides, $SrCuO_2$ [2),3)]and Sr_2CuO_3 [2]. In La_2CuO_4 characteristic two-peak structure was observed around 2 and 4 eV energy loss. It is interesting that the 2 eV peak shows a relatively large dispersion ($\sim$1 eV) along the symmetry line q=(0,0)-(π,0) in the Brillouin zone, and is drastically suppressed around q=(π,π), where q is the in-plane transferred momentum of the photon. In the Q1D cuprates, characteristic two-peak structure was observed around 2 and 6 eV energy loss. The 2 eV peak shows a relatively large dispersion. The 2 eV peak around q=0 shifts by about 1.1 eV at q=π. In the present study, we have analyzed the RIXS in these cuprates microscopically. The theoretical results reproduce the characteristic spectral properties in the recent experiments semi-quantitatively[4),5)].

2. Theory

In the Cu-K edge RIXS process, the Cu1s core electron is excited to the empty Cu4p band by the resonant absorption of the incident photon. The created core hole scatters the Cu3d electrons through the inter-orbital Coulomb interaction. The emitted photon loses the equal amount of energy to that required to the excitation of the Cu3d electrons.

In the calculation of the RIXS spectra, the antiferromagnetic ground state of the cuprates is described within the Hartree-Fock theory, and the strong many-body correlation effects in the excitation processes are taken into consideration within the random phase approximation, using the Keldysh diagrammatic technique[4]. Concerning the Cu1s-3d inter-orbital Coulomb interaction, we have applied the Born approximation simply. The electronic structure of the Cu-O system is described by dp-Hamiltonian, where the parameters are determined from LDA calculations.

3. Results

The obtained RIXS spectra for the Q1D cuprates are shown as a function of the photon energy loss in Fig. 1. The two main spectral weights around 2 and 6eV are reproduced. The low energy peak A exhibits a relatively large shift (1 eV) along the Cu-O chain, while the high energy peak B does not show, in agreement with experimental results. We have found that the strong many-body correlation effect is essential for this large dispersive behavior.

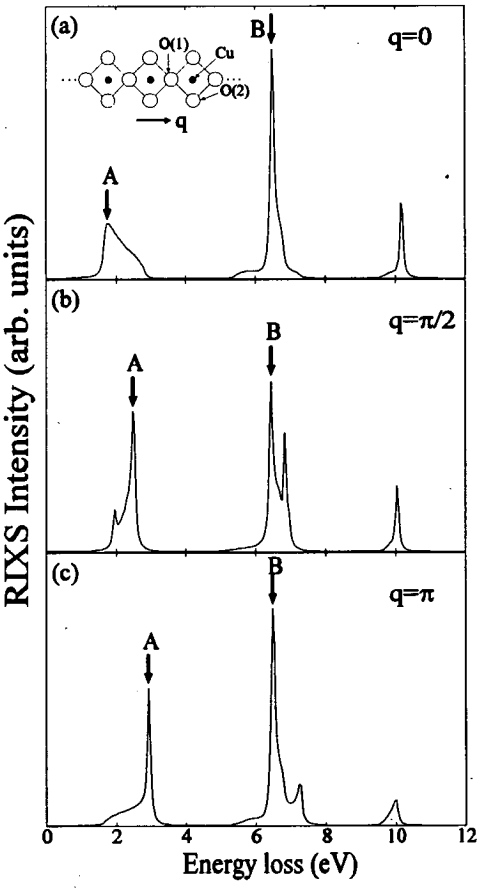

Fig. 1 The calculated RIXS spectra for the three cases of transferred momenta, q=0, π/2, π

References

1) Y.J. Kim, et al., Phys. Rev. Lett. **89,** 177003, 2002.
2) M.Z. Hasan, et al., Phys. Rev. Lett. **88,** 177403, 2002.
3) Y.J. Kim et al., Phys. Rev. Lett. **92,** 137402, 2004.
4) T. Nomura and J. Igarashi, J. Phys. Soc. Jpn. **73,** 1677, 2004.
5) T. Nomura and J. Igarashi, cond-mat/0312624.

6. List of publications

6.1 List of publications on Advanced Photon Research Center

High Peak Power Laser Development (Laser System Development Group)

1. Journals

1) 25J green beam generation using large aperture $CsLiB_6O_{10}$ frequency doubler
Kiriyama Hiromitsu, Inoue Norihiro*, Yamakawa Koichi
The Review of Laser Engineering 31, 4, 282-285 (2003/04)

2) High power pulsed green lasers
Kiriyama Hiromitsu
Recent Research Developments in Optics, Vol.3, 155-171 (2003/12)

3) Optimized energetic particle emissions from Xe clusters in intense laser fields
Fukuda Yuji*, Yamakawa Koichi, Akahane Yutaka, Aoyama Makoto*, Inoue Norihiro*, Ueda Hideki*, Kishimoto Yasuaki
Physical Review A 67, 6, 061201_1-061201_4 (2003/06)

4) 360-W average power operation with a single-stage diode-pumped Nd:YAG amplifier at a 1-kHz repetition rate
Kiriyama Hiromitsu, Yamakawa Koichi, Nagai Toru*, Kageyama Nobuto*, Miyajima Hirofumi*, Kan Hirofumi*, Yoshida Hidetsugu*, Nakatsuka Masahiro*
Optics Letters 28, 18, 1671-1673 (2003/09)

5) 0.85-PW, 33-fs Ti:sapphire laser
Aoyama Makoto*, Yamakawa Koichi, Akahane Yutaka, Ma J.*, Inoue Norihiro*, Ueda Hideki*, Kiriyama Hiromitsu
Optics Letters 28, 17, 1594-1596 (2003/09)

6) 30-mJ, diode-pumped, chirped-pulse Yb:YLF regenerative amplifier
Kawanaka Junji, Yamakawa Koichi, Nishioka Hajime*, Ueda Kenichi*
Optics Letters 28, 21, 2121-2123 (2003/11)

7) Two-color chirped-pulse amplification in an ultrabroadband Ti:sapphire ring regenerative amplifier
Yamakawa Koichi, Barty C. P. J.*
Optics Letters 28, 23, 2402-2404 (2003/12)

8) Ionization of many-electron atoms by ultrafast laser pulses with peak intensities greater than 10^{19} W/cm^2
Yamakawa Koichi, Akahane Yutaka, Fukuda Yuji*, Aoyama Makoto, Inoue Norihiro*, Ueda Hideki*
Physical Review A 68, 6, 065403_1-065403_4 (2003/12)

9) All solid-state ultrashort-pulse laser by using ytterbiumu-doped materials (in Japanese)
Nishioka Hajime*, Kawanaka Junji
Optical Alliance 14, 11, 21-25 (2003/11)

10) Laser pulse compression and amplification by stimulated backword Raman scattering of $Ba(NO_3)_2$} and $CaCO_3$ crystals (in Japanese)
Deki Kyoichi*, Matsuoka Fumiaki*, Tei Kazuyoku*, Arisawa Takashi
The Review of Laser Engineering 31, 12, 854-859 (2003/12)

11) X-ray study of microdroplet plasma formation under the action of superintense laser radiation
Fukuda Yuji*, Yamakawa Koichi, Akahane Yutaka, Aoyama Makoto, Inoue Norihiro*, Ueda Hideki*, Abdallah Jr. J.*, Csanak G.*, Faenov A. Y.*, Magunov A. I.*, Pikuz T. A.*, Skobelev I. Y.*, Boldarev A. S.*, Gasilov V. A. *
JETP Letters 78, 3, 115-118 (2003/08)

12) Time-dependent Boltzmann kinetic model of X rays produced by ultrashort-pulse laser irradiation of argon clusters
Abdallah Jr. J.*, Csanak G.*, Fukuda Yuji*, Akahane Yutaka, Aoyama Makoto, Inoue Norihiro*, Ueda Hideki*, Yamakawa Koichi, Faenov A. Y.*, Magunov A. I.*, Pikuz T. A.*, Skobelev I. Y.*
Physical Review A 68, 6, 063201_1-063201_8 (2003/12)

13) Table-top lasers create ultrahigh peak powers (in Japanese)
Yamakawa Koichi
OYO BUTURI 73, 2, 186-193 (2004/02)

14) Many-electron dynamics of a Xe atom in strong and super-strong laser fields
Yamakawa Koichi, Akahane Yutaka, Fukuda Yuji, Aoyama Makoto, Inoue Norihiro, Ueda Hideki, Utsumi Takayuki
Physical Review Letters, 92, 12, 123001_1-123001_4 (2004/03)

2. Proceedings

1) X-ray radiation of clusters irradiated by ultrafast, high-intensity laser pulses
Fukuda Yuji*, Akahane Yutaka, Aoyama Makoto, Inoue Norihiro*, Ueda Hideki*, Kishimoto Yasuaki, Yamakawa Koichi, Faenov A. Y.*, Magunov A. I.*, Pikuz T. A.*, Skobelev I. Y.*, Abdallah Jr. J.*, Csanak G.*, Boldarev A. S.*, Gasilov V. A.*
Laser-Generated & Other Lab. X-Ray & EUV Sources (Proceedings of SPIE Volume 5196) 234-243 (2004)

2) Development of high power pulsed green lasers (in Japanese)
Kiriyama Hiromitsu, Yamakawa Koichi
Reports on the 313th Topical Meeting of the Laser Society of Japan, Advanced Solid State Lasers and Their applications No. RTM-03-18～26 1-6(2003/09)

3. JAERI-Reports

1) Development of a high-energy, ultrabroadband Ti:sapphire ring regenerative amplifier
Yamakawa Koichi
JAERI-Research 2003-017 (2003/09)

2) Ionization dynamics of a xenon atom in super-strong laser fields
Yamakawa Koichi, Akahane Yutaka, Fukuda Yuji*, Aoyama Makoto, Inoue Norihiro*, Ueda Hideki*, Utsumi Takayuki*
JAERI-Research 2003-030 (2003/12)

4. Patents

(1) Patents pending

1) Laser amplifier
Kawanaka Junji
Japan patent application number 2004-011482

2) Method for amplifying a solid-state laser light
Kiriyama Hiromitsu, Yamakawa Koichi
Japan patent application number 2004-060438

3) Amplifier for solid-state laser light
Kiriyama Hiromitsu, Yamakawa Koichi
Japan patent application number 2004-078355

(2) Patent

1) Method for laser-diode (LD) pumping of a solid-state laser light
Kiriyama Hiromitsu, Maruyama Yoichiro, Arisawa Takashi
Japan patent number 3514981

X-ray Laser Development (X-ray Laser Research Group)

1. Journals

1) Measuremernt of the gain medium of plasma X-ray laser with spatial resolution
Tanaka Momoko, Kawachi Tetsuya
Journal of Plasma and Fusion Research 79, 4, 386-390 (2003/04)

2) X-ray laser beam with diffraction-limited divergence generated with two gain media
Tanaka Momoko, Nishikino Masaharu*, Kawachi Tetsuya, Hasegawa Noboru, Kado Masataka, Kishimoto Maki, Nagashima Keisuke, Kato Yoshiaki
Optics Letters 28, 18, 1680-1682 (2003/09)

3) Development of a pumping laser system for X-ray laser research
Kawachi Tetsuya, Kado Masataka, Tanaka Momoko, Hasegawa Noboru, Nagashima Keisuke, Sukegawa Kouta*, Lu P.*, Takahashi Kenjiro*, Namba Shinichi*, Koike Masato, Nagashima Akira, Kato Yoshiaki
Applied Optics 42, 12, 2198-2205 (2003/04)

4) Demonstration of a soft-X-ray laser at 13.9 nm with full spatial coherence
Nishikino Masaharu*, Tanaka Momoko, Nagashima Keisuke, Kishimoto Maki, Kado Masataka, Kawachi Tetsuya, Sukegawa Kouta*, Ochi Yoshihiro, Hasegawa Noboru, Kato Yoshiaki
Physical Review A 68, 6, 061802_1-061802_4 (2003/12)

5) Study of the anisotropy of electron energy distribution of optical-field ionized oxygen plasma by using polarization spectroscopy
Kim J.*, Kim D. E.*, Kawachi Tetsuya, Hasegawa Noboru, Sukegawa Kouta*, Iwamae Atsushi*, Fujimoto Takashi*
Journal of the Optical Society of Korea 7, 3, 145-149 (2003/09)

6) Population kinetics of lithiumlike and berylliumlike ions in low temperature dense recombining plasma
Kawachi Tetsuya
Phys. Rev. E 67, 016409, 1-8 (2003)

7) Development of soft X-ray microscopy system using X-ray laser in JAERI Kansai
Kishimoto Maki, Tanaka Momoko, Tai RenZhong, Sukegawa Kouta, Kado Masataka, Hasegawa Noboru, Tang Huajing, Kawachi Tetsuya, Lu P., Nagashima Keisuke, Daido Hiroyuki, Kato Yoshiaki, Nagai K., Takenaka H.
J. Phys. IV France 104, 141-143 (2003)

8) Development of a laser-pumped X-ray laser with full spatial coherence
Nagashima Keisuke, Tanaka Momoko, Nishikino Masaharu*, Kishimoto Maki, Kado Masataka, Kawachi Tetsuya, Hasegawa Noboru, Ochi Yoshihiro, Sukegawa Kouta*, Tai RenZhong*
Journal of Plasma and Fusion Research 80, 3, 236-240 (2004/03)

9) Observation of strong soft-x-ray amplification at 8.8 nm in the transient collisional-excitation scheme
Kawachi Tetsuya, Sasaki Akira, Tanaka Momoko, Kishimoto Maki, Hasegawa Noboru, Nagashima Keisuke, Koike Masato, Daido Hiroyuki, Kato Yoshiaki
Phys. Rev. A69, 033805 (2004)

2. Proceeding

1) Demonstration of Soft X-ray Laser with Full Spatial coherence and Diffraction Limited Divergence
Nishikino Masaharu, Tanaka Momoko, Kishimoto Maki, Kado Masataka, Kawachi Tetsuya, Sukegawa Kouta, Ochi Yoshihiro, Hasegawa Noboru, Nagashima Keisuke, Kato Yoshiaki
Inertial Fusion Science and Applications 2003 (Monterey, California, 2003, Sep.)

2) Development of a full spatial coherent x-ray laser at 13.9 nm
Nagashima Keisuke, Tanaka Momoko, Nishikino Masaharu, Kishimoto Maki, Kado Masataka, Kawachi Tetsuya, Hasegawa Noboru, Ochi Yoshihiro, Sukegawa Kouta, Tai RenZhong, Kato Yoshiaki
Proceedings of SPIE, 5197, 1-8 (2003)

3) Development of a full spatial coherent x-ray laser at 13.9 nm and its applications
Nagashima Keisuke, Tanaka Momoko, Nishikino Masaharu, Kishimoto Maki, Kado Masataka, Kawachi Tetsuya, Hasegawa Noboru, Ochi Yoshihiro, Sukegawa Kouta, Tai RenZhong, Kato Yoshiaki
Proceedings of Applications of High Field and Short Wavelength Sources X, 25-27 (2003)

4) Measurement of temporal duration of transient excitation x-ray lasers
Ochi Yoshihiro, Kawachi Tetsuya, Hasegawa Noboru, Sasaki Akira, Nagashima Keisuke, Sukegawa Kouta, Kishimoto Maki, Tanaka Momoko, Nishikino Masaharu, Kado Masataka, Daido Hiroyuki
Proceedings of Applications of High Field and Short Wavelength Sources X, 2003

5) Observation of the Ferroelectric Material with Instantaneous X-ray Laser Speckle
Tai RenZhong, Namikawa Kazumichi, Kishimoto Maki, Tanaka Momoko, Sawada A., Hasegawa Noboru, Kawachi Tetsuya, Sukegawa Kouta, Kado Masataka, Ochi Yoshihiro, Nishikino

Masaharu, Nagashima Keisuke, Daido Hiroyuki, Kato K., Maruyama H., Ando M.
AIP Conference Proceedings 705, 1122-1125 (2004)

6) Coherent x-ray laser generation by use of double target amplification
Tanaka Momoko, Nishikino Masaharu, Kawachi Tetsuya, Hasegawa Noboru, Kado Masataka, Kishimoto Maki, Nagashima Keisuke
The Japan Society of Applied Physics, The 64th Autumn Meeting, August 2003

7) Full coherent x-ray laser beam by double-target amplification
Nishikino Masaharu, Tanaka Momoko, Kishimoto Maki, Kado Masataka, Kawachi Tetsuya, Sukegawa Kouta, Hasegawa Noboru, Ochi Yoshihiro, Nagashima Keisuke
The Japan Society of Applied Physics, The 64th Autumn Meeting, August 2003

8) Development of a full spatial coherent x-ray laser
Nagashima Keisuke, Tanaka Momoko, Nishikino Masaharu, Kishimoto Maki, Kado Masataka, Kawachi Tetsuya, Hasegawa Noboru, Ochi Yoshihiro, Sukegawa Kouta, Tai RenZhong
Japan Society of Plasma Science and Nuclear Fusion Research, The 20th annual meeting, November 2003

9) Measurement of laser induced plasma with Bi-mirror interference microscopy
Nishikino Masaharu, Kado Masataka, Kishimoto Maki, Sukegawa Kouta, Ishino Masahiko, Nagashima Keisuke, Daido Hiroyuki, Tang Huajing., Guilbaud O., Ros D., Klisnick A., Joyeux D., Phalippou D.
The 7th Symposium of X-ray imaging, November 2003

10) Temporal characteristics of the TCE X-ray lasers
Ochi Yoshihiro, Kawachi Tetsuya, Hasegawa Noboru, Sasaki Akira, Nagashima Keisuke, Sukegawa Kouta, Kishimoto Maki, Tanaka Momoko, Nishikino Masaharu, Kado Masataka, Tai RenZhong
59th annual meeting of Japan Physical Society, Fukuoka, March 2004

3. JAERI-Report

1) Generation of nano scale X-ray laser beam using fresnel zoneplate (in Japanese)
Nagashima Keisuke, Kado Masataka, Nishikino Masaharu*
JAERI-Research 2003-035 (2004/02)

Free Electron Laser Development (Free Electron Laser Research Group)

1. Journals

1) Projectile Coulomb excitation of ^{78}Se
Hayakawa Takehito, To Yosuke, Oshima, Masumi, Osa Akihiko, Koizumi Mitsuo, Hatsukawa Yuichi, Utsuno Yutaka, Katakura Junichi, Matsuda Makoto, Morikawa Tsuneyasu*, Sugawara Masahiko*, Kusakari, Hideshige*, Czosnyka, T.*
Physical Review C 67, 064310_1 - 064310_6 (2003/06)

2) Neutron capture cross section to ^{186}Re isomeric state
Hayakawa Takehito, Shizuma Toshiyuki, Yamauchi Toshihiko, Minehara Eisuke, Arisawa Takashi
Nuclear Physics A 718, 665c-667c (2003/05)

3) High spin states in ^{158}Dy
Hayakawa Takehito, To Yosuke, Oshima Masumi, Matsuda Makoto, Hatsukawa Yuichi, Shizuma Toshiyuki, Katakura Junichi, Iimura Hideki, Mitarai Shiro*, Zhang, Y.*, Sugawara Masahiko*, Kusakari, Hideshige*
Physical Review C 68, 6, 067303_1-067303_4 (2003/12)

4) Inelastic excitation of ^{187}Re
Shizuma Toshiyuki, To Yosuke, Oshima Masumi, Sugawara, Masahiko*, Matsuda Makoto, Hayakawa Takehito, Koizumi Mitsuo, Osa Akihiko, Zhang, Y. H.*,Liu, Z.*
European Physical Journal A 17, 2, 159-165 (2003/06)

5) Medical free-electron lasers (in Japanese)
Minehara Eisuke
Ionizing Radiation and Advanced Medical Treatment Technologies, Chapter Name: Advanced Medical Treatments Related analyzing and Apparatus Technologies, Radiation Technology for

Advanced Medical Care, NSA (Nuclear Systems Association) Commentaries Series No.11, 135-142 (2003/06)

6) Generation of a self-chirped few-cycle optical pulse in an FEL oscillator
Hajima Ryoichi, Nagai Ryoji
Physical Review Letters 91, 2, 024801_1-024801_4 (2003/07)

7) A First-order matrix approach to the analysis of electron beam emittance growth caused by coherent synchrotron radiation
Hajima Ryoichi
Japanese Journal of Applied Physics, Part 2, 42, 8A, L974-L976 (2003/08)

8) High-spin structure in ^{185}Os
Shizuma Toshiyuki, Mitarai Shiro*, Sletten G.*, Bark R. A.*, Gjorup N. L.*, Jensen H. J.*, Piiparinen M.*, Wrzesinski J.*, Shimizu Yoshifumi*
Physical Review C 69, 2, 024305_1-024305_18 (2004/02)

9) Free-Electron Lasers (Road Maps for Laser Manufacturing)
Minehara Eisuke
Optoelectronic Technology Roadmap for Optical Processing (2003/06)

10) Shot noise in short pulse free electron lasers
Xie Ming, Hajima Ryoichi
Nuclear Instruments and Methods in Physics Research

11) A full-DC injector for an energy-recovery linac
Hajima Ryoichi, Minehara Eisuke, Nagai Ryoji
Nuclear Instruments and Methods in Physics Research

12) Emittance Compensation in a Return Arc of an Energy-Recovery Linac
Hajima Ryoichi
Nuclear Instruments and Methods in Physics Research

13) Optical Resonator Optimization of JAERI ERL-FEL
Nagai Ryoji, Hajima Ryoichi, Sawamura Masaru, Nishimori Nobuyuki, Kikuzawa Nobuhiro, Minehara Eisuke
Nuclear Instruments and Methods in Physics Research

14) Study of HOM Instability of the JAERI ERL-FEL
Sawamura Masaru, Hajima Ryoichi, Nagai Ryoji, Kikuzawa Nobuhiro, Nishimori Nobuyuki, Minehara Eisuke
Nuclear Instruments and Methods in Physics Research

15) Control system upgrade of JAERI ERL-FEL
Kikuzawa Nobuhiro
Nuclear Instruments and Methods in Physics Research

16) A Study on Decomposition of Dioxin Analogues by FEL
Yamauchi Toshihiko, Minehara Eisuke, Ito S.
Nuclear Instruments and Methods in Physics Research

17) A new isomer in ^{136}Ba populated by deep-inelastic collisions
Shizuma Toshiyuki, Gan Z., Ogawa K., Nakata J., Oshima M., Tou Y., Hayakawa Takehito, Hatsukawa Y, Sugawara M., Utsuno Y., Liu Z.
European Physical Journal A

2. Proceedings

1) First demonstration of energy-recovery operation in the JAERI superconducting linac for a high-power free-electron laser
Hajima Ryoichi, Shizuma Toshiyuki, Sawamura Masaru, Nagai Ryoji, Nishimori Nobuyuki, Kikuzawa Nobuhiro, Minehara Eisuke
Nuclear Instruments and Methods in Physics Research A 507, 1-2, 115-119 (2003/07)

2) Electron beam dynamics through a return-arc and a deceleration path of the JAERI Energy-Recovery Linac
Hajima Ryoichi, Minehara Eisuke
Nuclear Instruments and Methods in Physics Research A 507, 1-2, 141-145 (2003/07)

3) Formation of an FEL field with uniform and constant phase due to the slippage effect
Nishimori Nobuyuki, Hajima Ryoichi, Nagai Ryoji, Minehara Eisuke

Nuclear Instruments and Methods in Physics Research A 507, 1-2, 79-83 (2003/07)

4) Performance and upgrade of the JAERI ERL-FEL
Sawamura Masaru, Hajima Ryoichi, Kikuzawa Nobuhiro, Minehara Eisuke, Nagai Ryoji, Nishimori Nobuyuki
Proceedings of 2003 Particle Accelerator Conference (PAC 2003) (CD-ROM) 3446-3448 (2003)

5) Linac optics optimization for energy recovery Linacs
Nagai Ryoji, Hajima Ryoichi, Kikuzawa Nobuhiro, Minehara Eisuke, Nishimori Nobuyuki, Sawamura Masaru
Proceedings of 2003 Particle Accelerator Conference (PAC 2003) (CD-ROM) 3443-3445 (2003)

6) Cost estimation of an energy recovery Linac light source
Sawamura Masaru, Hajima Ryoichi, Kikuzawa Nobuhiro, Minehara Eisuke, Nagai Ryoji, Nishimori Nobuyuki
Proceedings of 2003 Particle Accelerator Conference (PAC 2003) (CD-ROM) 3449-3451 (2003)

7) Doubling of the microbunch repetition rate of a thermionic electron gun in JAERI-FEL (in Japanese)
Nishimori Nobuyuki, Nagai Ryoji, Minehara Eisuke, Kikuzawa Nobuhiro, Hajima Ryoichi, Sawamura Masaru
Proceedings of 28th Linear Accelerator Meeting in Japan 159-161 (2003/08)

8) Electric length stabilization of RF reference distribution cable (in Japanese)
Nagai Ryoji, Sawamura Masaru, Kikuzawa Nobuhiro, Hajima Ryoichi, Nishimori Nobuyuki, Minehara Eisuke
Proceedings of 28th Linear Accelerator Meeting in Japan 315-317 (2003/08)

9) Mode calculation of optical resonator for free-electron laer by fast-fourie-transform (in Japanese)
Nagai Ryoji, Hajima Ryoichi, Sawamura Masaru, Nishimori Nobuyuki, Kikuzawa Nobuhiro, Minehara Eisuke
Proceedings of 28th Linear Accelerator Meeting in Japan 381-383 (2003/08)

10) Analyses of coherent synchrotron radiation effect on an electron beam motion using first-order matrices (in Japanese)
Hajima Ryoichi
Proceedings of 28th Linear Accelerator Meeting in Japan 288-290 (2003/08)

11) Development of 10kW FEL at the JAERI energy recovery linac (in Japanese)
Hajima Ryoichi, Sawamura Masaru, Nagai Ryoji, Kikuzawa Nobuhiro, Nishimori Nobuyuki, Minehara Eisuke
Proceedings of 28th Linear Accelerator Meeting in Japan 390-392 (2003/08)

12) Control system upgrade of JAERI ERL-FEL (in Japanese)
Kikuzawa Nobuhiro
Proceedings of 28th Linear Accelerator Meeting in Japan 437-439 (2003/08)

13) An Analysis of the coherent synchrotron radiation effect in an energy-recovery linac by first-order transfer matrix
Hajima Ryoichi
Proceedings of the 14th Symposium on Accelerator Science and Technology 401-403 (2003/11)

14) JAERI ERL-FEL; Status and future plans
Hajima Ryoichi, Sawamura Masaru, Nagai Ryoji, Kikuzawa Nobuhiro, Nishimori Nobuyuki, Minehara Eisuke
Proceedings of the 14th Symposium on Accelerator Science and Technology 696-698 (2003/11)

15) Development of a control system with μ iTRON for the JAERI ERL-FEL (in Japanese)
Kikuzawa Nobuhiro
Proceedings of the 14th Symposium on Accelerator Science and Technology 269-271 (2003/11)

16) Analysis of an FEL oscillator at zero detuning length of an optical cavity in the early stage of the field evolution
Nishimori Nobuyuki
Proceedings of the 14th Symposium on Accelerator Science and Technology 108-110 (2003/11)

17) Stabilization of RF reference cable for JAERI ERL-FEL (in Japanese)
Nagai Ryoji, Sawamura Masaru, Kikuzawa Nobuhiro, Hajima Ryoichi, Nishimori Nobuyuki, Minehara Eisuke
Proceedings of the 14th Symposium on Accelerator Science and Technology 362-364 (2003/11)

18) A 400m-long superconducting RF linac cryostat design for an ERL light source
Minehara Eisuke
Proceedings of the 14th Symposium on Accelerator Science and Technology 247 (2003/11)
19) Phase shift induced by Free Electron Laser interaction with electrons on resonance
Nishimori Nobuyuki, Hajima Ryoichi, Nagai Ryoji
Proceedings of the 25th Free Electron Laser conference
20) Analysis of the saturation field in an FEL oscillator at zero detuning of an optical cavity
Nishimori Nobuyuki
Proceedings of the 25th Free Electron Laser conference
21) Status of the JAERI energy-recovery linac FEL
Hajima Ryoichi, Sawamura Masaru, Nagai Ryoji, Kikuzawa Nobuhiro, Nishimori Nobuyuki, Minehara Eisuke
Proceedings of the 25th Free Electron Laser conference
22) Femtosecond pulse generation from a self-chirped FEL oscillator
Hajima Ryoichi, Nagai Ryoji
Proceedings of the 25th Free Electron Laser conference
23) HOM properties of the JAERI ERL-FEL
Sawamura Masaru, Nagai Ryoji, Kikuzawa Nobuhiro, Hajima Ryoichi, Nishimori Nobuyuki, Minehara Eisuke
Proceedings of the 27th Linear Accelerator Meeting in Japan
24) JAERI Femtosecond pulsed and Tens-Kilowatts Average-powered Free-Electron Lasers and Their Applications of Larger-scaled Non-thermal Peering, Cutting and Drilling in Nuclear Industry
Minehara Eisuke, Nishimura M., Tsukada Takashi
Proceedings of the 5th International Symposium on Laser Precision Microfabrication
25) Development of an Energy-Recovery Linac for a High-Power FEL at JAERI
Hajima Ryoichi, Sawamura Masaru, Nagai Ryoji, Kikuzawa Nobuhiro, Nishimori Nobuyuki, Minehara Eisuke
Proceedings of The Asian Particle Accelerator Conference
26) R-Matrix Analysis of the CSR Effect in a Future ERL Light Source
Hajima Ryoichi
Proceedings of The Asian Particle Accelerator Conference
27) 20.8 MHz Electron Gun System for an Energy Recovery Linac FEL at JAERI
Nishimori Nobuyuki, Nagai Ryoji, Minehara Eisuke, Hajima Ryoichi, Kikuzawa Nobuhiro, Sawamura Masaru
Proceedings of The Asian Particle Accelerator Conference

3. Patents pending

1) Stress removal method on stainless steel surface by ultrashort laser pulses
Japan patent application number 2003-349489
Minehara Eisuke, Nishimura Akihiko, Tsukada Takashi
2) A device to provide narrow-band synchrotron radiation for multiple beam lines simultaneously
Hajima Ryoichi
Japan patent application number 2004-033225

Optics Research and Development (Novel Optics Research Group)

1. Journals

1) Soft X-ray laminar-type varied-line-spacing holographic gratings
Sano Kazuo*, Koike Masato
Journal of Plasma and Fusion Research 79, 4, 391-397 (2003/04)
2) Fabrication of multilayer mirrors consisting of oxide and nitride layers for continual use across the K-absorption edge of carbon
Ishino Masahiko, Yoda Osamu
Applied Optics 43, 9, 1849-1855 (2004/03)

2. Proceedings

1) Heat stability of Mo/Si multilayers inserted with compound layers
Ishino Masahiko, Yoda Osamu, Takenaka Hisataka*, Sano Kazuo*, Koike Masato
Surface and Coatings Technology 169-170, 1-3, 628-631 (2003/06)
2) Nd:YVO_4 and YVO_4 laser crystal integration by a direct bonding technique
Sugiyama Akira, Fukuyama Hiroyasu*, Katsumata Masaki*, Okada Yukikatsu*
Integrated Optical Devices: Fabrication and Testing (Proceedings of SPIE Volume 4944) 361-368 (2003)
3) A New High Energy-resolution Soft-X-ray Spectrometer for A Transmission Electron Microscope
Terauchi M., Koike Masato
Microscopy & Microanalysis, 9 (supple.2), 894-895 (2003)
4) Conical Diffraction Monochromator Equipped with Holographic Gratings in Energy Region of 1-4keV
Koike Masato, Namioka Takeshi
Proc. of the Eighth International Conference on Synchrotron Radiation Instrumentation, edited by T. Warwick et al., AIP-CP705, 865-868 (2004)

3. JAERI-Reports
1) Feasibility study of a direct bonding method for laser crystals; Evaluations of YVO_4 yttrium orthovanadate bonded laser crystals (in Japanese)
Sugiyama Akira, Nara Yasunaga
JAERI-Research 2003-023 (2003/11)

4. Patent pending
1) Fabrication method of soft X-ray transmission-type polarization elements
Ishino Masahiko, Koike Masato, Imazono Takashi
Japan patent application number 2004-003644

Advanced Photon Simulation Research (Simulation Group for Advanced Photon Science)

1. Journals
1) Theoretical EUV spectrum of near Pd-like Xe
Sasaki Akira
Journal of Plasma and Fusion Research 79, 4, 315-317 (2003/04)
2) Acceleration of injected electron beam by ultra-intense laser pulses with phase disturbances
Nakamura Tatsushi, Kato Susumu, Koga James, Tanimoto Mitsushi, Koyama Kazuyoshi, Kato T.
Journal of Plasma Fusion Research 79, 4, 318-320 (2003/04)
3) Light intensification towards the Schwinger limit
Bulanov S. V.*, Esirkepov T. Z.*, Tajima Toshiki
Physical Review Letters 91, 8, 085001_1-085001_4 (2003/08)
4) Direct electron acceleration by stochastic laser fields in the presence of self-generated magnetic fields
Tanimoto M., Kato S., Miura E., Saito N., Koyama K., Koga James. K.
Phys. Rev. E 68, 1, 026401_1-026401_8 (2003)
5) On the upper limit of the energy of ions accelerated at the front of relativistic electron cloud expanding into a vacuum
Bulanov S.V., Esirkepov T.Zh., Koga James.K., Tajima Toshiki, Farina D.
Plasma Physics Reports 30, 1, 18-29 (2004)
6) Accurate basis set by the CIP method for the solutions of the Schrödinger equation
Utsumi Takayuki*, Yabe Takashi*, Koga J. K., Aoki Takayuki*, Sekine Masatoshi*
Computer Physics Communications 157, 2, 121-138 (2004/02)
7) Thermodynamics in density-functional theory and force theorems
Chihara Junzo*, Yamagiwa, Mitsuru
Progress of Theoretical Physics 111, 3, 339-359 (2004/03)
8) Effect of self-injection on ultraintense laser wake-field acceleration
Zhidkov Alexei, Koga James, Kinoshita K., Uesaka Mitsuru
Phys. Rev. E, 69, 3, 035401_1-035401_4 (2004)

2. Proceedings

1) Parallel implementation of the solver for the one-dimensional Vlasov-Poisson equation based on the DA-CIP method
Utsumi Takayuki*, Koga J. K., Kunugi Tomoaki*
Parallel Computational Fluid Dynamics; New Frontiers and Multi-Disciplinary Applications 539-546 (2003)

2) X-ray emission from inner-shell ionization of Ne-like ions
Moribayashi Kengo, Kagawa Takashi*, Kim D. E.*
Nuclear Instruments and Methods in Physics Research B 205, 334-336 (2003/05)

3) Short wavelength X-ray emission generated by high intensity laser irradiation on Xe clusters
Moribayashi Kengo
Nuclear Instruments and Methods in Physics Research B 205, 346-349 (2003/05)

4) Functional distributed server controlled system managing large-scale simulation (in Japanese)
Ueshima Yutaka, Kondo Takao*, Isogai Kentaro*
IPSJ Symposium Series (ISSSN 1344-0640) 2003, 14, 151-158 (2003/10)

3. JAERI-Reports

1) Proceedings of Conferences on the Large Data Management; January 29-31, 2003, Advanced Photon Research Center, Kyoto (in Japanese)
JAERI-Conf 2004-002, 81 (2004/03)

2) Proceedings of the 4th Symposium of Large Data Management for Creative Research; September 2-4, 2002, Advanced Photon Research Center, Kyoto, Japan (in Japanese)
JAERI-Conf 2004-003, 62 (2004/03)

High Peak Power Laser Application (Applied Photon Research Group)

1. Journals

1) Photodissociation of acetaldehyde, $CH_3CHO \rightarrow CH_3+HCO$; Direct ab initio molecular dynamics study
Kurosaki Yuzuru, Yokoyama Keiichi
Chemical Physics Letters 371, 5-6, 568-575 (2003/04)

2) Energetic protons from a few-micron metallic foil evaporated by an intense laser pulse
Matsukado Koji*, Esirkepov T. Z.*, Kinoshita Kenichi*, Daido Hiroyuki, Utsumi Takayuki*, Li Zhong*, Fukumi Atsushi*, Hayashi Yukio, Orimo Satoshi, Nishiuchi Mamiko, Bulanov S. V.*, Tajima Toshiki, Noda Akira*, Iwashita Yoshihisa*, Shirai Toshiyuki*, Takeuchi Takeshi*, Nakamura Shu*, Yamazaki Atsushi*, Ikegami Masahiro*, Mihara Takanori*, Morita Akio*, Uesaka Mitsuru*, Yoshii Koji*, Watanabe Takahiro*, Hosogai Tomonao*, Zhidkov Alexei*, Ogata Atsushi*, Wada Yoshio*, Kubota Tetsuo*
Physical Review Letters 91, 21, 215001_1-215001_4 (2003/11)

3) Potentiality of the laboratory astrophysics using high repetition rate and high intensity lasers (in Japanese)
Nishiuchi Mamiko, Daido Hiroyuki, Takabe Hideaki*, Matsukado Koji*
The Review of Laser Engineering 31, 11, 711-720 (2003/11)

4) Preface to topical papers on science and technology created by ultra-short and ultra-high intensity lasers (in Japanese)
Daido Hiroyuki
The Review of Laser Engineering 31, 11, 696-697 (2003/11)

5) Ultra-short ultra-high intensity laser-matter interaction (in Japnaese)
Daido Hiroyuki
The Review of Laser Engineering 31, 11, 698-706 (2003/11)

6) Global ab initio potential energy surfaces for the lowest three doublet states ($1^2A'$, $2^2A'$, and $1^2A''$) of the BrH_2 system
Kurosaki Yuzuru, Takayanagi Toshiyuki
Journal of Chemical Physics 119, 15, 7838-7856 (2003/10)

7) Development of the laser-plasma ion source for cancer therapy (in Japanese)

Matsukado Koji*, Bulanov S. V.*, Daido Hiroyuki
The Review of Laser Engineering 31, 11, 721-729 (2003/11)

8) Temperature dependence of femtosecond time-resolved fluorescence intensity of a dye molecule in solution
Murakami Hiroshi
Journal of Luminescence 102, 295-300 (2003)

9) Direct ab initio molecular dynamics study of the two photodissociation channels of formic acid
Kurosaki Yuzuru, Yokoyama Keiichi, Teranishi Yoshiaki
Chem. Phys. in press

10) Characterization or preformed plasmas with an interferometer for ultra-short high-intensity laser-plasma interaction
Sagisaka Akito, Daido Hiroyuki, Ogura Koichi, Orimo Satoshi, Hayashi Yukio, Nishiuchi Mamiko, Mori Michiaki, Katsukado Koji, Fukumi Atsushi, Li Zhong, Nakamura Shu, Takagaki Kenichi, Hazama Hisanao, Suzuki Masato, Utsumi Takayuki, Bulanov S. V., Esirkepov T.
Appl. Phys. B78, 919-922 (2004)

11) Photophysics of 1,5-diarylpenta-1,4-diene-3-one in the excited singlet state: Is the aromatic dienone a vinylogue of benzophenone?
Hagiri M., Ichinose N., Shiroyama T. Murakami Hiroshi, Kishimoto Maki, Daido Hiroyuki, Nakayama T.
Chemical Physics Letters

2. Proceeding

1) Temperature dependence of the ultrafast solvation of a dye molecule in alcohol
Murakami Hiroshi, Tanaka Momoko
Slow Dynamics in Complex Systems: 3rd International symposium, 739-740 (2004)

3. Patent pending

1) Fabrication technique for nano-meter sized crystalline fibers and crystalline silicon nano-meter sized fibers
Daido Hiroyuki
Japan patent application number 2003-389641

Advanced Photon Research

1. JAERI-Reports

1) Proceedings of the 4th Symposium on Advanced Photon Research; November 28-29, Advanced Photon Research Center, Kyoto, Japan (in Japanese)
JAERI-Conf 2003-008 (2003/07)

2) Proceedings of the 5th Symposium on Advanced Photon Research; November 20-21, Advanced Photon Research Center, Kyoto, Japan (in Japanese)
JAERI-Conf 2004-009 (2004/06)

6.2 List of Publications on Synchrotron Radiation Research Center

Experimental facilities development (Experimental Facilities Development Group)

1. Reports

1) Annual Report of Kansai Research Establishment 2002; April 1, 2002 - March 31, 2003
KANSAI Research Establishment
JAERI-Review 2003-042,140,(2004/02)
2) Setup of the X-ray mirror system on BL11XU at SPring-8
KIRIYAMA Koji, TAKAHASHI Masamitsu, SHIWAKU Hideaki
JAERI-Tech 2004-017,39,(2004/03)
3) Characterization of cryogenically cooled silicon crystals, for the double-crystal monochromator on BL11XU at SPring-8
TOZAWA Kazukiyo, KIRIYAMA Koji, MITSU Takaya, SHIWAKU Hideaki, HARAMI Taikan
JAERI-Tech 2004-041,27,(2004/03)

2. Journals

1) Evidence for a Narrow S = +1 Baryon Resonance in Photoproduction from the Neutron
T. NAKANO, D. S. AHN, J. K. AHN, H. AKIMUNE, Y. ASANO, W. C. CHANG, S. DATE, H. EJIRI, H. FUJIMURA M. FUJIWARA, K. HICKS, T. HOTTA, K. IMAI, T. ISHIKAWA, T. IWATA, H. KAWAI, Z. Y. KIM, K. KINO, H. KOHRI, N. KUMAGAI, S. MAKINO, T. MATSUMURA, N. MATSUOKA, T. MIBE, K. MIWA, M. MIYABE, Y. MIYACHI, M. MORITA, N. MURAMATSU, M. NIIYAMA, M. NOMACHI, Y. OHASHI, T. OOBA, H. OHKUMA, D. S. OSHUEV, C. RANGACHARYULU, A. SAKAGUCHI, T. SASAKI, P. M. SHAGIN, Y. SHIINO, H. SHIMIZU, Y. SUGAYA, M. SUMIHAMA, H. TOYOKAWA, A. WAKAI, C. W. WANG, S. C. WANG, K. YONEHARA,T. YORITA, M. YOSHIMURA, M. YOSOI and R. G. T. ZEGERS
Phys. Rev. Lett. 91, 012002 (2003)
2) Beam-Polarization Asymmetries for the p(g,K+) and p(g,K+) 0 Reactions for E = 1.5 to 2.4 GeV
R. G. T. ZEGERS, M. SUMIHAMA, D. S. AHN, J. K. AHN, H. AKIMUNE, Y. ASANO, W. C. CHANG, S. DATE H. EJIRI, H. FUJIMURA, M. FUJIWARA, K. HICKS, T. HOTTA, K. IMAI, T. ISHIKAWA, T. IWATA, H. KAWAI, Z. Y. KIM, K. KINO, H. KOHRI, N. KUMAGAI, S. MAKINO, T. MATSUMURA, N. MATSUOKA, T. MIBE, K. MIWA, M. MIYABE, Y. MIYACHI, M. MORITA, N. MURAMATSU, T. NAKANO, M. NIIYAMA, M. NOMACHI, Y. OHASHI T. OOBA, H. OHKUMA, D. S. OSHUEV, C. RANGACHARYULU, A. SAKAGUCHI T. SASAKI, P. M. SHAGIN, Y. SHIINO, H. SHIMIZU, Y. SUGAYA, H. TOYOKAWA, A. WAKAI, C. W. WANG, S. C. WANG, K. YONEHARA, T. YORITA, M. YOSHIMURA and M. YOSOI
Phys. Rev. Lett. 91, 092001 (2003)
3) Baking effect for NdFeB magnets against demagnetization induced by high energy electrons
T.BIZEN, Y.ASANO, T.HARA, X.MARECHAL, T.SEIKE, T. TANAKA, H.S.LEE, D.E.KIM, C.W.CHUNG and H.KITAMURA
Nucle. Instr. and Methods. A515 850-852 (2003)

3. Proceeding

1) Radiation measurement around a 10-T superconducting wiggler at SPring-8
M.SHOJI,K.SOUTOME,N.KUMAGAI,J.TADA,T.MAGOME,M.OISHI,T.OHSHIMA,S.SASAKI,M.TAKAO,T.TAKAGI, K.TSUMAKI,T.YORITA H.YONEHARA and Y.ASANO
Particle accelerator conference 3p 2003 Orland Oregon USA (2003)

High pressure science (High Pressure Science Group)

1. Journals

1) Addendum to "Doping-Dependent Magnetic Structure of $Tb_{1-x}Ca_xMnO_3$"
MACHIDA Akihiko, MORITOMO Yutaka, OYAMA Kenji
Journal of the Physical Society of Japan,72,5,1312,(2003/05)

2) X-ray structural studies on elemental liquids under high pressures
KATAYAMA Yoshinori, TSUJI Kazuhiko
Journal of Physics; Condensed Matter,15,36,6085-6103,(2003/09)
3) Congruent melting of gallium nitride at 6 GPa and its application to single-crystal growth
UTSUMI Wataru, SAITO Hiroyuki, KANEKO Hiroshi, WATANUKI Tetsu, AOKI Katsutoshi, SHIMOMURA Osamu
Nature Materials,2,11,735-738,(2003/11)
4) Phase relations and equations of state for FeS at high pressures and high temperatures and implications to the internal structure of Mars
S. URAKAWA, K. SOMEYA, H. TERASAKI, T. KATSURA, S. YOKOSHI, K. FUNAKOSHI, W. UTSUMI, Y. KATAYAMA, Y. SUEDA and T. IRIFUNE
Phys.Earth Planet.Inter. 143-144, 469-479 (2004/02)
5) A Kawai-type High-pressure and High-temperature Apparatus for in situ X-ray observation, 'SPEED-Mk.II'
T. KATSURA, K. FUNAKOSHI, A. KUBO, N. NISHIYAMA, Y. TANGE, Y. SUEDA, T. KUBO and W. UTSUMI
"New Developments in High Pressure Mineral Physics and Applications to the Earth's Interior"
Phys.Earth Planet.Inter.143-144, 497-506 (2004/02)
6) Nucleation and growth in bulk metallic glass under high pressure investigated using in situ x-ray diffraction
W. H. WANG, P. Pen, D. O. ZHAO, M. X. PAN, T. OKADA and W. UTSUMI
Appl. Phys.Lett. 83, 5202-5204 (2003/12)
7) Melting and crystallization of $Nd_{60}Al_{10}Fe_{20}Co_{10}$ bulk metallic glass under high pressure
D. Q. ZHAO, M. X. PAN, W. H. WANG, B. C. WEI, T. OKADA and W. UTSUMI
J. Phys.: Condens. Matt. 15, L1-L5 (2003/10)
8) Effect of pressure on nucleation and growth in the ZrTiCuNiBe bulk glass forming alloy investigated using in situ x-ray diffraction
W. H. WANG, T. OKADA, P. WEN, X.-L. WANG, M. X. PAN and W. UTSUMI
Phys.Rev.B 68, 184105-1-184105-6 (2003/06)
9) Formation and crystallization of CuZrHfTi bulk metallic glass under ambient and high pressures
Z. X. WANG, D. Q. ZHAO, M. X. PAN, W. H. WANG, T. OKADA and W. UTSUMI
J.Phys.: Condens.Matter 15, 5923-5932 (2003/05)
10) In situ x-ray diffraction of graphite-diamond transformation using various catalysts under high pressures and high temperatures
W. UTSUMI, T. OKADA, T. TANIGUCHI, K. FUNAKOSHI, T. KIKEGAWA, N. HAMAYA and O. SHIMOMURA
J.Phys.: Condens.Matt.16, S1017 -S1026 (2004/01)
11) Anharmonicity of platinum under HP and HT
M. OKUBE, A. YOSHIASA, O. OHTAKA and Y. KATAYAMA
High Pressure Res. 23, 247-251(2003/09)
12) Structural transformations in liquid, crystalline and glassy B_2O_3 under high pressure
V. V. BRAZHKIN, Y. KATAYAMA, Y. INAMURA, M. V. KONDRIN, A. G. LYAPIN, S. V. POPOVA and R. N. VOLOSHIN,
JETP Lett, 78, 393-397 (2003/09)
13) Stability of magnesite and its high-pressure form in the lowermost
Maiko ISSHIKI, Tetsuo IRIFUNE, Kei HIROSE, Shigeaki ONO, Yasuo OHISHI, Tetsu WATANUKI, Eiji NISHIBORI, Masaki TAKATA and Makoto SAKATA
Nature 427, 60-62(2004/01)

Structural physics research (Structural Physics Research Group)

1. Journals

1) Electrochemical synthesis of superconductive MgB_2 from molten salts
YOSHII Kenji, ABE Hideki
Physica C,388-389,1-4,113-114,(2003/05)
2) Resonant X-ray scattering study on the filled skutterudite $PrFe_4P_{12}$

ISHII Kenji, INAMI Toshiya, MURAKAMI Yoichi, Hao, L., IWASA Kazuaki, KOGI Masafumi, AOKI Yuji, SUGAWARA Hitoshi, SATO Hideyuki, IMADA Shin, NAKAO Hironori, SAWA Hiroshi, WAKABAYASHI Yusuke
Physica B; Condensed Matter,329-333,1-4,467-468,(2003/05)

3) Time-resolved X-ray diffraction study on surface structure and morphology during molecular beam epitaxy growth
TAKAHASHI Masamitsu, YONEDA Yasuhiro, INOUE Hirotane, YAMAMOTO Naomasa, MIZUKI Junichiro
Journal of Crystal Growth,251,1-4,51-55,(2003/04)

4) RHEED observation of $BaTiO_3$ thin films grown by MBE
YONEDA Yasuhiro, SAKAUE Kiyoshi, TERAUCHI Hikaru
Surface Science,529,3,283-287,(2003/04)

5) Relation between the structure and catalytic activity for automotive emissions; Use of X-ray anomalous dispersion effect
MIZUKI Junichiro, NISHIHATA Yasuo, TANAKA Hirohisa
"Journal of the Crystallographic Society of Japan"(in Japanese) 45,3,203-208,(2003/06)

6) Stacking-fault-induced intermediate structure in bismuth titanate
YONEDA Yasuhiro, MIZUKI Junichiro, KATAYAMA Ryoko, YAGI Kenichiro, TERAUCHI Hikaru, HAMAZAKI Shinichi, TAKASHIGE Masaaki
Applied Physics Letters,83,2,275-277,(2003/07)

7) Domain boundaries in the GaAs(001)-2×4 surface
TAKAHASHI Masamitsu, YONEDA Yasuhiro, YAMAMOTO Naomasa, MIZUKI Junichiro
Physical Review B,68,8,085321_1-085321_5,(2003/08)

8) Charge-ordered state in single-crystalline $CaFeO_3$ thin film studied by X-ray anomalous diffraction
AKAO Tadahiro, AZUMA Yusuke, USUDA Manabu, NISHIHATA Yasuo, MIZUKI Junichiro, HAMADA Noriaki, HAYASHI Naoaki, TERASHIMA Takahito, TAKANO Mikio
Physical Review Letters,91,15,156405_1-156405_4,(2003/10)

9) Electrochemical thin-film fabrication of superconductive boride MgB_2
YOSHII Kenji, ABE Hideki
"Chemistry and Industry"(in Japanese) 56,7,802-804,(2003/00)

10) Sagittal focusing bender for SPring-8 bending magnet beamlines
YONEDA Yasuhiro, MATSUMOTO Norimasa, FURUKAWA Yukito, ISHIKAWA Tetsuya
"SPring-8 Information"(in Japanese) 8,6,397-400,(2003/11)

11) Surface structure of electrode by X-ray scattering measurement
TAKAHASHI Masamitsu
"Electrochemistry"(in Japanese) 72,2,128-132,(2004/02)

2. Report

1) Setup of the cryogenic cooling system on BL11XU at SPring-8
KIRIYAMA Koji, SHIWAKU Hideaki, TOZAWA Kazukiyo
JAERI-Tech 2003-061,21(2003/07)

Surface chemistry research (Surface Chemistry Research Group)

1. Journals

1) Orientation effect on phot-fragmentation and ion-desorption from the topmost layers of molecular solids
SEKIGUCHI Tetsuhiro, IKEURA Hiromi, BABA Yuji
Surface Science,532-535,1-3,1079-1084,(2003/06)

2) Real-time monitoring of oxidation on the Ti(0001) surface by synchrotron radiation photoelectron spectroscopy and RHEED-AES
TAKAKUWA Yuji, ISHIZUKA Shinji, YOSHIGOE Akitaka, TERAOKA Yuden, YAMAUCHI Yasuhiro, MIZUNO Yoshiyuki, TONDA Hideki, HOMMA Teiichi
Applied Surface Science,216,1-4,395-401,(2003/06)

3) Coexistence of passive and active oxidation for O_2/Si(001) system observed by SiO mass spectrometry and synchrotron radiation photoemission spectroscopy

TERAOKA Yuden, MORITANI Kosuke, YOSHIGOE Akitaka
Applied Surface Science,216,1-4,8-14,(2003/06)

4) SiO mass spectrometry and Si-2p photoemission spectroscopy for the study of oxidation reaction dynamics of Si(001) surface by supersonic O_2 molecular beams under 1000 K
TERAOKA Yuden, YOSHIGOE Akitaka, MORITANI Kosuke
Japanese Journal of Applied Physics, Part 1,42,7B,4671-4675,(2003/07)

5) Real-time observation of initial stages thermal oxidation on Si(001) surface by using synchrotron radiation photoemission spectroscopy
YOSHIGOE Akitaka, MORITANI Kosuke, TERAOKA Yuden
"Vacuum"(in Japanese) 46,5,424-428,(2003/05)

6) Real time observation of initial thermal oxidation using O_2 gas on Si(001) surface by means of synchrotron radiation Si-2p photoemission spectroscopy
YOSHIGOE Akitaka, MORITANI Kosuke, TERAOKA Yuden
Applied Surface Science,216,1-4,388-394,(2003/06)

7) Real-time monitoring of initial thermal oxidation on Si(001) surfaces by synchrotron radiation photoemission spectroscopy
YOSHIGOE Akitaka, MORITANI Kosuke, TERAOKA Yuden
Japanese Journal of Applied Physics, Part 1,42,6B,3976-3982,(2003/06)

8) Real-time observation of initial stage on Si(001) oxidation studied by O-1s photoemission spectroscopy using synchrotron radiation
YOSHIGOE Akitaka, MORITANI Kosuke, TERAOKA Yuden
Japanese Journal of Applied Physics, Part 1,42,7B,4676-4679,(2003/07)

9) Oxidation of aqueous HF-treated Si(001) surface induced by translational kinetic energy of O_2 at room temperature
YOSHIGOE Akitaka, TERAOKA Yuden
Japanese Journal of Applied Physics, Part 1,42,9A,5749-5750,(2003/09)

10) Spectroscopic study of site selective DNA damage induced by intense soft X-rays
FUJII Kentaro
"Synchrotron Radiation"(in Japanese) 16,3,151-158,(2003/05)

11) In-situ observation of growth of very thin oxide on Ti surfaces by real-time photoelectron spectroscopy
TAKAKUWA Yuji, ISHIZUKA Shinji, YOSHIGOE Akitaka, TERAOKA Yuden
"Chemical Industry"(in Japanese) 54,9,687-692,(2003/09)

12) Chemical-state analysis for low-dimensional Si and Ge films on graphite
NATH, K. G., SHIMOYAMA Iwao, SEKIGUCHI Tetsuhiro, BABA Yuji
Journal of Applied Physics,94,7,4583-4588,(2003/10)

13) In-situ observation of oxidation of Ti(0001) surface by real-time photoelectron spectroscopy using synchrotron radiation
TAKAKUWA Yuji, ISHIZUKA Shinji, YOSHIGOE Akitaka, TERAOKA Yuden, MIZUNO Yoshiyuki, TONDA Hideki, HOMMA Teiichi
"Surface Science"(in Japanese) 24,8,500-508,(2003/08)

14) Actively controlled oxidation of Cu{001} with hyperthermal O_2 molecular beam
OKADA Michio, MORITANI Kosuke, GOTO Seishiro, KASAI Toshio, YOSHIGOE Akitaka, TERAOKA Yuden
Journal of Chemical Physics,119,14,6994-6997,(2003/10)

15) Characterization of B-C-N hybrid prepared by ion implantation
SHIMOYAMA Iwao, BABA Yuji, SEKIGUCHI Tetsuhiro, NATH, K. G., SASAKI Masayoshi, OKUNO Kenji
Journal of Vacuum Science and Technology A,21,6,1843-1848,(2003/11)

16) Control of O_2 adsorption and SiO desorption by incident energy of O_2 molecules in the O_2/Si(001) surface reaction system
TERAOKA Yuden, YOSHIGOE Akitaka, MORITANI Kosuke
Atomic Collision Research in Japan, No.29,68-70,(2003/00)

17) SR-excited process
TERAOKA Yuden
"Dictionary of Nanotechnology"(in Japanese) 340-351,(2003/12)

18) Active Control of Site-Specificity in Ion Desorption by Core Excitation
Shin-ichi WADA, Erika O. SAKO, Ryohei SUMII, Satoshi WAKI, Kouji ISARI, Tetsuhiro SEKIGUCHI, Tetsuji SEKITANI, and Kenichiro TANAKA
Nucl.Inst. Meth. Phys. Res. B, 199, 361-365 (2003/04).
19) Active control of chemical bond scission by site-specific core excitation
Shin-ichi WADA, Ryouhei SUMII, Kouji ISARI, Satoshi WAKI, Erika O. SAKO, Tetsuhiro SEKIGUCHI, Tetsuji SEKITANI, Kenichiro TANAKA
Surface Science, 528, 242-248 (2003/04).

3. Report

1) Chemisorption of CH_3Cl on Si(001) surface under UHV condition
IMANAKA Soichi, OKADA Michio, KASAI Toshio, TERAOKA Yuden, YOSHIGOE Akitaka
JAERI-Tech 2003-066,36,(2003/08)

Heavy atom science (Heavy Atom Science Research Group)

Journals

1) Charge disproportionation and magnetic properties in perovskite iron oxides
KUZUSHITA Kaori, MORIMOTO Shotaro, NASU Saburo
Physica B; Condensed Matter,329-333,1-4,736-737,(2003/05)
2) Magnetic ordering and spin dynamics in potassium jarosite; A Heisenberg kagome lattice antiferromagnet
NISHIYAMA Masahide, MAEGAWA Satoru, INAMI Toshiya, OKA Yoshio
Physical Review B,67,22,224435_1-224435_11,(2003/06)
3) Development of scanning-type synchrotron radiation m"ossbauer microscope using focused X-ray
MITSUI Takaya, KOBAYASHI Yasuhiro, SETO Makoto
Japanese Journal of Applied Physics, Part 1,43,1,389-393,(2004/01)
4) Resonant X-ray Study on the Bi-Layered Perovskite Mn Oxide $LaSr_2Mn_2O_7$,
Yusuke WAKABAYASHI, Youichi MURAKAMI, Ichiro KOYAMA, Tsuyoshi KIMURA, Y. TOKURA, Y. MORITOMO, Y. ENDOH and Kazuma HIROTA
J. Phys. Soc. Japan 72, (2003) 618-626.
5) The appearance of the spin-Peierls phase under pressure in $Cu_{1-x}MgxGeO_3$,
T. MASUDA, D. YANO, R. KURODA, K. UCHINOKURA, H. KUROE, T. SEKINE, Y. KATSUKI, K. OHWADA, Y. FUJII, H. NAKAO and Y. MURAKAMI,
Phys. Rev. B 67, 024423 (2003).
6) Orbital excitations in $LaMnO_3$ studied by resonant inelastic x-ray scattering,
T. INAMI, T. FUKUDA, J. MIZUKI, S. ISHIHARA, H. KONDO, H. NAKAO, T. MATSUMURA, K. HIROTA, Y. MURAKAMI, S. MAEKAWA and Y. ENDOH
Phys. Rev. B 67 (2003) 045108 1-6.
7) Pressure effects on an organic radical ferromagnet: 2,5-difluorophenyl-α-nitronyl nitroxide,
M. MITO, H. DEGUCHI, T. TANIMOTO, T. KAWAE, S. NAKATSUJI, H. MORITOMO, H. ANZAI, H. NAKAO, Y. MURAKAMI, K. TAKEDA
Phys. Rev. B 67 (2003) 024427-1-8.
8) Pressure Effects on an S=1 Haldane Compound $Ni(C_5H_{14}N_2)_2N_3(PF_6)$,
Masaki MITO, Hironori AKAMA, Hiroyuki DEGUCHI, Seichi TAKAGI, Tatsuya KAWAE, Kazuyoshi TAKEDA, Tomohiko ISHII, Masahiro YAMASHITA, Hironori NAKAO, Youichi MURAKAMI and Shoji YAMAMOTO,
J. Phys. Soc. Japan 72 (2003) 399-404.
9) Resonant X-ray Scattering in Perovskite Manganite Superlattice -- Observation of "Orbital Superlattice" –
Takashi KIYAMA, Yusuke WAKABAYASHI, Hironori NAKAO, Hiroyuki OHSUMI, Youichi MURAKAMI, Makoto IZUMI, Masashi KAWASAKI, and Yoshinori TOKURA
J. Phys. Soc. Japan 72 (2003) 785-788
10) Experimental Elucidation: Microscopic Mechanism of Resonant X-Ray Scattering in Manganite Films,
H. OHSUMI, M. KUBOTA, Y. MURAKAMI, T. KIYAMA, H. NAKAO, Y. WAKABAYASHI, Y.

KONISHI, M. IZUMI, M. KAWASAKI and Y. TOKURA
J. Phys. Soc. Japan 72 (2003) 1006-1009.

11) Charge and orbital ordered states in $Nd_{1-x}Sr_{1+x}MnO_4$ (x=0.67, 0.75),
H. NAKAO, T. SATOH, J. SATOH, Y. MURAKAMI, M. KUBOTA, Y. WAKABAYASHI, H. SAWA, T. KIMURA, Y. TOKURA
Physica B 329-333 (2003) 809-810.

12) Pressure effect on the magnetism and structure of a spin-Peierls substance: MEM-$[TCNQ]_2$
Kouji EJIMA, Takayuki TAJIRI, Hiroyuki DEGUCHI, Masaki MITO, Seishi TAKAGI, Kenji OHWADA, Hironori NAKAO, Youichi MURAKAMI
Physica B 329-333 (2003) 1195-1196.

13) Critical phenomena in helical magnet β-MnO_2: X-ray magnetic scattering study
Hirohiko SATO, Yoichi KAWAMURA, Toshiyuki OGAWA, Youichi MURAKAMI, Hiroyuki OHSUMI, Masaichiro MIZUMAKI, Naoshi IKEDA
Physica B 329-333 (2003) 757-758.

14) Resonant X-ray scattering study on the filled skutterudite $PrFe_4P_{12}$
K. ISHII, T. INAMI, Y. MURAKAMI, L. HAO, K. IWASA, M. KOHGI, Y. AOKI, H. SUGAWARA, H. SATO, S. IMADA, H. NAKAO, H. SAWA, Y. WAKABAYASHI
Physica B 329-333 (2003) 467-468.

15) High Pressure X-Ray Diffraction Study of URu_2Si_2
K. KUWAHARA, H. SAGAYAMA, K. IWASA, M. KOHGI, S. MIYAZAKI, J. NOZAKI, J. NOGAMI, M. YOKOYAMA, H. AMITSUKA, H. NAKAO and Y. MURAKAMI
Acta Physica Polonica B, 34 (2003) 4307-4310.

16) Reply to "Comment on 'X-ray resonant scattering studies of orbital and charge ordering in $Pr_{1-x}Ca_xMnO_3$' "
M. V. ZIMMERMANN, S. GRENIER, C. S. NELSON, J. P. HILL, DOON GIBBS, M. BLUME, D. CASA, B. KEIMER, Y. MURAKAMI, C.-C. KAO, C. VENKATARAMAN, T. GOG, Y. TOMIOKA and Y. TOKURA
Phys. Rev. B 68, 127102: 1-2 (2003).

17) Low-temperature zigzag charge-ordering structure of alpha'-NaV_2O_5,
H. SAWA, Y. WAKABAYASHI, E. NINOMIYA, T OHAMA, H. NAKAO, Y. MURAKAMI, K. OHWADA, Y. FUJII, Y. NODA, M. ISOBE and Y. UEDA
Physica B, 329, 878-879 (2003).

18) Change in Mn 3d orbital state related to a metal-insulator transition in a bilayer manganite studied by magnetic Compton profile measurement
A. KOIZUMI, T. NAGAO, Y. KAKUTANI, N. SAKAI, K. HIROTA and Y. MURAKAMI
Phys. Rev. B 69 060401: 1-4 (2004).

19) Commensurate-Incommensurate Crossover of Charge Stripe in $La_{2-x}Sr_xNiO_3$(x=1/3)
K. ISHIZUKA, T. ARIMA, Y. MURAKAMI, R. KAJIMOTO, H. YOSHIZAWA, N. NAGAOSA and Y. TOKURA
Phys. Rev. Lett. 92, 196404: 1-4 (2004).

20) Resonant magnetic x-ray scattering from antiferromagnetic order in GdAs,
D. OKUYAMA, T. MATSUMURA, Y. MURAKAMI, Y. WKAKABAYASHI, H. SAWA and D. B. LI
Physica B 345, 63-65 (2004).

21) Application of a portable pulsed magnet to synchrotron radiation experiments
Y. H. MATSUDA, Y. UEDA, H. NOJIRI, T. TAKAHASHI, T. INAMI, K. OHWADA, Y. MURAKAMI and T. ARIMA
Physica B 346-347, 519-523 (2004).

22) Controlled Carrier Generation at a Polarity-Discontinued Perovskite Heterointerface
Jun NISHIMURA, Akira OHTOMO, Atsushi OHKUBO, Youichi MURAKAMI, Masashi KAWASAKI
Jpn. J. Appl. Phys. Vol.43 (2004) No.8A pp.L1032 - L1034

Electric material science (Electronic Material Science Group)

1. Journals

1) Nearly localized nature of f electrons in Ce[T]In_5 ([T]=Rh, Ir)

FUJIMORI Shinichi, OKANE Tetsuo, OKAMOTO Jun, MAMIYA Kazutoshi, MURAMATSU Yasuji, FUJIMORI Atsushi, HARIMA Hisatomo, AOKI Dai, IKEDA Shugo, SHISHIDO Hiroaki, TOKIWA Yoshifumi, HAGA Yoshinori, ONUKI Yoshichika
Physical Review B,67,14,144507_1-144507_5,(2003/04)

2) Angle-resolved soft X-ray emission and absorption spectroscopy of hexagonal boron nitride
MURAMATSU Yasuji, KANEYOSHI Takahiro, GULLIKSON, E. M., PERERA , R. C. C.
Spectrochimica Acta, Part A,59,9,1951-1957,(2003/07)

3) Take-off/incident-angle-dependence of π/σ peak intensity ratio in soft X-ray emission and absorption spectra of graphite and hexagonal boron nitride
MURAMATSU Yasuji, GULLIKSON, E. M., PERERA, R. C. C.
"Advances in X-ray Chemical Analysis" (in Japanese) 34,153-163,(2003/00)

4) Characterization of carbon films on the Japanese smoked roof tile "Ibushi-Kawara" by high-resolution soft X-ray spectroscopy
MURAMATSU Yasuji, MOTOYAMA Muneyuki, DENLINGER, J. D., GULLIKSON, E. M., PERERA, R. C. C.
Japanese Journal of Applied Physics, Part 1,42,10,6551-6555,(2003/10)

5) Soft X-ray emission and absorption spectra of typical solid carbon compounds
MURAMATSU Yasuji, GULLIKSON, E. M., PERERA, R. C. C.
"Advances in X-ray Chemical Analysis" (in Japanese) 35,125-136,(2004/00)

2. Reports

1) Study of closed orbit distortion from high speed phase switching of variably-polarizing undulator APPLE-2 in 2001 March-June
NAKATANI Takeshi, TANAKA Hitoshi, TAKAO Masaru, AGUI Akane, YOSHIGOE Akitaka, TAKEUCHI Masao, AOYAGI Hideki, OKUMA Haruo
JAERI-Tech 2003-048,29,(2003/05)

2) Four-blade-drive style X-ray beam position monitor for soft X-ray beamline BL23SU at SPring-8
AGUI Akane, AOYAGI Hideki, YOSHIGOE Akitaka, NAKATANI Takeshi
JAERI-Tech 2003-089,23,(2003/12)

Synchrotron radiation simulation research (Simulation Group for Materials Science)

1. Journals

1) Bandgaps of $Ga_{1-x}In_xN$ by all-electron GWA calculation
USUDA Manabu, HAMADA Noriaki, SHIRAISHI Kenji, OSHIYAMA Atsushi
Physica Status Solidi (C),0,7,2733-2736,(2003/12)

2) Cooperative Jahn-Teller effect on the X-ray diffraction spectra in DyB_2C_2
NAGAO Tatsuya, IGARASHI Junich
Physica B; Condensed Matter,345,1-4,70-73,(2004/03)

3) Lattice distortion and resonant X-ray scattering in DyB_2C_2
IGARASHI Junichi, NAGAO Tatsuya
Journal of the Physical Society of Japan,72,5,1279-1286,(2003/05)

4) X-ray magnetic circular dichroism at the K edge of Mn_3GaC
TAKAHASHI Manabu, IGARASHI Junichi
Physical Review B,67,24,245104_1-245104_5,(2003/06)

5) Interference between thomson scattering and resonant scattering in X-Ray diffraction from CeB_6
NAGAO Tatsuya, IGARASHI Junichi
Journal of the Physical Society of Japan,72,9,2381-2384,(2003/09)

6) *Ab-Initio* calculation of magnetic resonant X-ray scattering spectra in NiO
USUDA Manabu, TAKAHASHI Manabu, IGARASHI Junichi
Physical Review B,69,1,014408_1-014408_7,(2004/01)

7) Band structures of Wurtzite InN and $Ga_{1-x}In_xN$ by all-electron *GW* calculation
USUDA Manabu, HAMADA Noriaki, SHIRAISHI Kenji, OSHIYAMA Atsushi
Japanese Journal of Applied Physics, Part 2,43,3B,L407-L410,(2004/03)

8) Magnetic resonant x-ray scattering at the Ga K edge in UGa_3: A band theoretical approach,
M. USUDA, J. IGARASHI and A. KODAMA,

Phys. Rev. B **69**, 224402(1-5), 2004.
9) Higher Order Perturbation Expansion for Pairing Interaction in Repulsive Hubbard Model,
T. NOMURA and K. YAMADA,
J. Phys. Soc. Jpn. **72**, 2053-2063, 2003.
10) Theory of Superconductivity in Strongly Correlated Electron Systems,
Y. YANASE, T. JUJO, T. NOMURA, H. IKEDA, T. HOTTA AND K. YAMADA,
Phys. Reports **387**, 1-149, 2003.
11) Possibility of f-Wave Spin-Triplet Superconductivity in the CoO_2 Superconductor: A Case Study on a 2D Triangular Lattice in the Repulsive Hubbard Model,
H. IKEDA, Y. NISIKAWA and K. YAMADA
J. Phys. Soc. Jpn. **73**, 17-20, 2004.

2. Proceedings

1) Resonant X-ray scattering in $KCuF_3$
TAKAHASHI Manabu, IGARASHI Junichi
Physica B; Condensed Matter,329-333,Part2,870-871,(2003/05)
2) Mechanism of resonant X-ray scattering in DyB_2C_2
NAGAO Tatsuya, IGARASHI Junichi
Physica B; Condensed Matter,329-333,Part2,628-630,(2003/05)
3) Magnetic resonant X-ray scattering in $RbMnF_3$: an ab initio study
Manabu USUDA, Manabu TAKAHASHI and Jun-ichi IGARASHI
Physica B, **345**, 30-33, 2004.
4) Ab initio study of magnetic nonresonant and resonant X-ray scattering in $KCuF_3$,
Manabu TAKAHASHI, Manabu USUDA and Jun-ichi IGARASHI
Physica B, **345**, 26-29, 2004.
5) Cooperative Jahn-Teller effect on the X-ray diffraction spectra in DyB_2C_2,
T. NAGAO and Jun-ichi IGARASHI
Physica B, **345**, 70-73, 2004.

Appendix A Activities of the Research Committee

1. The research committee was organized in FY1996 to promote activities on advanced photon and synchrotron radiation research in Kansai Research Establishment, JAERI. There were three technical subcommittees for Laser System, Laser Utilization and Synchrotron Radiation Utilization, under the committee until FY2001. In FY2002 the technical subcommittees are re-organized to the two subcommittees.

1.1 Committee for Advanced Photon and Synchrotron Radiation Research

First meeting	March 21	1997	Tokyo
Second meeting	February 3	1998	Tokyo
Third meeting	March 9	1999	Tokyo
Fourth meeting	February 10	2000	Tokyo
Fifth meeting	March 2	2001	Kashiwa
Sixth meeting	March 11	2002	Kizu
Seventh meeting	February 18	2003	Kizu (Joint meeting*1)
Eighth meeting	December 19	2003	Kizu

Technical Subcommittee for Laser System

First meeting	December 8	1997	Tokyo
Second meeting	July 30	1998	Tokyo
Third meeting	December 13	1999	Tokyo
Fourth meeting	February 1	2001	Tokyo
Fifth meeting	February 12	2002	Kashiwa (Joint meeting*2)

Technical Subcommittee for Laser Utilization

First meeting	December 10	1997	Tokyo
Second meeting	December 3	1998	Tokyo
Third meeting	December 24	1999	Tokyo
Fourth meeting	February 15	2001	Kizu
Fifth meeting	February 12	2002	Kashiwa (Joint meeting*2)

↓ **Re-organized**

1.2 Technical Subcommittee for Advanced Photon Research

First meeting	February 18	2003	Kizu (Joint meeting*1)

Technical Subcommittee for Synchrotron Radiation Utilization

First meeting	December 9	1997	Tokyo
Second meeting	November 27	1998	Harima (SPring-8)
Third meeting	February 8	2000	Harima (SPring-8)
Fourth meeting	February 28	2001	Harima (SPring-8)
Fifth meeting	February 25	2002	Harima (SPring-8)

↓ **Re-organized**

1.3 Technical Subcommittee for Synchrotron Radiation Research

First meeting	February 18	2003	Kizu (Joint meeting*1)

2. The local organizing committee for the 25th International Free Electron Laser Conference was organized in FY2002 to prepare and organize the International Conference. There is a technical subcommittees for the Conference Program under the committee.

2.1 Local Organizing Committee for the 25th International Free Electron Laser Conference

First meeting	October 11	2002	Kashiwa
Second meeting	August 7	2003	Tokyo

2.2 Technical Subcommittee for the Program of the 25th International Free Electron Laser Conference

3. The technical subcommittee for photon science under the committee for evaluation of JAERI research was organized in FY2001.

Technical Subcommittee for Photon Science under the Committee for Evaluation of JAERI Research

First meeting	June 21	2001	Kizu
Second meeting	November 26	2002	Kizu

4. Two technical subcommittees for advanced photon and synchrotron radiation under the committee for JAERI's Facility Use were organized in FY2000.

4.1 Technical Subcommittee for Advanced Photon under the Committee for JAERI's Facility Use

First meeting	December 19	2000	Kizu
Second meeting	January 18	2002	Kizu
Third meeting	January 20	2003	Kizu
Forth meeting	January 16	2004	Kizu

4.2 Technical Subcommittee for Synchrotron Radiation under the Committee for JAERI's Facility Use

First meeting	January 22	2001	Harima (SPring-8)
Second meeting	January 21	2002	Harima (SPring-8)
Third meeting	January 24	2003	Harima (SPring-8)
Forth meeting	January 21	2004	Harima (SPring-8)

Member of Committee

Committee for Advanced Photon and Synchrotron Radiation Research (FY2003)

Chair	Susumu	NAMBA	Professor, Technical Research Center, Nagasaki Institute of Applied Science
Vice-Chair	Seishi	KIKUTA	Executive Director, Deputy Director General, Synchrotron Radiation Research Laboratory, Japan Synchrotron Radiation Research Institute
	Yoshiyuki	AMEMIYA	Professor, Graduate School of Frontier Science, University of Tokyo
	Toshiyuki	IIDA	Professor, Graduate School of Engineering, Osaka University
	Yasukazu	IZAWA	Director, Institute of Laser Engineering, Osaka University
	Kenichi	IMAI	Professor, Graduate School of Science, Kyoto University
	Kenichi	UEDA	Director, Institute for Laser Science, University of Electro-communications
	Tokuhiko	OKAMOTO	Professor, Research Organization of Science and Engineering, Ritsumeikan University
	Hiroshi	KAWATA	Professor, Institute of Materials Science, High Energy Accelerator Research Organization
	Shinichi	KUROKAWA	Deputy Director, Accelerator Laboratory, High Energy Accelerator Research Organization
	Hiroyuki	SAKAKI	Professor, Institute of Industrial Science, University of Tokyo
	Noriko	SHIOMI	Professor, Research Center for Advanced Science and Technology, Nara Institute of Science and Technology
	Akira	NODA	Professor, Institute for Chemical Research, Kyoto University
	Tatsuhiko	YAMANAKA	Director, Institute of Laser Engineering, Osaka University
	Katsumi	MIDORIKAWA	Principal Scientist, Laser Technology Laboratory, Institute of Physical and Chemical Research
	Hirotake	MORIYAMA	Professor, Graduate School of Engineering, Kyoto University
	Tamio	YOSHIDA	Director, Shimadu Corporation
	Toshiki	TAJIMA	Director General, Kansai Research Establishment, JAERI
	Sohei	OKADA	Director, Office of Planning, JAERI
Secretary	Toyoaki	KIMURA	Director, Advanced Photon Research Center, JAERI
	Osamu	SHIMOMURA	Director, Synchrotron Radiation Research Center, JAERI
	Haruyuki	KIMURA	Senior Staff, Office of Planning, JAERI

Local Organizing Committee for the 25th International Free Electron Laser Conference (FY2003)

Chair	Koichi	SHIMODA	Professor Emeritus, University of Tokyo
Vice-Chair	Tetsuo	YAMAZAKI	Professor, Institute of Advanced Energy, Kyoto University
Vice-Chair	Takio	TOMIMASU	Team Leader, Saga Prefectural Regional Industry Support Center
	Haruo	KURODA	Professor, Research Institute for Science and Technology, Science University of Tokyo
	Hiroyuki	HAMA	Professor, Graduate School of Science, Tohoku University
	Kazuo	IMASAKI	Principal Scientist, Laser Process Group, Institute for Laser Technology
	Kawakatsu	YAMADA	Prime Scientist, Photonics Research Institute, National Institute of Advanced Industrial Science and Technology
	Kunio	AWAZU	Professor, Graduate School of Engineering, Osaka University
	Yusuke	TOMITA	Director, Kansai Research Institute, JAERI
	Toyoaki	KIMURA	Director, Advanced Photon Research Center, JAERI
	Taikan	HARAMI	Principal Scientist, Synchrotron Radiation Research Center, JAERI
	Haruyuki	KIMURA	Senior Staff, Office of Planning, JAERI
Secretary	Eisuke	MINEHARA	Principal Scientist, Advanced Photon Research Center, JAERI
	Ryoichi	HAJIMA	Principal Scientist, Advanced Photon Research Center, JAERI
	Masaru	SAWAMURA	Senior Scientist, Advanced Photon Research Center, JAERI
	Ryoji	NAGAI	Senior Scientist, Advanced Photon Research Center, JAERI
	Shigeru	MORI	Administrative Manager, Advanced Photon Research Center, JAERI

Technical Subcommittee for the Program of the 25th International Free Electron Laser Conference (FY2003)

Chief	Tetsuo	YAMAZAKI	Professor, Institute of Advanced Energy, Kyoto University
Committee	Kawakatsu	YAMADA	Prime Scientist, Photonics Research Institute, National Institute of Advanced Industrial Science and Technology
	Kunio	AWAZU	Professor, Graduate School of Engineering, Osaka University
Subcommittee	Kuniyoshi	YOKOO	Professor, Research Institute of Electrical Communication, Tohoku University
	Akira	IWATA	Professor, Research Institute for Science and Technology, Science University of Tokyo
	Ken	TAKAYAMA	Professor, Accelerator Laboratory, High Energy Accelerator Research Organization
	Hideo	KITAMURA	Principal Scientist, Harima Institute, Institute of Physical and Chemical Research
	Tsumoru	SHINTAKE	Principal Scientist, Harima Institute, Institute of Physical and Chemical Research
	Isamu	SATO	Professor, Institute of Quantum Science, Nihon University
	Masayuki	KAWAI	Special Advisor, Kawasaki Heavy Industries, Ltd.
	Natsuro	TSUBOUCHI	Professor, Graduate School of Engineering, Osaka University
	Makoto	ASAKAWA	Assistant Professor, Graduate School of Engineering, Osaka University
	Goro	ISOYAMA	Professor, Institute of Scientific and Industrial Research, Osaka University
	Ryuko	KATO	Assistant Professor, Institute of Scientific and Industrial Research, Osaka University
	Shuji	MIYAMOTO	Assistant Professor, Laboratory of Advanced Science and Technology for Industry, Himeji Institute of Technology
	Yoshiaki	TSUNAWAKI	Professor, Faculty of engineering, Osaka Sangyo University
	Masahito	HOSAKA	Assistant Researcher, Institute for Molecular Science, Okazaki National Research Institute
	Hideaki	OGAKI	Assistant Professor, Institute of Advanced Energy, Kyoto University
	Kai	MASUDA	Assistant Researcher, Institute of Advanced Energy, Kyoto University
	Hirobumi	SAITO	Professor, Research Division for Spacecraft Engineering, Institute of Space and Astronautical Science
	Takahide	MIZUNO	Assistant Professor, Center for Advanced Spacecraft Technology, Institute of Space and Astronautical Science
	Shigeru	YAMAMOTO	Professor, Institute of Material Structure Science, High Energy Accelerator Research Organization
	Shigenori	HIRAMATSU	Professor, Accelerator Laboratory, High Energy Accelerator Research Organization
	Ken	HAYAKAWA	Assistant Professor, Institute of Quantum Science, Nihon University
	Shuichi	OKUDA	Professor, Research Institute for Advanced Science and Technology, Osaka Prefecture University
	Norihiro	SEI	Principal Scientist, Collaboration Department, National Institute of Advanced Industrial Science and Technology
	Hironari	YAMADA	Professor, Faculty of Science and Engineering, Ritsumeikan University
	Hiroshi	HORIIKE	Professor, Graduate School of Engineering, Osaka University

Technical Subcommittee for Advanced Photon under the Committee for JAERI's Facility Use (FY2003)

Chief	Kunio	SHINOHARA	Visiting Professor, Tokyo Metropolitan Organization for Medical Research, The Tokyo Metropolitan Institute of Medical Science
Vice-chief	Takashi	FUJIMOTO	Professor, Graduate School of Engineering, Kyoto University
Subcommittee	Yoshihiko	KANAMITSU	Professor, Graduate School of Materials Science, Nara Institute of Science and Technology (until December) Professor, Institute for Chemical Research, Kyoto University (from January)
	Hiroo	KINOSHITA	Professor, Laboratory of Advanced Science and Technology for Industry, Himeji Institute of Technology
	Yutaka	TSUCHIYA	Deputy Director General, Central Research Laboratory, Hamamatsu Photonics K.K.
	Katsunobu	NISHIHARA	Professor, Institute of Laser Engineering, Osaka University
	Akira	NODA	Professor, Institute for Chemical Research, Kyoto University
	Atsushi	YOKOYAMA	Director, Department of Materials Science, JAERI
	Shigeru	TANAKA	Deputy Director, Department of Material Development, JAERI
	Toyoaki	KIMURA	Director, Advanced Photon Research Center, JAERI
	Akira	NAGASHIMA	Deputy Director, Advanced Photon Research Center, JAERI
	Mitsuru	YAMAGIWA	Principal Scientist, Advanced Photon Research Center, JAERI
	Masato	KOIKE	Principal Scientist, Advanced Photon Research Center, JAERI

Technical Subcommittee for Synchrotron Radiation under the Committee for JAERI's Facility Use (FY2003)

Chief	Yoshichika	OHNUKI	Professor, Graduate School of Science, Osaka University Invited Researcher, Advanced Science Research Center, JAERI
Vice-chief	Haruki	KAWAMURA	Professor, Faculty of Science, Himeji Institute of Technology
Subcommittee	Hiroshi	SAWA	Assistant Professor, Institute of Materials Structure Science, High Energy Accelerator Research Organization
	Makoto	SAKATA	Professor, Graduate School of Engineering, Nagoya University Invited Researcher, Synchrotron Radiation Research Center, JAERI
	Ken'ichiro	TANAKA	Professor, Graduate School of Science, Hiroshima University
	Kazuhisa	KAKURAI	Group Leader, Advanced Science Research Center, JAERI
	Hirofumi	NAMATAME	Professor, Hiroshima Synchrotron Radiation Center, Hiroshima University
	Osamu	SHIMOMURA	Director, Synchrotron Radiation Research Center, JAERI
	Jun'ichiro	MIZUKI	Deputy Director, Synchrotron Radiation Research Center, JAERI

Appendix B Organization of Kansai Research Establishment

(April 1, 2003～March 31, 2004)

- Kansai Research Establishment (Director General: **T.TAJIMA**)
  - **Department of Administrative Services** (Director: **Y.TOMITA**(until September) **T.KANAZAWA**(from October))
    - Administrative Services Division (G. M.: **T.SATO**)
    - Accounts Division (G. M.: **H.TANAKA**)
    - Utilities and Maintenance Division (G. M.: **T.KONNO**(until September) **T.KANAZAWA**(from October))
    - Safety Division (G. M.: **I.MANABE**)
  - **Advanced Photon Research Center** (Director: **T.KIMURA**)
    - Division of Advanced Photon Research Promotion (G. M.: **A.NAGASHIMA**)
    - Laser System Development Group (G. L.: **A.NAGASHIMA**)
    - X-ray Laser Research Group (G. L.: **K.NAGASHIMA**)
    - Novel Optics Research Group (G. L.: **M.KOIKE**)
    - Laser Acceleration Research Group (G. L.: **K.NAKAJIMA**)
    - Simulation Group for Advanced Photon Science (G. L.: **M.YAMAGIWA**)
    - Free Electron Laser Research Group (G. L.: **E.MINEHARA**)
    - Applied Photon Research Group (G. L.: **H.DAIDO**)
  - **Synchrotron Radiation Research Center** (Director: **O.SHIMOMURA**) (until March)
    - Synchrotron Radiation Administration Division (G. M.: **H.YOSHIDA**) (until March)
    - Experimental Facilities Development Group (G. L.: **T.HARAMI**)
    - High Pressure Science Group (G. L.: **K.AOKI**)
    - Structural Physics Research Group (G. L.: **J.MIZUKI**)
    - Surface Chemistry Research Group (G. L.: **Y.BABA**)
    - Heavy Atom Science Group (G. L.: **Y.MURAKAMI**)
    - Electronic Material Science Group (G. L.: **Y.MURAMATSU**)
    - Simulation Group for Materials Science (G. L.: **J.IGARASHI**) (until March)

G. M.: General Manager G. L.: Group Leader

Appendix C Personnel

(April 1, 2003～March 31, 2004)

Personnel at Advanced Photon Research Center

Toyoaki KIMURA
Akira NAGASHIMA
Norio OGIWARA(until September)
Osamu YAMASHITA
Shigeru MORI
Masaaki AKUTSU
Rika SUMITANI
Masako SHIGENARI
Yoko GENBA(from November)
Miwa ARAI(from December)
Yasuo HOTTA(from June)

Division of Advanced Photon Research Promotion
Akira NAGASHIMA
Masataka KADO
Sayaka HARAYAMA
Shuichi FUJITA(until May)
Ichiro YAMASAKI(from June)
Jun NAKAJIMA(until August)
Midori NAKAO
(from September)
Naoyuki SINOHARA
(until December)
Masamitsu OIKAWA
(from January until February)
Toshihiro OSAKI(from March)

Laser System Development Group
Koichi YAMAKAWA
Akihiko NISHIMURA
Junji KAWANAKA
Hiromitsu KIRIYAMA
Yutaka AKAHANE
Makoto AOYAMA
Keiichi YOKOYAMA
Fumiaki MATSUOKA
Norihiro INOUE
Yoshiki NAKAI
Tadashi TAMADA
Yuji FUKUDA
Kazuhiko SUMIMURA
Yukio TOYA
Hidetaka YAMADA
Akihiro SUGITA
Hideki UEDA
Koichi TSUJI
Yoichi YAMAMOTO

X-ray Laser Research Group
Keisuke NAGASHIMA
Maki KISHIMOTO
Yoji SUZUKI
Tetsuya KAWACHI
Noboru HASEGAWA
Momoko TANAKA
Yoshihiro OCHI
Kouta SUKEGAWA
Renzhong TAI
Masaharu NISHIKINO
Kazumichi NAMIKAWA
(from October)

Novel Optics Research Group
Masato KOIKE
Yuichi SHIMIZU
Osamu YODA
Akira SUGIYAMA
Masahiko ISHINO
Yasunaga NARA
Takashi IMAZONO
Kazuo SANO

Applied Photon Research Group
Hiroyuki DAIDO
Yuzuru KUROSAKI
Koichi OGURA
Hiroshi MURAKAMI
Akito SAGISAKA
Satoshi ORIMO
Yukio HAYASHI
Mamiko NISHIUCHI
Michiaki MORI
Etsuya YANASE(until May)
Hisanao HAZAMA
(from June)
Yoshiaki TERANISHI
Shu NAKAMURA
Kenichi TAKAGAKI
Koji MATSUKADO
Atsushi FUKUMI
Zhong LI
Alexander PIROZHKOV
(from November)

Laser Acceleration Research Group
Kazuhisa NAKAJIMA
Yuichi SHIMIZU
Shuhei KANAZAWA
Hideyuki KOTAKI
Shuji KONDO
Masaki KANDO
Takayuki HONMA
Shinichi MASUDA
Igor V. SNETANIN
(until September)
Atsushi YAMAZAKI
(from October)
Izuru DAITO(from January)

Simulation Group for Advanced Photon Science
Mitsuru YAMAGIWA
Akira SASAKI
James KOGA
Kengo MORIBAYASHI
Yutaka UESHIMA
Takayuki UTSUMI
Takao KONDO(until September)
Nayu TSUJI(until September)
Kanji SAITO(from November)
Timur ESIRKEPOV
Sergei V. BULANOV
(from October)

Free Electron Laser Research Group
Eisuke MINEHARA
Toshihiko YAMAUCHI
Ryoichi HAJIMA
Masaru SAWAMURA
Ryoji NAGAI
Takehito HAYAKAWA
Nobuhiro KIKUZAWA
Nobuyuki NISHIMORI
Toshiyuki SHIZUMA
Kiyomi ENDOH

(April 1, 2003～March 31, 2004)

Personnel at Synchrotron Radiation Research Center

Osamu SHIMOMURA(until March)
Jun'ichiro MIZUKI
Noboru TSUCHIDA
Isao TAKARIKO(until September)
Teikichi SASAKI(until March)
Hiroko NISHIZAKI
Sae TAMURA

Experimental Facilities Development Group
Taikan HARAMI
Hiroyuki KONISHI
Yoshihiro ASANO
Hideaki SHIWAKU
Kazukiyo TOZAWA(until March)
Takahisa SHOBU
Koji KIRIYAMA
Masayoshi TAKEYAMA(from July)

High Pressure Science Group
Katsutoshi AOKI
Nozomu HAMAYA
Makoto SAKATA(until March)
Wataru UTSUMI
Yoshinori KATAYAMA
Tetsu WATANUKI
Akihiko MACHIDA
Hiroshi KANEKO
Yasuhiro INAMURA(until March)
Tomohiro IKEDA(until March)
Hiroyuki SAITOH(from April)

Structural Physics Research Group
Jun'ichiro MIZUKI
Yasuo NISHIHATA
Kentaro SUZUYA(until September)
Norimasa MATSUMOTO(until March)
Kenji YOSHII
Masamitsu TAKAHASHI
Yasuhiro YONEDA
Tatsuo FUKUDA
Kazuhisa TAMURA
Yuka OKAJIMA
Takahiro SHINOHARA(from April)

Simulation Group for Materials and Science
Jun'ichi IGARASHI(until March)
Takuji NOMURA(from April)
Manabu USUDA
Yunori NISHIKAWA(from April)

Surface Chemistry Research Group
Yuji BABA
Akinari YOKOYA(until March)
Yuden TERAOKA
Tetsuhiro SEKIGUCHI
Akitaka YOSHIGOE
Iwao SHIMOYAMA
Kentaro FUJII(until March)
Krishna G. NATH
Kosuke MORITANI
Shunsuke HACHIUE(from April)
Masahito TANAKA(from April- until March)
Uddin Md. NIZAM(from April)

Heavy Atom Science Group
Youichi MURAKAMI
Makoto SETO
Toshiya INAMI
Takaya MITSUI
Kenji ISHII
Kenji OHWADA
Kaori KUZUSHITA

Electronic Material Science Group
Yasuji MURAMATSU
Atsushi FUJIMORI
Tetsuo OKANE
Yuji SAITOH
Akane AGUI
Takeshi NAKATANI(until March)
Shin'ichi FUJIMORI
Jun OKAMOTO(until March)
Kazutoshi MAMIYA(until August)
Kota TERAI(from April)
Yukiharu TAKEDA(from October)
Kentoro KURAMOTO(until March)
Ayuko FUJIMOTO(from April- until March)

Synchrotron Radiation Administration Division
Hiroshi YOSHIDA(until March)
Yukio SHINPO(until March)
Masahiko MATSUMOTO
Toshinori SUZUKI(until March)
Sachiko MITSUDERA
Junko MARUO(until September)
Kyoko NISHIMURA(from October)

(April 1, 2003～March 31, 2004)

Personnel at Kansai Research Establishment

Toshiki TAJIMA
Takashi ARISAWA
Hitoshi IHARA

Personnel at Department of Administrative Services

Yusuke TOMITA(until September)
Tetsuo Kanazawa(from October)
Hiroshi YOSHIDA

Administrative Services Division

Takashi SATO
Hiroshi YOSHIDA
Mamoru SUZUKI
Daisuke USHIJIMA
Tatsuki SUKEGAWA
Yuji HASHIMOTO
Yuko HASEGAWA
Michiyo HASHIMOTO
Sumika HATAYAMA

Accounts Division

Hiroshi TANAKA
Shintaro EJIRI
Yuichi SUNAOSHI
Yoji MIYAMOTO
Hitoshi YAMAGUCHI
Nobuyuki UENO
Keiichi TSUKAMOTO
Kazumi TAKEDA
Reiko IYORI

Utilities and Maintenance Division

Toshio KONNO(until September)
Toshihiko SENZAKI
Ryuichi OI
Yuki MIYOSHI
Akio SUGANUMA(from October)
Tetsuya YAMAMOTO
Kotomi WAKI

Safety Division

Iwao MANABE
Masayuki UENO
Yaichi FUKUSHIMA
Akira MIHARA
Koichi IKENO(from October)
Isao TAKARIKO(until September)
Sadahisa RINSAKA(from November)
Izumi TAMURA

Appendix D Symposia

FY1997

(1) The first JAERI-Kansai International Workshop on Ultrashort-pulse Ultrahigh-power Lasers and Simulation for Laser-plasma Interactions (held as "Joint ICFA/JAERI-Kansai International Workshop '97", organized by International Committee for Future Accelerators, hosted by Japan Atomic Energy Research Institute and High Energy Accelerator Research Organization)

July 14-18, **1997**, Kyoto, Japan

JAERI-Conf 98-004, "Proceedings of The first JAERI-Kansai International Workshop on Ultrashort-pulse Ultrahigh-power Lasers and Simulation for Laser-plasma Interactions, July 14-18, 1997, Kyoto Research Park, Kyoto, Japan", March 1998.

(2) The 6th International Conference on Synchrotron Radiation Instrumentation (cosponsored by Japan Atomic Energy Research Institute, Japanese Society for Synchrotron Radiation Research, RIKEN and Japan Synchrotron Radiation Research Institute)

August 4-8, **1997**, Himeji, Japan

J. Synchrotron Radiation, 5 part 3, "SRI'97 Proceedings", May 1998.

FY1998

(3) 6th International Conference on X-Ray Lasers (cosponsored by Japan Atomic Energy Research Institute and Osaka University)

August 31-September 4, **1998**, Kyoto, Japan

Institute of Physics Conference Series Number 159, "Proceedings of the 6th International Conference on X-Ray Lasers held in Kyoto, Japan, August 31-September 4, 1998"

(4) The Second International Conference on Synchrotron Radiation in Materials Science (cosponsored by Japan Atomic Energy Research Institute, RIKEN and Japan Synchrotron Radiation Research Institute)

October 31-November 3, **1998**, Kobe, Japan

Jpn. J. Appl. Phys. Suppl., 38-1, "Proceedings of the SRMS-2", June 1999.

FY1999

(5) The First Symposium on Advanced Photon Research

November 8-9, **1999**, Kyoto, Japan

JAERI-Conf 2000-006, "Proceedings of The First Symposium on Advanced Photon Research, November 8-9, 1999, Keihanna Plaza/Advanced Photon Research Center, Kyoto, Japan", March 2000.

(6) Workshop on Surface and Interface Using Synchrotron Radiation

March 16-17, **2000**, SPring-8, Japan

FY2000

(7) The Second Symposium on Advanced Photon Research

November 9-10, **2000**, Kyoto, Japan

JAERI-Conf 2001-011, "Proceedings of The Second Symposium on Advanced Photon Research, November 9-10, 2000, Advanced Photon Research Center, Kyoto, Japan", July 2001.

(8) 2nd UK-Japan International Seminar of Application Radiation to Studies of Nano-structured Materials

(cosponsored by institute of Molecular Science, Japan Atomic Energy research Institute, RIKEN and JASRI)

July 9-10, **2000**, SPring-8, Japan

(9) International Workshop on "Crystallography at High Pressure and High Temperature using X-ray and Neutrons"

(cosponsored by Synchrotron Radiation Research Center of JAERI, JASRI and International Union of Crystallography Commission on High Pressure)

September 30-October 3, **2000**, SPring-8, Japan

FY2001

(10) OECD Global Science Forum "Workshop on Compact High-Intensity Short-Pulse Lasers: Future Directions and Applications"
(cosponsored by OECD Global Science Forum and JAERI)
May 28-30, **2001**, Kansai Research Establishment, Kyoto, Japan
OECD Global Science Forum, "Final Report from the Workshop"

(11) The Third Symposium on Advanced Photon Research
December 13-14, **2001**, Kyoto, Japan
JAERI-Conf 2002-008, "Proceedings of The Third Symposium on Advanced Photon Research, December 13-14, 2001, Advanced Photon Research Center, Kyoto, Japan", July 2002.

(12) Korean-Japanese International workshop on Strongly Correlated Electron Systems
September 3-4, **2001**, SPring-8, Japan

FY2002

(13) International Workshop on Photoionization (IWP2002)
(hosted by Japan Synchrotron Radiation Research Institute (JASRI), RIKEN (The Institute of Physical and Chemical Research), Japan Atomic Energy Research Institute (JAERI), Hyogo Prefecture)
August 22-26, **2002**, SPring-8, Hyogo, Japan

(14) JAERI Symposium on Control of Lasers for Strong Field Phenomena
September 12-13, **2002**, Kyoto, Japan

(15) The 5th SRRTNet Workshop "Interface between theory, computation and experiments"
(Organized by Japan Atomic Energy Research Institute (JAERI), Research Institute of Chemical Sciences (RIKEN), High Energy Physics Research Organization (KEK-PF) and Japan Synchrotron Radiation Research Institute (JASRI))
October 15-16, **2002**, SPring-8, Japan

(16) The Fourth Symposium on Advanced Photon Research
November 28-29, **2002**, Kyoto, Japan
JAERI-Conf 2003-008, "Proceedings of The Fourth Symposium on Advanced Photon Research, November 28-29, 2002, Advanced Photon Research Center, Kyoto, Japan", July 2003.

FY2003

(17) 25th International Free Electron Laser Conference & 10th FEL Users Workshop (FEL2003)
Septemberr 8-12, **2003**, Tsukuba, Japan
Proceedings of the 25th Free Electron Laser Conference, August 2004

(18) The Fifth Symposium on Advanced Photon Research
November 20-21, **2003**, Kyoto, Japan
JAERI-Conf 2004-009, "Proceedings of The Fifth Symposium on Advanced Photon Research, November 20-21, 2003, Advanced Photon Research Center, Kyoto, Japan", June 2004.

(19) JAERI International Workshop on "X-Ray Scattering and Electronic Structure"
(Supported by Japan Atomic Energy Research Institute (JAERI), Japan Synchrotron Radiation Research Institute (JASRI))
December 11, 12, **2003**, SPring-8, Japan

(20) International Kickoff Workshop; Relativistic Engineering and Extreme Field Science
Januray 6-7, **2004**, Kyoto, Japan

(21) Domestic Workshop "Development and View of Physical-properties Science using Synchrotron

Radiation"
(Supported by Japan Atomic Energy Research Institute (JAERI))
March 18-19, **2004**, SPring-8, Japan

国際単位系 (SI) と換算表

表 1　SI基本単位および補助単位

量	名称	記号
長さ	メートル	m
質量	キログラム	kg
時間	秒	s
電流	アンペア	A
熱力学温度	ケルビン	K
物質量	モル	mol
光度	カンデラ	cd
平面角	ラジアン	rad
立体角	ステラジアン	sr

表 2　SIと併用される単位

名称	記号
分，時，日	min，h，d
度，分，秒	°，′，″
リットル	l，L
トン	t
電子ボルト	eV
原子質量単位	u

1 eV = 1.60218 × 10^{-19} J

1 u = 1.66054 × 10^{-27} kg

表 5　SI接頭語

倍数	接頭語	記号
10^{18}	エクサ	E
10^{15}	ペタ	P
10^{12}	テラ	T
10^{9}	ギガ	G
10^{6}	メガ	M
10^{3}	キロ	k
10^{2}	ヘクト	h
10^{1}	デカ	da
10^{-1}	デシ	d
10^{-2}	センチ	c
10^{-3}	ミリ	m
10^{-6}	マイクロ	μ
10^{-9}	ナノ	n
10^{-12}	ピコ	p
10^{-15}	フェムト	f
10^{-18}	アト	a

表 3　固有の名称をもつSI組立単位

量	名称	記号	他のSI単位による表現
周波数	ヘルツ	Hz	s^{-1}
力	ニュートン	N	m·kg/s^2
圧力，応力	パスカル	Pa	N/m^2
エネルギー，仕事，熱量	ジュール	J	N·m
工率，放射束	ワット	W	J/s
電気量，電荷	クーロン	C	A·s
電位，電圧，起電力	ボルト	V	W/A
静電容量	ファラド	F	C/V
電気抵抗	オーム	Ω	V/A
コンダクタンス	ジーメンス	S	A/V
磁束	ウェーバ	Wb	V·s
磁束密度	テスラ	T	Wb/m^2
インダクタンス	ヘンリー	H	Wb/A
セルシウス温度	セルシウス度	℃	
光束	ルーメン	lm	cd·sr
照度	ルクス	lx	lm/m^2
放射能	ベクレル	Bq	s^{-1}
吸収線量	グレイ	Gy	J/kg
線量当量	シーベルト	Sv	J/kg

表 4　SIと共に暫定的に維持される単位

名称	記号
オングストローム	Å
バーン	b
バール	bar
ガル	Gal
キュリー	Ci
レントゲン	R
ラド	rad
レム	rem

1 Å = 0.1 nm = 10^{-10} m

1 b = 100 fm^2 = 10^{-28} m^2

1 bar = 0.1 MPa = 10^5 Pa

1 Gal = 1 cm/s^2 = 10^{-2} m/s^2

1 Ci = 3.7 × 10^{10} Bq

1 R = 2.58 × 10^{-4} C/kg

1 rad = 1 cGy = 10^{-2} Gy

1 rem = 1 cSv = 10^{-2} Sv

（注）

1. 表1－5は「国際単位系」第5版，国際度量衡局 1985年刊行による。ただし，1 eVおよび1 uの値はCODATAの1986年推奨値によった。
2. 表4には海里，ノット，アール，ヘクタールも含まれているが日常の単位なのでここでは省略した。
3. barは，JISでは流体の圧力を表わす場合に限り表2のカテゴリーに分類されている。
4. EC閣僚理事会指令ではbar，barnおよび「血圧の単位」mmHgを表2のカテゴリーに入れている。

換算表

力	N(=10^5 dyn)	kgf	lbf
	1	0.101972	0.224809
	9.80665	1	2.20462
	4.44822	0.453592	1

粘度　1 Pa·s(N·s/m^2) = 10 P(ポアズ)(g/(cm·s))

動粘度　1 m^2/s = 10^4 St(ストークス)(cm^2/s)

圧力	MPa(=10 bar)	kgf/cm^2	atm	mmHg(Torr)	lbf/in^2(psi)
	1	10.1972	9.86923	7.50062 × 10^3	145.038
	0.0980665	1	0.967841	735.559	14.2233
	0.101325	1.03323	1	760	14.6959
	1.33322 × 10^{-4}	1.35951 × 10^{-3}	1.31579 × 10^{-3}	1	1.93368 × 10^{-2}
	6.89476 × 10^{-3}	7.03070 × 10^{-2}	6.80460 × 10^{-2}	51.7149	1

エネルギー・仕事・熱量	J(=10^7 erg)	kgf·m	kW·h	cal(計量法)	Btu	ft·lbf	eV
	1	0.101972	2.77778 × 10^{-7}	0.238889	9.47813 × 10^{-4}	0.737562	6.24150 × 10^{18}
	9.80665	1	2.72407 × 10^{-6}	2.34270	9.29487 × 10^{-3}	7.23301	6.12082 × 10^{19}
	3.6 × 10^6	3.67098 × 10^5	1	8.59999 × 10^5	3412.13	2.65522 × 10^6	2.24694 × 10^{25}
	4.18605	0.426858	1.16279 × 10^{-6}	1	3.96759 × 10^{-3}	3.08747	2.61272 × 10^{19}
	1055.06	107.586	2.93072 × 10^{-4}	252.042	1	778.172	6.58515 × 10^{21}
	1.35582	0.138255	3.76616 × 10^{-7}	0.323890	1.28506 × 10^{-3}	1	8.46233 × 10^{18}
	1.60218 × 10^{-19}	1.63377 × 10^{-20}	4.45050 × 10^{-26}	3.82743 × 10^{-20}	1.51857 × 10^{-22}	1.18171 × 10^{-19}	1

1 cal = 4.18605 J (計量法)

= 4.184 J (熱化学)

= 4.1855 J (15 °C)

= 4.1868 J (国際蒸気表)

仕事率　1 PS (仏馬力)

= 75 kgf·m/s

= 735.499 W

放射能	Bq	Ci
	1	2.70270 × 10^{-11}
	3.7 × 10^{10}	1

吸収線量	Gy	rad
	1	100
	0.01	1

照射線量	C/kg	R
	1	3876
	2.58 × 10^{-4}	1

線量当量	Sv	rem
	1	100
	0.01	1

（86年12月26日現在）

Annual Report of Kansai Research Establishment 2003 April 1, 2003 – March 31, 2004

R100
古紙配合率100%
白色度70%再生紙を使用しています。